

**BACTERIAL POPULATION DYNAMICS  
UNDER MULTIDRUG TREATMENTS**

A thesis submitted to attain the degree of  
DOCTOR OF SCIENCES  
(Dr. sc. ETH Zurich)

presented by  
**MALTE MÜTTER**  
MSc., Technische Universität Berlin  
born on December 1st, 1992

accepted on the recommendation of  
Prof. Dr. Sebastian Bonhoeffer, examiner  
Prof. Dr. Roland R. Regoes, co-examiner  
Prof. Dr. Tobias Bollenbach, co-examiner



## Summary

---

Since the discovery of penicillin, antibiotics have been a cornerstone of modern medicine. This achievement is now under threat, as bacteria have evolved resistance to antibiotics across all major drug classes. Slowing the rise of resistance will require changes in how existing antibiotics are deployed. In this thesis, we investigate the pharmacodynamics of drug combinations and how multidrug treatment strategies shape the dynamics of plasmid-mediated resistance.

In time-critical clinical emergencies such as sepsis, therapy cannot wait for phenotypic susceptibility testing and therefore relies on predefined empirical strategies. To assess how these strategies affect the persistence of plasmid-mediated resistance and the emergence of double resistance, we conducted large-scale automated *in vitro* experiments that mimic hospital-like transmission dynamics. Across most scenarios, treating patients with two antibiotics simultaneously (combination therapy) was the most effective strategy.

Because the effectiveness of combination therapy is shaped by drug interactions (i.e. synergy, antagonism, or independence), defined via deviations from expected combined effects. To assess treatment effects at clinically relevant inhibitory conditions in high throughput, we evaluated whether bioluminescence-based light intensity is a suitable proxy for cell number dynamics. For 20 antimicrobials, we compared bioluminescence trajectories to colony-forming unit (CFU) counts and supplemented these experiments with microscopy. We found that bioluminescence aligns better with biomass dynamics than with cell number dynamics, but both measures show similar dynamics when cell size remains approximately constant. Conversely, we observed that CFU-based estimates can be biased by drug-induced changes in culturability and by antibiotic carry-over.

Using the bioluminescence method, we quantified antibiotic interactions for 15 drug pairs across checkerboards spanning sub-inhibitory to inhibitory concentrations. We found that interaction types at sub-inhibitory concentrations frequently differ from those at inhibitory concentrations. In addition, interaction types can vary with mixing ratio and depend on the chosen reference model. Together, these results highlight the potential of combination therapy, provide methodological insights to optimise it, and caution against uncritical extrapolation of findings across the measured concentration space



## Zusammenfassung

---

Seit der Entdeckung des Penicillins sind Antibiotika ein Grundpfeiler der modernen Medizin. Diese Errungenschaft ist heute bedroht, da Bakterien Resistenzmechanismen gegen die meisten Antibiotikaklassen entwickelt haben. Um den Anstieg der Resistenz zu verlangsamen, sind Änderungen in der Art, wie Antibiotika eingesetzt werden, notwendig. In dieser Arbeit untersuchen wir die Pharmakodynamik von Antibiotikakombinationen und wie multidrug Behandlungsstrategien die Dynamik plasmidvermittelter Resistenz beeinflussen. In zeitkritischen klinischen Notfällen wie einer Sepsis kann die Therapie nicht auf phänotypische Empfindlichkeitstests warten und stützt sich daher auf vordefinierte empirische Behandlungsstrategien. Um zu untersuchen, wie solche Strategien die Persistenz plasmidvermittelter Resistenz und das Entstehen doppelter Resistenz beeinflussen, führten wir großskalige automatisierte *in vitro*-Experimente durch, die krankenhausähnliche Transmissionsdynamiken nachbilden. Über die meisten Szenarien hinweg war es am effektivsten, Patienten mit zwei Antibiotika gleichzeitig zu behandeln (Kombinationstherapie).

Da die Wirksamkeit der Kombinationstherapie durch Arzneimittelinteraktionen (d. h. Synergie, Antagonismus oder Unabhängigkeit) geprägt wird, die als Abweichungen von erwarteten kombinierten Effekten definiert sind. Um Behandlungseffekte unter klinisch relevanten hemmenden Bedingungen in hohem Durchsatz erfassen zu können, prüften wir, ob biolumineszenzbasierte Lichtintensität ein geeigneter Proxy für die Zellzahldynamik ist. Für 20 antimikrobielle Wirkstoffe verglichen wir Biolumineszenz-Zeitreihen mit Koloniebildenden Einheiten (CFU) und ergänzten diese Experimente durch Mikroskopie. Wir fanden, dass Biolumineszenz die Biomassedynamik besser abbildet als die Zellzahldynamik, dass jedoch beide Maße ähnliche Dynamiken zeigen, wenn die Zellgröße näherungsweise konstant bleibt. Andererseits beobachteten wir, dass CFU-basierte Schätzungen durch wirkstoffinduzierte Veränderungen der Kultivierbarkeit und durch Antibiotika-Übertrag (carry-over) verzerrt sein können.

Mithilfe dieser biolumineszenzbasierten Methode quantifizierten wir Antibiotikainteraktionen für 15 Wirkstoffpaare auf Checkerboards, die nicht-hemmende bis hemmende Konzentrationen abdecken. Wir fanden, dass Interaktionstypen bei nicht-hemmenden Konzentrationen häufig von denen bei hemmenden Konzentrationen abweichen. Zudem können Interaktionstypen vom Mischnungsverhältnis abhängen und vom gewählten Referenzmodell beeinflusst werden. Zusammen zeigen diese Ergebnisse das Potenzial der Kombinationstherapie, liefern methodische Einsichten zu ihrer Optimierung und mahnen zur Vorsicht bei der unkritischen Extrapolation von Befunden über den gemessenen Konzentrationsraum hinweg.

## Contents

---

<b>Chapter 1 General Introduction</b>	<b>1</b>
1.1 Antibiotic Resistance Evolution . . . . .	2
1.2 Treatment Strategies . . . . .	2
1.3 Drug interactions . . . . .	3
1.4 Thesis outline . . . . .	4
<b>Chapter 2 The Impact of Treatment Strategies on the Epidemiological Dynamics of Plasmid-Conferred Antibiotic Resistance</b>	<b>9</b>
2.1 Introduction . . . . .	10
2.2 Results . . . . .	11
2.3 Discussion . . . . .	17
2.4 Methods . . . . .	20
<b>Chapter 3 High-Throughput Quantification of Population Dynamics using Luminescence</b>	<b>27</b>
3.1 Introduction . . . . .	28
3.2 Results . . . . .	29
3.3 Discussion . . . . .	37
3.4 Methods . . . . .	39
<b>Chapter 4 Antimicrobial Combination Effects at Sub-inhibitory Doses do not Reliably Predict Effects at Inhibitory Concentrations</b>	<b>45</b>
4.1 Introduction . . . . .	46
4.2 Results . . . . .	47
4.3 Discussion . . . . .	52
4.4 Methods . . . . .	54
<b>Chapter 5 Concluding Remarks</b>	<b>61</b>
<b>Appendix A The Impact of Treatment Strategies on the Epidemiological Dynamics of Plasmid-Conferred Antibiotic Resistance</b>	<b>67</b>
<b>Appendix B High-Throughput Quantification of Population Dynamics using Luminescence</b>	<b>101</b>
<b>Appendix C Antimicrobial Combination Effects at Sub-inhibitory Doses do not Reliably Predict Effects at Inhibitory Concentrations</b>	<b>137</b>

## Chapter 1

### General Introduction

---

For most of human history, bacterial infections were a leading cause of illness and death. Two notorious examples are *Yersinia pestis* (*Y. pestis*), which likely caused the Justinianic Plague (541–750) [<https://doi.org/10.1371/journal.ppat.1003349>] and later the Black Death (1347–1351) that killed about one third of Europe's population [<https://doi.org/10.1128/cmr.00044-19>], and *Mycobacterium tuberculosis* (*M. tuberculosis*). During the 1800s, tuberculosis was so frequent that it caused about one in four deaths in parts of Europe and North America [1] and even became a common theme in operas, including *La Traviata*, *La Bohème*, and *Les Contes d'Hoffmann*, and possibly *Manon*. While these are examples of particularly dangerous pathogens, in the absence of effective treatment options, many lethal infections were caused by bacteria that are harmless in their usual niches but can become life-threatening when they gain access to vulnerable tissues or the bloodstream.

This pre-antibiotic era ended with the discovery of antibiotics, such as sulfonamides (1910) and penicillins (1928). For the first time in history, many bacterial diseases became effectively treatable. Despite early reports of emerging resistance [2], the golden age of antibiotics began, as the rapid development of new drug classes outpaced the evolution of resistance. Especially in high-income countries, premature deaths from bacterial infections were massively reduced, and diseases such as plague and tuberculosis have receded in public perception from everyday experience to problems of faraway places or a shadow of the past.

However, this success is fading. Due to increased antibiotic consumption, bacteria have evolved resistance across all major drug classes that have been introduced, and the time it takes for resistance to emerge is decreasing [3]. At the same time, new antibiotic classes are increasingly difficult to discover, slowing the pace at which novel drugs are introduced. Together, these trends have led to an increasing frequency and diversity of resistance genes and multidrug-resistant (MDR) strains, including MDR-*M. tuberculosis* [<https://doi.org/10.1016/j.drup.2025.101265>] and streptomycin-resistant *Y. pestis* strains [[ciab606](#), [ijantimicag201709015](#)].

As a consequence, 1.14 million deaths were directly attributable to resistant infections in 2021 alone [4].

To curb the rise of antibiotic resistance and to retain the benefits of living in a world with effective antibiotics, we need a deep understanding of how antibiotic treatment shapes the evolution of bacterial resistance.

### 1.1 Antibiotic Resistance Evolution

The evolution of antibiotic resistance is driven by two key processes: mutation and selection. De-novo resistance can arise through mutations in the bacterial chromosome or on extrachromosomal DNA, such as plasmids (small circular DNA molecules) or bacteriophages (viruses targeting bacteria). Once established, resistance genes can spread in two fundamentally different ways: *vertically*, when a mother cell passes them to its progeny during division, or *horizontally*, when bacteria acquire foreign DNA. A frequent form of horizontal DNA acquisition is receiving conjugative plasmids, transferred through a pilus—a physical tunnel connecting donor and recipient cells. Some plasmids can actively initiate conjugation by assembling the required machinery, while others exploit the conjugation apparatus of co-resident plasmids to transfer. In this way, plasmids can facilitate gene exchange across bacterial lineages and even (rarely) across kingdom boundaries [5]. This not only accelerates the spread of resistance across species but also makes the accumulation of multiple resistance genes in one bacterium more likely.

Whether resistance genes can persist and increase in frequency depends on selection. Selection reflects a balance between the fitness costs of resistance and its benefits. In the absence of antibiotics, de novo resistance mutations are usually lost, whereas frequent exposure shifts the balance towards maintaining resistance. Because many antibiotics are natural products [6], diverse resistance mechanisms preexist in nature at low frequency [7]. However, today the dominant selective pressure is driven by human antibiotic production and use [8, 9], through clinical prescriptions, large-scale use in livestock and aquaculture, and the release of antibiotic residues from manufacturing into natural ecosystems.

Given that each contact between bacteria and antibiotics constitutes a selection pressure, obvious measures to combat antibiotic resistance are to reduce contact between bacteria and antibiotics, e.g., by minimising the misuse of antibiotics, restricting use where it is not strictly necessary (e.g., in farming to increase weight gain), and ensuring that production residues are inactivated before their release into the environment. Less obvious is how we can continue to use antibiotics to the benefit of patients while minimising the selection for resistant bacteria.

### 1.2 Treatment Strategies

In an ideal scenario, the treatment of infections is tailored to the resistance phenotype of the infecting pathogen by identifying resistance before treatment. However, in clinical practice, this is often not feasible: first, resistance may exist at frequencies below detection thresholds and go unnoticed; and second, in emergency settings, immediate treatment is required while microbiological characterisation can take 24 to 72 hours [10]. Consequently, for initial treatment, clinicians often rely on empirical treatment strategies that aim to clear infections while minimising the risk of selecting for resistance in the absence of phenotypical data.

Commonly discussed approaches include combination therapy (simultaneous use of multiple an-

tibiotics), mixing (random patient allocation to different antibiotics), and cycling (periodic rotation of antibiotics over time). Among these, combination therapy is often considered the most promising strategy in theoretical models [11–13]. The rationale is that, to survive treatment, a pathogen must acquire resistance to multiple drugs simultaneously, which is much less likely than acquiring resistance to just one drug. Combination therapy has been discussed for decades in the context of slowing the evolution of resistance in plant pathogens, including through fungicide mixtures [14–16]. There is also a long history of combining drugs in traditional Chinese medicine, which has prescribed multi-herb formulations with up to 20 herbs for more than two millennia [17]. In the clinical context, combination therapy plays a central role in clinical protocols for fast evolving pathogens such as *HIV*, *M. tuberculosis*, and *Plasmodium falciparum* [18].

Despite its potential advantages, combination therapy raises several concerns. Given the observed correlation between overall antibiotic consumption and resistance [8, 9], it has been argued that using multiple antibiotics could increase selection for resistance in both the focal pathogen population and within the microbiome [19]. Combining antibiotics may also increase complications in patients due to a higher risk of toxicity [20]. Finally, the clinical evidence remains inconclusive, as a recent meta-analysis found no consistent advantage of combination therapy in reducing the emergence of resistance [21].

The discrepancy between theoretical predictions and inconclusive clinical outcomes can stem from simplifications in theoretical models or from limitations in clinical studies. On the theoretical side, models often rely on simplifying assumptions and may overlook important biological complexities, such as heterogeneity in patients and pathogens, toxicity, treatment responses, and drug mechanisms. On the clinical side, most clinical trials are not primarily designed to detect differences in resistance evolution, lacking the statistical power to capture small differences between treatment arms [22]. Additional variability in meta-analyses arises from differences in study design, pathogens, treatment regimens, and clinical endpoints.

To bridge the gap between theoretical models and clinical studies, Angst et al. [23] developed an experimental setup that mimics within- and between-host dynamics in an *in vitro* “hospital ward” under multidrug treatment strategies. The appeal of this work is that it incorporates some biological complexity by using real drugs and bacteria while maintaining a high degree of controllability. Angst et al. showed that combination therapy typically performs better at preventing the emergence of chromosomal resistance than other multidrug strategies. The questions we address in Chapter 2 are whether these resistance dynamics under multidrug treatment differ when resistance is preexisting on plasmids and whether the superiority of combination therapy holds under this condition.

### 1.3 Drug interactions

Meta-analyses aggregate results from clinical studies that differ, among other factors, in the drug combinations used. Because drug combinations can differ in how they interact, the choice of

combination can strongly influence treatment efficacy and the evolution of bacterial resistance [24], and may therefore contribute to variability in outcomes relative to single-drug treatment. Drug interactions are commonly classified by comparing observed combination effects to a reference (null) model such as Loewe additivity [25] or Bliss independence [26]. If the observed combined effect exceeds the model prediction, the interaction is synergistic; if it falls below, the interaction is antagonistic.

However, assessing drug interactions remains difficult for multiple reasons. Estimating interactions under the conditions of interest typically requires tracking population size over time to quantify treatment effects. At sub-inhibitory concentrations, this can be done in high throughput using optical density (OD) measurements. At therapeutically relevant inhibitory concentrations, OD cannot be used because it does not distinguish between live and dead cells. At inhibitory concentrations, most studies rely on colony-forming unit (CFU) counts to quantify population change. This approach is labour-intensive, making it difficult to cover a substantial fraction of the enormous condition space arising from the combinatorial explosion of possible drug pairs and clinically relevant concentrations. Consequently, many studies focus on the sub-inhibitory range, while inhibitory drug interactions remain underexplored.

This raises two questions. First, how can we assess population dynamics under inhibitory conditions in high throughput? We address this question in Chapter 3. Second, can interaction types inferred at sub-inhibitory concentrations be transferred to inhibitory concentrations? We address this question in Chapter 4.

#### 1.4 Thesis outline

In this thesis, we develop experimental and analytical methods to quantify how multidrug treatment influences bacterial population dynamics at both on within-host and between-host scales.

In Chapter 2, we compare the influence of treatment strategies on plasmid-mediated resistance dynamics in an *in vitro* hospital-ward model. Specifically, we conducted large-scale experiments simulating epidemiological dynamics in six parallel “wards,” each assigned to one of six arms: three multidrug strategies (combination, mixing, cycling), two monotherapies (Mono A, Mono B), and an untreated control. We found that combination therapy was either one of the; or the most effective strategy for suppressing plasmid-borne double resistance across scenarios. Surprisingly, we also found that omitting treatment entirely can accelerate the emergence of multi-resistance. To explain both results, we decomposed the emergence process into two components: (i) the probability of superinfection, which is the probability that a patient with an A-resistant infection infects another patient who is infected with B-resistant bacteria (or vice versa), and (ii) the probability that double resistance emerges in a superinfected patient. We found that combination therapy is effective because it suppresses superinfections and reduces the probability that superinfections result in double resistance. Conversely, omitting treatment proved counterproductive as it maximises both

the probability of superinfection and the probability that superinfection leads to double resistance. In Chapter 3, we assess the applicability of bioluminescence assays as a high-throughput method to estimate net growth at inhibitory concentrations. To this end, we compare time courses of light intensity with trajectories of colony-forming units (CFU). We found that inferred decline rates agree for about half of the 20 antimicrobials tested and disagree for the other half. To investigate these discrepancies, we combined supplementary experiments with mathematical modelling. First, we found that bioluminescence correlates more strongly with biomass than with cell number, which can lead to differences relative to CFU when cells filament. Second, we found that CFU can underestimate the number of viable bacteria for drugs that induce a viable-but-nonculturable state or due to antibiotic carryover (at high drug concentrations) that can cause continued killing after plating, both of which reduce the probability that a plated viable cell forms a colony.

In Chapter 4, we ask whether drug interactions measured at sub-inhibitory concentrations can reliably predict interactions at inhibitory concentrations. To this end, we quantified interactions for 15 drug pairs on  $12 \times 12$  concentration checkerboards spanning both sub-inhibitory and inhibitory regimes. To assess the treatment effect in high throughput, we used bioluminescence assays described in Chapter 3. We found that interaction patterns at sub-inhibitory concentrations do not reliably predict interactions at inhibitory concentrations. In addition, we observed that inferred interaction types can vary with the mixing ratio of the two drugs.

## Bibliography

- [1] .T. M. Daniel, J. H. Bates, and K. A. Downes. "History of Tuberculosis". In: *Tuberculosis: Pathogenesis, Protection, and Control*. Ed. by B. R. Bloom. Washington, DC: American Society for Microbiology, 1994, pp. 13–33.
- [2] .W. M. M. Kirby. "Extraction of a Highly Potent Penicillin Inactivator from Penicillin Resistant Staphylococci". In: *Science* 99.2579 (1944), pp. 452–453. doi: 10.1126/SCIENCE.99.2579.452.
- [3] .C. Witzany, S. Bonhoeffer, and J. Rolff. "Is antimicrobial resistance evolution accelerating?" In: *PLoS Pathog.* 16.10 (2020), pp. 5–9. issn: 15537374. doi: 10.1371/journal.ppat.1008905. url: <http://dx.doi.org/10.1371/journal.ppat.1008905>.
- [4] .M. Naghavi et al. "Global burden of bacterial antimicrobial resistance 1990–2021: a systematic analysis with forecasts to 2050". In: *The Lancet* 404.10459 (2024), pp. 1199–1226. doi: 10.1016/S0140-6736(24)01867-1.
- [5] .S. Bates, A. M. Cashmore, and B. M. Wilkins. "IncP Plasmids Are Unusually Effective in Mediating Conjugation of *Escherichia coli* and *Saccharomyces cerevisiae*: Involvement of the Tra2 Mating System". In: *Journal of Bacteriology* 180.24 (1998), pp. 6538–6543. doi: 10.1128/jb.180.24.6538-6543.1998.
- [6] .H. K. Allen et al. "Call of the wild: antibiotic resistance genes in natural environments". In: *Nature Reviews Microbiology* 8.4 (2010), pp. 251–259. doi: 10.1038/nrmicro2312.
- [7] .J. Davies and D. Davies. *Origins and Evolution of Antibiotic Resistance*. 2010. doi: 10.1128/mmb.00016-10.
- [8] .B. G. Bell, F. Schellevis, E. Stobberingh, H. Goossens, and M. Pringle. "A systematic review and meta-analysis of the effects of antibiotic consumption on antibiotic resistance". In: *BMC Infectious Diseases* 14.1 (2014). doi: 10.1186/1471-2334-14-13.
- [9] .S. Rahman and A. Hollis. "The effect of antibiotic usage on resistance in humans and food-producing animals: a longitudinal, One Health analysis using European data". In: *Front. Public Heal.* 11 (June 2023), p. 1170426. issn: 22962565. doi: 10.3389/FPUBH.2023.1170426/BIBTEX.
- [10] .S. Leekha, C. L. Terrell, and R. S. Edson. "General principles of antimicrobial therapy". In: *Mayo Clin. Proc.* 86.2 (Feb. 2011), pp. 156–167. issn: 00256196. doi: 10.4065/MCP.2010.0639/ATTACHMENT/B634B4F6-DE05-47F7-842C-1EED7A2B7D35/MMC1.PDF. url: [https://www.mayoclinicproceedings.org/action/showFullText?pii=S0025619611601407%20https://www.mayoclinicproceedings.org/article/S0025-6196\(11\)60140-7/abstract](https://www.mayoclinicproceedings.org/action/showFullText?pii=S0025619611601407%20https://www.mayoclinicproceedings.org/action/showAbstract?pii=S0025619611601407%20https://www.mayoclinicproceedings.org/article/S0025-6196(11)60140-7/abstract).
- [11] .S. Bonhoeffer, M. Lipsitch, and B. R. Levin. "Evaluating treatment protocols to prevent antibiotic resistance". In: *Proc. Natl. Acad. Sci. U. S. A.* 94.22 (1997), pp. 12106–12111. issn: 00278424. doi: 10.1073/pnas.94.22.12106.
- [12] .B. Tepekule, H. Uecker, I. Derungs, A. Frenoy, and S. Bonhoeffer. "Modeling antibiotic treatment in hospitals: A systematic approach shows benefits of combination therapy over cycling, mixing, and mono-drug therapies". In: *PLoS Comput. Biol.* 13.9 (2017), pp. 1–22. issn: 15537358. doi: 10.1371/journal.pcbi.1005745.
- [13] .H. Uecker and S. Bonhoeffer. "Antibiotic treatment protocols revisited: The challenges of a conclusive assessment by mathematical modelling". In: *J. R. Soc. Interface* 18.181 (2021). issn: 17425662. doi: 10.1098/rsif.2021.0308.
- [14] .P. F. Kable and H. Jeffery. "Selection for Tolerance in Organisms Exposed to Sprays of Biocide Mixtures: A Theoretical Model". In: *Phytopathology* 70.1 (1980), pp. 8–12. issn: 0031-949X. doi: 10.1094/phyto-70-8.
- [15] .C. J. Delp. "Coping with resistance to plant disease". In: *Plant Dis.* 64 (1980), pp. 652–657. doi: 10.1094/PD-64-652.
- [16] .G. Skylakakis. "Effects of Alternating and Mixing Pesticides on the Buildup of Fungal Resistance". In: *Phytopathology* 71.11 (1981), pp. 1119–1121. issn: 0031-949X. doi: 10.1094/phyto-71-1119.
- [17] .R. Yuan. "Traditional Chinese medicine an approach to scientific proof and clinical validation". In: *Pharmacology & Therapeutics* 86.2 (2000), pp. 191–198. doi: 10.1016/S0163-7258(00)00039-5.
- [18] .D. E. Goldberg, R. F. Siliciano, and W. R. Jacobs. "Outwitting evolution: Fighting drug-resistant TB, Malaria, and HIV". In: *Cell* 148.6 (2012), pp. 1271–1283. issn: 10974172. doi: 10.1016/j.cell.2012.02.021.
- [19] .C. Jernberg, S. Löfmark, C. Edlund, and J. K. Jansson. "Long-term ecological impacts of antibiotic administration on the human intestinal microbiota". In: *The ISME Journal* 1.1 (2007), pp. 56–66. doi: 10.1038/ISMEJ.2007.3.
- [20] .P. D. Tammaro, S. E. Cosgrove, and L. L. Maragakis. "Combination Therapy for Treatment of Infections with Gram-Negative Bacteria". In: *Clinical Microbiology Reviews* 25.3 (2012), pp. 450–470. doi: 10.1128/CMR.05041-11.
- [21] .B. Siedentop et al. "The effect of combining antibiotics on resistance: A systematic review and meta-analysis". In: *eLife* (2024). doi: 10.7554/eLife.93740.1.
- [22] .B. Siedentop et al. "The effect of combining antibiotics on resistance : A systematic review and meta-analysis". In: *eLife* 13 (2024), pp. 1–25. doi: 10.7554/eLife.93740.1.
- [23] .D. C. Angst, B. Tepekule, L. Sun, B. Bogos, and S. Bonhoeffer. "Comparing treatment strategies to reduce antibiotic resistance in an *in vitro* epidemiological setting". In: *Proc. Natl. Acad. Sci. U. S. A.* 118.13 (2021), pp. 1–7. issn: 10916490. doi: 10.1073/PNAS.2023467118.

- [24] .E. Gjini and K. B. Wood. "Price equation captures the role of drug interactions and collateral effects in the evolution of multidrug resistance". In: *eLife* 10 (2021). doi: [10.7554/eLife.64851](https://doi.org/10.7554/eLife.64851).
- [25] .S. Loewe and H. Muischnek. "Über Kombinationswirkungen". In: *Archiv für Experimentelle Pathologie und Pharmakologie* 114.5-6 (1926), pp. 313–326. doi: [10.1007/BF01952257](https://doi.org/10.1007/BF01952257).
- [26] .C. I. BLISS. "THE TOXICITY OF POISONS APPLIED JOINTLY1". In: *Annals of Applied Biology* 26.3 (1939), pp. 585–615. doi: [10.1111/j.1744-7348.1939.tb06990.x](https://doi.org/10.1111/j.1744-7348.1939.tb06990.x).



## Chapter 2

### The Impact of Treatment Strategies on the Epidemiological Dynamics of Plasmid-Conferred Antibiotic Resistance

---

**Authors:** Malte Muetter<sup>a</sup>, Daniel C. Angst<sup>a</sup>, Roland R. Regoes<sup>a</sup>, Sebastian Bonhoeffer<sup>a</sup>

<sup>a</sup>*Institute of Integrative Biology, Department for Environmental System Science, ETH Zurich, 8092 Zurich, Switzerland*

**Contributions:** MM, DCA, RR, and SB designed research; MM and DCA performed experiments; DCA and MM created the used strains; MM developed the mathematical model; MM analyzed data; MM, DCA, RR and SB wrote the manuscript.

---

#### Abstract

The issue of antibiotic resistance is a critical concern for public health, prompting numerous investigations into the impact of treatment strategies on preventing or slowing down the emergence of resistance. While existing studies have predominantly focused on chromosomal resistance mutations, the consequences of often clinically more relevant plasmid-conferred resistance remain insufficiently explored. To address this gap, we conducted three extensive *in vitro* experiments utilising a liquid-handling platform. These experiments evaluated the efficacy of five distinct treatment strategies using two antibiotics (tetracycline and ceftazidime) along with two horizontally transmissible clinical resistance plasmids conferring the respective resistances. Among the experimentally investigated treatment strategies, combination therapy proved to be the most effective in preventing the emergence of double resistance while minimising the number of infections. To verify the reliability of these findings, we constructed a computational model of our experiments that we parameterised using the experimental data. We employed this model to augment the experimental data by conducting an *in silico* parameter sensitivity analysis. The sensitivity analysis corroborated our experimental results, demonstrating that combination therapy consistently outperformed other treatment strategies across a range of parameter values.

## 2.1 Introduction

In light of the growing threat of antimicrobial resistance (AMR) to human health, various multidrug strategies are being considered to improve the sustainability of antibiotic use. These approaches include combination therapy (simultaneous use of multiple antibiotics), mixing therapy (randomly assigning patients to receive different antibiotics), and cycling therapy (alternating between multiple antibiotics over time).

Combination, originally proposed alongside cycling therapy to prevent biocide resistance in plant pathogens [1–3], was later adopted in human medicine. Combination therapy proved its effectiveness in preventing resistance evolution in highly adaptable pathogens such as HIV, *Mycobacterium tuberculosis*, and *Plasmodium falciparum* [4]. However, a recent meta-analysis investigating the effect of combination therapy on resistance across various bacterial infections and antibiotic combinations found no evidence for a difference in the risk of resistance acquisition [5]. Also, a comprehensive cluster-randomised crossover study comparing mixing and cycling by van Duijn et al. [6], spanning nearly two years across eight ICUs, found no significant differences in outcomes.

A review of the available model literature by Uecker et al. [7] reveals the complexity and context-dependent efficacy of treatment strategies such as combination, cycling or mixing strategies. Yet, theoretical models often identify combination therapy as the best strategy to prevent new resistance [8, 9]. It remains unclear whether the inconclusive results regarding the effectiveness of multidrug treatment strategies in the literature are due to the theoretical models failing to account for key processes, or if clinical studies lack statistical power, as suggested by Siedentop et al. [5]. This lack of power may be caused by patient and bacterial strain heterogeneity, stochasticity in infection dynamics, and other unknown factors that make it difficult to isolate single effects.

We recently started experiments to make a foray into the large gap between theoretical models and clinical trials. In an *in vitro* experiment mimicking the epidemiological scenario of transmission in a hospital ward, Angst et al. [10] investigated the effect of cycling, mixing, and combination therapy on resistance evolution and showed that for chromosomal resistance mutations combination therapy outperformed the other strategies. One potential reason why combination therapy succeeded in that study and tends to be superior in mathematical models is that it increases the genetic barrier to resistance by requiring the acquisition of multiple mutations in the same background.

Here, we explore the effect of horizontal gene transfer (HGT) on resistance evolution under treatment by conducting three large-scale *in vitro* experiments. The experiments mimic epidemiological transmission dynamics of symptomatic infections by a focal strain in an intensive care unit (ICU) and include patient discharge and admission, infection between patients, and treatment. We use two antibiotics, ceftazidime (A) and tetracycline (B), along with two clinical resistance plasmids [11] we call  $p_A$  and  $p_B$ , conferring resistance to the corresponding antibiotics. The plasmids are compatible, can conjugate, and were isolated from clinical samples collected and characterised in a study at University Hospital Basel [12]. We model patients as wells in a 384-well microtiter

plate filled with LB medium. These “patients” can be infected with a mixture of bacteria, which may carry up to two resistance plasmids. Depending on the presence of bacteria and resistance, we assign each “patient” a resistance profile: uninfected ( $U$ ), sensitive infected ( $S$ ), single-resistant ( $A_r$ ,  $B_r$ , or  $(A_r \& B_r)$ ), or double-resistant ( $AB_r$ ).

In each experiment, we model six hospital wards to assess the ability of five treatment strategies (mixing, cycling, combination therapy with two antibiotics and two monotherapies with each antibiotic alone) and one control (no antibiotics) to contain the spread of plasmid-borne resistance and prevent the emergence of double resistance. All patients in each ward are treated daily according to the assigned strategy. A schematic of the experimental setup is shown in Fig. A1. Each of the three experiments addresses a different scenario (Table 2.1), varying in patient turnover probability (admission/discharge), infection probability, and the distribution of resistance profiles for incoming patients (sampling proportions). The *prevention* scenario addresses a situation with low levels of pre-existing single and no double resistance brought into the hospital ward from the community. The *containment* scenario focuses on the ability of treatment strategies to contain pre-existing double resistance and in the *maximum-emergence* scenario, we maximised the opportunities for emerging double resistance through HGT by admitting single-resistant patients only.

Alongside our experiments, we created a computational model that mimics the experiment and is parameterised but not fitted using the experimental data. We used the model to assess the robustness of our findings to the randomisation of the experimental decisions and conducted an *in silico* sensitivity analysis to augment the experimental data.

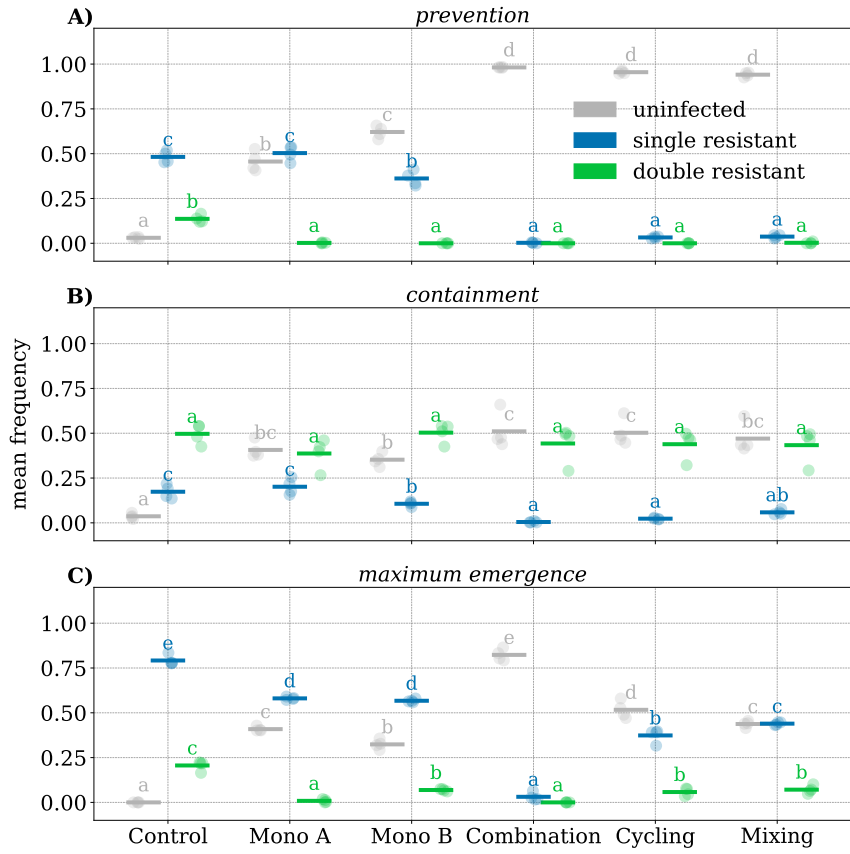
## 2.2 Results

In each of our three experiments, we simulated the transition dynamics across six hospital wards on six 384-well plates. Each 384-well plate simulates four replicate hospital wards, with each replicate comprising 96 wells representing 94 patients and two negative controls. We replace each assay plate daily to renew the treatment and medium (Table A1). Based on the turnover probability  $\tau$ , we randomly decide if a patient stays. If this is the case, we inoculate the well on the new plate from the same well on the old plate. Else we replace this patient with a new incoming patient by inoculating the well on the new plate from a strain plate containing all resistance profiles. The

Table 2.1 – **Parameter sets** and  $R_0$  used in the three experiments:  $c_\phi$  is the proportion of admitted patients with resistance profile  $\phi$ ,  $\tau$  denotes the probability that a patient is replaced with a new patient sampled from the community and  $\beta$  denotes the infection probability.

scenario	$c_S$	$c_{Ar}$	$c_{Br}$	$c_{ABr}$	$c_U$	$\tau$	$\beta$	$R_0$
<i>prevention</i>	0.75	0.05	0.05	0	0.15	0.20	0.30	1.5
<i>containment</i>	0.58	0.11	0.11	0.05	0.15	0.20	0.35	1.75
<i>maximum-emergence</i>	0	0.50	0.50	0	0	0.50	0.25	0.5

Fig. 2.1 – Panels A–C show the mean frequency of uninfected (grey), single-resistant infected (blue), and double-resistant infected wells (green) during the last four transfers of the three scenarios. Circles represent replicates ( $n = 4$ ), and bars represent means. Within resistance categories, bars not sharing a letter are significantly different (pairwise Tukey post hoc test,  $p < 0.05$ ; ANOVA tables and all p-values can be found in Table A34 – Table A50).



resistance profile of the incoming patient is randomly selected based on predefined probabilities (sampling proportions  $c_\phi$ ). Based on the infection probability  $\beta$ , we randomly decide if a patient will infect another randomly chosen patient. These infections are then simulated *in vitro* by passing a drop to the infected well on the new plate. All inoculations are carried out using the same pintool.

**Multidrug strategies keep the overall number of infections lowest and best suppress single resistance.** The *prevention* scenario is characterised by a moderate proportion of single-resistant admissions to the hospital ward, the absence of pre-existing double resistance, and a moderately spreading infection dynamic ( $R_0 = 1.5$ , Equation A1, SI Methods). In this scenario, there are no differences between combination, mixing, and cycling on the frequency of uninfected, single-resistant-infected and double-resistant-infected wells (Fig. 3.2A, time series in Fig. A2).

However, all multidrug strategies are significantly better at suppressing single resistance and increasing the number of cleared wells than the single-drug strategies and the control without treatment (Fig. 3.2A). In all scenarios, combination therapy was one of the most successful treatment strategies in minimising single-resistant and overall infections. At the same time, we observed most single and double resistance in the untreated control. All strategies (but not the control) were able

to clear sensitive infections effectively with clearance probabilities of 97% for drug A, 73% for drug B, and 86% for AB (Table A8).

**All treatment strategies fail to contain pre-existing double resistance.** The *containment* scenario explores a situation in which patients infected with double-resistant bacteria are continuously admitted to the hospital. No strategy was able to contain the spread of double resistance, resulting in increased frequencies of double resistance ( $> 40\%$ ) in all treatment arms at the conclusion of the experiment (Fig. 3.2B).

**Treatment strategies affect the emergence of double resistance.** In our experiments, double resistance primarily emerges in wells inoculated with both single-resistance plasmids via HGT, as the evolution of de novo resistance (e.g. by point mutations) to high drug concentrations ( $> 50 \times \text{MIC}$ ) is unlikely. As the inoculum volumes for turnover, infection, and passage are identical in our experiments, we do not distinguish between wells containing A-resistance ( $A_r$ ) infecting wells containing B-resistance ( $B_r$ ) or vice versa and simply refer to these events as superinfections.

During the *prevention* and *containment* scenario, we could not identify differences in the strategies' abilities to suppress the emergence of double resistance. We attribute this to a lack of statistical power because we observed only a few instances of double resistance emerging, mostly in the untreated control. To address this, we selected parameters for the *maximum-emergence* scenario designed to maximise superinfection opportunities between wells carrying complementary resistance. To this end, all admitted patients carried bacteria with only one of the two resistance plasmids (at equal proportions). In addition, we set the probability of admission and discharge to  $\tau = 0.5$  and the infection probability to  $\beta = 0.25$ , resulting in a basic reproduction number  $R_0 = 0.5$  (Equation A1). An  $R_0 < 1$  makes double resistance more likely to be replaced by newly admitted patients than to spread, thus maintaining a high potential for emergence. We implement this scenario to explore emergence under a magnifying glass, being aware that it does not reflect a likely clinical situation. In this scenario, combination therapy and monotherapy with drug A lead to the lowest frequency of double resistance during the last four transfers (Fig. 3.2C, Fig. 2.2).

For the *maximum-emergence* scenario, we observed that combination therapy, cycling, and monotherapy with drug A were most effective in preventing newly emerging double resistance. Combination was the only strategy in which we did not observe a single case of emerging double resistance after the first transfer (Fig. 2.3A). Furthermore, combination therapy is the most successful treatment strategy in minimising the number of both single-resistant and overall infections, while the control leads to the highest number of double- and single-resistant, and overall infections.

**Combination therapy suppresses the emergence of double resistance by preventing superinfections.** Treatment strategies can impact the emergence of double resistance by suppressing superinfections. The number of superinfections  $n_{\mathcal{S}}$  is dependent on the abundance of the single

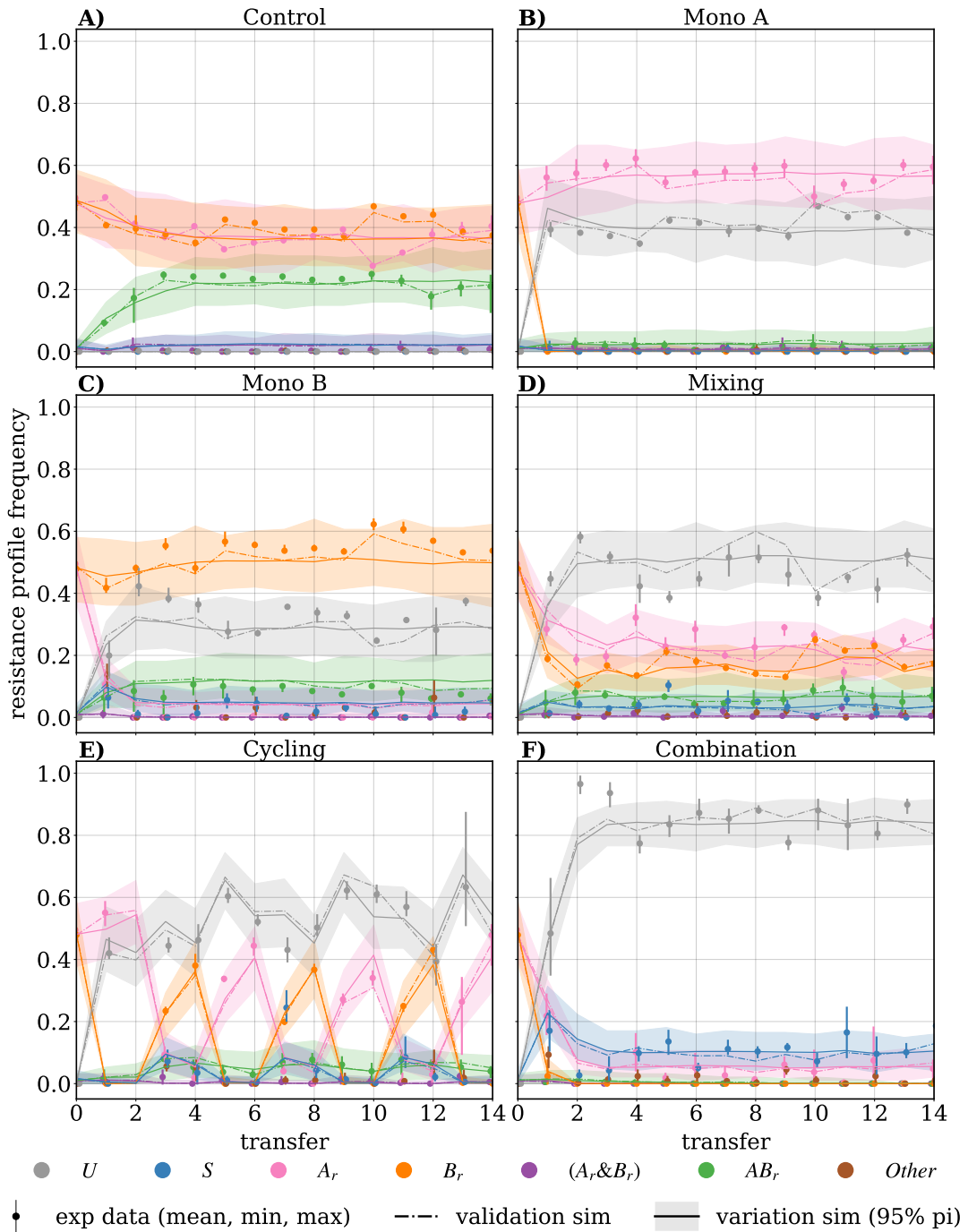


Fig. 2.2 – Frequencies of resistance profiles over time during the *maximum-emergence* scenario. Panels (A–F) show the six tested strategies. Dots and bars show the mean and min/max interval of the four replicates. The dash-dotted line shows the mean value of 100 stochastic simulations based on the instruction set used in the *in vitro* experiment (*validation simulation*). The solid line shows the mean value of 100 simulations with randomly created instruction sets based on the parameter set used in the experiment (*variation simulations*). The shaded error band indicates the 95-percentile interval between the *variation simulations*.

resistance carrying wells  $A_r$  and  $B_r$ . Hence, we expect the highest number of superinfections and most opportunities for emerging double resistance when both single resistances are unaffected by the treatment and the fewest if the treatment successfully suppresses both single resistances. Our measurements confirmed these expectations during the *maximum-emergence* scenario. Here  $n_{\mathcal{S}}$  is highest in the control group (no treatment) and lowest under combination therapy (Fig. 2.3B).

**Treatment strategies influence the emergence of double resistance within superinfected wells.**

We observed the highest average frequency of superinfections developing double resistance ( $\frac{n_E}{n_{\mathcal{S}}}$ ) in antibiotic-free medium and in medium treated with antibiotic B (tetracycline). In contrast, superinfections resulting in double resistance rarely occur in medium treated with antibiotic A (ceftazidime) or both drugs (Fig. 2.3C). We think the impact of treatment on cell densities within superinfected wells (both in infected and infecting wells) can best explain these findings.

Firstly, applying a drug affects the in-well population dynamics of superinfected wells. Reducing the cell density for one or both single-resistant strains within a superinfected well reduces the probability of bacteria with complementary resistance to encounter and conjugate (see [SI Results](#)). As drug A (bactericidal) decreases the cell density faster than drug B (bacteriostatic), more conjugation opportunities occur in wells treated with drug B.

Secondly, the treatment strategies influence the number of transferred single-resistant bacteria that inoculate superinfections by curbing the bacterial density within the infecting wells (see [SI Results](#)).

Due to the differences in the abilities of drugs A and B to prevent conjugation, there are times (cycles) and places (beds) during cycling and mixing where using drug B offers increased opportunities for the emergence of double resistance, which is never the case with combination therapy.

**Computational model corroborates the robustness of experimental outcomes.** The experiments are conducted by a liquid handling platform that carries out predefined instructions, specifying which infections occur and who is admitted or discharged. The instructions are randomized based on parameter sets we defined for each scenario, including the overall infection and turnover probability as well as the distribution of the resistance profiles of admitted patients. We call the entirety of all instructions that come up during one experiment an ‘instruction set’. Due to the scale and technical complexity of the experiments, it was not feasible to carry out individual instruction sets for each replicate, so we opted to apply the same instruction sets for all replicates. This raises the question of whether the experimental results are a consequence of a specific instance of this random process and whether they are robust to the randomisation in the instruction set. To address this, we developed a discrete-time stochastic model comprising 94 individual *in silico* patients mimicking the epidemiological dynamics of the experiment ([SI Computational Model](#)). The model was parametrised, but not fitted, with transition probabilities (Table A18–Table A25) that we estimated based on the transition frequencies measured *in vitro*. We used the same transition probabilities in

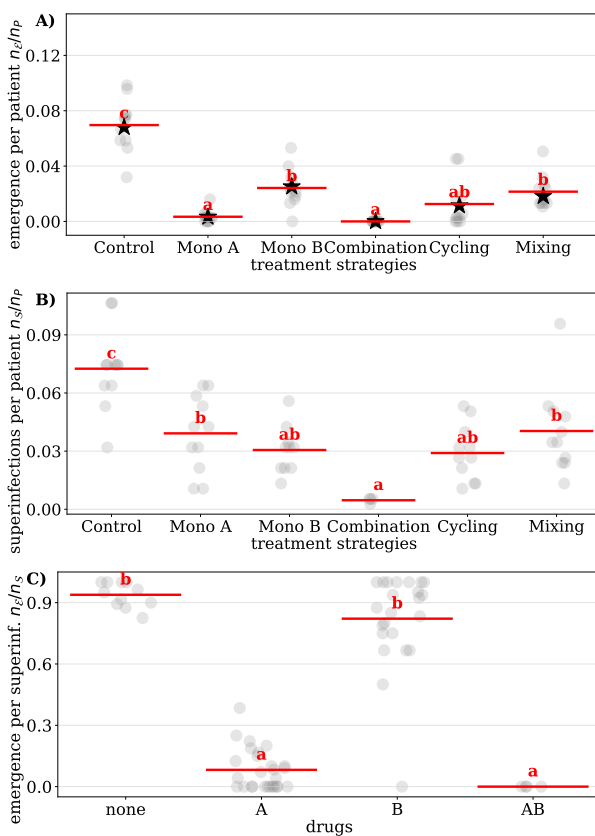


Fig. 2.3 – Analysis of the emergence of double resistance *in vitro* and superinfection between single resistant  $A_r$  and  $B_r$  wells during the *maximum-emergence* scenario, from transfer four onwards. Each dot corresponds to data from a single plate, with each plate representing a distinct treatment arm, encompassing 376 patients for one transfer. Mean values are represented by red bars. Bars not sharing a letter are significantly different ( $p < 0.05$ , ANOVA tables and pairwise Tukey post hoc results can be found in Table A51 – Table A56). **A)** number of newly emerged cases of double resistance per plate ( $n_E$ ), normalised to the total number of patients (wells) per plate ( $n_P = 376$ ). Here the stars indicate predictions based on the ratio of superinfections per patient and the emergence per superinfection ([SI Computational Model](#)). **B)** Number of superinfections per plate ( $n_S$ ), normalised to the total number of patients (wells) per plate ( $n_P = 376$ ). **C)** Number of superinfected wells treated with (A, B, AB and none) that develop double resistance ( $n_E$ ) divided by the number of all superinfected wells ( $n_S$ ) receiving the respective treatment.

the simulations for all scenarios.

First, we validated the model by averaging 100 *validation simulations*, each employing the identical instruction sets used *in vitro*. The aim of the *validation simulations* is to recreate the experiments *in silico* (Fig. A3B). We found that the simulation results are in good agreement with the experimental data, indicating that the model reflects the dynamics observed in the *in vitro* experiments well (see Fig. 2.2, Fig. A2, and Fig. A4). One exception is the spread of A-resistance during the *prevention* scenario in control and Mono A. This could indicate an increased number of contaminations at the beginning of the *prevention* scenario. We also observe some discrepancies for the spread of double resistance during the *prevention* scenario, which we attribute to contamination artefacts in the transition probabilities (see [SI Computational Model](#)).

Second, we averaged 100 *variation simulations* to assess the robustness of the experimental outcomes against variations in the instruction sets. In these *variation simulations*, each of the 100 instruction sets was randomized based on the same three parameter sets used *in vitro* (Fig. A3C). Differences between the *validation* and *variation simulations* indicate differences in outcome due

to the randomization of the instruction sets. For instance, with a turnover probability  $\tau = 0.2$  and an admission probability  $c_A = 0.05$ , we expect  $0.94 A_r$  admissions per transfer. However, random fluctuations can result in either more (or fewer)  $A_r$  admissions, leading to a temporarily higher (or lower) frequency of  $A_r$  in the *validation simulations*, creating a temporary spread between the *validation* and *variation simulations*. We observed that the *validation simulations* fluctuate around the *variation simulations* and never diverge far (see Fig. 2.2, Fig. A2, and Fig. A4), indicating robustness of the experimental results to the randomisation of the instruction sets.

**In silico sensitivity analysis indicates that the superiority of combination therapy is robust.** Given that the *validation simulations* agreed well with the experiments, we used the model to perform an *in silico* parameter sensitivity analysis of the experimental results (Fig. A3D). To this end, we ran ten simulations for each of 20,000 randomly generated parameter sets by varying the turnover and infection probability and the five sampling proportions for incoming patients: ( $\tau, \beta, c_S, c_{A_r}, c_{B_r}, c_{AB_r}, c_U$ ). For half of the parameter sets, we forced the frequency of incoming patients with double resistance ( $c_{AB_r}$ ) to zero.

We used the frequency of uninfected *in silico* patients to measure treatment success. Using this criterion, the control strategy (no treatment) always performed worst, and accordingly, we excluded this treatment arm from the following analysis. Strategies were then classified as (i) 'single winners' if they are significantly better than all other strategies; (ii) 'winners' if they are not outperformed by any other strategy; (iii) 'losers' if they do not outperform at least one other strategy; or (iv) 'single losers' if all other strategies outperform them.

In parameter sets with and without pre-existing double resistance, combination therapy ranks most often as one of the best strategies (87% and 98%, respectively). It is the single best strategy in 55% of the tested parameter sets with pre-existing double resistance and in 93% of cases without pre-existing double resistance (Fig. 2.4, Table A14, Table A15).

In some situations (for example, when one strategy is much worse than all others), it is more important to avoid the worst strategy than selecting the very best strategy among the good ones. Our analysis finds that combination therapy is almost never among the worst strategies, while usually one of the two monotherapies performs worst. As expected, single-drug strategies perform particularly poorly when there is a high frequency of pre-existing single-resistance to the applied drug (Table A11, Table A13).

Cycling and mixing lose substantially less than the monotherapies but are rarely the single best strategy.

## 2.3 Discussion

In our study, multi-drug strategies, particularly combination therapy, outperformed monotherapies in reducing overall infections and the emergence of double resistance across most scenarios, while

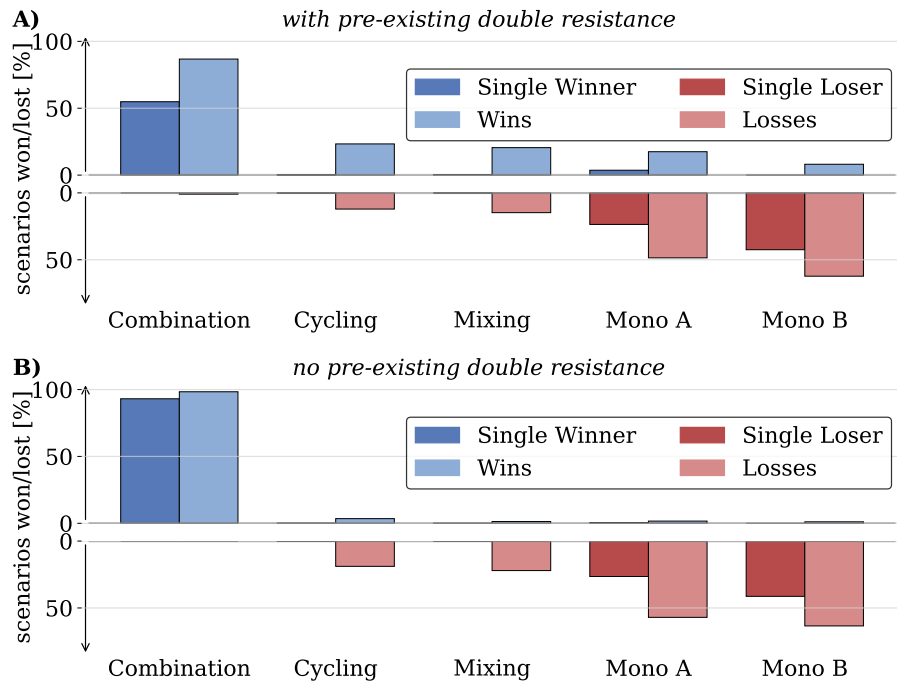


Fig. 2.4 – Effectiveness of the five treatment strategies in maximising the frequency of uninfected individuals across randomly generated parameter sets. Strategies not significantly better than any other are marked as losers (pastel red), and those significantly worse than all others as single losers (dark red). Strategies not significantly worse than any other are classified as winners (pastel blue), and those significantly better than all others as single winners (dark blue). Strategies without significant differences were excluded. **(A)** 10,000 parameter sets with pre-existing double resistance. 606/10,000 sets yielded no significant difference between the strategies. **(B)** 10,000 parameter sets without pre-existing double resistance. 100/10,000 sets yielded no significant difference between the strategies.

we observed most emergence of double resistance in the untreated control. Interestingly, the effectiveness of combination therapy does not stem from an increased efficacy associated with higher doses. This is because an asymmetrical antagonism exists between the bactericidal antibiotic cefazidime (drug A) and the bacteriostatic antibiotic tetracycline (drug B), resulting in a lower clearance rate for the combination A+B compared to drug A alone ([SI Results](#)). This observation implies that combination therapy may be even more advantageous when drugs are neutral or synergistic towards each other.

Why does the absence of treatment lead to worse outcomes, and why is combination therapy preventing the emergence of double resistance so effectively?

First, we measured the presence, not the density, of resistant bacteria in wells by assessing if small aliquots of the liquid culture could grow on treated agar plates. This approach quantifies the num-

ber of wells hosting a specific resistance but can not quantify the frequency of resistance in the in-well population. The information about presence/absence alone yields important information about potential treatment success and is used in analogous clinical diagnostic methods, such as disk diffusion tests [13].

We would only recognize a loss of resistance (in the experiments and clinical samples) if the resistant strain were fully outcompeted. This was not observed during the *containment* scenario in the untreated control. Such an outcome was expected due to the short average patient stay of 2–5 days in our experiments and 5–6 days in clinical situations [14]. For the same reason, we would not expect an eradication of resistance but only a shift in resistance density, even if there were more substantial costs of resistance or higher segregational loss. In our experiments, we found no evidence of a cost of resistance (see [SI Methods](#), Fig. A6, and Table A3) or segregational loss (see [SI Methods](#) and Table A4).

Second, in our experiments, the emergence of double resistance requires conjugation, which relies on superinfection between hosts with complementary resistance profiles. As demonstrated in Fig. 2.3B, the lowest number of superinfections occur in combination therapy, where both single-resistant strains can be cleared. Conversely, without treatment, the abundance of single resistance is highest resulting in the highest number of superinfections.

Third, the applied antibiotics affect the frequency of superinfections leading to double resistance, likely by influencing the growth dynamics within the superinfected well and potentially the conjugation rate [15]. However, our experimental data are unsuitable for supporting or rejecting the impact on conjugation rates. We observed the least emergence of double resistance in superinfected wells treated with both drugs and most in untreated wells, contributing to the superiority of combination therapy and the high rates of double resistance in the absence of treatment (Fig. 2.3C). This effect on the in-well dynamics may be a property of the chosen drugs and concentrations, and we expect better results for cycling and mixing if both drugs were equally effective in suppressing double resistance or worse results for combination therapy if the combination of both drugs was less effective.

Fourth, we observed that the number of single-resistant bacteria inoculating superinfections impacts the frequency of emerging double resistance (see [SI Results](#), Table A1). In our setup, superinfected wells receive two inocula, with at least one inoculum transferred from the previous plate (by infection) that has already undergone treatment for one day. When prior treatment led to a low bacterial density in the source wells, we did not observe any cases of double resistance emerging. This could magnify the effectiveness of combination therapy, where all potential single-resistant inocula transferred from the previous plate contain low bacterial densities due to effective treatment. On the one hand, this may be more a characteristic of our experimental setup due to the fixed length of the treatment interval and high clearance probabilities. On the other hand, we indeed expect fewer cases of emergence in superinfected patients if the infecting inocula are small.

In our experiments and simulations, combination therapy showed superior results in minimizing infections and preventing double resistance. This advantage may partly result from assumptions and simplifications, including the chosen strain, drugs, plasmids, and inoculum size, the discrete setup with fixed treatment durations, colonization-independent infection and turnover probabilities, and the absence of an immune system and microbiome. Also, treating all patients irrespective of colonization diverges from clinical reality in two ways: i) in a clinical setting, some untreated patients may serve as a sanctuary for resistance and a potential source of double resistance and ii) treating all patients, regardless of infection status, contrasts with clinical efforts to promote targeted antibiotic use. However, since patients as we model them in our *in vitro* experiments lack a microbiome, treating uninfecteds should have no impact on the resistance dynamics.

Despite the numerous differences between our experiments and a real clinical situation, we argue that the relative effectiveness of combination therapy in suppressing double resistance would likely translate to real patients. The reason is that the emergence of double resistance hinges on two critical processes: 1) preventing superinfections between patients carrying bacteria with complementary resistance plasmids and 2) the probability that superinfected hosts develop double resistance. We think that combination therapy offers a strategic advantage in addressing both processes.

Our results complement the findings by Angst et al. [10], who observed similar outcomes in the context of chromosomal resistance. We believe that such *in vitro* experimental models, which explore admittedly idealised and simplified epidemiological scenarios, can help to bridge the divide between mathematical models and randomised clinical trials. However, ultimately the evidence for or against the benefits of combination therapy must be confirmed by rigorous clinical trials with sufficient statistical power to support or challenge the effectiveness of combination therapy.

## 2.4 Methods

**Drugs and Media.** In all experiments, we used LB (Sigma L3022) with 25  $\mu\text{g}/\text{ml}$  (*prevention scenario*) or 5  $\mu\text{g}/\text{ml}$  (*containment* and *max-emergence scenario*) chloramphenicol as a liquid medium and the same LB and drugs with 1.5% agar as a solid medium. Chloramphenicol was added to prevent external contaminations. We could not measure any significant growth effects of the chloramphenicol concentrations on the chloramphenicol-resistant strains (see Table A5). We used 80  $\mu\text{g}/\text{ml}$  ceftazidime as drug A and 40  $\mu\text{g}/\text{ml}$  tetracycline as drug B, with identical concentrations for liquid and solid media.

**Strains and Plasmids.** We used two compatible plasmids  $p_A$  and  $p_B$  derived from samples ESBL9 and ESBL25 from a clinical transmission study [12]. Samples were kindly provided by Adrian Egli and sequenced and analysed by Huisman et al. [11]. Plasmids  $p_A$  and  $p_B$  provide (among other resistances) resistance against drug A and drug B, respectively. We used these plasmids and the chloramphenicol-resistant host MDS42-YFP [16] (sensitive to drugs A and B) to create three additional strains by conjugation (Table A2) (i) A-resistant, containing  $p_A$ ; (ii) B-resistant, containing

$p_B$ ; and (iii) AB-resistant, containing both plasmids (see [SI Methods](#)).

**Treatment arms.** We simulated the epidemiological dynamics of six hospital wards *in vitro*, with each ward exploring a different treatment arm: (i) control with no treatment, (ii) monotherapy with ceftazidime (mono A), (iii) monotherapy with tetracycline (mono B), (iv) cycling therapy (A, A, B, B, ...), (v) mixing therapy (treatment A and B are randomly assigned daily, without knowledge of prior treatment), and (vi) combination therapy (treating all patients with both drugs, each at full concentration).

**Assay plates.** Each hospital ward was simulated *in vitro* on a 384-well microtiter plate (Greiner 781186). Wells are interpreted as beds in four replicate hospital wards with 94 beds each. The remaining wells contained only growth medium and remained untouched, acting as sentinels for contamination. Across all experiments and treatment arms, 2752 control wells were used, 67 of which became contaminated. Wells with growth medium but no bacteria represent uninfected patients, whereas wells with growth medium and (resistant or sensitive) bacteria represent infected patients.

**Experimental procedure.** Experiments were performed using a Tecan Evo 200 automated liquid handling system (Tecan) with an integrated, automated incubator (Liconic STX100, Liconic), a Tecan Infinite F200 spectrophotometer (Tecan), and a camera (Pickolo, SciRobotics).

Every day new assay plates were filled with 45  $\mu$ l fresh medium and 5  $\mu$ l antibiotic stock, according to its designated treatment strategy (see Fig. A1). At each of these transfers, we simulate patients staying overnight in the hospital (passage), the admission and discharge of patients (turnover), and infections between patients (infection). Passage, turnover and infections were all done by inoculating the new plate using a pintool with retractable pins, as detailed below, carrying  $\approx$ 0.3  $\mu$ l drops between wells ( $\approx$  1 : 150 dilution) leading to an approximately 6-8 hours exponential phase. The assay plates were then incubated at 37 °C and 95% relative humidity. The incubation duration varied due to variations in the time it takes to set up a new transfer and occasional transfer repetitions made necessary because of machine errors or user mistakes. The mean incubation duration was 27 hours.

We initiated the experiment by inoculating one 384-well plate from fresh overnight cultures representing patients from an outside community. We assume that this community is sufficiently large to be unaffected by interactions with the hospital ward. Incoming patients are either uninfected or carry one of the four strains (sensitive, each single resistant or double resistant) and are sampled according to predefined sampling proportions, defining the probability of a resistance profile being admitted to the hospital. (Table 2.1). This initial plate remained untreated and was used as the initial population for all six treatment arms.

**Turnover.** Every transfer, each patient has a turnover probability  $\tau$  to be discharged from the hospital and replaced by a newly admitted patient. Wells representing staying patients were passed from the previous to the new assay *plate* using the pintoool. Here, the pins for discharged patients are retracted. Vacant beds on the assay *plate* were then reoccupied by patients from the community analogous to the initial setup.

**Infections.** To simulate infections, each well has an infection probability  $\beta$  to infect another randomly chosen well on the next assay *plate* during the transfer. Therefore, each patient can infect at most one other patient per transfer, but several patients could potentially infect the same patient.

**Resistance Profiles.** To assess the resistance profile of each well, we spotted the previous assay *plate* onto four agar *plates*, using the pintoool. Three plates were treated with antibiotics (A, B, or AB), while one was untreated (none). After incubation at 37 °C and 95% relative humidity, images of the agar *plates* are taken and analysed using the Pickolo package (SciRobotics, Kfar Saba, Israel). The software automatically detects the presence of colonies at each well position, which we also manually verified. The growth pattern on the four agar *plates* allowed us to determine the resistance profile of a well, which reflects how the well would behave if treated.

By default, we distinguish six resistance profiles (Table A6). The wells may either be 1) uninfected ( $U$ ), 2) exclusively infected with sensitive bacteria ( $S$ ), 3) infected with A-resistant bacteria ( $A_r$ ), 4) infected with B-resistant bacteria ( $B_r$ ), 5) infected with AB-resistant bacteria ( $AB_r$ ), 6) or be infected with a mixed population containing A-resistant and B-resistant bacteria, but no AB-resistant bacteria ( $(A\&B)_r$ ). The way we classify the resistance profiles of the bacterial population in a well leads to the dominance of resistance, in the sense that a predominantly sensitive population harbouring a resistant minority would be classified as resistant (see Table A7). Any observed growth pattern not corresponding to the six resistance profiles mentioned above is classified as ‘other’. The resistance profile ‘other’ primarily occurs when bacterial densities are low (see also [SI Methods](#)).

**Scenarios.** We conducted experiments for three scenarios (*prevention*, *containment*, and *maximum-emergence*) with 14 to 27 transfers each. Each experiment was defined by a different parameter set consisting of (i) the infection probability  $\beta$  within the hospital, (ii) the turnover probability  $\tau$  and (iii) the sampling proportions  $c_\phi$  of patients with resistance profile  $\phi \in \{U, S, A_r, B_r, AB_r\}$  (see Table 2.1).

The *prevention* scenario (Fig. A2) addresses how the treatment strategies perform with a moderately resistant community and a moderate infection regime in the hospital ward and how well they are able to prevent the upcoming double resistance.

The *containment* scenario (Fig. A4) corresponds to a scenario in which some patients entering the hospital are infected with double-resistant bacteria to compare the ability of treatment strategies to

contain the spread of pre-existing double resistance.

During the *maximum-emergence* scenario (Fig. 2.2) 50 % of the incoming patients are infected with A-resistant bacteria, and the other 50 % are infected with B-resistant bacteria. These conditions maximally favour opportunities for horizontal gene transfer. The basic reproduction number was set to  $R_0 = 0.5$  (Equation A1) to ensure that double-resistant strains are flushed out, reducing the stochastic dependency on earlier emergence events while maintaining a high potential for new emergence.

**Instruction Sets.** Based on the parameter defined for each experiment (see Table 2.1), we generated instructions that were passed to the liquid handling platform. These instructions specify which patients are passaged or discharged and admitted, who infects whom, and the treatment for mixing therapy. Instructions are randomly generated prior to each transfer. We call the entirety of all instructions that come up during an experimental run an instruction set. Instruction sets are identical across all treatment arms and replicates.

**Computational Model.** We created a stochastic model ([SI Computational Model](#)) incorporating 94 *in silico* patients, each capable of adopting one of six resistance profiles  $\phi \in \{U, S, A_r, B_r, AB_r, (A_r \& B_r)\}$ . The model is structured analogue to the *in vitro* experiments (Fig. A1) and alternates between modelling the transactions between wells and the effect of treatment during incubation.

Admission and discharge (turnover) were simulated by replacing the resistance profile of the current patient with that of the incoming patient, as defined by the instruction set. Infections are simulated by combining the resistance profiles of the receiving well  $i$  and the infecting well  $j$ . The resulting resistance profile  $\phi_i + \phi_j$  is determined using the rules based on the dominance of resistance specified in Table A9. Calculations involving more than two resistance profiles apply the associative law and are determined pairwise, e.g.  $(U + S) + A_r = S + A_r = A_r$ .

To model treatment effects, we use transition probabilities to assign the post-incubation resistance profile  $\phi(\hat{T})$  stochastically based on the treatment and the pre-incubation resistance profile  $\phi(T)$ . The transition probabilities (Table A18 – A25) were estimated based on experimental data across all experiments.

**In Silico Sensitivity Analysis.** To augment the experimental data, we conducted an *in silico* sensitivity analysis. We randomly generated 10,000 parameter sets with and 10,000 without pre-existing double resistance. Turnover and infection probabilities were uniformly sampled [0.05, 0.95], allowing for  $R_0 \in [0.0526, 19]$ . The sampling proportions  $c_\phi$  for all incoming resistance profiles ( $\phi \in \{U, S, A_r, B_r, AB_r\}$ ) were randomised by sampling a number  $n_\phi \in [0, 1]$  from a uniform distribution and subsequently normalising by the sum:  $c_\phi = n_\phi / \sum_j n_j$ . We created ten randomised

instruction sets for each parameter set and conducted one simulation per instruction set (Fig. A3D) for 28 transfers.

For this analysis, the frequency of non-infected individuals during the last four transfers was used as a performance metric for treatment strategies, as it also indirectly reflects the frequency of both double- and single-resistant patients. We conducted an ANOVA test to assess if the effect of the treatment strategies significantly ( $p < 0.05$ ) influences the frequency of uninfecteds. For significant tests, we proceeded with Tukey's post hoc analysis ( $p < 0.05$ ), identifying significantly distinct pairs of strategies. Strategies not significantly inferior to others were classified as 'winners', while strategies not significantly superior to any were classified as 'losers'. Strategies that win or lose a parameter set alone are 'single winners' or 'single losers'.

**Data Availability** Experimental data and analysis scripts, as well as code for the computational model, have been deposited in Zenodo (<https://doi.org/10.5281/zenodo.14137410>).

#### Acknowledgments

We thank Adrian Egli for generously providing the ESBL samples containing the plasmids and Fabienne Benz and Jana Huisman for their assistance with selecting them. We also thank Lukas Graz from the Seminar for Statistics (ETHZ) for his statistical consultation. We used Grammarly and OpenAI's ChatGPT for proofreading and grammar checking. We thank ETH Zurich for providing funding.

## Bibliography

- [1] .P. F. Kable and H. Jeffery. "Selection for Tolerance in Organisms Exposed to Sprays of Biocide Mixtures: A Theoretical Model". In: *Phytopathology* 70.1 (1980), pp. 8–12. issn: 0031-949X. doi: 10.1094/phyto-70-8.
- [2] .C. J. Delp. "Coping with resistance to plant disease". In: *Plant Dis.* 64 (1980), pp. 652–657. doi: 10.1094/PD-64-652.
- [3] .G. Skylakakis. "Effects of Alternating and Mixing Pesticides on the Buildup of Fungal Resistance". In: *Phytopathology* 71.11 (1981), pp. 1119–1121. issn: 0031-949X. doi: 10.1094/phyto-71-1119.
- [4] .D. E. Goldberg, R. F. Siliciano, and W. R. Jacobs. "Outwitting evolution: Fighting drug-resistant TB, Malaria, and HIV". In: *Cell* 148.6 (2012), pp. 1271–1283. issn: 10974172. doi: 10.1016/j.cell.2012.02.021.
- [5] .B. Siedentop et al. "The effect of combining antibiotics on resistance : A systematic review and meta-analysis". In: *eLife* 13 (2024), pp. 1–25. doi: 10.7554/eLife.93740.1.
- [6] .P. J. van Duijn et al. "The effects of antibiotic cycling and mixing on antibiotic resistance in intensive care units: a cluster-randomised crossover trial". In: *Lancet Infect. Dis.* 18.4 (2018), pp. 401–409. issn: 14744457. doi: 10.1016/S1473-3099(18)30056-2.
- [7] .H. Uecker and S. Bonhoeffer. "Antibiotic treatment protocols revisited: The challenges of a conclusive assessment by mathematical modelling". In: *J. R. Soc. Interface* 18.181 (2021). issn: 17425662. doi: 10.1098/rsif.2021.0308.
- [8] .S. Bonhoeffer, M. Lipsitch, and B. R. Levin. "Evaluating treatment protocols to prevent antibiotic resistance". In: *Proc. Natl. Acad. Sci. U. S. A.* 94.22 (1997), pp. 12106–12111. issn: 00278424. doi: 10.1073/pnas.94.22.12106.
- [9] .B. Tepekule, H. Uecker, I. Derungs, A. Frenoy, and S. Bonhoeffer. "Modeling antibiotic treatment in hospitals: A systematic approach shows benefits of combination therapy over cycling, mixing, and mono-drug therapies". In: *PLoS Comput. Biol.* 13.9 (2017), pp. 1–22. issn: 15537358. doi: 10.1371/journal.pcbi.1005745.
- [10] .D. C. Angst, B. Tepekule, L. Sun, B. Bogos, and S. Bonhoeffer. "Comparing treatment strategies to reduce antibiotic resistance in an in vitro epidemiological setting". In: *Proc. Natl. Acad. Sci. U. S. A.* 118.13 (2021), pp. 1–7. issn: 10916490. doi: 10.1073/PNAS.2023467118.
- [11] .J. S. Huisman et al. "The effect of sequencing and assembly on the inference of horizontal gene transfer on chromosomal and plasmid phylogenies". In: *Philos. Trans. R. Soc. B Biol. Sci.* 377.1861 (2022). issn: 14712970. doi: 10.1098/rstb.2021.0245.
- [12] .S. Tschudin-Sutter et al. "Prospective validation of cessation of contact precautions for extended-spectrum β-lactamase-producing *Escherichia coli*". In: *Emerg. Infect. Dis.* 22.6 (2016), pp. 1094–1097. issn: 10806059. doi: 10.3201/eid2206.150554.
- [13] .European Committee on Antimicrobial Susceptibility Testing (EUCAST). *Antimicrobial susceptibility testing EUCAST disk diffusion method Version 12.0 January*. 2024.
- [14] .K. Hofstetter, E. Salgado-Thalmann, and M. Bachmann. *Kennzahlen der Schweizer Spitäler 2015*. 2017.
- [15] .B. Headd and S. A. Bradford. "Physicochemical factors that favor conjugation of an antibiotic resistant plasmid in non-growing bacterial cultures in the absence and presence of antibiotics". In: *Front. Microbiol.* 9 (2018), pp. 1–14. issn: 1664302X. doi: 10.3389/fmicb.2018.02122.
- [16] .T. Fehér et al. "Competition between transposable elements and mutator genes in bacteria". In: *Mol. Biol. Evol.* 29 (2012), pp. 3153–3159. issn: 0737-4038. doi: 10.1093/molbev/mss122.



## Chapter 3

### High-Throughput Quantification of Population Dynamics using Luminescence

---

**Authors:** Malte Muetter<sup>a</sup>, Daniel C. Angst<sup>a</sup>, Roland R. Regoes<sup>a</sup>, Sebastian Bonhoeffer<sup>a</sup>

<sup>a</sup>*Institute of Integrative Biology, Department for Environmental System Science, ETH Zurich, 8092 Zurich, Switzerland*

**Contributions:** MM, DCA, RRR, and SB designed research; MM and DCA constructed the strains used; MM performed experiments, developed the mathematical model, and analyzed data; MM, DCA, RRR, and SB wrote the manuscript.

---

#### Abstract

The dynamics of bacterial population decline at antibiotic concentrations above the minimum inhibitory concentration (MIC) remain poorly characterized. This is because measuring colony-forming units (CFU), the standard assay to quantify inhibition, is slow, labour-intensive, costly, and can be unreliable at high drug concentrations. Luminescence assays are widely used to quantify population dynamics at subinhibitory concentrations, yet their limitations and reliability at super-MIC concentrations remain underexplored. To fill this gap, we compared luminescence- and CFU-based rates across 20 antimicrobials. In our experiments luminescence- and CFU-based rates did not differ significantly for half of them. For the other half, CFU-based estimates of rates of decline were consistently higher. The estimates differed for two main reasons: First, because light intensity tracks biomass more closely than population size, luminescence declined more slowly than the population when bacteria filamented. Second, CFU-based estimates indicated a steeper decline when antimicrobial treatment reduced the number of colonies formed per plated bacterium. This effect can result from changes in clustering behaviour, physiological changes that impair culturability, or antimicrobial carry-over. Thus, the suitability of luminescence to quantify bacterial decline depends on the physiological effects of the antimicrobial used (e.g. filamentation) and whether the quantity of interest is cell number or biomass. Within these limitations, luminescence can serve as an efficient, high-throughput alternative for quantifying bacterial dynamics at super-MIC concentrations.

### 3.1 Introduction

Accurate characterization of changes in population size under treatment is essential for understanding the evolution of antibiotic resistance. Commonly, the effect of treatment on bacterial populations is quantified by pharmacodynamic (PD) curves. PD curves quantify the relationship between drug concentration and the rate of population change (net growth) [1]. These range from no antibiotic, through sub-MIC concentrations that only reduce population growth, to super-MIC concentrations that kill bacteria and lead to a population decline.

The growth parameter most often used in PD curves is the exponential rate of change in living bacteria,  $\psi_B$ , reflecting both division and death. However, other population properties, such as changes in the number of culturable bacteria or total biomass, may also be relevant, depending on the specific biological question.

In practice, PD-curves are fitted to the rate of change of a measured proxy signal such as optical density (OD), colony-forming units (CFU) or bioluminescent light intensity.

OD is a cost-effective approach for real-time, high-throughput monitoring of culture turbidity without sacrificing the population. OD is positively correlated (within a certain range) to cell density. However, since OD cannot distinguish between living and dead cells, this estimate of cell density is only reliable for increasing or stable population sizes, making it unsuitable for quantifying negative rates (kill rates).

CFU assays estimate bacterial density by counting the colonies that grow on permissive agar media from plated samples. They remain the gold standard for measuring population size under both sub-MIC and super-MIC conditions and are widely used to quantify pharmacodynamic curves (e.g. [1, 2]).

Luminescence assays measure the light emitted by bioluminescent bacterial cultures and can be used as a proxy to estimate changes in population size. Two main approaches for biological assays are: eukaryotic *luc* systems and the prokaryotic *lux* systems. The *luc* system, derived from eukaryotes such as fireflies, uses an ATP-dependent luciferase that oxidises luciferin to emit light [3]. It was adapted for bacterial reporters by chromosomal integration in *Mycobacterium tuberculosis* [4] and later tested for quantifying antibiotic killing in *Streptococcus gordonii* [5]. However, *luc*-based assays are limited by sensitivity to intracellular ATP, the need for addition of a costly substrate, and luciferin degradation, making continuous measurement in the same culture impractical.

By contrast, the *lux* operon of prokaryotes such as *Photobacterium luminescens* encodes all components required to sustain the bioluminescence reaction [6, 7]. No external substrate is needed, so light production can be recorded continuously in the same culture, making the *lux* system better suited for high-throughput applications than the *luc* system. Accordingly, it has been widely used to record growth curves and quantify sub-MIC treatment effects [8–13].

While high-throughput OD and luminescence measurements at sub-MIC concentrations provide

valuable insights into drug effects on growth rates, the super-MIC range is clinically more relevant. A comprehensive investigation of super-MIC population dynamics (for example, pharmacodynamics of drug combinations or resistance mutations) using CFU remains impractical, as it is labor-intensive and inherently low-throughput.

Whether lux luminescence can be extended to super-MIC ranges remains unclear, as direct comparisons between CFU- and luminescence-based measurements are scarce and so far limited to only a few drugs [14–16]. Here we evaluate the limitations of lux luminescence assays and assess whether they can reliably quantify growth rates at super-MIC concentrations. For this, we compare changes in light intensity with changes in CFU counts across 20 antimicrobials spanning 11 classes, including penicillins, cephalosporins, carbapenems, polymyxins, quinolones, rifamycins, tetracyclines, amphenicols, folate antagonists, fosfomycin, and antimicrobial peptides. Luminescence- and CFU-based rates aligned for some antimicrobials (e.g., colistin, amoxicillin) but diverged for others (e.g., ciprofloxacin). Here, we explore the potential and limitations of both methods, identify the conditions under which they align with the rate of change of population size, and discuss their implications for studying antimicrobial effectiveness across sub-MIC and super-MIC ranges.

### 3.2 Results

To investigate the validity of luminescence assays as a high-throughput measure for bacterial population size and its change across the entire range of antimicrobial concentrations, we compared this measure to the number of colony-forming units (CFU). Specifically, we tested whether the rates of change in light intensity,  $\psi_I$ , and CFU,  $\psi_{\text{CFU}}$ , agree for various drugs, and if not, we explored the reasons for any discrepancies.

We used a modified luminescence operon *luxCDABE* from *P. luminescence*. To minimize plasmid copy-number effects on the light emitted by a single cell (cell-specific luminosity), we excised the operon from the pCS-λ plasmid ([8]) and inserted it into the *Escherichia coli* chromosome.

**Light intensity is proportional to bacterial density.** We first evaluated how the observed bioluminescent light intensity,  $I$ , which represents a fraction  $\kappa$  of the total light emitted by the culture, correlates with bacterial density. To this end, we prepared three replicate overnight cultures of bioluminescent *E. coli*, serially diluted them tenfold, and measured the light intensity for each dilution. We found that light intensity increased linearly with bacterial density for signals above approximately 20 rlu (Fig. B1;  $R^2 = 0.987$ ,  $n = 20$ ,  $p < 10^{-14}$ ), with a proportionality constant  $m = 0.006 \frac{\text{rlu}}{\text{CFU}}$ . From this observation, we conclude that  $\kappa$  remains independent of bacterial density, indicating that, up to one-tenth of the stationary-phase density, high cell densities do not attenuate emitted light. Thus, provided we maintain the same luminescence plate-reader setup, we can assume  $\kappa$  to be constant for all subsequent analyses.

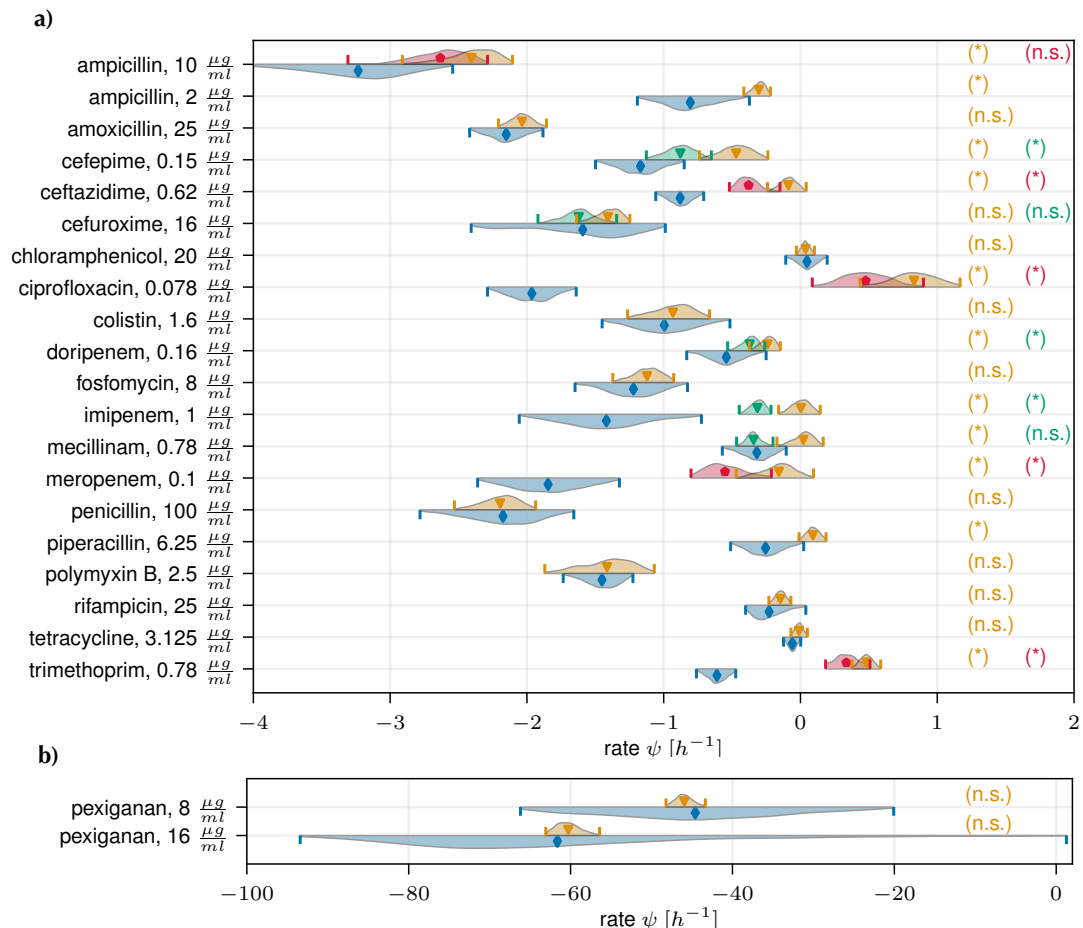


Fig. 3.1 – Comparison of CFU-based and luminescence-based rates of change. For each drug, we generated 2000 bootstrapped datasets by resampling time-series CFU and light-intensity data with replacement and fitted an exponential function to each bootstrap replicate to obtain distributions of rates. Panel (a) shows these distributions for 20 drug-concentration assays across 19 antibiotics; panel (b) shows the antimicrobial peptide pexiganan at 8  $\mu\text{g}/\text{mL}$  and 16  $\mu\text{g}/\text{mL}$ . The distribution of  $\psi_{\text{CFU}}$  is shown in blue (lower half of each violin, diamond). The distribution of  $\psi_I$  is shown in orange (upper half, triangle). Green distributions ( $\psi_I^*$ ; triangle) represent luminescence-based rates calculated from data starting at the first peak onward. Red distributions show volume-adjusted luminescence rates ( $\psi_J$ ; pentagon). Vertical lines mark the 95 % confidence intervals. Asterisk (\*) or letters (n.s.) indicate whether CFU-based rates differ significantly from the corresponding luminescence-based rate or not (see Methods), with color coding matching the respective luminescence-based distribution. Wide confidence intervals for pexiganan reflect biphasic killing, steep curves, and noisy CFU data.

**Luminescence-based rates agree with CFU-based kill rates in 11 out of 22 antimicrobial assays.**

Given the linearity between light intensity and bacterial density shown above, we tested whether the rate of change of light intensity  $\psi_I$  aligns with the rate of change of bacterial population size ( $\psi_B$ ) under super-MIC antimicrobial concentrations. Since we cannot measure  $\psi_B$  directly, we first compared  $\psi_I$  to the CFU-based rate,  $\psi_{CFU}$ , and then discussed their relation to  $\psi_B$ . We measured CFU and light intensity over time for 20 drugs (Table B1) using an automated liquid handler (Methods) and estimated the distributions of the rates of change of CFU ( $\psi_{CFU}$ ) and light intensity ( $\psi_I$ ) by bootstrap (Fig. 3.1, Table B2). We classified the luminescence and CFU-based rate distributions as “not significantly different” (n.s.) if each mean fell within the other’s 95% percentile and otherwise significantly different (\*). All time-series data are presented in Figures B2–B20. For amoxicillin, cefuroxime, chloramphenicol, colistin, fosfomycin, penicillin, pexiganan, polymyxin B, rifampicin, and tetracycline,  $\psi_I$  and  $\psi_{CFU}$  did not differ significantly. However, we observed significant discrepancies for ampicillin, cefepime, ceftazidime, ciprofloxacin, doripenem, imipenem, mecillinam, meropenem, piperacillin, and trimethoprim.

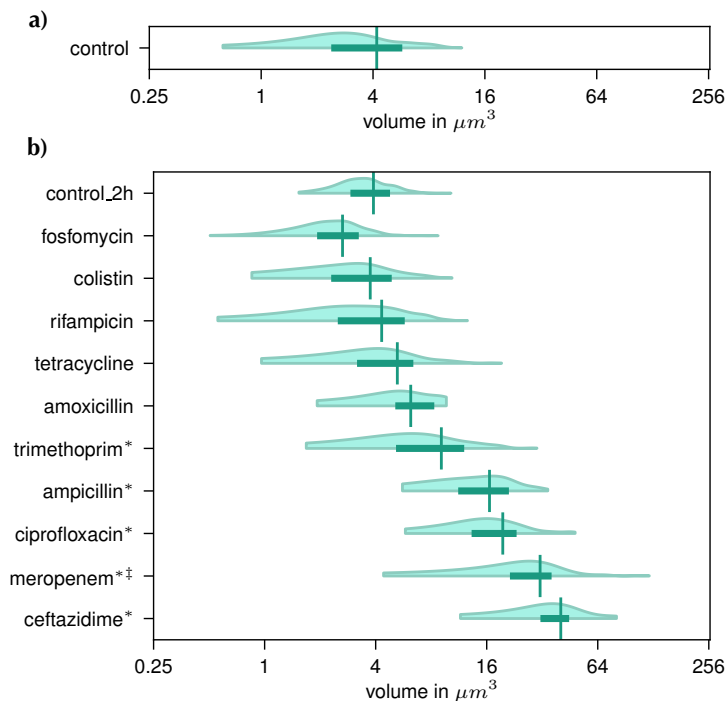
For all cases where significant discrepancies were observed, the light intensity declined more slowly than the CFU signal. In the following we investigate potential reasons why the light signal may decline more slowly and the CFU signal more rapidly than the “true”  $\psi_B$ .

**No support for SOS-driven increase in luminescence promoter activity.** To explain the observed discrepancies between CFU- and luminescence-based rates, we tested whether the SOS response might upregulate lux expression, increasing the cell-specific luminosity. To this end, we exposed the strains to UV light to induce the SOS response. Specifically, we alternated between measuring light intensity and optical density, and exposing cultures to UV (Appendix B3).

UV treatment impaired bacterial growth significantly, yet the OD-normalized light intensity ( $\propto$  cell-specific luminosity) of UV-treated cells was lower than that of untreated controls (Fig. B21d; t-test,  $p = 3 \cdot 10^{-5}$  for the last time point). This implies that SOS induction did not upregulate lux expression, as cells under SOS had lower light output per cell than controls. While we cannot exclude the possibility that a non-UV-induced SOS response enhances cell-specific luminosity, our findings suggest that promoter upregulation is unlikely to explain why luminescence-based rates exceed CFU-based rates.

**Filamentation aligns with divergence between CFU- and luminescence-based rates.** Antibiotic pressure is known to impair septation and induce bacterial filamentation. Our second hypothesis was that larger, filamented cells might emit more light per cell, thereby driving the divergence between CFU- and luminescence-based rates. We explored this for a subset of the antibiotics tested by imaging bacteria before and after two hours of antibiotic treatment (Fig. B22–B34; see Methods). From these images, we measured bacterial length and width (Fig. B35) and calculated the cell volumes (??, Appendix B3).

Fig. 3.2 – Panels A–C show the mean frequency of uninfected (grey), single-resistant infected (blue), and double-resistant infected wells (green) during the last four transfers of the three scenarios. Circles represent replicates ( $n = 4$ ), and bars represent means. Within resistance categories, bars not sharing a letter are significantly different (pairwise Tukey post hoc test,  $p < 0.05$ ; ANOVA tables and all p-values can be found in Table A34 – Table A50).



For antibiotics where microscopy showed no significant filamentation (amoxicillin, colistin, fosfomycin, rifampicin, and tetracycline, Table B3), luminescence-based and CFU-based rates did not differ significantly (Fig. 3.1, Table B2). In contrast, for those drugs where microscopy data indicated significant filamentation (ampicillin, ceftazidime, ciprofloxacin, meropenem, and trimethoprim), luminescence-based rates were significantly higher than CFU-based rates.

**Filamentation model predicts divergence between luminescence- and CFU-based rates.** To further investigate the link between filamentation and the recorded light signal, we developed a simplified population dynamical model which incorporates bacterial filamentation (Appendix B2). In this model, cells elongate linearly [17], causing the population to converge to an equilibrium cell volume, provided the division rate remains above zero (Fig. B36). We assume that cell-specific luminosity scales with cell volume — i.e., the volume-specific luminosity remains constant.

We simulate filament-inducing treatment by reducing the division rate by  $\Delta\lambda$ , which causes an initial rapid increase in average cell size. As the mean cell volume stabilizes and cell-specific luminosity reaches equilibrium, the luminescence-based rate converges to the rate of change of population size  $\psi_B$  (Fig. B36). Depending on the division and death rates, this dynamic can result in an initial peak in light intensity followed by a decline (Fig. B36b).

This initial peak in light intensity, as predicted by the model, was experimentally observed for several drugs associated with filamentation (Figures B3, B5, B9, B11, B12, and B13).

To investigate the dependence of  $\psi_B$  and  $\psi_I$  on treatment-induced changes in division rate and death rate ( $\delta$ ), we simulated four hours of treatment (details and parameters in Appendix B2). Our model shows that a reduction in  $\lambda$  leads to higher luminescence-based rates  $\psi_I$  relative to the rate of change of population size  $\psi_B$ , with particularly large discrepancies when the death rate is low (Fig. 3.3). The results from this model suggest that excluding early data points, where the mean cell volume changes rapidly, improves agreement between the estimated rates  $\psi_I$  and  $\psi_B$ . This is evident in Fig. B36b, where the slopes inferred from luminescence and from population size differ initially but are nearly identical at later times.

We tested this approach by refitting all experimentally acquired luminescence-based rates that exhibited an initial peak, excluding data points recorded before the light signal reached its maximum. The resulting distributions of  $\psi_I^*$  (green) are shown in Fig. 3.1. An exception was made for meropenem, for which we know the change of cell volume and thus applied an alternative correction as described below. This adjustment substantially reduced the difference between CFU- and luminescence-based estimates for all tested drugs and fully eliminated the discrepancy for mecillinam.

**Adjusting luminescence intensities by changes in volume narrows the gap between CFU- and luminescence-based rates.** Given the model-predicted differences between  $\psi_I$  and  $\psi_B$  in filamenting populations, we next tested whether combining morphological data with measured light intensities can help infer  $\psi_B$ . This approach only works if the volume-specific luminosity is constant (Appendix B1, Equation B12). We used the mean cell volume data acquired by microscopy imaging before ( $v_{\text{obs},0}$ , ??a), and after treatment ( $v_{\text{obs},2h}$ , ??b), for all drugs that caused significant filamentation (ampicillin, ceftazidime, ciprofloxacin, meropenem, and trimethoprim). The light intensities were then volume-corrected as  $J(t) = I(t) v_{\text{obs},0} / v(t)$ , where  $v(t)$  is derived from the filamentation model ((B44), Appendix B2). The free parameters were determined by minimizing Equation B51. All adjusted light signals  $J$  are shown in Figures B2a, B4, B7, and B13.

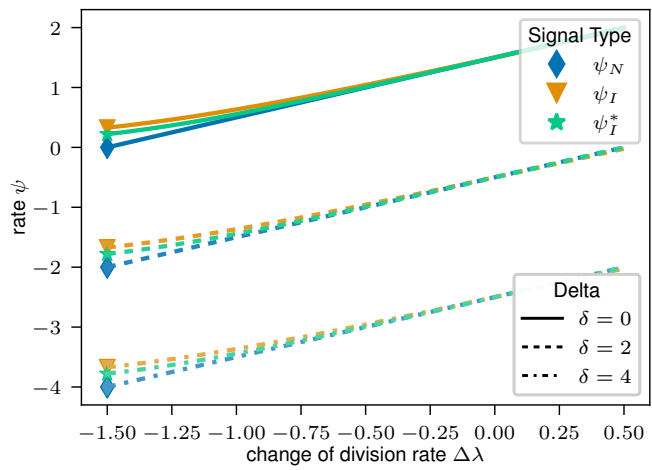
For ampicillin, the CFU-based and volume-corrected luminescence-based rates ( $\psi_J$ ) did not differ significantly (Table B2). For ceftazidime, ciprofloxacin, and meropenem, volume correction reduced the discrepancy, but  $\psi_J$  remained significantly above  $\psi_{\text{CFU}}$ . We observed in all experiments that volume correction narrowed but never reversed the discrepancy ( $\psi_{\text{CFU}} \leq \psi_J \leq \psi_I$ , Equation B23). From this observation and the derivation in the SI (Appendix B1), we conclude that  $\psi_I$  is closer to  $\psi_V$  (rate of total cell volume change) than to  $\psi_B$  (rate of bacterial number change).

Three factors may explain these residual differences: (i) the assumption of constant volume-specific luminosity may not hold; (ii) the approximation of  $v(t)$  may be inaccurate, and excluding entangled or overlapping cells from the analysis introduces a bias that underestimates the volume of heavily filamented cells; (iii) the CFU-based method may underestimate  $\psi_B$ .

For ciprofloxacin, the large disparity between  $\psi_{\text{CFU}}$  and  $\psi_I$  is unlikely to be explained by factors

(i) and (ii) alone. Bringing the two rates into agreement solely by adjusting cell-specific luminosity would require an almost four-order-of-magnitude increase, which appears implausible. We therefore conclude that, in this case, CFU-based measurements likely overestimate the rate of population decline, corresponding to an underestimation of  $\psi_B$  (iii).

Fig. 3.3 – Simulations based on the filamentation model quantifying how changes in division rate due to treatment ( $\Delta\lambda$ ) and death rate ( $\delta$ ) influence the rate of change of population size ( $\psi_B$ , blue), the rate of change of light intensity ( $\psi_I$ , orange), and the rate of change of light intensity when the first 2 hours of data are excluded ( $\psi_I^*$ , green). These illustrative simulations were conducted using an initial division rate  $\lambda_0 = 1.5 \text{ h}^{-1}$ . More details and all parameter values can be found in Appendix B2.



**CFU-based estimates can overestimate the rate of population decline.** After exploring why luminescence assays can underestimate the rate of population decline, we now explore why CFU assays may overestimate it. By definition, the rate of change of the CFU signal,  $\psi_{\text{CFU}}$ , only matches  $\psi_B$  if the number of colonies emerging per plated bacterium,  $\eta \in [0, 1]$  (Equation B4), is constant over time (Appendix B1, Equation B6). This assumption can be problematic for three main reasons:

- a) **Loss of culturability:** The number of colonies emerging per plated bacterium,  $\eta$ , depends on the division rate  $\lambda$ , which can be affected temporarily or permanently by treatment ([18]), e.g. due to DNA damage. In extreme cases, viable and culturable cells can be converted into viable but non-culturable (VBNC) cells ([19–21]), meaning they continue to be metabolically active but cease to divide ( $\lambda = 0$ ) and therefore no longer form colonies on agar. Typically, cells can reproduce at the start of a time-kill assay but may, depending on the drug, partially or completely lose this ability as the assay progresses, causing an underestimation of  $\psi_B$ .
- b) **Antimicrobial carryover:** Antibiotics transferred onto agar by plating a diluted culture can experience a residual treatment effect; either on the division rate  $\lambda$  or the death rate  $\delta$ , depending on the mode of action of the drug and thus reduce the probability of colony formation. This phenomenon, known as antimicrobial carryover, has been described in previous studies [22–

24]. Its effect is usually minimal at the start of a time-kill assay, when bacterial density is high and plated samples are highly diluted. However, as the assay progresses and bacterial density declines, less dilution is needed, increasing the concentration of the transferred antibiotic. As a consequence, CFU-based rates would underestimate  $\psi_B$  between two time points  $t_0$  and  $t_1$  by  $\frac{\ln(\eta_1) - \ln(\eta_0)}{\Delta t}$ , where  $\eta_i$  denotes the mean number of colonies formed per plated bacterium at time  $t_i$ .

- c) **Aggregation:** Filamentation or altered cell adhesiveness can change the size distribution of colony-initiating clusters on agar after plating (Equation B3). Changes in cluster size in turn, affect the average number of clusters per plated bacterium, thereby biasing estimates of  $\psi_B$ .

**Partial loss of culturability causes CFU to underestimate  $\psi_B$  for ciprofloxacin and trimethoprim treatment.** During ciprofloxacin treatment, CFU counts fell steeply while light intensity continued to rise (Fig. B7). This discrepancy is consistent with previous reports comparing CFU and luminescence during fluoroquinolone killing [14, 25]. To investigate the cause of this discrepancy, we plated treated cultures on phosphate-buffered saline (PBS) agar containing propidium iodide (PI), a red fluorescent dye that binds to nucleic acids but cannot penetrate intact cell membranes. PI is a red fluorescent dye that binds to nucleic acids and is widely used to stain permeable cells due to its inability to penetrate intact cell membranes. Microscopic imaging (Fig. B27) revealed almost no red fluorescence, indicating that the cells remained impermeable. Although impermeability alone does not confirm viability, additional observations support the conclusion that most cells were still alive: the absence of bacterial debris (as has been observed for drugs with similar decline in CFU such as amoxicillin), visible growth indicated by increased cell size compared to two hours earlier, and continued (and even increased) light emission. These findings suggest that most cells remain alive but are unable to form colonies under the provided conditions, possibly due to DNA damage induced by ciprofloxacin [26]. This observation aligns well with previous studies on ciprofloxacin, which found that CFU can underestimate viability relative to non-culture-based methods [19, 27, 28].

Trimethoprim treatment showed similar, though less pronounced, results (Fig. B19). Trimethoprim, which impairs DNA replication ([29]), likewise caused an increase in light intensity and a decline in CFU counts, while microscopy revealed intact, mostly impermeable, filamented cells (Fig. B34).

**Antimicrobial carryover causes underestimation of  $\psi_B$  for pexiganan using CFU.** Building on our understanding of when luminescence assays accurately estimate  $\psi_B$ , we hypothesized that antimicrobial peptides (AMPs) would be an ideal application for this method. We expected that, during the AMP's short killing phase, changes in the cell-specific luminosity would remain negligible compared to the high kill rates AMPs can achieve.

Initially, however, we failed to recover almost any colonies on agar, despite the light intensity indicating a high enough bacterial density. Moreover, colony counts were inconsistent across dilutions: wells diluted 100-fold and 1000-fold from the same time point yielded similar colony numbers, instead of reflecting the tenfold difference. We suspected that AMPs from the liquid culture, including those attached to the bacterial surface, were carried over into the PBS dilution medium, causing continued cell death during dilution and after plating.

To test this, cultures treated with pexiganan for 1 min were diluted 1:100 in PBS and subsequently sampled and plated at four time points, approximately 45 minutes apart. As dilution medium, we tested PBS supplemented with various concentrations of  $\text{CaCl}_2$  and  $\text{MgCl}_2$ . These compounds were selected based on prior evidence that they inhibit the activity of other AMPs ([30]).

Our results show that supplementing the dilution medium increased the measured CFU substantially (Fig. B38, Appendix B3). This indicates that bacterial survival probability increases when diluted in the supplemented medium. Conversely, diluting in unsupplemented PBS does not stop bacteria from dying. Supplementing 100 mM  $\text{MgCl}_2$  yielded the highest CFU count for the first time point (Table B4). Since CFU cannot systematically overestimate bacterial density, this count represents the best estimate of the bacterial density. Consequently, we supplemented the PBS with 100 mM  $\text{MgCl}_2$  in subsequent pexiganan experiments.

Given this insight into the residual killing effect of pexiganan and how to mitigate it, we repeated the CFU time-kill experiment using two different dilution media (Appendix B3). We recorded three replicates for each of the two time-kill curves. We diluted the cultures at each time point in either pure PBS or PBS supplemented with 100 mM  $\text{MgCl}_2$  and counted colonies on all agar plates from three dilution steps. To lower the detection limit by one order of magnitude, we increased the plated volume from 10  $\mu\text{L}$  to 100  $\mu\text{L}$ . Since this volume exceeds the capacity of the automated high-throughput setup, we used the standard manual CFU plating method instead.

We observed a much steeper initial decline in CFU for the cultures diluted in pure PBS compared to the supplemented ones (Fig. B39). In pure PBS, more highly diluted samples consistently yielded higher CFU estimates (Fig. B39a), supporting the antimicrobial carryover hypothesis. This pattern diminished over time, suggesting a reduction in the residual killing effect of pexiganan, which we discuss below.

**Luminescence and CFU show identical decline rates for pexiganan time-kill curves if residual killing is prevented.** To confirm that eliminating residual pexiganan killing aligns CFU and luminescence, we supplemented PBS with 100 mM  $\text{MgCl}_2$  and measured both signals at pexiganan concentrations of 8  $\frac{\mu\text{g}}{\text{mL}}$  and 16  $\frac{\mu\text{g}}{\text{mL}}$  using the “rapid luminescence-CFU assay setup” (Methods). We observed no significant difference between the CFU- and luminescence-based rates for either of the tested pexiganan concentrations (Fig. 3.1b, Table B2). However, examining the time series (Fig. B20) revealed that while CFU and luminescence signals declined in parallel for the 8  $\frac{\mu\text{g}}{\text{mL}}$  treat-

ment, they diverged for the  $16 \frac{\mu\text{g}}{\text{mL}}$  kill curve. In this case, the CFU signal initially declined much faster (rates below  $-200 \text{ h}^{-1}$ ), and subsequently declined more slowly than the corresponding luminescence signal, ultimately resulting in a similar average rate (approximately  $-60 \text{ h}^{-1}$ ).

This pattern suggests that luminescence assays may not be able to capture extremely rapid kill rates, potentially due to short delays between irreversible cell damage, actual cell death, and the subsequent cessation of luminescence. This limitation should not affect measurements for most conventional antibiotics, for which rates rarely exceed  $-10 \text{ h}^{-1}$ .

**Pexiganan rapidly loses killing capacity.** During the pexiganan experiments, we observed an initial steep decline in bacterial density, predicted by both CFU and luminescence, followed by almost constant signals (Figures B20, B39). Two possible, non-exclusive explanations for this observation are: first, pexiganan is deactivated or sequestered from the medium by attaching to targets on the bacteria over time; and second, the remaining bacteria are unaffected by the AMP because they are resistant or persisters. To investigate the first explanation, we exposed bacteria to pexiganan for 5 min at  $16 \frac{\mu\text{g}}{\text{mL}}$ , after which the supernatant was collected and tested for its ability to kill bacteria (Appendix B3). While the initial treatment showed rapid bacterial killing ( $\psi_{\text{CFU}} \approx -46 \text{ h}^{-1}$  between  $t_0 = 0$  and  $t_1 = 5 \text{ min}$ ), bacteria exposed to the supernatant alone showed no significant reduction in viability (Fig. B40, Table B5). These results show that the supernatant has no residual killing effect. This makes deactivation or sequestration through attachment of pexiganan the likely explanation for the flattening CFU signal, even though we did not assess whether the surviving cells are resistant or persisters.

### 3.3 Discussion

We evaluated whether luminescence can serve as a high-throughput proxy for population dynamics by comparing it with CFU assays. We found no significant difference between CFU- and luminescence-based rates for treatments that neither induce substantial changes in culturability nor provoke strong morphological changes, such as filamentation. However, for drugs that induce filamentation and/or loss of culturability, the two methods can yield significantly different results. The divergence between the two rates does not imply that either method is incorrect; rather, each captures a different aspect of the population.

The CFU method counts bacteria capable of forming colonies on permissive media (i.e., culturable cells). When inferring growth rates from CFU, the observed rate of change  $\psi_{\text{CFU}}$  reflects both the rate of change of population size  $\psi_B$  and changes in the probability that a plated bacterium forms a colony,  $\eta$  (Equation S3.4). The CFU-based rate equals  $\psi_B$  only if  $\eta$  remains constant over time.

However,  $\eta$  can change for three main reasons. First, altered clustering behavior can change how many bacteria seed a single colony. This directly shifts the observed colony count. Second, physiological changes to the bacteria may lead to a temporary or permanent change in culturability ([18–

21, 27, 31]), which may increase the fraction of viable cells that fail to form colonies, e.g. due to a reduced division rate. Third, residual drug activity carried over to the agar can alter on-plate conditions, thereby reducing division or increasing the death rate ([22–24]).

Preventing antibiotic carryover when handling low-density cultures treated with highly concentrated antimicrobials is challenging and, in some cases, infeasible. Centrifugation-based washing (pelleting bacteria and replacing the supernatant) can remove residual drug, but only if the processing delay is negligible relative to the antibiotic’s killing kinetics — a condition unlikely to hold for fast-acting agents such as pexiganan. Moreover, although bacteria generally tolerate high centrifugal forces ([32]), the impact on compromised cells, such as those with destabilized walls, is unknown. As an alternative, we found that supplementing the dilution medium with MgCl<sub>2</sub> effectively neutralizes residual AMP activity, preventing residual killing effects in CFU assays for pexiganan. However, this strategy is not generalizable, as for many antimicrobials the corresponding deactivating agents are unknown — or may not even exist. For these cases, it may be impossible to accurately derive  $\psi_B$  from CFU counts at high drug concentrations.

In contrast to CFU assays, luminescence assays become more reliable at high, fast-killing concentrations. This is because  $\psi_I$  reflects both the rate of population size change,  $\psi_B$ , and changes in cell-specific luminosity ([Equation S3.9](#)); when population declines rapidly,  $\psi_I$  converges to  $\psi_B$ . One exception was observed for extremely rapid kill rates (exceeding  $-60\text{ h}^{-1}$ ), as seen for highly concentrated pexiganan, likely due to short delays between cell death and cessation of luminescence.

For lower kill rates, we observed that the absence of filamentation was a good indicator of stable cell-specific luminosity. In cases where drugs induced filamentation, CFU- and luminescence-based rates diverged. We further demonstrated that correcting for the increased cell size partly compensates for the difference between CFU- and luminescence-based estimates, and we found that the rate of change in light intensity is closer to the change in total cell volume than to the change in total cell number ([SI Appendix 3.2](#)). This makes a constant volume-specific (or mass-specific) luminosity a better assumption than a constant cell-specific luminosity.

Changes in both CFU and luminescence are used as proxy signals for population net growth rates ([1, 2, 8–10, 12, 13]). Whether discrepancies between the changes in these proxy signals and the changes in living bacteria pose a problem depends on the underlying biological question. The rate of change of living bacteria,  $\psi_B$ , is most commonly applied in theoretical modeling to create predictions, making its estimation important. If, instead, the aim is to assess a population’s reproductive potential, for example, in studies focusing on evolutionary dynamics, examining changes in the number of culturable cells (as approximated by CFU) may be more relevant than  $\psi_B$ , as only culturable cells contribute to subsequent generations and thus to evolution. Additionally, tracking changes in total biomass (closer to  $\psi_I$ ) can be more relevant than the number of living bacteria, as biomass accounts for a potential “catch-up” effect, whereby filamented cells fragment into multiple

viable units once antibiotic pressure is removed ([31, 33]).

A notable challenge of using luminescence assays is the absence of a fundamental biological principle linking cell-specific luminosity uniquely to a single biological property, such as biomass, cell number, or gene copy number. We therefore recommend applying luminescence-based methods primarily over short to intermediate timescales, during which abiotic conditions remain relatively stable. When the impact of treatment on cell size is unknown, one should assume that  $\psi_I$  primarily reflects the rate of change of biomass rather than cell number. Thus, to reliably estimate  $\psi_B$ , it is essential to ensure either that cells do not filament, correct for changes in mean cell volume, or restrict analyses to intervals during which volume changes are minimal relative to population decline. Finally, because most drugs in this study were tested at only one concentration, the generalizability of our drug-specific findings remains to be shown.

Our results show that neither CFU nor luminescence is optimal for every experimental scenario. Instead, CFU and luminescence work best under different conditions, measure different population properties and complement each other well. At low and intermediate drug concentrations, changes in CFU accurately reflect changes in bacterial density, but CFU becomes unreliable at high drug concentrations.

Luminescence, by contrast, becomes more reliable at high concentrations, where CFU becomes unreliable. In practice, the luminescence method significantly reduces labor, consumables, and costs: eight PD curves with twelve concentrations and four replicates each can be fit on a single 384-well plate, whereas measuring CFU would require more than 8,000 agar plates, hundreds of dilution plates, and substantial manual labor. Given their scalability and cost-effectiveness, luminescence assays offer a valuable alternative for high-throughput analysis, particularly at high antimicrobial concentrations, where traditional methods become unreliable or even unusable.

### 3.4 Methods

**Strains.** We generated a bioluminescent strain by integrating a modified *P. luminescens luxCDABE* operon, driven by the constitutive  $\lambda$ -Pr promoter, together with a kanamycin resistance cassette (as a marker) into the chromosome of *Escherichia coli* MG1655. This integration replaced the galK gene and was achieved using  $\lambda$ -Red recombination ([34]), following a protocol by Hughes [35, pp. 19–26]. The integrated elements were derived from the pCS- $\lambda$  plasmid ([8, 36]). Primers are listed in [Table S3.6](#). For all time-course experiments, we prepared three replicate exponential cultures by diluting overnight cultures (grown for approximately 18 hours) 1:100 and growing them to exponential phase for 1–1.5 hours.

**Media.** We used LB (Sigma L3022) as a liquid medium and, as a solid medium for CFU plating, LB with 1.5% agar. Cultures were treated by diluting the tenfold working concentration of one of 20 antimicrobials 1:10. All MICs, determined by broth microdilution ([37]), and the concentra-

tions used are listed in [Table S3.1](#). Working concentrations were centered around the MIC, with some variation due to rounding convenience and variability in repeated MIC tests. For colistin and polymyxin B, we used lower concentrations, as higher concentrations in our setup consistently yielded too few colonies for meaningful analysis.

Phosphate-buffered saline (PBS, Sigma 79383) was used as the diluent for CFU assays. If cultures were treated with pexiganan, 100 mM MgCl<sub>2</sub> was added. For microscopy, we added 1  $\frac{\mu\text{g}}{\text{mL}}$  propidium iodide (PI) to the liquid medium and used PBS/PI agar plates (containing PBS with 1.5 % agar and 1  $\frac{\mu\text{g}}{\text{mL}}$  PI) as solid medium.

**Automated CFU plating.** We automated the high-throughput colony-count method described by [38] using an Evo 200 liquid-handling platform (Tecan) integrated with a Liconic STX100 incubator. The platform handles liquids and automatically moves, images, and incubates plates. We produced six colony streaks by spotting six 10  $\mu\text{L}$  drops of diluted bacterial culture onto a one-well agar plate. Plates were automatically tilted for 7 s on a custom-built tilter integrated into the handling platform, to spread the drops and distribute the bacteria. After incubation, plate images were captured using the Pickolo camera (SciRobotics).

The platform is controlled by custom-generated worklists executed in the native software “Evoware”. These worklists were generated using the Python package `pypetting` (version 1.0.1). We analyzed the captured images of the agar plates using a custom colony-recognition script that automatically identifies colonies and allowed the manual addition of unidentified colonies and the removal of mismatched ones. All Python classes for generating the worklists and analyzing colonies are available at Zenodo (DOI: 10.5281/zenodo.15261184).

**Luminescence measurements.** To record the luminescent light intensity, we used an Infinite F200 spectrophotometer plate reader (Tecan), which is also integrated into the liquid-handling platform, with an exposure time of one second. We set 20 rlu as the lower detection limit and excluded all data points below.

**Luminescence-CFU assay setup.** To measure the CFU and light intensity at seven time points, we treated the exponential cultures and then distributed them onto seven (one for each time point) white 384-well plates (Greiner, 781073), with each culture well containing 54  $\mu\text{L}$  medium and 6  $\mu\text{L}$  10x stock solution. We adjusted the duration of the experiments between two and five hours, depending on the anticipated kill rate. For each time point, an assay plate was transferred from the incubator to the plate reader for luminescence measurement. Subsequently, a dilution series was conducted directly in the white plate and plated using the automated plating method, after which the plate was discarded.

**Rapid luminescence-CFU assay setup.** This experiment is a variation of the *Luminescence-CFU assay setup*, adjusted to measure rapid kill curves for the antimicrobial peptide pexiganan. In this setup, we captured four time points within 5 min. Cultures were treated in a 96-deep-well plate (Greiner, 780285) by adding 100  $\mu$ L of the 10x stock solution to 900  $\mu$ L exponential phase culture. 60  $\mu$ L of the treated culture was then transferred to a 384-well white plate (Greiner, 781073) and placed in the plate reader for continuous luminescence recording. For the four CFU time points, samples were taken directly from the deep-well plate, automatically diluted in PBS supplemented with 100mM MgCl<sub>2</sub> in a 96-well plate (Greiner, 655101) to halt the antimicrobial activity and then plated.

**Morphology experiments.** To assess treatment-induced morphological changes, we imaged treated (for 2 hours) and untreated bacteria by spotting 2  $\mu$ L droplets onto PBS/PI-agar plates. The spots were cut out and flipped onto Ibidi  $\mu$ -dishes (Ibidi, 80136) for imaging. We used an Eclipse Ti2 microscope (Nikon) with a 100x objective connected to a DS-Qi2 Nikon Scientific CMOS (sCMOS) camera to image the bacterial cells. The microscope setup included an additional 1.5x zoom, which was used only for some images due to unintentional variation. We estimated the width and length of the bacterial cells using a custom Python script, as described in [SI Appendix 3.4](#).

**Fitting rates of change  $\psi$ .** To compare the rates of change of two signals, we first excluded all data below the detection limits (empty plates or light intensity below 20 rlu). We then truncated both signals at the latest time point where both remained above the detection limit, ensuring the same time frame was used for comparison. Next, we bootstrapped 200 datasets with replacement per signal, while ensuring that each dataset contained more than one time point. For each dataset, we applied a simple regression to fit an exponential function to all time points of each time-kill curve resulting in distributions with 200 rate estimates each.

**Significance.** We classify two distributions of rates as not significantly different (n.s.) if the mean of each distribution falls within the 95% confidence interval of the other. Otherwise, we classify them as significantly different (\*).

#### Data, Materials, and Software Availability

Experimental datasets are available at Zenodo (DOI: 10.5281/zenodo.15261454). Analysis scripts, plate-handling worklists, colony-recognition code, and model code are available at Zenodo (DOI: 10.5281/zenodo.15261184).

#### Acknowledgements

We thank Marco La Fortezza and Ricardo León Sampedro for assistance with microscopy imaging. During manuscript preparation, we used OpenAI's ChatGPT for editorial assistance (grammar, phrasing, and proofreading). This work was supported by funding from ETH Zurich.

## Bibliography

- [1] .R. R. Regoes et al. "Pharmacodynamic Functions: a Multiparameter Approach to the Design of Antibiotic Treatment Regimens". In: *Antimicrobial Agents and Chemotherapy* 48.10 (2004), pp. 3670–3676. doi: 10.1128/AAC.48.10.3670-3676.2004.
- [2] .S. Foerster, M. Unemo, L. J. Hathaway, N. Low, and C. L. Althaus. "Time-kill curve analysis and pharmacodynamic modelling for in vitro evaluation of antimicrobials against *Neisseria gonorrhoeae*". In: *BMC Microbiol.* 16.1 (2016), pp. 1–11. issn: 14712180. doi: 10.1186/s12866-016-0838-9. url: <http://dx.doi.org/10.1186/s12866-016-0838-9>.
- [3] .H. Vellend et al. *Application of firefly luciferase assay for adenosine triphosphate (ATP) to antimicrobial drug sensitivity testing*. 1977.
- [4] .W. R. Jacobs et al. "Rapid Assessment of Drug Susceptibilities of *Mycobacterium tuberculosis* by Means of Luciferase Reporter Phages". In: *Science (80-)*, 260.5109 (1993), pp. 819–822. issn: 0036-8075. doi: 10.1126/science.8484123.
- [5] .B. Loeliger et al. "Antibiotic-Dependent Correlation Between Drug-Induced Killing and Loss of Luminescence in *Streptococcus gordonii* Expressing Luciferase". In: *Microbial Drug Resistance* 9.2 (2003), pp. 123–131. doi: 10.1089/107662903765826705.
- [6] .J. Engebrecht, M. Simon, and M. Silverman. "Measuring Gene Expression with Light". In: *Science* 227.4692 (1985), pp. 1345–1347. doi: 10.1126/SCIENCE.2983423.
- [7] .E. A. Meighen. "Molecular biology of bacterial bioluminescence". In: *Microbiol. Rev.* 55.1 (1991), pp. 123–142. issn: 01460749. doi: 10.1128/mr.55.1.123-142.1991.
- [8] .R. Kishony and S. Leibler. "Environmental stresses can alleviate the average deleterious effect of mutations". In: *Journal of Biology* 2.2 (2003). doi: 10.1186/1475-4924-2-14.
- [9] .P. Yeh, A. I. Tschumi, and R. Kishony. "Functional classification of drugs by properties of their pairwise interactions". In: *Nature Genetics* 38.4 (2006), pp. 489–494. doi: 10.1038/ng1755.
- [10] .R. Chait, A. Craney, and R. Kishony. "Antibiotic interactions that select against resistance". In: *Nature* 446.7136 (2007), pp. 668–671. doi: 10.1038/nature05685.
- [11] .M. C. Larsson et al. "A luciferase-based assay for rapid assessment of drug activity against *Mycobacterium tuberculosis* including monitoring of macrophage viability". In: *Journal of Microbiological Methods* 106 (2014), pp. 146–150. doi: 10.1016/J.JMIMET.2014.08.015.
- [12] .B. Kavčič, G. Tkalcik, and T. Bollenbach. "Mechanisms of drug interactions between translation-inhibiting antibiotics". In: *Nature Communications* 11.1 (2020). doi: 10.1038/s41467-020-17734-z.
- [13] .S. A. Angermayr et al. "Growth-mediated negative feedback shapes quantitative antibiotic response". In: *Mol. Syst. Biol.* 18.9 (2022), pp. 1–19. issn: 1744-4292. doi: 10.15252/msb.202110490.
- [14] .V. Salisbury et al. "Use of a clinical *Escherichia coli* isolate expressing lux genes to study the antimicrobial pharmacodynamics of moxifloxacin". In: *Journal of Antimicrobial Chemotherapy* 43.6 (1999), pp. 829–832. doi: 10.1093/JAC/43.6.829.
- [15] .S. J. Beard, V. Salisbury, R. J. Lewis, J. A. Sharpe, and A. P. MacGowan. "Expression of lux genes in a clinical isolate of *Streptococcus pneumoniae*: Using bioluminescence to monitor gemifloxacin activity". In: *Antimicrob. Agents Chemother.* 46.2 (2002), pp. 538–542. issn: 00664804. doi: 10.1128/AAC.46.2.538-542.2002. url: <https://pmc.ncbi.nlm.nih.gov/articles/PMC127039/>.
- [16] .H. M. Alloush, V. Salisbury, R. J. Lewis, and A. P. MacGowan. "Pharmacodynamics of linezolid in a clinical isolate of *Streptococcus pneumoniae* genetically modified to express lux genes". In: *J. Antimicrob. Chemother.* 52.3 (2003), pp. 511–513. issn: 03057453. doi: 10.1093/jac/dkg334.
- [17] .P. Wang et al. "Robust growth of *Escherichia coli*". In: *Curr. Biol.* 20.12 (2010), pp. 1099–1103. issn: 09609822. doi: 10.1016/j.cub.2010.04.045. url: <http://dx.doi.org/10.1016/j.cub.2010.04.045>.
- [18] .H. Eagle and A. D. Musselman. "the slow recovery of bacteria from the toxic effects of penicillin". In: *J. Bacteriol.* 58 (1949), pp. 475–490. doi: 10.1128/jb.58.4.475-490.1949. url: <https://journals.asm.org/journal/jb>.
- [19] .V. Besnard, M. Federighi, E. Declercq, F. Juglau, and J. M. Cappelier. "Environmental and physico-chemical factors induce VBNC state in *Listeria monocytogenes*". In: *Vet. Res.* 33.4 (July 2002), pp. 359–370. issn: 09284249. doi: 10.1051/vetres:2002022. url: <http://dx.doi.org/10.1051/vetres:2002022>.
- [20] .J. D. Oliver. "The viable but nonculturable state in bacteria". In: *J. Microbiol.* 43 Spec No (Feb. 2005), pp. 93–100. issn: 1225-8873. url: <https://pubmed.ncbi.nlm.nih.gov/15765062/>.
- [21] .L. Li, N. Mendis, H. Trigui, J. D. Oliver, and S. P. Faucher. "The importance of the viable but non-culturable state in human bacterial pathogens". In: *Front. Microbiol.* 5.JUN (2014), pp. 1–1. issn: 1664302X. doi: 10.3389/fmicb.2014.00258.
- [22] .R. D. Pearson, R. T. Steigbigel, H. T. Davis, and S. W. Chapman. "Method for reliable determination of minimal lethal antibiotic concentrations". In: *Antimicrob. Agents Chemother.* 18.5 (1980), pp. 699–708. issn: 00664804. doi: 10.1128/AAC.18.5.699.
- [23] .R. H. Eng, S. M. Smith, C. E. Cherubin, and E. N. Tan. "Evaluation of two methods for overcoming the antibiotic carry-over effect". In: *Eur. J. Clin. Microbiol. Infect. Dis.* 10.1 (1991), pp. 34–38. issn: 09349723. doi: 10.1007/BF01967095.

- [24] .J. Coates et al. "Antibiotic-induced population fluctuations and stochastic clearance of bacteria". In: *eLife* 7 (2018), pp. 1–26. issn: 2050084X. doi: 10.7554/eLife.32976.
- [25] .C. N. H. Marques, V. C. Salisbury, J. Greenman, K. E. Bowker, and S. M. Nelson. "Discrepancy between viable counts and light output as viability measurements, following ciprofloxacin challenge of self-bioluminescent *Pseudomonas aeruginosa* biofilms". In: *Journal of Antimicrobial Chemotherapy* 56.4 (2005), pp. 665–671. doi: 10.1093/jac/dki285.
- [26] .C. Levine, H. Hiasa, and K. J. Marians. "DNA gyrase and topoisomerase IV: Biochemical activities, physiological roles during chromosome replication, and drug sensitivities". In: *Biochim. Biophys. Acta - Gene Struct. Expr.* 1400.1-3 (1998), pp. 29–43. issn: 01674781. doi: 10.1016/S0167-4781(98)00126-2.
- [27] .R. Wu et al. "Bacterial killing and the dimensions of bacterial death". In: *npj Biofilms Microbiomes* 2024 101 10.1 (Sept. 2024), pp. 1–8. issn: 2055-5008. doi: 10.1038/s41522-024-00559-9. url: <https://www.nature.com/articles/s41522-024-00559-9>.
- [28] .J. Fanous et al. "Limited impact of *Salmonella* stress and persisters on antibiotic clearance". In: *Nature* 639.8053 (2025), pp. 181–189. doi: 10.1038/s41586-024-08506-6.
- [29] .R. Gleckman, N. Blagg, and D. W. Joubert. "Trimethoprim: Mechanisms of Action, Antimicrobial Activity, Bacterial Resistance, Pharmacokinetics, Adverse Reactions, and Therapeutic Indications". In: *Pharmacother. J. Hum. Pharmacol. Drug Ther.* 1.1 (1981), pp. 14–19. issn: 18759114. doi: 10.1002/j.1875-9114.1981.tb03548.x.
- [30] .B. Deslouches et al. "Activity of the de novo engineered antimicrobial peptide WLBU2 against *Pseudomonas aeruginosa* in human serum and whole blood: Implications for systemic applications". In: *Antimicrob. Agents Chemother.* 49.8 (2005), pp. 3208–3216. issn: 00664804. doi: 10.1128/AAC.49.8.3208-3216.2005.
- [31] .F. Baquero et al. "Postantibiotic effect of imipenem on gram-positive and gram-negative micro-organisms". In: *J. Antimicrob. Chemother.* 18 Suppl. E.SUPPL. E (1986), pp. 47–59. issn: 0305-7453. doi: 10.1093/JAC/18.SUPPLEMENT\_E.47. url: <https://pubmed.ncbi.nlm.nih.gov/3546247/>.
- [32] .S. Deguchi et al. "Microbial growth at hyperaccelerations up to 403,627 x g". In: *Proc. Natl. Acad. Sci. U. S. A.* 108.19 (May 2011), pp. 7997–8002. issn: 00278424. doi: 10.1073/PNAS.1018027108. url: <https://www.pnas.org/doi/abs/10.1073/pnas.1018027108>.
- [33] .J. Cayron, A. Dedieu-Berne, and C. Lesterlin. "Bacterial filaments recover by successive and accelerated asymmetric divisions that allow rapid post-stress cell proliferation". In: *Mol. Microbiol.* 119.2 (Feb. 2023), pp. 237–251. issn: 13652958. doi: 10.1111/MMI.15016.
- [34] .K. A. Datsenko and B. L. Wanner. "One-step inactivation of chromosomal genes in *Escherichia coli* K-12 using PCR products". In: *Proc. Natl. Acad. Sci. U. S. A.* 97.12 (June 2000), pp. 6640–6645. issn: 00278424. doi: 10.1073/PNAS.120163297. url: <https://www.pnas.org/doi/10.1073/pnas.120163297>.
- [35] .D. Hughes, B. Lazazzera, and F. Yildiz. *Experiments in Bacterial Genetics*. Uppsala, 2013.
- [36] .J. Bjarnason, C. M. Southward, and M. G. Surette. "Genomic profiling of iron-responsive genes in *Salmonella enterica* serovar Typhimurium by high-throughput screening of a random promoter library". In: *J. Bacteriol.* 185.16 (2003), pp. 4973–4982. issn: 00219193. doi: 10.1128/JB.185.16.4973-4982.2003.
- [37] .European Committee on Antimicrobial Susceptibility Testing (EUCAST). *EUCAST broth microdilution reading guide updated*. 2025. url: [https://www.eucast.org/eucast%7B%5C\\_%7Dnews/news%7B%5C\\_%7Dsinglevew?tx%7B%5C\\_%7Dttnews%7B%5C%7D5Btt%7B%5C\\_%7Dnews%7B%5C%7D5D=362%7B%5C&%7DcHash=f2196d399c8618b7313ccb7f048f7af5%20https://www.eucast.org/ast%7B%5C\\_%7DoF%7B%5C\\_%7Dbacteria/mic%7B%5C\\_%7Ddetermination](https://www.eucast.org/eucast%7B%5C_%7Dnews/news%7B%5C_%7Dsinglevew?tx%7B%5C_%7Dttnews%7B%5C%7D5Btt%7B%5C_%7Dnews%7B%5C%7D5D=362%7B%5C&%7DcHash=f2196d399c8618b7313ccb7f048f7af5%20https://www.eucast.org/ast%7B%5C_%7DoF%7B%5C_%7Dbacteria/mic%7B%5C_%7Ddetermination) (visited on 10/03/2025).
- [38] .B. D. Jett, K. L. Hatter, M. M. Huycke, and M. S. Gilmore. "Simplified agar plate method for quantifying viable bacteria". In: *Biotechniques* 23.4 (1997), pp. 648–650. issn: 07366205. doi: 10.2144/97234BM22.



## Chapter 4

### Antimicrobial Combination Effects at Sub-inhibitory Doses do not Reliably Predict Effects at Inhibitory Concentrations

---

**Authors:** Malte Muetter<sup>a</sup>, Daniel C. Angst<sup>a</sup>, Roland R. Regoes<sup>a</sup>, Sebastian Bonhoeffer<sup>a</sup>

<sup>a</sup>*Institute of Integrative Biology, Department for Environmental System Science, ETH Zurich, 8092 Zurich, Switzerland*

**Contributions:** MM, DCA, RRR, and SB designed research; MM performed experiments, developed the mathematical model, and analyzed data; MM, DCA, RRR, and SB wrote the manuscript.

---

#### Abstract

Assessing whether drug combinations synergise or antagonise is difficult for several reasons: (i) measuring bacterial death rates at clinically relevant drug concentrations is methodologically challenging, (ii) there is no unifying definition of what constitutes synergistic or antagonistic interactions, and (iii) both synergism and antagonism may be concentration and mixing ratio dependent. To assess how well sub-inhibitory measurements predict inhibitory behaviour, we quantified drug interactions for 15 pairwise drug combinations on a concentration checkerboard covering a wide range of inhibitory and sub-inhibitory concentrations. To this end, we recorded 8640 time-resolved luminescence trajectories that have been shown to track bacterial population declines. To handle time-varying treatment effects and allow fair comparisons between drugs with distinct killing dynamics, we introduced a growth-integrated rate-like metric  $\psi$  to summarise each trajectory, and assigned interaction types (synergistic/independent/antagonistic) based on Bliss independence and Loewe additivity. We found that the interaction type frequently changes as the concentration increases from sub-inhibitory to inhibitory concentrations. Moreover, interaction type depended on the mixing ratio, implying that single-point sub-inhibitory measurements are not sufficient to predict interactions at clinically relevant concentrations.

#### 4.1 Introduction

Antimicrobial resistance (AMR) poses a major global health burden, with an estimated 1.14 million deaths directly attributable to resistant infections in 2021 alone [1]. Moreover, the lag between the introduction of a new antibiotic class and the emergence of clinical resistance appears to be shrinking [2]. To develop a more sustainable approach to antibiotic use, a deeper understanding of the influence of treatment on the evolution of resistance is necessary.

One strategy that has been shown to slow the evolution of resistance in notoriously fast-evolving pathogens, such as HIV, malaria, and tuberculosis, is combination therapy [3, 4]. In theoretical models, combination therapy seems to outperform other strategies (such as mixing or cycling) [5–7], and it also seems to perform best in in vitro simulations of epidemics [8, 9]. However, clinical evidence for the efficacy of combination therapy is inconclusive, and a comprehensive meta-analysis did not identify a significant overall benefit [10].

Several factors contribute to the inconclusiveness of clinical studies, ranging from ethical constraints that limit focal pathogens to comparatively benign ones (i.e. excluding HIV and *M. tuberculosis*) to the lack of statistical power to track resistance evolution [10]. Another potential reason is drug interactions. Drug combinations can exhibit synergistic or antagonistic interactions, depending on whether the combined effect is stronger or weaker than the expectation based on the effects of the single drugs. However, defining this expectation is non-trivial, as null models are numerous and the best choice to describe drug independence remains debated [11, 12]. Here, we use two classical and widely applied reference frameworks to define independence: the response-based Bliss independence [13] and dose-based Loewe additivity [14].

Bliss independence is based on the assumption that the probability of being affected by one drug is statistically independent of being affected by the other [13]:

$$p_{AB}^{\text{Bliss}} = p_A + p_B - p_A p_B. \quad (4.1)$$

Under this assumption, Bliss independence is expected to be more appropriate for drug pairs with distinct and non-overlapping mechanisms of action [15].

In contrast, Loewe additivity – first discussed as iso-additivity by Frei in 1913 [16] and later formalised by Loewe and Muischnek [14] – uses dose equivalence as a null model. A combination is considered additive if pairs of concentrations that produce the same effect  $\psi$  (i.e. a measure of net growth) lie on a linear isobole connecting the equivalent single-drug doses [14]:

$$\frac{c_A}{f_A^{-1}(\psi(c_A, c_B))} + \frac{c_B}{f_B^{-1}(\psi(c_A, c_B))} = 1. \quad (4.2)$$

Here  $f_i^{-1}$  represents the inverse of a pharmacodynamic function  $f_i(c)$  that maps drug concentrations  $c_i$  to an effect measure  $\psi$ .

There are many studies on drug interactions below the minimum inhibitory concentration (MIC) (e.g. [17–25]) and at the MIC level (e.g. [26–28]). However, studies covering the arguably clin-

cally more relevant inhibitory regime are scarce and often cover only a few points in the inhibitory range (e.g. [29–33]). The primary reason for this is methodological: under sub-inhibitory conditions, growth rates can be easily assessed at high throughput using optical density measurements, whereas inhibitory conditions typically require labour-intensive, low-throughput colony-forming unit assays [34]. This lack of data on effects at high concentrations is a problem, not only because inhibitory conditions are more relevant therapeutically, but also because the right, inhibitory, tail of the pharmacodynamic curve has a strong influence on resistance evolution [35].

It has already been shown that drug interactions can depend on dose and mixing ratio [18, 23, 36–38]. However, the existing literature provides limited quantitative insight into how frequently interaction classifications remain stable versus how often they change with concentration and mixing ratio. Here, we provide an extensive map of interactions for 15 antibiotic pairs, each measured on a  $12 \times 12$  concentration checkerboard that includes inhibitory concentrations using time-resolved bioluminescence trajectories. We quantify how often sub-inhibitory interaction classifications based on Bliss independence and Loewe additivity generalise to inhibitory conditions and how often they fail, including cases of qualitative reversals across regimes.

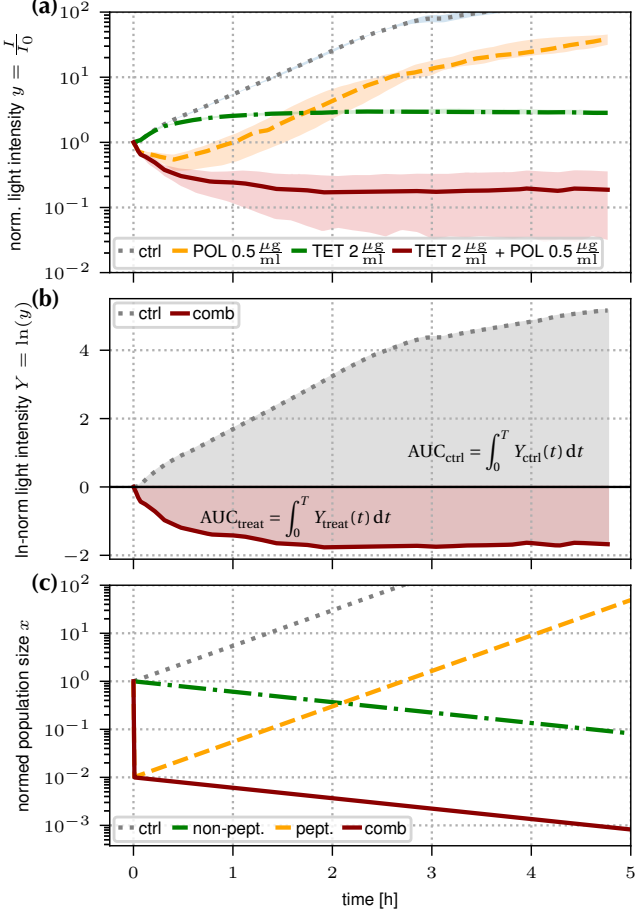
## 4.2 Results

We quantified drug interactions for 15 pairwise combinations of six antibiotics falling into three mechanistic classes: polymyxins (colistin, COL; polymyxin B, POL),  $\beta$ -lactams (amoxicillin, AMO; penicillin, PEN), and ribosome-targeting drugs (chloramphenicol, CHL; tetracycline, TET). For each drug pair, we assessed 144 conditions ( $c_A, c_B$ ) in a  $12 \times 12$  checkerboard. We measured light intensity trajectories  $I(t)$  for 8,640 bioluminescent cultures to infer changes in population size over time. Single-drug trajectories are shown in Fig. C1.

**Time-variant growth rates and treatment effects.** Most drug-interaction metrics are based on estimates of *treatment effects*, which collapse the trajectories of the bacterial population size into a scalar. These estimates are typically either rate-based, obtained by fitting an exponential rate of change to a growth trajectory [17, 31, 39–41], or area under the curve (AUC)-based, obtained by integrating a (transformed) growth trajectory over time [24, 30, 32, 33, 42, 43]. Rate-based approaches are easy to interpret and can be used directly in epidemiological models. However, slopes are sensitive to the choice of the fitting window when treatment effects are time-variant. This sensitivity is especially problematic when assessing interactions among drugs with very different killing dynamics (e.g., in the example shown in Fig. 4.1a), where treatment effects start at different time points and persist for different durations.

Given that many trajectories exhibited time-varying treatment effects, we summarised each trajectory by  $\psi$  (Methods), a time-weighted average of the instantaneous net growth rate  $\hat{\psi}(t)$  (Equation C1). This weighting emphasises early treatment effects, reflecting that early changes in net growth shape the population for a longer duration than equally sized changes occurring later.  $\psi$

Fig. 4.1 – Panel (a) shows the median of normalised light-intensity trajectories  $y(t) = I(t)/I(0)$  for the combination of polymyxin B (POL, 0.5  $\mu\text{g}$  mL $^{-1}$ ) and tetracycline (TET, 2  $\mu\text{g}$  mL $^{-1}$ ), together with the corresponding single-drug and untreated control trajectories, with shaded bands indicating the interquartile range across biological replicates. Panel (b) shows the log-transformed signal  $Y(t) = \ln(y(t))$  for the untreated control and the combination treatment from panel (a), together with their associated areas under the curve. Panel (c) shows a simple peptide–antibiotic interaction model illustrating qualitatively distinct dynamics under: no drugs, antibiotic (slow constant decline), peptide (rapid initial decline), and peptide plus antibiotic (rapid initial decline followed by a constant slow decline).



is proportional to the area under the log-normalised luminescence trajectory  $Y(t) = \ln(I(t)/I(0))$  (Equation C3). Treatment effects,  $\tau$ , are then defined as the difference between the time-weighted net growth rates of an untreated control and the treated condition, and correspond to the scaled area between curves (Fig. 4.1b).

Time-weighted net growth rates for one example (CHL+TET) are shown in Fig. 4.2, with markers indicating conditions as inhibitory (stars), sub-inhibitory (diamonds), or intermediate (no marker). Rates for all conditions are shown in Fig. C3. For further details see Methods. We then fitted pharmacodynamic curves to the single-drug estimates (Fig. C2).

For each condition  $(c_A, c_B)$  we estimate the bootstrap distribution  $\boldsymbol{\tau}(c_A, c_B)$  by resampling pairs of control and treatment wells with replacement (Methods, Appendix C7). Throughout this manuscript, we denote distributions with bold symbols. For each bootstrap draw  $b$ , we compute  $\tau_b(c_A, c_B) = \psi_b(\emptyset) - \psi_b(c_A, c_B)$ .

**Bliss independence implies additive treatment effects.** Because the original Bliss formulation is probabilistic, we have to translate it into our growth-based treatment-effect framework (see

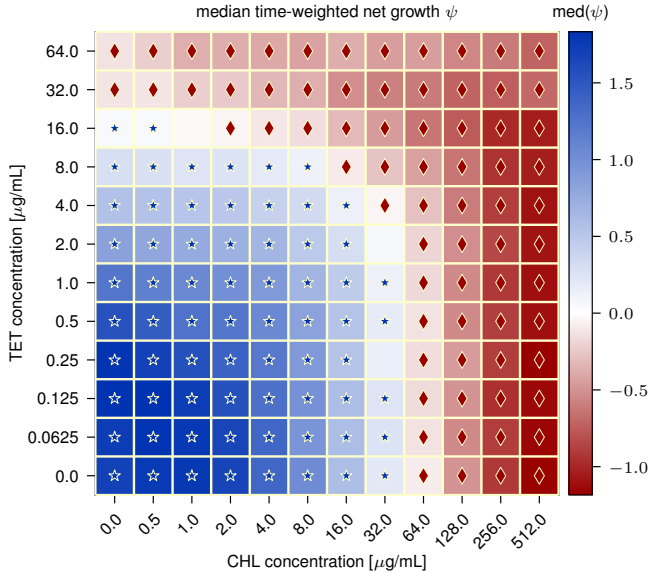


Fig. 4.2 – Time-weighted growth rate  $\psi$  for combinations of CHL and TET. Each cell corresponds to one concentration pair, with colour indicating the median of  $\psi$  across  $n = 4$  biological replicates. Markers denote whether the distribution of  $\psi$  is significantly different from zero (see Methods): stars indicate significantly positive values (net growth), and diamonds indicate significantly negative values (net killing).

Appendix C4). Bliss independence implies multiplicative survival  $S_{AB}(T) = S_A(T)S_B(T)$  (Equation C12). After substituting  $S_i(T) = \exp(-\int_0^T \hat{\tau}_i(u) du)$  with  $\hat{\tau}_i(t)$ , denoting the *instantaneous treatment effect*, we can derive that Bliss implies additive *time-weighted treatment effects*:

$$\tau^{\text{Bliss}}(c_A, c_B) = \tau(c_A) + \tau(c_B). \quad (4.3)$$

**Peptide – non-peptide interaction model.** We observed that a combination of non-peptide drugs with relatively constant inhibition dynamics and peptide-like drugs, which induce a sharp early decline followed by (almost) unimpaired growth, is dominated by the peptide drug in the early phase and by the non-peptide drug in the later phase. A well-behaved example of such a combination is shown in Fig. 4.1a for polymyxin B (POL) and tetracycline (TET). Because most interaction metrics do not explicitly account for time-varying effects, it is unclear what combined treatment effect to expect. To answer this, we constructed a mathematical model for an idealised scenario. Drug A immediately reduces the population by a factor  $\alpha$  but does not affect the subsequent dynamics, while drug B acts invariantly over time by constantly reducing the net growth rate from  $\hat{\psi}_{\text{ctrl}}$  to  $\hat{\psi}_B$ . In combination, the population is first reduced by  $\alpha$  and then grows with  $\hat{\psi}_B$  (Fig. 4.1c). Substituting our rate definition (Equation 4.4) into this model yields additive treatment effects,  $\tau_{AB} = \tau_A + \tau_B$  (see Appendix C6), equivalent to the Bliss prediction derived above.

**Interaction scores ( $\mu, \nu$ ).** Based on the Bliss prediction of combined treatment effects derived above, we define the Bliss interaction score  $\mu$  as the normalised deviation from the prediction (Equation 4.6). The distribution of  $\mu$  can be inferred based on the distributions of treatment effects  $\tau$  described above. For Loewe additivity, we define the interaction score  $\nu$  as the deviation from

dose equivalence (Equation 4.7). We obtain the distribution of  $\nu$  from the inverted single-drug pharmacodynamic curves  $f_i^{-1}(\psi)$  (Equation C10). We then assign interaction types (synergistic, independent, antagonistic) depending on whether the 95% interval of  $\mu$  or  $\nu$  lies below, contains, or lies above zero. The resulting interaction types based on  $\mu$  and  $\nu$  for each combination are shown in Figures C4 and C5.

**Disagreement between sub-inhibitory and inhibitory interaction types within reference models.** Using the per-condition distributions of interaction scores described above, we next assessed whether interaction classifications remain consistent across concentration regimes. We normalised concentrations  $c_i$  by the corresponding  $z\text{MIC}_i$  (defined by  $f_i(z\text{MIC}_i) = 0$ ; Table C1), setting  $z_i = c_i/z\text{MIC}_i$ . We then separately summarised inhibitory and sub-inhibitory conditions using a second, higher-level bootstrap. Specifically, we sampled conditions  $(c_A, c_B)_r$  for  $r = (1, \dots, 200)$  with replacement, weighted by their mixing ratio to bias the sampling towards more equal ratios (Equation C22). For each sampled condition, we drew one estimate from the condition's distributions  $\mu(c_A, c_B)$  and  $\nu(c_A, c_B)$ . To compare regimes and reference models, we define three alignment classes: agreement (same classification), soft disagreement (independent in one but synergistic or antagonistic in the other), and strong disagreement (opposite classifications). The resulting comparisons between sub-inhibitory and inhibitory regimes for  $\nu_{\text{sub}}$ ,  $\nu_{\text{inh}}$  and  $\mu_{\text{sub}}$ ,  $\mu_{\text{inh}}$  are shown in Fig. 4.3a,b and the resulting interaction types in Table C2.

Assuming Bliss independence, we observed six combinations with agreement and 9 cases of disagreement, of which one resulted in strong disagreement (AMO+PEN) and eight in soft disagreement. Assuming Loewe additivity, we observed agreement for six combinations (three of which also agreed under Bliss) and disagreement for nine combinations. Here, we observed two cases of strong disagreement (COL+TET and POL+TET) and seven with soft disagreement.

**Disagreement between reference models, within concentration regimes.** Fig. 4.3c replots the same interaction summaries described above, but now compares the Bliss interaction score  $\mu$  to the Loewe interaction score  $\nu$  across both sub-inhibitory and inhibitory regimes in a single panel. In Fig. C6a,b we show the same comparison but separated by regime. Across all 30 ( $2 \times 15$ ) comparisons, the Bliss and Loewe-based classifications agree in 14 cases, show soft disagreement in 15 cases, and show strong disagreement in one case (CHL+TET) (Fig. 4.3c).

**Interaction types can change with dose even at fixed mixing ratio.** Above, we compared interaction summaries between sub-inhibitory and inhibitory regimes by aggregating condition-wise estimates across a range of doses and mixing ratios. We next ask whether interaction types also change (i) as the dose increases at a fixed mixing ratio, and (ii) as the mixing ratio varies at a fixed effect level. To facilitate both analyses, we reparameterize concentration pairs  $(c_A, c_B)$  in polar

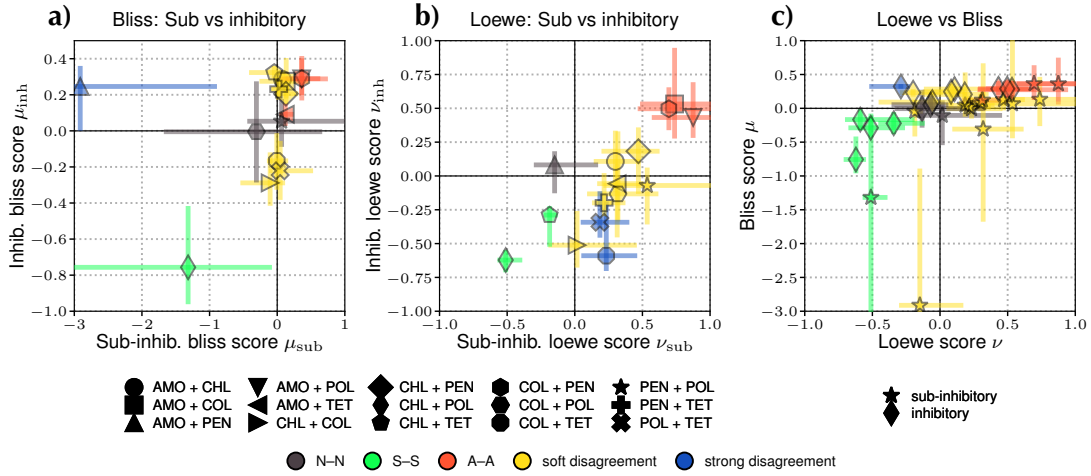
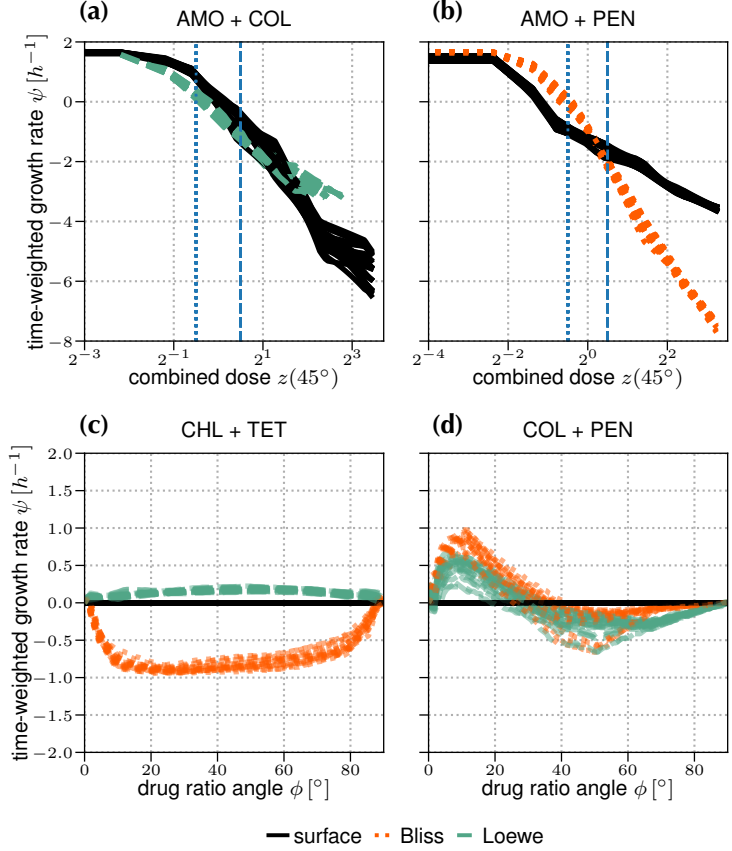


Fig. 4.3 – Interaction summaries across regimes and models. Panels (a) and (b) compare sub-inhibitory vs. inhibitory interaction scores, using (a) the Bliss interaction score  $\mu$  and (b) the Loewe interaction score  $\nu$ . Each point represents one drug combination, plotted as the median estimate in the sub-inhibitory regime (x-axis) against the median estimate in the inhibitory regime (y-axis), with 95% bootstrap intervals shown as horizontal and vertical error bars. (c) Loewe vs. Bliss comparison across regimes: each point corresponds to one combination and regime, plotted as the median Loewe interaction score  $\nu$  (x-axis) against the corresponding Bliss interaction score  $\mu$  (y-axis), with 95% bootstrap intervals. Markers encode the drug combination (shared legend for panels (a) and (b)), while marker shape encodes the regime in panel (c). We classify interactions as synergistic (S), antagonistic (A), or independent (N; not significantly different from zero). Colors indicate interaction type agreement between the two compared axes in each panel: *agreement* if the two interaction types coincide (N–N, S–S, A–A), *soft disagreement* if one interaction type is independent and the other is non-independent (N–S, N–A), and *strong disagreement* if the classifications are opposite (S–A).

coordinates  $(z, \phi)$ , where  $z$  is the *combined dose* and  $\phi$  is the *mixing angle* (Equation 4.8) that encodes the mixing ratio.

For each drug combination, we fitted 25 continuous, monotonically decreasing surface splines on bootstrap datasets of  $\psi(c_A, c_B)$  (Fig. C7). Based on these splines, we estimate *polar pharmacodynamic curves*, which show  $\psi$  as a function of the combined dose  $z$  at a fixed mixing angle  $\phi = 45^\circ$  (equal mixing in units of zMIC). At a given dose, predicted values above the observed  $\psi$  indicate synergy, whereas predicted values below the observed  $\psi$  indicate antagonism. For both reference models, there are examples where the interaction changes direction as the combined dose increases. For the combination AMO+COL (Fig. 4.4a), the Loewe-based interaction shifts from antagonism at lower doses to synergy at higher doses. For AMO+PEN (Fig. 4.4b) Bliss-based interaction flips, with synergy at lower doses and strong antagonism at higher doses. *Polar pharmacodynamic curves* at  $45^\circ$  for all combinations are shown in Fig. C8.

Fig. 4.4 – Panels (a,b) show *polar pharmacodynamic curves* at  $\phi = 45^\circ$  (corresponding to a 1:1 ratio in units of zMIC) for (a) AMO+COL and (b) AMO+PEN. The x-axis shows the combined dose  $z$ , where  $z = 1/\sqrt{2}$  (blue dotted line) corresponds to both single-drug doses equaling  $0.5z\text{MIC}$ , and  $z = \sqrt{2}$  (blue dashed line) corresponds to both equaling  $1z\text{MIC}$ . Panels (c,d) show the Bliss- and Loewe-based predictions for  $\psi$  over the mixing angle  $\phi$  along the observed isobole at  $\psi = 0 \frac{1}{h}$  for (c) COL+PEN and (d) CHL+TET.



**Interaction types can depend on the mixing ratio.** To assess whether interaction types depend on the mixing ratio at a fixed effect level, we extracted isoboles from the median surface spline, i.e., the path  $(z, \phi)_i$  along which the time-weighted net growth rate is constant ( $\psi_i = 0 \frac{1}{h}$ ; Fig. C9). Along each isobole, we evaluate Bliss- and Loewe-based predictions and plot these predictions as a function of  $\phi$ . For many combinations, the inferred interaction type is stable across  $\phi$ , as exemplified by CHL+TET (Fig. 4.4c). However, combinations showing mixing-ratio dependence are also common, as exemplified for COL+PEN (Fig. 4.4d). Plots for all combinations are shown in Fig. C10.

### 4.3 Discussion

We quantified interaction patterns across a wide concentration range for several drug combinations with different modes of action. Quantifying the size of the bacterial population is notoriously difficult because bacterial death has many facets, and no single method captures all of them [44, 45]. In this work, we used bioluminescence as a proxy for population size. This choice enabled us to record 8640 finely time-resolved (every 10 minutes for five hours) growth trajectories at high

throughput. Bioluminescence has been shown to be a better proxy for biomass than for cell number [45], which makes interpreting our readout as biomass the more robust interpretation. However, since we restricted our analysis to drugs for which changes in biomass align with changes in cell number (i.e. limited filamentation) [45], we do not expect qualitatively different conclusions when using an alternative readout of population size.

For many of the observed trajectories treated with higher concentrations of polymyxins (COL and POL), the light intensity dropped below the detection limit within the first few minutes. In principle, slope-based estimates can still be inferred for such curves. However, comparing these estimates across drugs with different onsets and durations of treatment effects is conceptually difficult to justify. To enable fair comparisons across drugs, we therefore used a weighted growth measure integrated over a shared timeframe that is equal for all trajectories ( $T \approx 2\text{h}$ ). However, this choice comes at the cost of having to discard all trajectories that fall below the detection limit too early.

To investigate how different treatment dynamics combine, we developed a simplified antibiotic-peptide interaction model. This model predicts that combinations of a short-acting, peptide-like drug with a drug with time-invariant treatment effects should follow Bliss independence. The observed isoboles for peptide–non-peptide pairs in Fig. C9 confirm this behaviour, as they were closer to the Bliss-based prediction than to the Loewe-based prediction for all pairs except COL+PEN.

To address our core question — how predictive sub-MIC interaction patterns are for inhibitory interactions — we aggregated interaction estimates for sub-inhibitory and inhibitory conditions and compared them. For both reference models (Bliss independence and Loewe additivity), more than half of the combinations showed soft disagreement between inhibitory and sub-inhibitory regimes, i.e., a significant synergy or antagonism in one regime but not in the other. This does not necessarily imply that sub-inhibitory measures are uninformative, because non-significance of synergistic/antagonistic interactions is not evidence of independence and can arise from variance. Such variance can result from aggregating across diverse conditions and mixing ratios, which we showed can influence the interaction type (Fig. C10). Importantly, for both reference models, we observed more cases of synergistic or antagonistic agreement than strong disagreement, indicating that sub-inhibitory interaction measures retain some qualitative predictive value.

Our results also confirm the practical limitations of Loewe-based interaction measures at high concentrations that have been reported previously ([46]). Since Loewe relies on the inverse of the single-drug pharmacodynamic functions, it is only defined when the combined effect lies within the effect ranges spanned by both single-drug treatments. For drug pairs with very different maximal killing rates, this condition fails in large parts of the checkerboard (see undefined regions in Fig. C5). This is a severe limitation that prohibits the quantification of drug interactions for a large number of therapeutically relevant conditions. Consistent with previous work (e.g. [47]), we found that the Bliss and Loewe frameworks can produce opposite classifications.

#### 4. ANTIMICROBIAL COMBINATION EFFECTS AT SUB-INHIBITORY DOSES DO NOT RELIABLY PREDICT EFFECTS AT INHIBITORY CONCENTRATIONS

---

Table 4.1 – Drugs used in the experiments, the solvent, the estimated zMIC (by fitting the single-drug pharmacodynamic curves), and the supplier with catalogue number.

drug	solvent	zMIC [ $\frac{\mu\text{g}}{\text{mL}}$ ]	supplier
amoxicillin (AMO)	water	8.42	ThermoFischer, J61290.14
chloramphenicol (CHL)	DMSO	54.11	Sigma, C0378
colistin (COL)	water	0.58	Sigma, C4461
penicillin (PEN)	water	153.86	Roth, HP48.2
polymyxin B (POL)	water	0.51	Roth, 0235.1
tetracycline (TET)	DMSO	15.15	Sigma, T3383

Our findings show that conclusions about synergy or antagonism depend on the concentration range, mixing ratio, and the reference model on the basis of which synergy or antagonism is determined. Accordingly, single-point measurements at a single sub-inhibitory concentration are insufficient to reliably characterise drug interactions at clinically relevant inhibitory concentrations.

#### 4.4 Methods

**Strains and Media.** We used the bioluminescent strain *Escherichia coli* MG1655  $\Delta$ galK::(kan<sup>R</sup>-luxCDABE) constructed previously [45]. Cultures were grown in LB medium (Sigma L3022).

**Drug preparation.** We explored drug interactions among six drugs (Table B1), resulting in 15 drug–drug pairs. For each pair, one compound was designated drug A and the other drug B. Each compound was prepared as a  $\times 20$  stock of its highest working concentration. We then performed a twofold dilution series in a 12-column deepwell plate, resulting in 11 diluted concentrations and one drug-free column. For drug A, we transferred 125  $\mu\text{L}$  per well into a 96-well plate (subreservoir A) with a horizontal concentration gradient. For drug B, we transferred 50  $\mu\text{L}$  per well into two 96-well plates (antibiotic reservoir plates I and II) with vertical concentration gradients (each  $6 \times 12$  layout). All plates were stored at  $-80^\circ\text{C}$  to minimise degradation over time, accepting a one-time freeze–thaw-related degradation.

**Dose response assays.** For each assay, we prepared four overnight cultures grown for 14 h. Cultures were distributed to fill an entire 384-well source plate (Greiner 781073), so that the replicates formed a  $2 \times 2$  block format (e.g. C1–rep1, C2–rep2, D1–rep3, D2–rep4). We then prefilled two white 384-well assay plates (Greiner 781073) with 54  $\mu\text{L}$  LB per well and transferred inocula from the source plate to both assay plates (I, II) using an Evo 200 liquid handling platform (Tecan) with a pintoool. The dilution is approximately 1:150, although we observed substantial well-to-well variation in the effective inoculum size (see below). Plates were incubated for 2 h to reach exponential

phase. Simultaneously, subreservoir A and both antibiotic-reservoir plates were thawed.  $50\text{ }\mu\text{L}$  from each well of the subreservoir A were transferred to the corresponding wells of both antibiotic-reservoir plates, generating a  $10\times$  mixture of drugs A and B. For both assay plates, the assay started as follows: a baseline luminescence reading was taken,  $6\text{ }\mu\text{L}$  of the  $10\times$  drug mixture was added (defining  $t = 0$  at dosing for the respective wells), and a second luminescence reading was taken. Subsequently, we alternated between reading assay plates I and II for a total duration of 5 h. Luminescence was recorded with an Infinite F200 plate reader (Tecan) using a 250 ms integration time.

**Data preprocessing.** To estimate stray.light contamination, we conducted a calibration experiment in which six source wells (E5, E12, E20, L5, L12, L20) contained stationary-phase cultures while all other wells remained empty. From a single luminescence read of the full plate, we constructed a distance-dependent stray-light kernel (Fig. C11) and corrected each well by subtracting the summed contributions from neighbouring wells (restricted to distances  $d \leq 3$ , Equation C8). We defined the lower limit of detection as  $I_{\text{LoD}} = 10\text{RLU}$  and the upper limit of detection as  $10^6\text{RLU}$ . We defined the common analysis horizon  $T$  as the earliest time point at which any untreated control well exceeded the upper detection limit, yielding  $T \approx 2\text{h}$ . For each well, we computed the fraction of observations up to  $T$  below  $I_{\text{LoD}}$ . Wells with more than 20% of observations below  $I_{\text{LoD}}$  were excluded from all subsequent analyses. For retained wells, values below  $I_{\text{LoD}}$  were censored by replacing them with  $I_{\text{LoD}}$ . For numerical integration, we interpolated the log-normalised signal to obtain values on the shared horizon  $t = T$  (see also Appendix C2).

**Time-weighted net growth rate.** We define  $\psi$  as the linearly time-weighted net growth rate (SI: Equation C1) over the common time horizon  $T$ . We infer  $\psi$  by calculating the scaled area under the log-normalised light intensity  $Y(t) = \ln(I(t)/I(0))$  (SI: Equation C2, Equation C3),

$$\psi = \frac{2}{T^2} \int_0^T Y(t) \text{d}t. \quad (4.4)$$

**Classification of inhibitory and sub-inhibitory conditions.** We classify each checkerboard condition as inhibitory, sub-inhibitory, or not significantly different from zero by testing whether replicate time-weighted growth-rate estimates  $\psi(c_A, c_B)$  are consistently positive or negative. With four replicates, the binomial probability of observing all positive (or all negative) signs with equal probability is  $0.5^4 = 0.0625$ . This classification is used to annotate the  $\psi$  heatmaps (Fig. 4.2, Fig. C3) and to define inhibitory and sub-inhibitory regime pools.

**Single-drug pharmacodynamic curve fitting.** For each drug, we aggregated all single-drug data across experiments and fitted pharmacodynamic curves  $f(c)$  to the corresponding time-weighted

growth-rate estimates  $\psi$ :

$$f(c) = \psi_0 - \frac{(\psi_0 - \psi_{\min})(c/zMIC)^{\kappa}}{(c/zMIC)^{\kappa} - (\psi_{\min}/\psi_0)}, \quad [0, \infty) \rightarrow [\psi_{\min}, \psi_0] \quad (4.5)$$

Here,  $\psi_0$  denotes the maximum and  $\psi_{\min}$  the minimum time-weighted growth rate, corresponding to  $c = 0$  and  $c \rightarrow \infty$ , respectively.  $\kappa$  denotes the Hill coefficient and zMIC the concentration at which  $f(zMIC) = 0$ . The model parameters  $\psi_0$ ,  $\psi_{\min}$ ,  $\kappa$ , zMIC were jointly estimated by least-squares fitting of Equation 4.5.

**Distribution of treatment effects.** We define the treatment effect  $\tau$  as the linearly time-weighted average difference between the untreated and treated instantaneous net growth rates over the common time horizon  $T$  (SI: Equation C6). Equivalently,  $\tau$  is the scaled area between the control and treatment trajectories on the log-normalised scale (illustrated in Fig. 4.1b). Because  $\tau$  is a comparative measure between one untreated and one treated trajectory, we bootstrap treated-control well pairs with replacement ( $B = 200$ ; details in Appendix C7). For each condition  $(c_A, c_B)$  and draw  $b$ , we compute  $\tau_b(c_A, c_B) = \psi_b(\emptyset) - \psi_b(c_A, c_B)$ , yielding the distribution of treatment effects  $\boldsymbol{\tau}(c_A, c_B)$ . Throughout this manuscript, distributions are denoted by bold symbols. We classify such bootstrap distributions as significant if the central 95% bootstrap interval excludes zero, and as not significant otherwise.

**Bliss-based interaction score  $\mu$ .** We define the Bliss based interaction score as the normalised deviation from the Bliss-prediction for combined treatment effects (see Appendix C4 and Equation 4.3):

$$\mu_b(c_A, c_B) = \frac{\tau_b(c_A) + \tau_b(c_B) - \tau_b(c_A, c_B)}{\text{median}(\boldsymbol{\tau}(c_A)) + \text{median}(\boldsymbol{\tau}(c_B))}. \quad (4.6)$$

To avoid misinterpreting noise as interaction, we only evaluate  $\nu(c_A, c_B)$  if  $\boldsymbol{\tau}(c_A, c_B)$  is significantly greater than zero and at least one of  $\boldsymbol{\tau}(c_A)$  or  $\boldsymbol{\tau}(c_B)$  is significantly greater than zero.

**Loewe-based interaction score  $\nu$ .** We define a Loewe interaction score (details in Appendix C5) that quantifies deviations from dose equivalence as

$$\nu_b(c_A, c_B) = \frac{c_A}{f_A^{-1}(\psi_b(c_A, c_B))} + \frac{c_B}{f_B^{-1}(\psi_b(c_A, c_B))} - 1. \quad (4.7)$$

Here  $f_i$  denotes a pharmacodynamic function mapping concentration to net growth,  $f_i(c) = \psi$ . The inverse  $f_i^{-1}(\psi)$  is the corresponding single-drug equivalent concentration of drug  $i$ . Our definition of  $\nu$  is analogous to the combination index (CI – 1) [36], but uses a different pharmacodynamic model  $f_i$  (either Equation C10 or inferred numerically from the single-drug edges of the surface splines). To avoid misinterpreting noise as interaction, we only evaluate  $\nu(c_A, c_B)$  if  $\boldsymbol{\tau}(c_A, c_B)$  is significantly greater than zero and at least one of  $\boldsymbol{\tau}(c_A)$  or  $\boldsymbol{\tau}(c_B)$  is significantly greater than zero.

**Polar reparametrization.** We normalise concentrations of drug  $i$  using the corresponding zMIC $_i$  estimates obtained from pharmacodynamic curve fits (Table B1):  $z_i = c_i/\text{zMIC}_i$ . We then define polar coordinates based on the normalised concentrations:

$$z = \sqrt{z_A^2 + z_B^2}, \quad \phi = \arctan 2(z_B, z_A), \quad (4.8)$$

with  $\phi$  corresponding to the *mixing angle* and  $z$  to the *combined dose*. These coordinates were used to plot polar pharmacodynamic curves, which show the treatment effect over the combined dose  $z$  for a fixed mixing angle  $\phi$ . These curves represent cross-sections through the surface splines at fixed  $\phi$ .

**Inoculum effects.** We noticed a much larger-than-expected variation in pre-treatment light intensity  $I_0$  in our data, which we use as a proxy for inoculum size. To assess the impact of this variation on the results, we regressed  $\psi$  for each single-drug and concentration on the pre-treatment signal  $I_0$  (Appendix C9). We found negligible inoculum effects for AMO, CHL, PEN, and TET, but substantial effects for COL and POL at intermediate concentrations (see Fig. C12). Because the size of the inoculum did not show a significant directional trend along the concentration index ( $p = 0.092$ ), the variance of the inoculum mainly adds noise at intermediate concentrations of COL and POL, contributing to an increased scatter in Fig. C2c,e.

### Data, Materials, and Software Availability

Experimental datasets and code are available at Zenodo (DOI: 10.5281/zenodo.18374151).

### Acknowledgements

We thank ETH Zurich for funding this work. During manuscript preparation, we used OpenAI's ChatGPT for editorial assistance (coding, grammar, and proofreading).

## Bibliography

- [1] .M. Naghavi et al. "Global burden of bacterial antimicrobial resistance 1990–2021: a systematic analysis with forecasts to 2050". In: *The Lancet* 404.10459 (2024), pp. 1199–1226. doi: 10.1016/S0140-6736(24)01867-1.
- [2] .C. Witzany, S. Bonhoeffer, and J. Rolff. "Is antimicrobial resistance evolution accelerating?" In: *PLoS Pathog.* 16.10 (2020), pp. 5–9. issn: 15537374. doi: 10.1371/journal.ppat.1008905. url: <http://dx.doi.org/10.1371/journal.ppat.1008905>.
- [3] .R. M. Gulick et al. "Treatment with Indinavir, Zidovudine, and Lamivudine in Adults with Human Immunodeficiency Virus Infection and Prior Antiretroviral Therapy". In: *New England Journal of Medicine* 337.11 (1997), pp. 734–739. doi: 10.1056/NEJM199709113371102.
- [4] .D. E. Goldberg, R. F. Siliciano, and W. R. Jacobs. "Outwitting evolution: Fighting drug-resistant TB, Malaria, and HIV". In: *Cell* 148.6 (2012), pp. 1271–1283. issn: 10974172. doi: 10.1016/j.cell.2012.02.021.
- [5] .S. Bonhoeffer, M. Lipsitch, and B. R. Levin. "Evaluating treatment protocols to prevent antibiotic resistance". In: *Proc. Natl. Acad. Sci. U. S. A.* 94.22 (1997), pp. 12106–12111. issn: 00278424. doi: 10.1073/pnas.94.22.12106.
- [6] .B. Tepekule, H. Uecker, I. Derungs, A. Frenoy, and S. Bonhoeffer. "Modeling antibiotic treatment in hospitals: A systematic approach shows benefits of combination therapy over cycling, mixing, and mono-drug therapies". In: *PLoS Comput. Biol.* 13.9 (2017), pp. 1–22. issn: 15537358. doi: 10.1371/journal.pcbi.1005745.
- [7] .H. Uecker and S. Bonhoeffer. "Antibiotic treatment protocols revisited: The challenges of a conclusive assessment by mathematical modelling". In: *J. R. Soc. Interface* 18.181 (2021). issn: 17425662. doi: 10.1098/rsif.2021.0308.
- [8] .D. C. Angst, B. Tepekule, L. Sun, B. Bogos, and S. Bonhoeffer. "Comparing treatment strategies to reduce antibiotic resistance in an in vitro epidemiological setting". In: *Proc. Natl. Acad. Sci. U. S. A.* 118.13 (2021), pp. 1–7. issn: 10916490. doi: 10.1073/PNAS.2023467118.
- [9] .M. Muetter, D. C. Angst, R. R. Regoes, and S. Bonhoeffer. "The impact of treatment strategies on the epidemiological dynamics of plasmid-conferred antibiotic resistance". In: *Proceedings of the National Academy of Sciences* 121.52 (2024). doi: 10.1073/PNAS.2406818121.
- [10] .B. Siedentop et al. "The effect of combining antibiotics on resistance: A systematic review and meta-analysis". In: *eLife* (2024). doi: 10.7554/eLife.93740.1.
- [11] .J. Foucquier and M. Guedj. "Analysis of drug combinations: current methodological landscape". In: *Pharmacology Research & Perspectives* 3.3 (2015). doi: 10.1002/PRP2.149.
- [12] .D. Duarte and N. Vale. "Evaluation of synergism in drug combinations and reference models for future orientations in oncology". In: *Current Research in Pharmacology and Drug Discovery* 3 (2022), p. 100110. doi: 10.1016/J.CRPBAR.2022.100110.
- [13] .C. I. BLISS. "THE TOXICITY OF POISONS APPLIED JOINTLY1". In: *Annals of Applied Biology* 26.3 (1939), pp. 585–615. doi: 10.1111/j.1744-7348.1939.tb06990.x.
- [14] .S. Loewe and H. Muischnek. "Über Kombinationswirkungen". In: *Archiv für Experimentelle Pathologie und Pharmakologie* 114.5-6 (1926), pp. 313–326. doi: 10.1007/BF01952257.
- [15] .D. Y. Baeder, G. Yu, N. Hozé, J. Rolff, and R. R. Regoes. "Antimicrobial combinations: Bliss independence and Loewe additivity derived from mechanistic multi-hit models". In: *Philosophical Transactions of the Royal Society B: Biological Sciences* 371.1695 (2016), p. 20150294. doi: 10.1098/rstb.2015.0294.
- [16] .W. Frei. "Versuche über Kombination von Desinfektionsmitteln". In: *Zeitschrift für Hygiene und Infektionskrankheiten* 75.1 (1913), pp. 433–496. doi: 10.1007/BF02207053.
- [17] .P. Yeh, A. I. Tschumi, and R. Kishony. "Functional classification of drugs by properties of their pairwise interactions". In: *Nature Genetics* 38.4 (2006), pp. 489–494. doi: 10.1038/ng1755.
- [18] .E. M. O'Shaughnessy, J. Meletiadis, T. Stergiopoulou, J. P. Demchok, and T. J. Walsh. "Antifungal interactions within the triple combination of amphotericin B, caspofungin and voriconazole against Aspergillus species". In: *Journal of Antimicrobial Chemotherapy* 58.6 (2006), pp. 1168–1176. doi: 10.1093/JAC/DKL392.
- [19] .G. Chevereau et al. "Quantifying the Determinants of Evolutionary Dynamics Leading to Drug Resistance". In: *PLoS Biol.* 13.11 (2015), pp. 1–18. issn: 15457885. doi: 10.1371/journal.pbio.1002299.
- [20] .D. Russ and R. Kishony. "Additivity of inhibitory effects in multidrug combinations". In: *Nature Microbiology* 3.12 (2018), pp. 1339–1345. doi: 10.1038/s41564-018-0252-1.
- [21] .I. Katzir, M. Cokol, B. B. Aldridge, and U. Alon. "Prediction of ultra-high-order antibiotic combinations based on pairwise interactions". In: *PLOS Computational Biology* 15.1 (2019), e1006774. doi: 10.1371/journal.pcbi.1006774.
- [22] .B. Kavčič, G. Tkalcík, and T. Bollenbach. "Mechanisms of drug interactions between translation-inhibiting antibiotics". In: *Nature Communications* 11.1 (2020). doi: 10.1038/s41467-020-17734-z.

- [23] .C. Rezzoagli, M. Archetti, I. Mignot, M. Baumgartner, and R. Kümmeli. "Combining antibiotics with antivirulence compounds can have synergistic effects and reverse selection for antibiotic resistance in *Pseudomonas aeruginosa*". In: *PLOS Biology* 18.8 (2020), e3000805. doi: 10.1371/JOURNAL.PBIO.3000805.
- [24] .D. L. Sánchez-Hevia, N. Fatsis-Kavalopoulos, and D. I. Andersson. "Sublethal interaction factor (SIF), a growth-based method to analyze antibiotic combinations at sub-inhibitory concentrations". In: *Microbiology Spectrum* 13.12 (2025). doi: 10.1128/SPECTRUM.01070-25.
- [25] .N. A. Lozano-Huntelman et al. "The evolution of resistance to synergistic multi-drug combinations is more complex than evolving resistance to each individual drug component". In: *Evolutionary Applications* 16.12 (2023), pp. 1901–1920. doi: 10.1111/eva.13608.
- [26] .B. Yang et al. "Combination Susceptibility Testing of Common Antimicrobials in Vitro and the Effects of Sub-MIC of Antimicrobials on *Staphylococcus aureus* Biofilm Formation". In: *Frontiers in Microbiology* 8 (2017). doi: 10.3389/FMICB.2017.02125.
- [27] .S. Ruden et al. "Synergy Pattern of Short Cationic Antimicrobial Peptides Against Multidrug-Resistant *Pseudomonas aeruginosa*". In: *Frontiers in Microbiology* 10 (2019). doi: 10.3389/FMICB.2019.02740.
- [28] .J.-F. Liu et al. "Interaction Tolerance Detection Test for Understanding the Killing Efficacy of Directional Antibiotic Combinations". In: *mBio* 13.1 (2022). doi: 10.1128/MBIO.00004-22.
- [29] .P. S. Ocampo et al. "Antagonism between bacteriostatic and bactericidal antibiotics is prevalent". In: *Antimicrob. Agents Chemother.* 58.8 (2014), pp. 4573–4582. issn: 1098-6596. doi: 10.1128/AAC.02463-14.
- [30] .G. Rao, J. Li, S. Garonzik, R. Nation, and A. Forrest. "Assessment and modelling of antibacterial combination regimens". In: *Clinical Microbiology and Infection* 24.7 (2018), pp. 689–696. doi: 10.1016/j.cmi.2017.12.004.
- [31] .G. Yu, D. Y. Baeder, R. R. Regoes, and J. Rolff. "Combination Effects of Antimicrobial Peptides". In: *Antimicrobial Agents and Chemotherapy* 60.3 (2016), pp. 1717–1724. doi: 10.1128/AAC.02434-15.
- [32] .V. Rico Caballero, S. Almarzoky Abuhussain, J. L. Kuti, and D. P. Nicolau. "Efficacy of Human-Simulated Exposures of Ceftolozane-Tazobactam Alone and in Combination with Amikacin or Colistin against Multidrug-Resistant *Pseudomonas aeruginosa* in an *In Vitro* Pharmacodynamic Model". In: *Antimicrobial Agents and Chemotherapy* 62.5 (2018). doi: 10.1128/AAC.02384-17.
- [33] .J. H. Chen, D. P. Nicolau, and J. L. Kuti. "Imipenem/Cilastatin/Relebactam Alone and in Combination against *Pseudomonas aeruginosa* in the *In Vitro* Pharmacodynamic Model". In: *Antimicrobial Agents and Chemotherapy* 64.12 (2020). doi: 10.1128/AAC.01764-20.
- [34] .B. Bognár, R. Spohn, and V. Lázár. "Drug combinations targeting antibiotic resistance". In: *npj Antimicrobials and Resistance* 2.1 (2024). doi: 10.1038/S44259-024-00047-2.
- [35] .G. Yu, D. Y. Baeder, R. R. Regoes, and J. Rolff. "Predicting drug resistance evolution: insights from antimicrobial peptides and antibiotics". In: *Proceedings of the Royal Society B: Biological Sciences* 285.1874 (2018), p. 20172687. doi: 10.1098/rspb.2017.2687.
- [36] .T.-C. Chou and P. Talalay. "Quantitative analysis of dose-effect relationships: the combined effects of multiple drugs or enzyme inhibitors". In: *Advances in Enzyme Regulation* 22 (1984), pp. 27–55. doi: 10.1016/0065-2571(84)90007-4.
- [37] .J. Meletiadis, T. Stergiopoulou, E. M. O'Shaughnessy, J. Peter, and T. J. Walsh. "Concentration-Dependent Synergy and Antagonism within a Triple Antifungal Drug Combination against *Aspergillus* Species: Analysis by a New Response Surface Model". In: *Antimicrobial Agents and Chemotherapy* 51.6 (2007), pp. 2053–2064. doi: 10.1128/AAC.00873-06.
- [38] .B. Kavčič, G. Tkalcík, and T. Bollenbach. "Minimal biophysical model of combined antibiotic action". In: *PLOS Computational Biology* 17.1 (2021), e1008529. doi: 10.1371/JOURNAL.PCBT.1008529.
- [39] .R. R. Regoes et al. "Pharmacodynamic Functions: a Multiparameter Approach to the Design of Antibiotic Treatment Regimens". In: *Antimicrobial Agents and Chemotherapy* 48.10 (2004), pp. 3670–3676. doi: 10.1128/AAC.48.10.3670-3676.2004.
- [40] .G. Chevereau and T. Bollenbach. "Systematic discovery of drug interaction mechanisms". In: *Molecular Systems Biology* 11.4 (2015). doi: 10.15252/msb.20156098.
- [41] .S. A. Angermayr et al. "Growth-mediated negative feedback shapes quantitative antibiotic response". In: *Mol. Syst. Biol.* 18.9 (2022), pp. 1–19. issn: 1744-4292. doi: 10.15252/msb.202110490.
- [42] .A. MacGowan. "Assessment of different antibacterial effect measures used in in vitro models of infection and subsequent use in pharmacodynamic correlations for moxifloxacin". In: *Journal of Antimicrobial Chemotherapy* 46.1 (2000), pp. 73–78. doi: 10.1093/JAC/46.1.73.
- [43] .J. R. Lenhard et al. "Evolution of *Staphylococcus aureus* under Vancomycin Selective Pressure: the Role of the Small-Colony Variant Phenotype". In: *Antimicrobial Agents and Chemotherapy* 59.2 (2015), pp. 1347–1351. doi: 10.1128/AAC.04508-14.
- [44] .R. Wu et al. "Bacterial killing and the dimensions of bacterial death". In: *npj Biofilms Microbiomes* 2024 101.10.1 (Sept. 2024), pp. 1–8. issn: 2055-5008. doi: 10.1038/s41522-024-00559-9. url: <https://www.nature.com/articles/s41522-024-00559-9>.

#### 4. ANTIMICROBIAL COMBINATION EFFECTS AT SUB-INHIBITORY DOSES DO NOT RELIABLY PREDICT EFFECTS AT INHIBITORY CONCENTRATIONS

---

- [45] .M. Muetter, D. Angst, R. Regoes, and S. Bonhoeffer. "High-Throughput Quantification of Population Dynamics using Luminescence". In: *eLife* (2026). doi: 10.7554/eLife.109213.1.
- [46] .C. T. Meyer et al. "Quantifying Drug Combination Synergy along Potency and Efficacy Axes". In: *Cell Systems* 8.2 (2019), 97–108.e16. doi: 10.1016/j.cels.2019.01.003.
- [47] .A. H. Vlot, N. Aniceto, M. P. Menden, G. Ulrich-Merzenich, and A. Bender. "Applying synergy metrics to combination screening data: agreements, disagreements and pitfalls". In: *Drug Discovery Today* 24.12 (2019), pp. 2286–2298. doi: 10.1016/j.drudis.2019.09.002.

## Chapter 5

### Concluding Remarks

---

Antimicrobial resistance (AMR) will remain a significant health threat for the foreseeable future. Avoiding a post-antibiotic era, in which common infections again become difficult or impossible to treat, therefore requires sustained changes in how antibiotics are produced and deployed. In this thesis, we focused on how antibiotics can be deployed while limiting the selection for resistance.

Given that theoretical and experimental work suggests that multidrug strategies, and in particular combination therapy, can limit the evolution of chromosomal resistance [Bonhoeffer, tepekule, ueker, 1], in Chapter 2 we asked how these insights extend to clinically important plasmid-borne resistance and to the pharmacodynamics of antibiotic combinations at inhibitory concentrations. We explored the impact of six treatment arms (combination, cycling, mixing, two monotherapies, and an untreated control) on the epidemiological dynamics of plasmid-mediated resistance in an *in vitro* hospital-ward model, with wells representing patients. The two plasmids were horizontally transferable and were isolated from clinical strains [SUttner2024]. One plasmid conferred resistance to ceftazidime (CAZ), while the other conferred resistance to tetracycline (TET). Interestingly, we observed a suppressive antagonistic interaction between CAZ and TET, meaning that CAZ alone achieved a stronger within-well clearance effect than the CAZ+TET combination. Despite these unfavourable conditions, combination therapy was consistently among the best strategies to maximise the number of uninfected patients, and it was the best strategy to prevent the emergence of double resistance. The superiority of combination therapy in preventing double resistance followed from two strategic advantages. First, it reduced the probability of *superinfection*, i.e. a host becoming infected by both single-resistant strains. Second, it reduced the probability that double resistance would emerge within a superinfected host via plasmid conjugation.

However, an *in vitro* ward is still a model, and important constraints that shape clinical decision-making—including toxicity, host heterogeneity, and patient-specific pharmacokinetics—are not represented. Ultimately, the efficacy of strategy-level interventions must be demonstrated in clinical studies. At present, randomised controlled trials are typically not designed or powered to detect within-patient resistance evolution [2], indicating that more targeted and better-powered trials will be required to evaluate how treatment strategies shape resistance evolution in patients.

Although combination therapy performed well in our experiments, treatment success largely depends on the interaction between the drugs applied. To explore these drug interactions at scale, we evaluated in Chapter 3 whether bioluminescence can be used to measure population decline at clinically relevant inhibitory concentrations. We found that for 10 of the 20 drugs tested, light intensity aligned well with cell numbers. These were cases where cells did not substantially fila-

ment. For the remaining drugs, light intensity aligned better with our microscopy-based estimates of biomass than with cell numbers. However, testing how robust this relationship is will require a follow-up study specifically designed to measure biomass, in contrast to our study, which primarily focused on cell numbers.

In Chapter 4, we used the bioluminescence method to test whether interaction patterns measured at sub-inhibitory concentrations predict interactions at inhibitory concentrations. Specifically, we investigated 15 pairwise drug combinations, each measured on  $12 \times 12$  checkerboards spanning sub-inhibitory to inhibitory regimes. We found that interaction classifications are frequently not transferable between concentration regimes. In addition, we found that interaction types can vary with mixing ratio and depend on the chosen reference model.

These results make generalising statements such as “this drug pair synergises” hard to justify. Furthermore, it is questionable whether interaction labels (synergy, antagonism, or independence) are of practical use. Synergy implies a higher combined clearance rate compared to an expectation based on the single-drug effects, whereas suppressive antagonism can deselect resistance [Chait]. It remains debatable which of these properties is more desirable. Furthermore, these labels contain no explicit information about the absolute clearance rate. For example, drugs A and B might antagonise while drugs C and D synergise, but this does not indicate whether clearance under A+B is stronger or weaker than under C+D. Importantly, this critique targets the practice of collapsing rich dose-response surfaces into a single interaction label, not the interaction models themselves. Such models remain useful for predicting combination effects when data are sparse and for inferring mechanisms.

Much of this ambiguity arises because the original question—which drug pairs maximise treatment success while minimising resistance—has been replaced by a heuristic question: which drug pairs synergise. Assessing treatment success or resistance risk directly, e.g., by advancing PK/PD models, would make such comparisons more interpretable. By providing pharmacodynamic data and offering methodological insights into how such data can be acquired, this thesis can help inform these models.

Finally, curbing the rise of antimicrobial resistance will require a bundle of complementary measures beyond clinical strategy design. Approaches that have been proven very effective at reducing AMR frequencies include reducing antibiotic use [3, 4], strengthening infection control and co-ordinated outbreak responses [5, 6], and expanding vaccination to reduce infections and, in turn, antibiotic exposure [7].

In conclusion, while continued increases in resistance would carry a substantial societal cost, I remain optimistic that a set of proven interventions can curb the rise of antimicrobial resistance. In this thesis, I showed that combination therapy can be one part of this broader approach and that combination pharmacodynamics can be quantified to optimise this strategy.

## Bibliography

- [1] .D. C. Angst, B. Tepekule, L. Sun, B. Bogos, and S. Bonhoeffer. "Comparing treatment strategies to reduce antibiotic resistance in an in vitro epidemiological setting". In: *Proc. Natl. Acad. Sci. U. S. A.* 118.13 (2021), pp. 1–7. issn: 10916490. doi: 10.1073/PNAS.2023467118.
- [2] .B. Siedentop et al. "The effect of combining antibiotics on resistance: A systematic review and meta-analysis". In: *Elife* (2024). doi: 10.7554/eLife.93740.1.
- [3] .Y. Agersø and F. M. Aarestrup. "Voluntary ban on cephalosporin use in Danish pig production has effectively reduced extended-spectrum cephalosporinase-producing *Escherichia coli* in slaughter pigs". In: *Journal of Antimicrobial Chemotherapy* 68.3 (2012), pp. 569–572. doi: 10.1093/jac/dks427.
- [4] .M. Lafaurie, R. Porcher, J.-L. Donay, S. Touratier, and J.-M. Molina. "Reduction of fluoroquinolone use is associated with a decrease in methicillin-resistant *Staphylococcus aureus* and fluoroquinolone-resistant *Pseudomonas aeruginosa* isolation rates: a 10 year study". In: *Journal of Antimicrobial Chemotherapy* 67.4 (2012), pp. 1010–1015. doi: 10.1093/jac/dkr555.
- [5] .J. D. Edgeworth, R. Batra, J. Wulff, and D. Harrison. "Reductions in Methicillin-resistant *Staphylococcus aureus*, *Clostridium difficile* Infection and Intensive Care Unit-Acquired Bloodstream Infection Across the United Kingdom Following Implementation of a National Infection Control Campaign". In: *Clinical Infectious Diseases* 70.12 (2019), pp. 2530–2540. doi: 10.1093/cid/ciz720.
- [6] .M. J. Schwaber et al. "Containment of a Country-wide Outbreak of Carbapenem-Resistant *Klebsiella pneumoniae* in Israeli Hospitals via a Nationally Implemented Intervention". In: *Clinical Infectious Diseases* 52.7 (2011), pp. 848–855. doi: 10.1093/cid/cir025.
- [7] .M. H. Kyaw et al. "Effect of Introduction of the Pneumococcal Conjugate Vaccine on Drug-Resistant *Streptococcus pneumoniae*". In: *New England Journal of Medicine* 354.14 (2006), pp. 1455–1463. doi: 10.1056/NEJMoa051642.



## Acknowledgements

---

I would like to thank my supervisors, Sebastian Bonhoeffer and Roland Regoes, for their support, trust, and guidance throughout my PhD. I am also deeply grateful to Daniel Angst for his close collaboration, for sharing his expertise and ideas, and for the many discussions that shaped this work. I thank the entire TB Group for the stimulating environment, for help and feedback, and for making the day-to-day work enjoyable. I am grateful to my parents for their continuous encouragement and support over the years. Most importantly, I thank my wife for her love, patience, and unwavering support, and my son for the joy, perspective, and balance he brought to this period of my life.



## **Appendix A**

### The Impact of Treatment Strategies on the Epidemiological Dynamics of Plasmid-Conferred Antibiotic Resistance

---

**Authors:** Malte Muetter<sup>a</sup>, Daniel C. Angst<sup>a</sup>, Roland R. Regoes<sup>a</sup>, Sebastian Bonhoeffer<sup>a</sup>

<sup>a</sup>*Institute of Integrative Biology, Department for Environmental System Science, ETH Zurich, 8092 Zurich, Switzerland*

---

*Supplementary Information*

## A1 SI Methods

**Strains.** We chose two plasmid-carrying donors, ESBL9 and ESBL25, and two drugs, ceftazidime and tetracycline, based on the resistance conferred by the plasmids contained in the strains and the compatibility of the plasmids. ESBL9 and ESBL25 were collected as part of a clinical transmission study at the University Hospital Basel, Switzerland [1] and fully sequenced, including identification of the carried plasmids [2]. The strains were a generous gift from Adrian Egli, University Hospital Basel.

ESBL9 contains an IncI1 plasmid, referred to here as  $p_A$ , conferring, among others, resistance to ampicillin and ceftazidime but not tetracycline or chloramphenicol. ESBL25 contains an IncF1 plasmid, referred to here as  $p_B$ , conferring, among others, resistance to ampicillin and tetracycline but not ceftazidime or chloramphenicol.

The two plasmids were transferred by conjugation from the original clinical isolates to the chloramphenicol-resistant and ampicillin-sensitive *Escherichia coli* MDS42-YFP (recipient) [3], followed by selection for ampicillin and chloramphenicol resistance. This results in the ceftazidime-resistant (A-resistant) strain and the tetracycline-resistant (B-resistant) strain. The double-resistant (AB-resistant) strain was created by a further round of conjugation to receive both plasmids and subsequent selection for ceftazidime and tetracycline resistance. Strains are listed in Table A2. All transconjugants were verified by PCR replicon typing using primers specific for the respective replicon [4].

**Drugs.** We used ceftazidime, referred to as drug A, at a concentration of  $80 \frac{\mu\text{g}}{\text{mL}}$ .  $80 \frac{\mu\text{g}}{\text{mL}}$  is substantially lower than the MIC for A-resistant bacteria and more than 50 times the MIC for sensitive or B-resistant bacteria. Using the same reasoning, we used tetracycline, referred to as drug B, at a concentration  $40 \frac{\mu\text{g}}{\text{mL}}$ . The antibiotic concentrations in the liquid and the solid media were identical. To avoid contamination, we used  $25 \frac{\mu\text{g}}{\text{mL}}$  chloramphenicol for *prevention* scenario and  $5 \frac{\mu\text{g}}{\text{mL}}$  chloramphenicol for *containment* and *maximum-emergence* scenarios. We could not measure any significant growth effects of the chloramphenicol concentrations on the chloramphenicol-resistant strains (see Table A5).

**Conjugation Protocol.** We used ampicillin-resistant and chloramphenicol-sensitive original donors [1, 5] and the chloramphenicol-resistant, ampicillin-sensitive recipient [3]. Fresh overnight cultures of both donors and recipients were diluted 1:1000 and grown to mid-exponential phase. Following this, the donor and recipient cultures were combined in a culture tube and incubated for four hours at  $37^\circ\text{C}$  with constant shaking at 180 rpm. We then spotted a  $100 \mu\text{l}$  drop of this mixture on an agar plate treated with  $25 \frac{\mu\text{g}}{\text{mL}}$  chloramphenicol and  $100 \frac{\mu\text{g}}{\text{mL}}$  ampicillin, allowing only the transconjugants to grow. Conjugation was verified by PCR replicon typing [4].

**Plasmid costs** To measure plasmid costs, we grew three replicates of overnight cultures of all strains in selective medium. The cultures were then diluted approximately 1:150 into LB with 5  $\mu\text{g}/\text{mL}$  chloramphenicol using the pintoool, following the same procedure as in the main experiments. Subsequently, we recorded OD growth curves using the same plate reader. The maximum growth rate was estimated by applying linear regression to a sliding window on the log-transformed data (window size: 1 hour, step size: approximately 5 minutes). Pairwise comparisons were performed between the maximum growth rates of the sensitive strain and the plasmid-carrying strains using the Mann-Whitney U test (scipy.stats [6]), followed by a Bonferroni correction to account for multiple testing. We observed no significant difference in the maximum growth rate between any of the pairs (Table A3).

**Segregational Loss** We estimated plasmid segregation loss over 24 hours ( $t_0-t_1$ ) without treatment and with treatment as a control. For this, we grew overnight cultures in selective medium for three replicates  $k \in \{1,2,3\}$  of each plasmid-carrying strain. We diluted the cultures and plated each on drug-free agar plates, followed by replica plating onto selective plates to identify the presence or absence of resistance plasmids in each colony. This initial step represents time point  $t_0$ . The overnight cultures were then transferred to i) drug-free medium and ii) selective medium (control), using the same pintoool as in the main experiments. The cultures were incubated for 24 hours, after which we diluted and plated them again on drug-free plates and used replica plating on selective plates to assess plasmid presence for time point  $t_1$ . We compared the frequencies  $f_k(t)$  of plasmid presence between time points  $t_0$  and  $t_1$  using the Mann-Whitney U test (scipy.stats [6]). No significant loss of plasmids was observed in either the control or the experimental conditions (Table A4). We estimated the mean frequency of plasmid presence  $f(t)$  for each strain and time point and the confidence intervals  $CI(t)$  for the frequency by bootstrapping the pooled colony presence-absence data.

**Growth rates and bacterial density.** We assessed the final bacterial density of overnight cultures following an 18-hour incubation period (Table A5) for each bacterial strain in its respective selective medium for two different chloramphenicol concentrations: 5  $\frac{\mu\text{g}}{\text{mL}}$  and 25  $\frac{\mu\text{g}}{\text{mL}}$ . To estimate the bacterial density, we plated 200  $\mu\text{L}$  of various dilutions of the cultures on agar plates using glass beads. The 95 % confidence intervals for the colony counts were calculated using the Poisson distribution.

In addition, we monitored the optical density (OD) in 384-well plates over an 18-hour period in the respective selective medium containing either 5  $\frac{\mu\text{g}}{\text{mL}}$  or 25  $\frac{\mu\text{g}}{\text{mL}}$  chloramphenicol. To determine the maximum growth rates, we employed a sliding window approach with a one-hour width, linearly fitting the growth rate to the log transformed values within this window for each replicate. The 95 % confidence intervals for the maximal growth rates were calculated using the Student's t-distribution.

**Basic Reproductive Number.**  $R_0$  represents the number of secondary infections generated by one patient in a fully susceptible population. Let  $\tau$  denote the probability that a patient leaves the hospital ward after one timestep,  $\tau' = 1 - \tau$  the probability that the patient stays and  $\beta$  the probability that a patient infects another during one timestep. Then we can write the total number of infections caused by one patient introduced into a susceptible population as a geometric series:

$$R_0 = (\tau')^0 \cdot \beta + (\tau')^1 \cdot \beta + (\tau')^2 \cdot \beta + \dots = \beta \sum_{n=0}^{\infty} (\tau')^n$$

This geometric series can then be rewritten as:

$$R_0 = \beta \cdot \frac{1}{1 - \tau'} = \frac{\beta}{\tau} \quad (\text{A1})$$

**Phenotyping – Limitations.** The phenotyping procedure enables high throughput identification of resistance profiles. Although this method is generally reliable and effective for most wells, it is difficult to accurately determine the resistance profile for wells with very low bacterial densities due to the potential for stochastic effects. We analysed 1784  $A_r$  turnover wells treated with antibiotic B during the *maximum-emergence* scenario. Here, we observed, alongside the expected  $A_r$  and  $U$  wells, 9% ‘other’ and 17%  $S$  wells, as detailed in Fig. A5a. It might be tempting to interpret the  $S$  wells as those in which all bacteria lost their plasmids and the ‘other’ wells as artefacts of measurement errors. Although these interpretations are not incorrect, a more critical factor influencing the measured resistance profile distribution is the inherent stochasticity of the method if applied to low-density wells.

As an example, we will analyse wells identified as  $A_r$ -wells during the previous transfer and subsequently treated with antibiotic B. To simplify the following analysis, we only consider *agar plates* treated with drug  $\vartheta \in \{N, A\}$  (no drug, drug A) and disregard plates treated with drug B (B-plates) and AB (AB-plates). Furthermore, we will use a prime ('') to indicate a counter probability ( $w' = 1 - w$ ). Drawing a drop with volume  $V_{\text{drop}}$  from a well with volume  $V_{\text{well}}$  leads to a probability  $p = \frac{V_{\text{drop}}}{V_{\text{well}}}$  of drawing a specific bacterium. The probability that the drawn drop contains no bacteria of phenotype  $\psi \in \{\emptyset, a\}$  (without resistance and A-resistance) is  $d'_\psi = (1 - p)^{Z_\psi}$ , with  $Z_\psi$  representing the number of bacteria with phenotype  $\psi$  inside the well. We denote the probability that a drop can grow on a plate treated with drug  $\vartheta$  as  $g_\vartheta$ . The probability  $g'_N$  of drawing a drop that will not form a colony on an N-plate can then be defined as  $g'_N = d'_\emptyset d'_a$ , and the probability  $g'_A$  of drawing a drop that will not grow on an A-plate is  $g'_A = d'_a$ .

Assuming that the drawn drop does not significantly alter the well volume and composition, we

obtain the following probabilities for the possible resistance profiles (see also Fig. A5b):

$$\begin{aligned}\mathbb{P}(U) &= g'_N \cdot g'_A \\ \mathbb{P}(S) &= g_N \cdot g'_A \\ \mathbb{P}(A_r) &= g_N \cdot g_A \\ \mathbb{P}(\text{other}) &= g'_N \cdot g_A\end{aligned}$$

Assuming  $p = 0.006$  (value for our experiment), a well containing 25 A-resistant and 15 sensitive bacteria will result in 70%  $U$ , 26%  $S$ , 3%  $A_r$ , and 11% *other*. This result is similar to the experimentally measured distribution (compare Fig. A5a).

**Advanced Resistance Profiles** We introduced advanced phenotypes into our analysis to determine the approximate bacterial density inside the wells. Wells that retain their phenotype after one transfer, despite being sensitive to a particular antibiotic, are expected to exhibit a low bacterial density post-treatment and are labelled  $\phi^l$ . Conversely, wells that were either untreated or treated with an ineffective antibiotic are expected to contain a high bacterial density and are labelled  $\phi^h$ . In addition, wells that underwent a change in resistance profile or were mixed with other wells are denoted as  $\phi^?$  and are excluded from further analysis. We summarised the influence of the bacterial densities within the inoculating wells on the frequency of superinfections developing double resistance in Table A1.

**Statistical Analysis.** To compare the performance of different treatment strategies *in vitro*, we summarized the resistance profiles into groups and focused our analysis on three groups: uninfected, single-resistant and double-resistant. These labels stem from the properties within the wells. That means single resistant wells ( $A_r$ ,  $B_r$  or  $(A_r \& B_r)$ ) would be wells that contain only single resistant (or sensitive) bacteria, but no double resistant bacteria and therefore can be cured by combining drugs. In contrast, double-resistant wells cannot be cured using both antibiotics simultaneously since they contain AB-resistant bacteria. We then averaged the frequency of each group over the last four transfers for every replicate. Four transfers correspond to a complete cycle in the cycling strategy with a period of 2 (e.g., A-A-B-B). The effect of the treatment strategy on the average frequencies of uninfected, single-resistant, and double-resistant wells was then tested using a one-way ANOVA. In the case of a significant test ( $p < 0.05$ ), we conducted a pairwise Tukey post hoc analysis to relate the mean frequencies.

In addition, we analysed superinfections between patients and the emergence of double resistance across different strategies in the *maximum-emergence* scenario. We considered all measurement points from the fourth transfer onwards as at near-stationary level for the non-cycling strategies. Consequently, the initial conditions for each new transfer remain approximately the same or are repeated every fourth transfer in the case of cycling.

For this analysis, we counted the number of newly emerged double-resistant wells  $n_{\mathcal{E}}$  and the number of superinfections  $n_{\mathcal{S}}$  across all replicates for each plate, with each plate representing one treatment arm for a single transfer. Newly emerged double-resistant wells are defined as those exhibiting double resistance but not having previously been passaged or infected by a double-resistant well. Additionally, for each plate, we analysed all wells treated with treatment  $\vartheta$ , counting the number of superinfected wells  $n_{\mathcal{S}}^{\vartheta}$  and those among them that developed double resistance  $n_{\mathcal{E}}^{\vartheta}$ .

We then tested whether the treatment strategy significantly affects the emergence frequency  $f_{\mathcal{E}} = n_{\mathcal{E}}/n_p$  and the frequency of superinfection  $f_{\mathcal{S}} = n_{\mathcal{S}}/n_p$ , with  $n_p$  being the number of patients in a hospital ward across all replicates (376) using an ANOVA. Additionally, we used an ANOVA to assess if treatment  $\vartheta$  significantly influences the frequency of superinfected wells that develop double resistance  $n_{\mathcal{E}}^{\vartheta}/n_{\mathcal{S}}^{\vartheta}$ .

Subsequent to a significant ANOVA test, we conducted pairwise Tukey post hoc comparisons between the treatment arms ( $p < 0.05$ ).

All statistical analyses were performed in Python 3.8.5 using SciPy's `f_oneway()` [6] for ANOVA tests and Statsmodels' `pairwise_tukeyhsd()` [7] for conducting Tukey's honest significant difference post hoc analyses.

**Maximum-emergence scenario: Predicting the Emergence Probability.** We counted for each plate  $i$  the number of superinfected wells  $n_{\mathcal{S}}^i$  and normalized them by the number of patients per plate  $n_p$  to calculate the frequency of superinfection ( $f_{\mathcal{S}}^i = \frac{n_{\mathcal{S}}^i}{n_p}$ ). Then, we estimated the probability of superinfection  $\mathbb{P}(\mathcal{S})$  for each treatment arm by averaging  $f_{\mathcal{S}}^i$ . In addition, we approximated the probability of emergence for superinfected wells  $\mathbb{P}_{\vartheta}(\mathcal{E}|\mathcal{S})$  under treatment  $\vartheta$ , by normalizing the total number of newly emerged resistances across all plates  $N_{\mathcal{E}}^{\vartheta}$  by the total number of superinfected wells under treatment  $\vartheta$  ( $N_{\mathcal{S}}^{\vartheta}$ ):  $\frac{N_{\mathcal{E}}^{\vartheta}}{N_{\mathcal{S}}^{\vartheta}}$ . The estimates for  $\mathbb{P}_{\vartheta}(\mathcal{E}|\mathcal{S})$  were then utilized to approximate the average probability of superinfected wells developing double resistance for each treatment arm. The weighted average of all  $\mathbb{P}_{\vartheta}(\mathcal{E}|\mathcal{S})$  were computed using the proportion of patients receiving treatment  $\vartheta$  as weights. For example, in mixing, the average probability  $\bar{\mathbb{P}}(\mathcal{E}|\mathcal{S})$  is given by  $0.5\mathbb{P}_A(\mathcal{E}|\mathcal{S}) + 0.5\mathbb{P}_B(\mathcal{E}|\mathcal{S})$ . We then used Equation A2 to predict the average probability of emerging double resistance  $\mathbb{P}(\mathcal{E})$  for each strategy, as indicated in Figure 3A by black stars.

$$\mathbb{P}(\mathcal{E}) = \mathbb{P}(\mathcal{S})\bar{\mathbb{P}}(\mathcal{E}|\mathcal{S}) \quad (\text{A2})$$

## A2 SI Results

**Impact of Treatment on the Emergence of Double Resistance.** As demonstrated in Figure 3B, our findings indicate that treatment substantially influences the frequency of emerging double resistance in superinfected wells. Population dynamics within wells can potentially explain these re-

sults. Here we approximate  $\mathbb{E}_\theta$ , the expected number of conjugations during one treatment phase under treatment  $\vartheta$ , as  $\mathbb{E}_\theta \propto \gamma_\theta \int_{t_1}^{t_2} {}^A X_\theta(t) {}^B X_\theta(t) dt$ .  ${}^i X$  represents the density of bacteria with resistance  $i$ , and  $\gamma_\theta$  is the treatment dependent conjugation rate. The experimentally generated data are insufficient for adequately estimating  $\gamma_\theta$ . However, if we assume identical initial bacterial populations, we can qualitatively rank the cumulative product of bacterial densities  $\int_{t_1}^{t_2} {}^A X_\theta(t) {}^B X_\theta(t) dt$ . The highest cumulative product is achieved when  ${}^A X$  and  ${}^B X$  grow without or with ineffective treatment. Additionally, we know that the clearance rate of ceftazidime (drug A) is substantially higher than that of tetracycline (drug B), as shown in Table A8, resulting in a larger cumulative product over time when treated with antibiotic B. Lastly, the lowest cumulative product is associated with treatment AB, where neither of the two strains can grow. Therefore, if we disregard  $\gamma_\theta$ , the above reasoning predicts the following ranking for the number of emergences per superinfection: None, B, A, AB. This predicted ranking aligns with the ranking observed in [Figure 3C](#).

Another potential explanation are potential differences in the plasmid-specific conjugation rates. If, for example,  $p_B$  had a higher conjugate rate than  $p_A$ , then drug A would have a stronger impact on the emergence of double resistance, even if we assumed identical clearance rates.

**Treatment strategies influence the number of bacteria inoculating superinfections.** We observed that the number of single-resistant bacteria that inoculate superinfections affects the emergence of double resistance (Table A1). At least one of the two superinfection-initiating inocula originates from infections between patients and is sourced from the previous assay plate. The cell densities and compositions within these source wells, which have already undergone treatment for one day, vary considerably depending on the resistance profile  $\phi$  and the treatment history. We used 'advanced phenotypes' (see SI Methods) to distinguish between high-density ( $\phi^h$ ) and low-density ( $\phi^l$ ) wells, assigning these based on the wells resistance profile ( $\phi$ ) and treatment history.

During the *maximum-emergence* scenario, which contained the highest number of superinfections, we made two noteworthy observations. First, superinfections between  $\phi^h$  and  $\phi^l$  ( $A_r^l + B_r^h$  (43 superinfections) and  $A_r^h + B_r^l$  (one superinfection)) occur significantly less frequently than superinfections between  $A_r^h + B_r^h$  (a total of 1176 superinfections, as outlined in Table A1). This discrepancy can be attributed to the high clearance rates of both drugs, resulting in a higher prevalence of  $\phi^h$  compared to  $\phi^l$ .

Second, none of the 44 superinfections involving  $A_r^l + B_r^h$  and  $A_r^h + B_r^l$  resulted in double resistance.

**Antagonism.** Adding the bacteriostatic antibiotic tetracycline (drug B) reduces the probability of clearing sensitive bacteria with the bactericidal antibiotic ceftazidime (drug A). The clearance probability drops from 0.97 to 0.86, as shown in Table A8. Antagonism between bactericidal and bacteriostatic antibiotics has been documented by various researchers since the 1950s, as exemplified by the works of Cates [8] and Jawetz [9], and also more recently by Ocampo [10]. The antagonis-

tic effect may arise because the bacteriostatic drug (tetracycline) lowers the growth rate, resulting in a decreased kill rate of the bactericidal drug (ceftazidime) [11]. Accordingly, this antagonistic effect is anticipated to be less pronounced for a tetracycline-resistant strain, where the impact on the growth rate is diminished. This hypothesis is supported by the measured clearance rates for  $B_r$  wells, where the clearance probability remains at 0.98 for treatment with drugs A and AB Table A8.

### A3 SI Computational Model

**Stochasticity** We conducted three experiments, each defined by one parameter set consisting of a turnover probability  $\tau$ , an infection probability  $\beta$  and the probability distribution for sampling patients  $c_\phi$  with different resistance profiles  $\phi \in \{U, S, A_r, B_r, AB_r\}$ . For each experiment, we randomly generated one instruction set based on the given parameter set. Due to the scale and complexity of the experiment, it was infeasible to conduct a unique instruction set for each replicate. Therefore, we opted to employ identical instruction sets for all replicates, which reduces the number of robot arm movements (and time) for infection and turnover by a factor of four.

As a consequence, our replicates may be interpreted as patients with identical histories regarding original infection, treatment and exchange with other patients. However, due to the accumulated biological stochasticity along the patient histories, their phenotypic properties may vary, as reflected by the variance of the replicates.

Since we only tested one instruction set per replicate *in vitro*, we wondered whether the measured results depend on the randomisation of the instruction set and if we would expect a qualitatively different result if we reran the experiment 100 times. To answer this question, we created a computational model that, for a given parameter set, rerandomises the instruction set and conducts a stochastic simulation to mimic the biological variability. In Fig. A3, we visualised the different sources of experimental and computational variability.

**Transition Probabilities.** We used the experimental data to calculate the transition frequencies for all pre-treatment  $\phi_\vartheta^i(T)$  to post-treatment  $\phi_\vartheta^i(\hat{T})$  resistance profile combinations for each plate  $i$  and treatment  $\vartheta$ .  $\phi(\hat{T})$  is measured during the phenotyping procedure, while  $\phi(T)$  is estimated by employing one plate-handling simulation step to  $\phi(\hat{T} - 1)$  as described in the methods (e.g.  $A_r + S \rightarrow A_r$ ). Then, we estimated the transition probabilities as the weighted average of transition frequencies across all plates, with the count of  $\phi_\vartheta(T)$  on each plate as a weight.

For each treatment  $\vartheta$ , we created one transition matrix  $M^\vartheta$ , with the pre-treatment resistance profile  $\phi(T)$  as columns and the post-treatment profile  $\phi(\hat{T})$  in the rows (Table A18–A21). To simulate the incubation phase, we use  $M^\vartheta$  to stochastically assign the post-treatment resistance profile  $\phi_\vartheta(\hat{T})$ , using the respective column of the transition matrix as a probability distribution.

**Transition Probabilities for Transfer 1.** All patients are untreated during transfer 0, leading to exceptionally high rates of superinfections and high emergence rates per superinfection during transfer 1. To account for this, we created four additional transition matrices for simulating the first transfer (see Table A22–A25).

**Choice of Model.** We also considered using a continuous model. However, a typical population-based model would not match the experimental measurements for effectively treated patients. This is due to the discrete nature of our experimental setup. Here, the frequency of infected patients has a local maximum before treatment and a local minimum after treatment, creating sawtooth-shaped frequencies over time. We conducted the phenotyping at the end of the incubation period, at the local low point, diverging from the average frequencies predicted by a continuous model. Therefore, a continuous model would either use realistic clearance rates and not fit through the experimental data points or use exaggerated clearance rates and fit through the data points. For example, treating an *S* well with a hypothetical drug C leads to a steady decline in bacterial density over time, resulting in a bacterial density below the detection limit after 24 hours (our first experimental measurement point). If initially, all wells are infected, and at the first measurement point, the infection drops to 0%, fitting a continuous compartmental model to these data would result in infinite clearance rates.

**Contamination of the Transition Matrix.** The computational simulations employ four transition matrices ( $M^{\text{none}}$ ,  $M^A$ ,  $M^B$ ,  $M^{AB}$ ) derived from the observed transitions during the three experiments. During the experiments, we observed a low rate of contamination affecting neighbouring wells, likely due to pipette and plate movements by the liquid handling platform. Quantifying the exact contamination rate is challenging, though the observed mean transition probability from *U* to *U* is 0.99%.

These contaminations can be inconsequential; for example, an *S* well contaminating an *A<sub>r</sub>* well will not cause a shift of the resistance profile in the contaminated well. However, they can also lead to artefactual transitions that are reflected in the transition matrices, such as  $U \rightarrow S$  (Table A18),  $U \rightarrow A_r$  (Table A19), or  $U \rightarrow B_r$  (Table A20). The impact of the recorded artefactual transitions in the transition matrices depends on the frequency and the transferred resistance profile. For instance, in Mono A, a high frequency of *A<sub>r</sub>* contaminations is observed due to the predominant presence of *A<sub>r</sub>* wells, creating the impossible transition  $U \rightarrow A_r$ , described above, which now occurs in all simulations independent of the presence or frequency of *A<sub>r</sub>* during the simulation. Similarly, in the *containment* experiment, the abundance of *AB<sub>r</sub>* wells in all treatment arms led to a higher rate of double-resistant contamination reflected in the transitions:  $A_r \rightarrow AB_r$  (Table A18) and  $A_r \rightarrow AB_r$  &  $B_r \rightarrow AB_r$  (Table A20). Resistance mutations could also explain these transitions; however, because they occurred mainly during the *containment* scenario and the fact that they exclusively came up in wells neighbouring double-resistant wells, we believe that they are an artefact of unintended

infections.

Artefactual transitions such as  $U \rightarrow S$ , or  $U \rightarrow A_r$  have a neglectable effect on the simulation of all scenarios, as their occurrence in the regular infection and admission processes outweighs the contribution through the artefactual transitions. Similarly, double-resistant contaminations minimally impact the simulations of both the *containment* scenario (where double resistance is regularly admitted) and the *maximum-emergence* scenario (due to a low  $R_0$  and frequent emergence of double resistance). However, they pose a problem to the simulation of *prevention* scenario, where a low (untruthful) influx of  $AB_r$  can spread ( $R_0 > 1$ ).

**Filtered Transition Probabilities.** To mitigate the effect of contaminated transition matrices, we introduced filtered transition matrices. For this, we assumed no resistance mutations and forbidding impossible transitions (by setting the transition probability  $U \rightarrow U$  to 1; see Table A26 – A33).

Using these filtered probabilities to simulate the *prevention* scenario leads to better-matching results, almost removing the spread of double resistance in Mono A and the multidrug strategies and thereby matching the experimental data better (compare the green error bands between Fig. A2 & Fig. A7). In addition, we conducted a secondary sensitivity analysis with these filtered probabilities (see Fig. A8). Because the overall conclusions are consistent between the simulations using filtered and unfiltered transition probabilities, we opted to use the unfiltered transition probabilities in the main paper for a more direct representation of the experimental data.

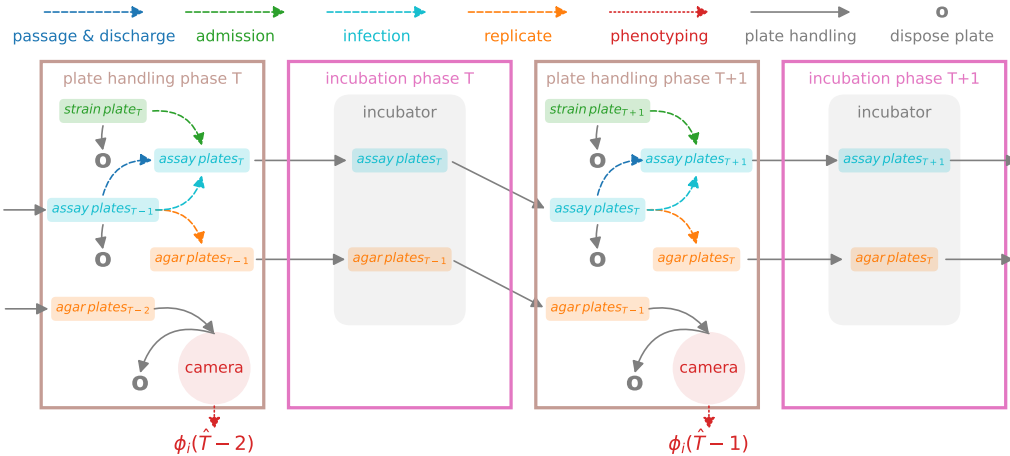
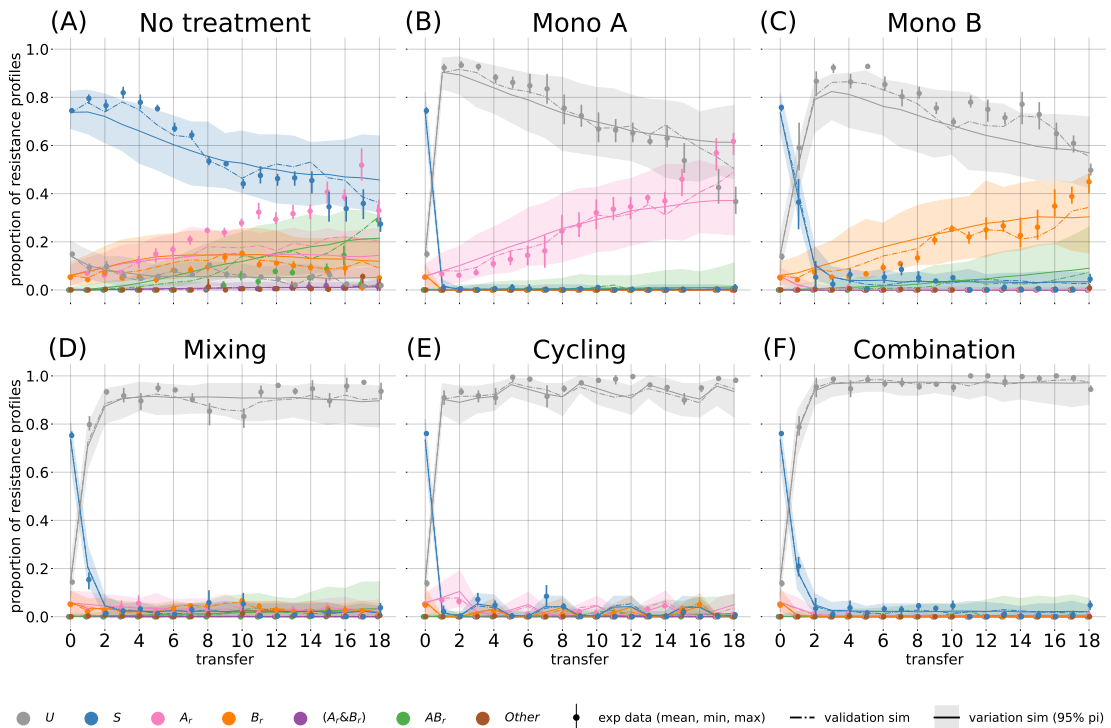


Fig. A1 – Schematic illustrating the procedure used in the experiment for transfers  $T$  and  $T+1$  in the liquid handling platform after adding medium and drugs to the *assay plates*. Every transfer (day), we provide new *assay* and *agar plates*. Plates from the previous transfers are removed. To inoculate the new *assay plates* with newly admitted patients from the *strain plate*, along with staying patients and infection between patients from the previous *assay plate*, we use a pintool with retractable pins (dashed lines). Discharged patients are not transferred (pins retracted) to the new *assay plates*. Plates are then automatically transferred (solid lines) to the incubator for overnight incubation. Subsequently, we replicate each *assay plate* onto four *agar plates* using the pintool. These plates are treated with antibiotics A, B, and AB, and one remains untreated. Once the *agar plates* have been incubated overnight, we capture images (dotted lines) to determine the resistance profile  $\phi_i$  for each well  $i$ .



**Fig. A2 – Prevention scenario:** Frequencies of resistance profiles (colours) over time during the *prevention scenario*. The dots show the experimental measurements, and the error bar indicates the min/max interval between the replicates. The dash-dotted line shows the mean value of 100 stochastic simulations based on the instruction set used in the *in vitro* experiment. The solid line represents the mean value of 100 simulations with randomly created instruction sets based on the parameter set used in the experiment. The shaded error band indicates the 95-percentile interval between the simulations.

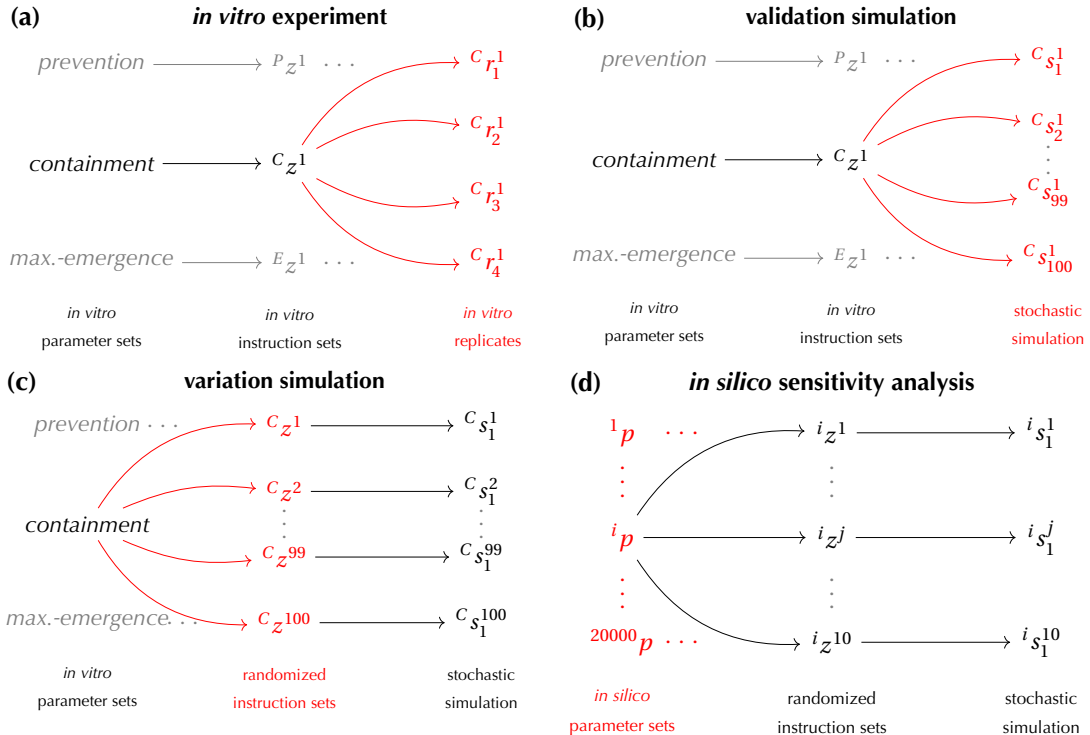


Fig. A3 – Illustration depicting the various sources of stochasticity and variation in experiments and simulations. Our experiments and simulations investigate various sources of stochasticity and their contributions to the variability of the outcome. In panels A-D, we sketch the different sources of stochasticity for each experiment and simulation, highlighting our primary focus in red. **(a) In vitro Experiment.** Each experiment explores a scenario and is defined by a distinct parameter set (*prevention* (P), *containment* (C), *maximum emergence* (E)). We randomly generated one instruction set for each parameter set  $i$ :  $i_z^1$ . For each instruction set  $i_z^1$ , we replicated the cumulative in-well dynamics four times  $i_r_j^1$ . **(b) Validation Simulation.** To assess our computational model, we employed identical parameter sets and instruction sets  $i_z^1$ , as employed in the *in vitro* experiments. For each instruction set  $i_z^1$ , we conducted 100 stochastic simulations  $i_s_j^1$ . **(c) Variation Simulation.** For every *in vitro* parameter set, we randomly generated 100 alternative instruction sets  $i_z^k$  to quantify the influence of experimental decisions on the experiment's outcomes. For each instruction set, we performed one simulation  $i_s_1^k$ . **(d) In Silico Sensitivity Analysis.** We examined the sensitivity of our experimental findings to the input parameters by examining the effects of varying the input parameters on the resulting frequency of uninfected cases for different treatment strategies. To achieve this, we generated 20,000 alternative parameter sets  $i_p$ . We created ten randomised instruction sets  $i_z^k$  for each parameter set  $i_p$  and simulated each instruction set one time ( $i_s_1^k$ ).

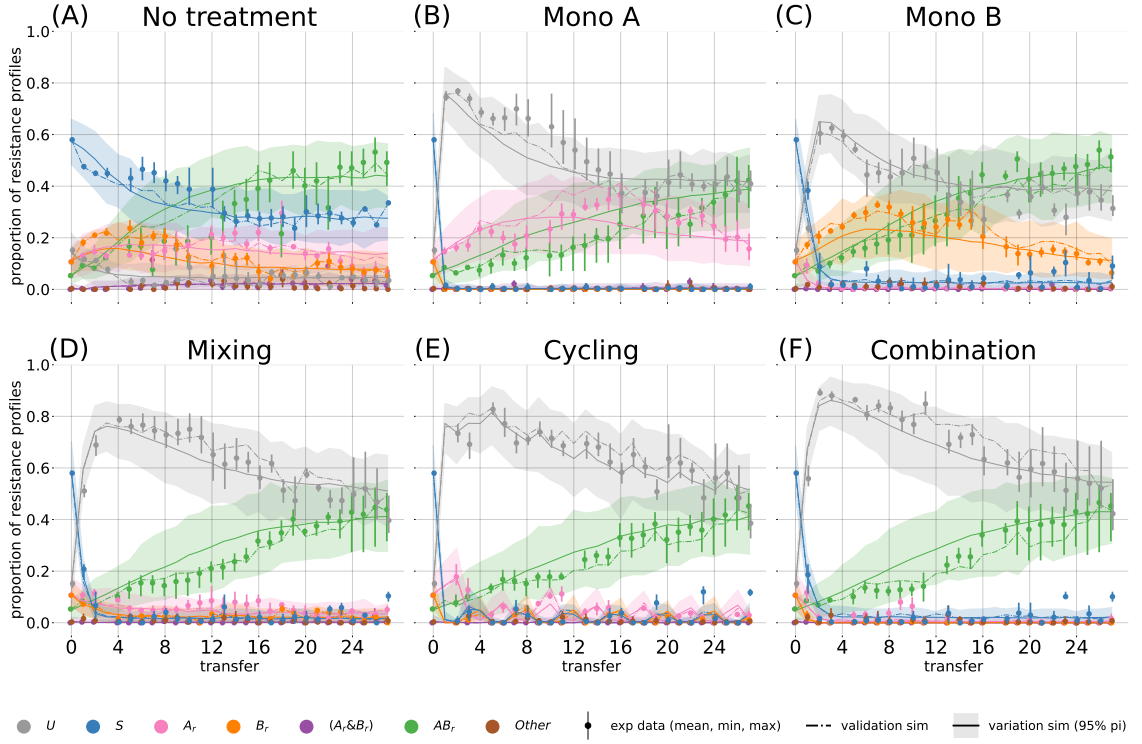


Fig. A4 – **Containment scenario:** Frequencies of resistance profiles (colours) over time during the *containment* scenario. The dots show the experimental measurements, and the error bar indicates the min/max interval between the replicates. The dash-dotted line shows the mean value of 100 stochastic simulations based on the instruction set used in the *in vitro* experiment. The solid line represents the mean value of 100 simulations with randomly created instruction sets based on the parameter set used in the experiment. The shaded error band indicates the 95-percentile interval between the simulations.

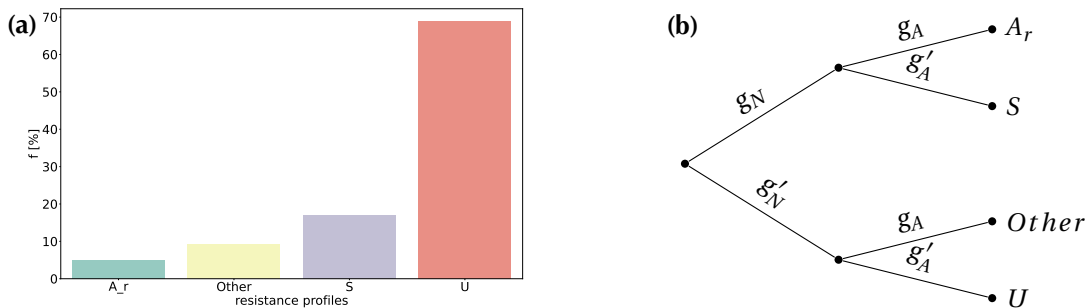


Fig. A5 – (A) Experimentally measured resistance profiles for 1784 wells with the pre-treatment profile  $A_r$  and treatment with drug B during the *maximum-emergence* scenario. (B) Decision tree to calculate the distribution of measured phenotypes for a well that contains  $Z_\emptyset$  sensitive and  $Z_A$  A-resistant bacteria.  $g_\vartheta$  is the probability of drawing a drop that forms a colony on a plate treated with drug  $\vartheta$ , while  $g'_\vartheta$  is the probability that it does not form a colony.

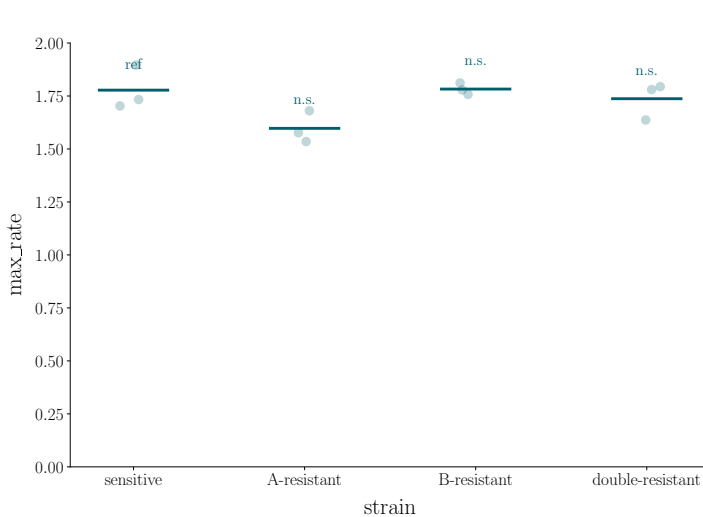


Fig. A6 – Maximum growth rates of sensitive and plasmid-carrying strains, measured using OD-growth curves. Each dot represents an individual well, and vertical bars indicate the mean. The sensitive strain was used as the reference ("ref") for pairwise comparisons to the plasmid-carrying strains to identify potential plasmid costs. We used the Mann-Whitney U tests with the Bonferroni correction to identify significant differences in growth rates. All pairwise comparisons were not significant (n.s.).

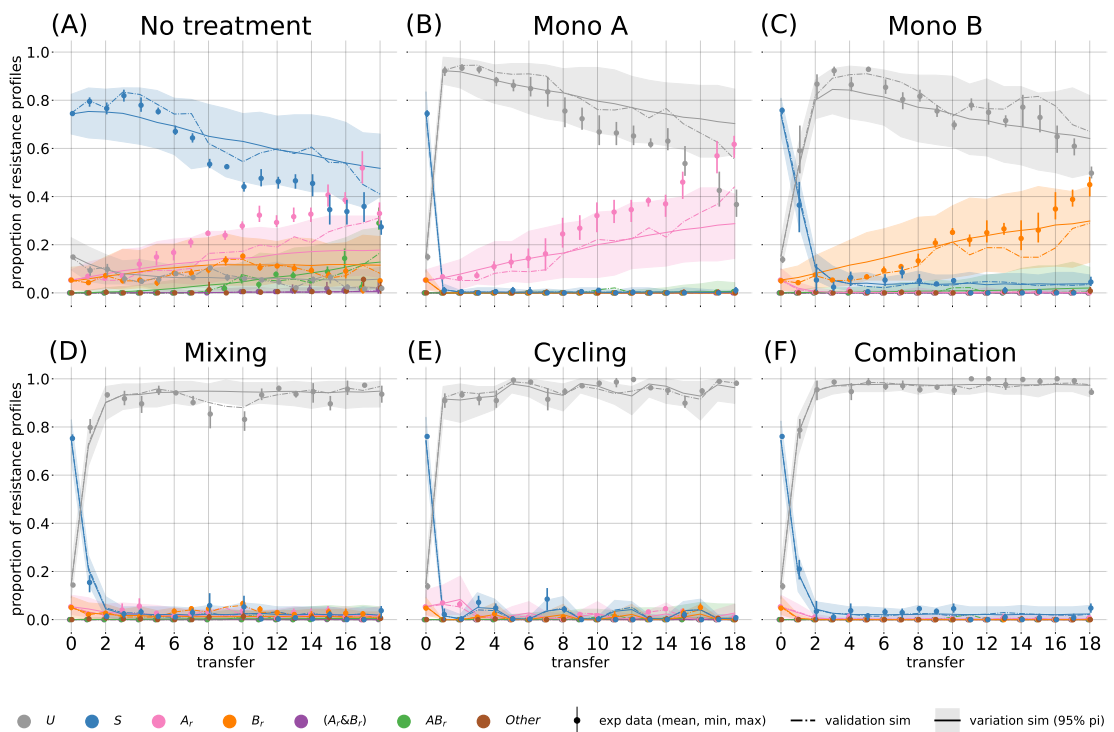


Fig. A7 – **Prevention scenario with filtered transition probabilities.** Frequencies of resistance profiles (colours) over time during the *prevention* scenario. The dots show the experimental measurements, and the error bar indicates the min/max interval between the replicates. The dash-dotted line shows the mean value of 100 stochastic simulations based on the instruction set used in the *in vitro* experiment. The solid line represents the mean value of 100 simulations with randomly created instruction sets based on the parameter set used in the experiment. The shaded error band indicates the 95-percentile interval between the simulations.

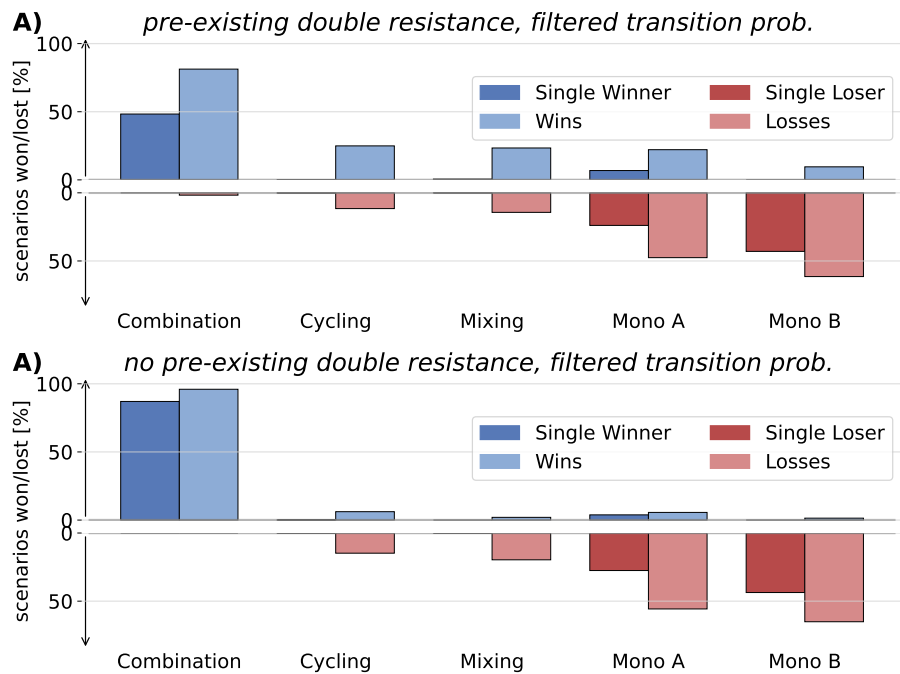


Fig. A8 – Sensitivity analysis using filtered transition probabilities. We evaluated the effectiveness of the five treatment strategies in maximising the frequency of uninfected *in silico* patients across randomly generated parameter sets. Strategies not significantly better than any other are marked as losers (pastel red), with those significantly worse than all others being labelled as single losers (dark red). Conversely, strategies that are not significantly worse than any other are classified as winners (pastel blue), and those significantly better than all others as single winners (dark blue). **(A)** Evaluation of 10,000 parameter sets with preexisting double resistance. 659 out of 10,000 parameter sets yielded no significant difference between the strategies. **(B)** Evaluation of 10,000 parameter sets without preexisting double resistance. 8 out of 10,000 parameter sets yielded no significant difference between the strategies.

Table A1 – Number of superinfections ( $N_{\mathcal{S}}$ ) between high- and low-concentrated  $A_r$  and  $B_r$  wells and the number of double resistances that emerged ( $N_{\mathcal{E}}$ ) under treatment  $\vartheta$  across all three experiments.

Treatment $\vartheta$	$A_r^x$	$B_r^x$	$N_{\mathcal{E}}^\vartheta$	$N_{\mathcal{S}}^\vartheta$	$\frac{N_{\mathcal{E}}^\vartheta}{N_{\mathcal{S}}^\vartheta}$
A	$A_r^h$	$B_r^h$	55	399	0.14
AB	$A_r^h$	$B_r^h$	2	35	0.06
B	$A_r^h$	$B_r^h$	257	322	0.8
none	$A_r^h$	$B_r^h$	390	420	0.93
A	$A_r^h$	$B_r^l$	0	1	0.0
A	$A_r^l$	$B_r^h$	0	13	0.0
AB	$A_r^l$	$B_r^h$	0	15	0.0
B	$A_r^l$	$B_r^h$	0	15	0.0

Table A2 – Strains used in this study and their relevant phenotypes. The phenotype in brackets is conferred by the respective plasmid. Cm<sup>R</sup>: Chloramphenicol resistance, Amp<sup>R</sup>: Ampicillin resistance, Caz<sup>R</sup>: Ceftazidime resistance, Tet<sup>R</sup>: Tetracycline resistance.

Name	Relevant phenotype	Reference
<i>Escherichia coli</i> MDS42-YFP	Cm <sup>R</sup>	[3]
A-resistant	Cm <sup>R</sup> pA (Amp <sup>R</sup> , Caz <sup>R</sup> )	this study, [2]
B-resistant	Cm <sup>R</sup> pB (Amp <sup>R</sup> , Tet <sup>R</sup> )	this study, [2]
AB-resistant	Cm <sup>R</sup> pA (Amp <sup>R</sup> , Caz <sup>R</sup> ) pB (Amp <sup>R</sup> , Tet <sup>R</sup> )	this study, [2]

Table A3 – Statistical comparison of maximum growth rates between the sensitive and plasmid-carrying strains. We used a Mann-Whitney U test for pairwise comparisons, and the p-values were adjusted using the Bonferroni correction.

Comparison	U-statistic	P-value	Cor. P-value	Sig. after Bonferroni
sensitive vs A-resistant	9.000000	0.100000	0.300000	False
sensitive vs B-resistant	3.000000	0.700000	1.000000	False
sensitive vs double-resistant	5.000000	1.000000	1.000000	False

Table A4 – Plasmid segregation loss was estimated over 24 hours without treatment and with selective treatment as a control. Frequencies of plasmid retention were compared between  $t_0$  –  $t_1$  using the Mann-Whitney U test. Confidence intervals and the mean frequencies were estimated by bootstrapping the binary data (plasmid retained or lost) pooled across replicates. No significant plasmid loss was observed in either the main data or the control.

plasmids	$f(t_0)$	$CI(t_0)$	$f(t_1)$	$CI(t_1)$	$p\text{-val}$	$f(t_1)$ ctrl	$CI(t_1)$ ctrl	$p\text{-value}$ ctrl
$p_A$	1.00	(1.0, 1.0)	1.00	(1.0, 1.0)	1.00	1.00	(1.0, 1.0)	1.00
$p_B$	1.00	(1.0, 1.0)	0.97	(0.93, 1.0)	0.20	1.00	(1.0, 1.0)	1.00
$p_A \& p_B$	0.99	(0.97, 1.0)	1.00	(1.0, 1.0)	0.50	1.00	(1.0, 1.0)	0.50

Table A5 – 95 % confidence intervals for the final bacterial density measured by colony plating and the maximal growth rates measured by evaluating OD-growth curves.

strain	antibiotic	cmp [ $\mu\text{g}/\text{ml}$ ]	cfu [1/ $\mu\text{l}$ ]	growthrate [1/h]
double-resistant	AB	5	$(2.14 - 3.33) \times 10^5$	(0.43 – 0.86)
double-resistant	AB	25	$(2.68 - 3.99) \times 10^5$	(0.4 – 0.85)
A-resistant	A	5	$(1.58 - 2.62) \times 10^5$	(0.51 – 0.7)
A-resistant	A	25	$(2.05 - 3.21) \times 10^5$	(0.46 – 0.71)
sensitive	None	5	$(1.03 - 1.27) \times 10^6$	(0.68 – 0.74)
sensitive	None	25	$(1.15 - 1.4) \times 10^6$	(0.55 – 0.96)
B-resistant	B	5	$(4.05 - 5.62) \times 10^5$	(0.45 – 0.74)
B-resistant	B	25	$(3.53 - 5.01) \times 10^5$	(0.4 – 0.87)

Table A6 – Definition of resistance profiles (rows) by growth patterns on differently treated agar plates (columns). X indicates colony formation, whereas o indicates no growth.

	None	A	B	AB
U	o	o	o	o
S	X	o	o	o
$A_r$	X	X	o	o
$B_r$	X	o	X	o
$(A_r \& B_r)$	X	X	X	o
$AB_r$	X	X	X	X

Table A7 – Association between bacterial phenotypes (rows) and resistance profiles  $\phi$  (columns). An 'X' denotes that a phenotype is obligatory for a given profile, while a '✓' indicates that it is optional.

	U	S	$A_r$	$B_r$	$(A_r \& B_r)$	$AB_r$
sensitive	X	✓	✓	✓	✓	
A-resistant		X		X		✓
B-resistant			X	X		✓
double-resistant						X

Table A8 – Clearance probability of well phenotypes across the three experiments.

	S	$A_r$	$B_r$
A	0.97	0.02	0.98
B	0.73	0.62	0.01
AB	0.86	0.4	0.98

Table A9 – **Mixing rules.** During the plate-handling phase, we mix wells due to infections. The resulting phenotype of the two mixed wells can be calculated using this table. More than two phenotypes can be combined by applying associative logic.

$\phi_1(\hat{T}) \backslash \phi_2(\hat{T})$	U	S	$A_r$	$B_r$	$(A_r \& B_r)$	$AB_r$
U	U	S	$A_r$	$B_r$	$(A_r \& B_r)$	$AB_r$
S	S	S	$A_r$	$B_r$	$(A_r \& B_r)$	$AB_r$
$A_r$	$A_r$	$A_r$	$A_r$	$(A_r \& B_r)$	$(A_r \& B_r)$	$AB_r$
$B_r$	$B_r$	$B_r$	$(A_r \& B_r)$	$B_r$	$(A_r \& B_r)$	$AB_r$
$(A_r \& B_r)$	$(A_r \& B_r)$	$(A_r \& B_r)$	$(A_r \& B_r)$	$(A_r \& B_r)$	$(A_r \& B_r)$	$AB_r$
$AB_r$	$AB_r$	$AB_r$	$AB_r$	$AB_r$	$AB_r$	$AB_r$

Table A10 – Mean parameter leading to  $n$  single wins during the sensitivity analysis without preexisting double resistance. Strategies that did not yield at least one single win were excluded.

	turnover	infection	U	S	A_r	B_r	AB_r	n
Combination	0.50	0.50	0.26	0.24	0.24	0.25	0.00	9311.00
Mono A	0.80	0.27	0.26	0.29	0.37	0.08	0.00	56.00
Cycling	0.10	0.39	0.33	0.42	0.14	0.10	0.00	4.00
Mixing	0.11	0.33	0.12	0.49	0.38	0.01	0.00	1.00

Table A11 – Mean parameter leading to  $n$  single losses during the sensitivity analysis without preexisting double resistance. Strategies that did not yield at least one single loss were excluded.

	turnover	infection	U	S	A_r	B_r	AB_r	n
Mono B	0.60	0.43	0.26	0.25	0.16	0.33	0.00	4132.00
Mono A	0.55	0.43	0.27	0.25	0.36	0.12	0.00	2648.00
Cycling	0.07	0.87	0.28	0.34	0.27	0.11	0.00	8.00
Mixing	0.07	0.90	0.69	0.25	0.01	0.05	0.00	1.00

Table A12 – Mean parameter leading to  $n$  single wins during the sensitivity analysis with preexisting double resistance. Strategies that did not yield at least one single win were excluded.

	turnover	infection	U	S	A_r	B_r	AB_r	n
Combination	0.61	0.47	0.21	0.18	0.22	0.22	0.17	5487.00
Mono A	0.52	0.56	0.23	0.20	0.16	0.15	0.26	365.00
Mixing	0.13	0.30	0.23	0.21	0.18	0.15	0.22	40.00
Cycling	0.14	0.20	0.23	0.20	0.21	0.20	0.16	9.00

Table A13 – Mean parameter leading to  $n$  single losses during the sensitivity analysis with preexisting double resistance. Strategies that did not yield at least one single loss were excluded.

	turnover	infection	U	S	A_r	B_r	AB_r	n
Mono B	0.57	0.46	0.21	0.19	0.13	0.28	0.18	4250.00
Mono A	0.51	0.43	0.23	0.19	0.30	0.10	0.18	2359.00
Cycling	0.42	0.72	0.23	0.21	0.14	0.14	0.28	6.00
Mixing	0.34	0.71	0.23	0.20	0.18	0.09	0.30	2.00

APPENDIX A. THE IMPACT OF TREATMENT STRATEGIES ON THE EPIDEMIOLOGICAL DYNAMICS OF PLASMID-CONFERRED ANTIBIOTIC RESISTANCE

---

Table A14 – Wins and losses during the sensitivity analysis. With preexisting double resistance. 606 parameter sets yielded an insignificant result.

strategy	single winner [%]	single loser [%]	loser [%]	winner [%]	single winner	single loser	loser	winner
Combination	54.87	0.00	0.95	86.76	5487	0	95	8676
Cycling	0.09	0.06	12.10	23.32	9	6	1210	2332
Mixing	0.40	0.02	14.78	20.54	40	2	1478	2054
Mono A	3.65	23.59	48.57	17.49	365	2359	4857	1749
Mono B	0.00	42.50	62.29	8.11	0	4250	6229	811

Table A15 – Wins and losses during the sensitivity analysis without preexisting double resistance. 100 parameter sets yielded an insignificant result.

strategy	single winner [%]	single loser [%]	loser [%]	winner [%]	single winner	single loser	loser	winner
Combination	93.11	0.00	0.00	98.35	9311	0	0	9835
Cycling	0.04	0.08	18.89	3.49	4	8	1889	349
Mixing	0.01	0.01	22.05	1.32	1	1	2205	132
Mono A	0.56	26.48	57.03	1.65	56	2648	5703	165
Mono B	0.00	41.32	63.44	1.11	0	4132	6344	111

Table A16 – Wins and losses during the sensitivity analysis, using filtered transition probabilities and preexisting double resistance. 659 parameter sets yielded an insignificant result.

strategy	single winner [%]	single loser [%]	loser [%]	winner [%]	single winner	single loser	loser	winner
Combination	48.31	0.00	1.72	81.27	4831	0	172	8127
Cycling	0.07	0.10	11.57	24.94	7	10	1157	2494
Mixing	0.59	0.03	14.34	23.40	59	3	1434	2340
Mono A	6.85	23.91	47.57	22.15	685	2391	4757	2215
Mono B	0.00	42.97	61.45	9.57	0	4297	6145	957

Table A17 – Wins and losses during the sensitivity analysis with filtered transition matrices and no preexisting double resistance. 8 parameter sets yielded an insignificant result.

strategy	single winner [%]	single loser [%]	loser [%]	winner [%]	single winner	single loser	loser	winner
Combination	87.04	0.00	0.00	95.98	8704	0	0	9598
Cycling	0.08	0.06	14.80	6.16	8	6	1480	616
Mixing	0.00	0.04	19.66	2.00	0	4	1966	200
Mono A	3.82	27.53	55.71	5.62	382	2753	5571	562
Mono B	0.00	43.67	65.10	1.41	0	4367	6510	141

Table A18 –  $M^{\text{none}}$ . Unfiltered transition matrix for untreated wells.

$\phi(\hat{T})$	$\phi(T)$					
$\phi(\hat{T})$	U	S	$A_r$	$B_r$	$(A_r \& B_r)$	$AB_r$
U	0.97	0.0	0.0	0.0	0.0	0.0
S	0.03	0.98	0.01	0.02	0.01	0.01
$A_r$	0.0	0.01	0.96	0.0	0.07	0.03
$B_r$	0.0	0.01	0.0	0.97	0.02	0.0
$(A_r \& B_r)$	0.0	0.0	0.01	0.01	0.08	0.04
$AB_r$	0.0	0.0	0.02	0.0	0.82	0.92

Table A19 –  $M^A$ . Unfiltered transition matrix for wells treated with antibiotic A.

$\phi(\hat{T})$	$\phi(T)$					
$\phi(\hat{T})$	U	S	$A_r$	$B_r$	$(A_r \& B_r)$	$AB_r$
U	0.99	0.96	0.02	0.97	0.03	0.02
S	0.0	0.02	0.0	0.01	0.0	0.0
$A_r$	0.01	0.02	0.98	0.01	0.59	0.01
$B_r$	0.0	0.0	0.0	0.01	0.0	0.0
$(A_r \& B_r)$	0.0	0.0	0.0	0.0	0.18	0.01
$AB_r$	0.0	0.0	0.0	0.0	0.2	0.96

Table A20 –  $M^B$ . Unfiltered transition matrix for wells treated with antibiotic B.

$\phi(\hat{T})$	$\phi(T)$					
$\phi(\hat{T})$	U	S	$A_r$	$B_r$	$(A_r \& B_r)$	$AB_r$
U	0.99	0.8	0.63	0.01	0.03	0.02
S	0.0	0.19	0.18	0.0	0.0	0.0
$A_r$	0.0	0.0	0.18	0.0	0.0	0.0
$B_r$	0.01	0.01	0.0	0.98	0.21	0.0
$(A_r \& B_r)$	0.0	0.0	0.0	0.0	0.03	0.0
$AB_r$	0.0	0.0	0.01	0.01	0.73	0.98

Table A21 –  $M^{AB}$ . Unfiltered transition matrix for wells treated with antibiotic AB.

$\phi(\hat{T})$	$\phi(T)$					
$\phi(\hat{T})$	U	S	$A_r$	$B_r$	$(A_r \& B_r)$	$AB_r$
U	1.0	0.9	0.49	0.98	1.0	0.02
S	0.0	0.1	0.32	0.02	0.0	0.0
$A_r$	0.0	0.0	0.19	0.0	0.0	0.0
$B_r$	0.0	0.0	0.0	0.0	0.0	0.0
$(A_r \& B_r)$	0.0	0.0	0.0	0.0	0.0	0.0
$AB_r$	0.0	0.0	0.0	0.0	0.0	0.98

Table A22 –  $M_1^{\text{none}}$ . Unfiltered transition matrix for the first time point in untreated wells.

$\phi(\hat{T})$	$\phi(T)$					
$\phi(\hat{T})$	U	S	$A_r$	$B_r$	$(A_r \& B_r)$	$AB_r$
U	0.96	0.0	0.0	0.0	0.0	0.0
S	0.03	0.99	0.0	0.0	0.0	0.0
$A_r$	0.01	0.01	1.0	0.0	0.0	0.0
$B_r$	0.0	0.0	0.0	1.0	0.17	0.0
$(A_r \& B_r)$	0.0	0.0	0.0	0.0	0.02	0.0
$AB_r$	0.0	0.0	0.0	0.0	0.81	1.0

Table A23 –  $M_1^A$ . Unfiltered transition matrix for the first time point in wells treated with antibiotic A.

$\phi(\hat{T})$	$\phi(T)$					
$\phi(\hat{T})$	U	S	$A_r$	$B_r$	$(A_r \& B_r)$	$AB_r$
U	0.99	0.97	0.0	0.99	0.23	0.0
S	0.0	0.02	0.0	0.01	0.0	0.0
$A_r$	0.01	0.01	1.0	0.0	0.54	0.0
$B_r$	0.0	0.0	0.0	0.0	0.0	0.0
$(A_r \& B_r)$	0.0	0.0	0.0	0.0	0.11	0.0
$AB_r$	0.0	0.0	0.0	0.0	0.12	1.0

Table A24 –  $M_1^B$ . Unfiltered transition matrix for the first time point in wells treated with antibiotic B.

$\phi(\hat{T})$	$\phi(T)$					
$\phi(\hat{T})$	U	S	$A_r$	$B_r$	$(A_r \& B_r)$	$AB_r$
U	1.0	0.48	0.51	0.02	0.01	0.0
S	0.0	0.52	0.21	0.01	0.0	0.0
$A_r$	0.0	0.0	0.28	0.0	0.0	0.0
$B_r$	0.0	0.0	0.0	0.97	0.31	0.0
$(A_r \& B_r)$	0.0	0.0	0.0	0.0	0.1	0.0
$AB_r$	0.0	0.0	0.0	0.0	0.58	1.0

Table A25 –  $M_1^{AB}$ . Unfiltered transition matrix for the first time point in wells treated with antibiotic AB.

$\phi(\hat{T})$	$\phi(T)$					
$\phi(\hat{T})$	U	S	$A_r$	$B_r$	$(A_r \& B_r)$	$AB_r$
U	0.98	0.79	0.32	0.67	0.24	0.0
S	0.02	0.21	0.21	0.24	0.21	0.0
$A_r$	0.0	0.0	0.47	0.0	0.41	0.0
$B_r$	0.0	0.0	0.0	0.09	0.02	0.0
$(A_r \& B_r)$	0.0	0.0	0.0	0.0	0.07	0.0
$AB_r$	0.0	0.0	0.0	0.0	0.05	1.0

Table A26 –  $M^{\text{none}}$ . Filtered transition matrix for untreated wells.

$\phi(\hat{T})$	$\phi(T)$					
	$U$	$S$	$A_r$	$B_r$	$(A_r \& B_r)$	$AB_r$
$U$	1.0	0.0	0.0	0.0	0.0	0.0
$S$	0.0	1.0	0.01	0.02	0.01	0.01
$A_r$	0.0	0.0	0.99	0.0	0.07	0.03
$B_r$	0.0	0.0	0.0	0.98	0.02	0.0
$(A_r \& B_r)$	0.0	0.0	0.0	0.0	0.08	0.04
$AB_r$	0.0	0.0	0.0	0.0	0.82	0.92

Table A27 –  $M^A$ . Filtered transition matrix for wells treated with antibiotic A.

$\phi(\hat{T})$	$\phi(T)$					
	$U$	$S$	$A_r$	$B_r$	$(A_r \& B_r)$	$AB_r$
$U$	1.0	0.98	0.02	0.98	0.03	0.02
$S$	0.0	0.02	0.0	0.01	0.0	0.0
$A_r$	0.0	0.0	0.98	0.0	0.59	0.01
$B_r$	0.0	0.0	0.0	0.01	0.0	0.0
$(A_r \& B_r)$	0.0	0.0	0.0	0.0	0.18	0.01
$AB_r$	0.0	0.0	0.0	0.0	0.2	0.96

Table A28 –  $M^B$ . Filtered transition matrix for wells treated with antibiotic B.

$\phi(\hat{T})$	$\phi(T)$					
	$U$	$S$	$A_r$	$B_r$	$(A_r \& B_r)$	$AB_r$
$U$	1.0	0.8	0.64	0.01	0.03	0.02
$S$	0.0	0.2	0.18	0.0	0.0	0.0
$A_r$	0.0	0.0	0.18	0.0	0.0	0.0
$B_r$	0.0	0.0	0.0	0.99	0.21	0.0
$(A_r \& B_r)$	0.0	0.0	0.0	0.0	0.03	0.0
$AB_r$	0.0	0.0	0.0	0.0	0.73	0.98

Table A29 –  $M^{AB}$ . Filtered transition matrix for wells treated with antibiotic AB.

$\phi(\hat{T})$	$\phi(T)$					
	$U$	$S$	$A_r$	$B_r$	$(A_r \& B_r)$	$AB_r$
$U$	1.0	0.9	0.49	0.98	1.0	0.02
$S$	0.0	0.1	0.32	0.02	0.0	0.0
$A_r$	0.0	0.0	0.19	0.0	0.0	0.0
$B_r$	0.0	0.0	0.0	0.0	0.0	0.0
$(A_r \& B_r)$	0.0	0.0	0.0	0.0	0.0	0.0
$AB_r$	0.0	0.0	0.0	0.0	0.0	0.98

Table A30 –  $M_1^{\text{none}}$ . Filtered transition matrix for the first time point in untreated wells.

$\phi(\hat{T})$	$\phi(T)$					
	$U$	$S$	$A_r$	$B_r$	$(A_r \& B_r)$	$AB_r$
$U$	1.0	0.0	0.0	0.0	0.0	0.0
$S$	0.0	1.0	0.0	0.0	0.0	0.0
$A_r$	0.0	0.0	1.0	0.0	0.0	0.0
$B_r$	0.0	0.0	0.0	1.0	0.17	0.0
$(A_r \& B_r)$	0.0	0.0	0.0	0.0	0.02	0.0
$AB_r$	0.0	0.0	0.0	0.0	0.81	1.0

Table A31 –  $M_1^A$ . Filtered transition matrix for the first time point in wells treated with antibiotic A.

$\phi(\hat{T})$	$\phi(T)$					
	$U$	$S$	$A_r$	$B_r$	$(A_r \& B_r)$	$AB_r$
$U$	1.0	0.98	0.0	0.99	0.23	0.0
$S$	0.0	0.02	0.0	0.01	0.0	0.0
$A_r$	0.0	0.0	1.0	0.0	0.54	0.0
$B_r$	0.0	0.0	0.0	0.0	0.0	0.0
$(A_r \& B_r)$	0.0	0.0	0.0	0.0	0.11	0.0
$AB_r$	0.0	0.0	0.0	0.0	0.12	1.0

Table A32 –  $M_1^B$ . Filtered transition matrix for the first time point in wells treated with antibiotic B.

$\phi(\hat{T})$	$\phi(T)$					
	$U$	$S$	$A_r$	$B_r$	$(A_r \& B_r)$	$AB_r$
$U$	1.0	0.48	0.51	0.02	0.01	0.0
$S$	0.0	0.52	0.21	0.01	0.0	0.0
$A_r$	0.0	0.0	0.28	0.0	0.0	0.0
$B_r$	0.0	0.0	0.0	0.97	0.31	0.0
$(A_r \& B_r)$	0.0	0.0	0.0	0.0	0.1	0.0
$AB_r$	0.0	0.0	0.0	0.0	0.58	1.0

Table A33 –  $M_1^{AB}$ . Filtered transition matrix for the first time point in wells treated with antibiotic AB.

$\phi(\hat{T})$	$\phi(T)$					
	$U$	$S$	$A_r$	$B_r$	$(A_r \& B_r)$	$AB_r$
$U$	1.0	0.79	0.32	0.67	0.24	0.0
$S$	0.0	0.21	0.21	0.24	0.21	0.0
$A_r$	0.0	0.0	0.47	0.0	0.41	0.0
$B_r$	0.0	0.0	0.0	0.09	0.02	0.0
$(A_r \& B_r)$	0.0	0.0	0.0	0.0	0.07	0.0
$AB_r$	0.0	0.0	0.0	0.0	0.05	1.0

Table A34 – *Prevention* scenario: Effect of treatment strategies on the frequency of uninfecteds (ANOVA).

	Sum of Squares	df	Mean Square	F	Sig.
Between Groups	2.833	5	0.567	779.436	< 0.001
Within Groups	0.013	18	< 0.001		
Total	2.846	23			

Table A35 – *Prevention* scenario: Multiple comparison between the effects of treatment strategies on the frequencies of uninfecteds using Tukey's post-hoc analysis.

group1	group2	meandiff	p-adj	lower	upper	reject
Combination	Cycling	-0.027	0.729	-0.087	0.034	False
Combination	Mixing	-0.041	0.317	-0.101	0.020	False
Combination	Mono A	-0.525	0.000	-0.586	-0.465	True
Combination	Mono B	-0.360	0.000	-0.421	-0.300	True
Combination	No treatment	-0.951	0.000	-1.011	-0.890	True
Cycling	Mixing	-0.014	0.975	-0.074	0.047	False
Cycling	Mono A	-0.499	0.000	-0.559	-0.438	True
Cycling	Mono B	-0.334	0.000	-0.394	-0.273	True
Cycling	No treatment	-0.924	0.000	-0.985	-0.864	True
Mixing	Mono A	-0.485	0.000	-0.545	-0.424	True
Mixing	Mono B	-0.320	0.000	-0.380	-0.259	True
Mixing	No treatment	-0.910	0.000	-0.971	-0.850	True
Mono A	Mono B	0.165	0.000	0.104	0.226	True
Mono A	No treatment	-0.425	0.000	-0.486	-0.365	True
Mono B	No treatment	-0.590	0.000	-0.651	-0.530	True

Table A36 – *Prevention* scenario: Effect of treatment strategies on the frequency of single resistance (ANOVA).

	Sum of Squares	df	Mean Square	F	Sig.
Between Groups	1.133	5	0.227	290.494	< 0.001
Within Groups	0.014	18	< 0.001		
Total	1.147	23			

Table A37 – *Prevention* scenario: Multiple comparison between the effects of treatment strategies on the frequencies of single resistance using Tukey's post-hoc analysis.

group1	group2	meandiff	p-adj	lower	upper	reject
Combination	Cycling	0.030	0.659	-0.033	0.093	False
Combination	Mixing	0.035	0.518	-0.028	0.097	False
Combination	Mono A	0.501	0.000	0.438	0.563	True
Combination	Mono B	0.359	0.000	0.296	0.422	True
Combination	No treatment	0.479	0.000	0.417	0.542	True
Cycling	Mixing	0.005	1.000	-0.058	0.067	False
Cycling	Mono A	0.471	0.000	0.408	0.533	True
Cycling	Mono B	0.329	0.000	0.266	0.392	True
Cycling	No treatment	0.450	0.000	0.387	0.512	True
Mixing	Mono A	0.466	0.000	0.403	0.529	True
Mixing	Mono B	0.325	0.000	0.262	0.387	True
Mixing	No treatment	0.445	0.000	0.382	0.508	True
Mono A	Mono B	-0.142	0.000	-0.204	-0.079	True
Mono A	No treatment	-0.021	0.884	-0.084	0.042	False
Mono B	No treatment	0.120	0.000	0.058	0.183	True

Table A38 – *Prevention* scenario: Effect of treatment strategies on the frequency of double resistance (ANOVA).

	Sum of Squares	df	Mean Square	F	Sig.
Between Groups	0.061	5	0.012	157.486	< 0.001
Within Groups	0.001	18	< 0.001		
Total	0.063	23			

Table A39 – *Prevention* scenario: Effect of treatment strategies on the frequency of double resistance (ANOVA).

group1	group2	meandiff	p-adj	lower	upper	reject
Combination	Cycling	0.000	1.000	-0.020	0.020	False
Combination	Mixing	0.003	0.998	-0.017	0.022	False
Combination	Mono A	0.002	1.000	-0.018	0.022	False
Combination	Mono B	0.000	1.000	-0.020	0.020	False
Combination	No treatment	0.136	0.000	0.117	0.156	True
Cycling	Mixing	0.003	0.998	-0.017	0.022	False
Cycling	Mono A	0.002	1.000	-0.018	0.022	False
Cycling	Mono B	0.000	1.000	-0.020	0.020	False
Cycling	No treatment	0.136	0.000	0.117	0.156	True
Mixing	Mono A	-0.001	1.000	-0.021	0.019	False
Mixing	Mono B	-0.003	0.998	-0.022	0.017	False
Mixing	No treatment	0.134	0.000	0.114	0.153	True
Mono A	Mono B	-0.002	1.000	-0.022	0.018	False
Mono A	No treatment	0.134	0.000	0.115	0.154	True
Mono B	No treatment	0.136	0.000	0.117	0.156	True

Table A40 – *Containment* scenario: Effect of treatment strategies on the frequency of uninfecteds (ANOVA).

	Sum of Squares	df	Mean Square	F	Sig.
Between Groups	0.639	5	0.128	28.906	< 0.001
Within Groups	0.080	18	0.004		
Total	0.718	23			

Table A41 – *Containment* scenario: Multiple comparison between the effects of treatment strategies on the frequencies of uninfecteds using Tukey's post-hoc analysis.

group1	group2	meandiff	p-adj	lower	upper	reject
Combination	Cycling	-0.008	1.000	-0.157	0.141	False
Combination	Mixing	-0.041	0.951	-0.190	0.109	False
Combination	Mono A	-0.104	0.282	-0.253	0.046	False
Combination	Mono B	-0.158	0.034	-0.308	-0.009	True
Combination	No treatment	-0.474	0.000	-0.623	-0.325	True
Cycling	Mixing	-0.033	0.980	-0.182	0.117	False
Cycling	Mono A	-0.096	0.361	-0.245	0.054	False
Cycling	Mono B	-0.150	0.048	-0.300	-0.001	True
Cycling	No treatment	-0.466	0.000	-0.616	-0.317	True
Mixing	Mono A	-0.063	0.758	-0.212	0.086	False
Mixing	Mono B	-0.118	0.175	-0.267	0.032	False
Mixing	No treatment	-0.433	0.000	-0.583	-0.284	True
Mono A	Mono B	-0.054	0.850	-0.204	0.095	False
Mono A	No treatment	-0.370	0.000	-0.520	-0.221	True
Mono B	No treatment	-0.316	0.000	-0.465	-0.166	True

Table A42 – *Containment* scenario: Effect of treatment strategies on the frequency of single resistance (ANOVA).

	Sum of Squares	df	Mean Square	F	Sig.
Between Groups	0.129	5	0.026	40.881	< 0.001
Within Groups	0.011	18	< 0.001		
Total	0.140	23			

Table A43 – *Containment* scenario: Multiple comparison between the effects of treatment strategies on the frequencies of single resistance using Tukey's post-hoc analysis.

group1	group2	meandiff	p-adj	lower	upper	reject
Combination	Cycling	0.019	0.895	-0.038	0.075	False
Combination	Mixing	0.054	0.067	-0.003	0.110	False
Combination	Mono A	0.197	0.000	0.140	0.253	True
Combination	Mono B	0.102	0.000	0.045	0.158	True
Combination	No treatment	0.169	0.000	0.112	0.225	True
Cycling	Mixing	0.035	0.389	-0.021	0.092	False
Cycling	Mono A	0.178	0.000	0.122	0.235	True
Cycling	Mono B	0.083	0.002	0.027	0.140	True
Cycling	No treatment	0.150	0.000	0.094	0.207	True
Mixing	Mono A	0.143	0.000	0.086	0.199	True
Mixing	Mono B	0.048	0.125	-0.009	0.104	False
Mixing	No treatment	0.115	0.000	0.059	0.172	True
Mono A	Mono B	-0.095	0.001	-0.152	-0.039	True
Mono A	No treatment	-0.028	0.626	-0.084	0.029	False
Mono B	No treatment	0.067	0.015	0.011	0.124	True

Table A44 – *Containment* scenario: Effect of treatment strategies on the frequency of double resistance (ANOVA).

	Sum of Squares	df	Mean Square	F	Sig.
Between Groups	0.038	5	0.008	1.169	0.362
Within Groups	0.116	18	0.006		
Total	0.154	23			

Table A45 – *Maximum-emergence* scenario: Effect of treatment strategies on the frequency of uninfecteds (ANOVA).

	Sum of Squares	df	Mean Square	F	Sig.
Between Groups	1.432	5	0.286	383.054	< 0.001
Within Groups	0.013	18	< 0.001		
Total	1.445	23			

Table A46 – *Maximum-emergence* scenario: Multiple comparison between the effects of treatment strategies on the frequencies of uninfecteds using Tukey's post-hoc analysis.

group1	group2	meandiff	p-adj	lower	upper	reject
Combination	Cycling	-0.306	0.000	-0.368	-0.245	True
Combination	Mixing	-0.386	0.000	-0.447	-0.324	True
Combination	Mono A	-0.414	0.000	-0.476	-0.353	True
Combination	Mono B	-0.499	0.000	-0.561	-0.438	True
Combination	No treatment	-0.823	0.000	-0.885	-0.762	True
Cycling	Mixing	-0.079	0.008	-0.141	-0.018	True
Cycling	Mono A	-0.108	0.000	-0.169	-0.046	True
Cycling	Mono B	-0.193	0.000	-0.254	-0.131	True
Cycling	No treatment	-0.517	0.000	-0.578	-0.455	True
Mixing	Mono A	-0.029	0.681	-0.090	0.033	False
Mixing	Mono B	-0.114	0.000	-0.175	-0.052	True
Mixing	No treatment	-0.438	0.000	-0.499	-0.376	True
Mono A	Mono B	-0.085	0.004	-0.146	-0.024	True
Mono A	No treatment	-0.409	0.000	-0.470	-0.347	True
Mono B	No treatment	-0.324	0.000	-0.385	-0.262	True

Table A47 – *Maximum-emergence* scenario: Effect of treatment strategies on the frequency of single resistance (ANOVA).

	Sum of Squares	df	Mean Square	F	Sig.
Between Groups	1.311	5	0.262	524.241	< 0.001
Within Groups	0.009	18	< 0.001		
Total	1.320	23			

Table A48 – *Maximum-emergence* scenario: Multiple comparison between the effects of treatment strategies on the frequencies of single resistance using Tukey's post-hoc analysis.

group1	group2	meandiff	p-adj	lower	upper	reject
Combination	Cycling	0.342	0.000	0.292	0.393	True
Combination	Mixing	0.408	0.000	0.358	0.459	True
Combination	Mono A	0.549	0.000	0.499	0.600	True
Combination	Mono B	0.536	0.000	0.486	0.586	True
Combination	No treatment	0.761	0.000	0.710	0.811	True
Cycling	Mixing	0.066	0.006	0.016	0.116	True
Cycling	Mono A	0.207	0.000	0.157	0.257	True
Cycling	Mono B	0.194	0.000	0.143	0.244	True
Cycling	No treatment	0.418	0.000	0.368	0.469	True
Mixing	Mono A	0.141	0.000	0.091	0.191	True
Mixing	Mono B	0.128	0.000	0.077	0.178	True
Mixing	No treatment	0.352	0.000	0.302	0.403	True
Mono A	Mono B	-0.013	0.956	-0.064	0.037	False
Mono A	No treatment	0.211	0.000	0.161	0.262	True
Mono B	No treatment	0.225	0.000	0.174	0.275	True

Table A49 – *Maximum-emergence* scenario: Effect of treatment strategies on the frequency of double resistance (ANOVA).

	Sum of Squares	df	Mean Square	F	Sig.
Between Groups	0.109	5	0.022	71.779	< 0.001
Within Groups	0.005	18	< 0.001		
Total	0.115	23			

Table A50 – *Maximum-emergence* scenario: Effect of treatment strategies on the frequency of double resistance (ANOVA).

group1	group2	meandiff	p-adj	lower	upper	reject
Combination	Cycling	0.058	0.002	0.019	0.097	True
Combination	Mixing	0.071	0.000	0.032	0.110	True
Combination	Mono A	0.009	0.980	-0.031	0.048	False
Combination	Mono B	0.069	0.000	0.030	0.108	True
Combination	No treatment	0.206	0.000	0.167	0.245	True
Cycling	Mixing	0.013	0.884	-0.026	0.052	False
Cycling	Mono A	-0.049	0.009	-0.088	-0.010	True
Cycling	Mono B	0.011	0.937	-0.028	0.051	False
Cycling	No treatment	0.148	0.000	0.109	0.188	True
Mixing	Mono A	-0.062	0.001	-0.102	-0.023	True
Mixing	Mono B	-0.002	1.000	-0.041	0.037	False
Mixing	No treatment	0.135	0.000	0.096	0.174	True
Mono A	Mono B	0.060	0.001	0.021	0.100	True
Mono A	No treatment	0.198	0.000	0.158	0.237	True
Mono B	No treatment	0.137	0.000	0.098	0.176	True

Table A51 – *Maximum-emergence* scenario: Effect of treatment strategies on the frequency of newly emerging double resistance (ANOVA).

	Sum of Squares	df	Mean Square	F	Sig.
Between Groups	0.035	5	0.007	41.272	< 0.001
Within Groups	0.010	60	< 0.001		
Total	0.045	65			

Table A52 – *Maximum-emergence* scenario: Multiple comparison between the effects of treatment strategies on the frequencies of newly emerging double resistance using Tukey's post-hoc analysis.

group1	group2	meandiff	p-adj	lower	upper	reject
Combination	Cycling	0.013	0.227	-0.004	0.029	False
Combination	Mixing	0.021	0.004	0.005	0.038	True
Combination	Mono A	0.003	0.990	-0.013	0.020	False
Combination	Mono B	0.024	0.001	0.008	0.041	True
Combination	No treatment	0.070	0.000	0.053	0.086	True
Cycling	Mixing	0.009	0.597	-0.007	0.025	False
Cycling	Mono A	-0.009	0.569	-0.026	0.007	False
Cycling	Mono B	0.012	0.308	-0.005	0.028	False
Cycling	No treatment	0.057	0.000	0.041	0.073	True
Mixing	Mono A	-0.018	0.022	-0.035	-0.002	True
Mixing	Mono B	0.003	0.997	-0.014	0.019	False
Mixing	No treatment	0.048	0.000	0.032	0.065	True
Mono A	Mono B	0.021	0.005	0.004	0.037	True
Mono A	No treatment	0.066	0.000	0.050	0.083	True
Mono B	No treatment	0.045	0.000	0.029	0.062	True

Table A53 – *Maximum-emergence* scenario: Effect of treatment strategies on the frequency of superinfections (ANOVA).

	Sum of Squares	df	Mean Square	F	Sig.
Between Groups	0.019	5	0.004	11.731	< 0.001
Within Groups	0.017	52	< 0.001		
Total	0.036	57			

Table A54 – *Maximum-emergence* scenario: Multiple comparison between the effects of treatment strategies on the frequencies of superinfections using Tukey's post-hoc analysis.

group1	group2	meandiff	p-adj	lower	upper	reject
Combination	Cycling	0.024	0.202	-0.007	0.055	False
Combination	Mixing	0.036	0.015	0.005	0.067	True
Combination	Mono A	0.035	0.021	0.004	0.066	True
Combination	Mono B	0.026	0.160	-0.005	0.057	False
Combination	No treatment	0.068	0.000	0.037	0.099	True
Cycling	Mixing	0.011	0.674	-0.011	0.034	False
Cycling	Mono A	0.010	0.768	-0.013	0.033	False
Cycling	Mono B	0.002	1.000	-0.022	0.025	False
Cycling	No treatment	0.043	0.000	0.021	0.066	True
Mixing	Mono A	-0.001	1.000	-0.024	0.021	False
Mixing	Mono B	-0.010	0.810	-0.033	0.013	False
Mixing	No treatment	0.032	0.001	0.009	0.055	True
Mono A	Mono B	-0.009	0.881	-0.032	0.015	False
Mono A	No treatment	0.033	0.001	0.011	0.056	True
Mono B	No treatment	0.042	0.000	0.019	0.065	True

Table A55 – *Maximum-emergence* scenario: Effect of drug  $\vartheta$  on the frequency of emergence per superinfection (ANOVA).

	Sum of Squares	df	Mean Square	F	Sig.
Between Groups	10.194	3	3.398	143.661	< 0.001
Within Groups	1.443	61	0.024		
Total	11.637	64			

Table A56 – *Maximum-emergence* scenario: Multiple comparison between the effects of drug  $\vartheta$  on the frequencies of emergence per superinfection using Tukey's post-hoc analysis.

group1	group2	meandiff	p-adj	lower	upper	reject
A	AB	-0.082	0.752	-0.300	0.136	False
A	B	0.740	0.000	0.624	0.855	True
A	none	0.857	0.000	0.711	1.002	True
AB	B	0.822	0.000	0.602	1.042	True
AB	none	0.939	0.000	0.701	1.176	True
B	none	0.117	0.174	-0.032	0.266	False

## Bibliography

- [1] .S. Tschudin-Sutter et al. "Prospective validation of cessation of contact precautions for extended-spectrum  $\beta$ -lactamase-producing *Escherichia coli*1". In: *Emerg. Infect. Dis.* 22.6 (2016), pp. 1094–1097. issn: 10806059. doi: 10.3201/eid2206.150554.
- [2] J. S. Huisman et al. "The effect of sequencing and assembly on the inference of horizontal gene transfer on chromosomal and plasmid phylogenies". In: *Philos. Trans. R. Soc. B Biol. Sci.* 377.1861 (2022). issn: 14712970. doi: 10.1098/rstb.2021.0245.
- [3] .T. Fehér et al. "Competition between transposable elements and mutator genes in bacteria". In: *Mol. Biol. Evol.* 29 (2012), pp. 3153–3159. issn: 0737-4038. doi: 10.1093/molbev/mss122.
- [4] .A. Carattoli et al. "Identification of plasmids by PCR-based replicon typing". In: *J. Microbiol. Methods* 63.3 (2005), pp. 219–228. issn: 01677012. doi: 10.1016/j.mimet.2005.03.018.
- [5] J. S. Huisman et al. "Estimating plasmid conjugation rates: A new computational tool and a critical comparison of methods". In: *Plasmid* 121.September 2021 (2022), p. 102627. issn: 10959890. doi: 10.1016/j.plasmid.2022.102627. url: <https://doi.org/10.1016/j.plasmid.2022.102627>.
- [6] .P. Virtanen et al. "SciPy 1.0: fundamental algorithms for scientific computing in Python". In: *Nat. Methods* 17.3 (2020), pp. 261–272. issn: 15487105. doi: 10.1038/s41592-019-0686-2. arXiv: 1907.10121.
- [7] .S. Seabold and J. Perktold. "Statsmodels: Econometric and Statistical Modeling with Python". In: *Proc. 9th Python Sci. Conf.* 2010, pp. 92–96. doi: 10.25080/majora-92bf1922-011.
- [8] J. E. Cates, R. Christie, and L. P. Garrod. "Penicillin-resistant subacute bacterial endocarditis treated by a combination of penicillin and streptomycin". In: *Br. Med. J.* 31.11 (1951), pp. 1120–1120. doi: 10.1136/bmj.1.4708.653.
- [9] .E. Jawetz, J. B. Gunisson, and V. R. Coleman. "Observations on the mode of action of Synergism and Antagonism". In: *Antibiot. Annu.* 5 (1954), pp. 520–528. issn: 05703131.
- [10] .P. S. Ocampo et al. "Antagonism between bacteriostatic and bactericidal antibiotics is prevalent". In: *Antimicrob. Agents Chemother.* 58.8 (2014), pp. 4573–4582. issn: 1098-6596. doi: 10.1128/AAC.02463-14.
- [11] .S. A. Angermayr et al. "Growth-mediated negative feedback shapes quantitative antibiotic response". In: *Mol. Syst. Biol.* 18.9 (2022), pp. 1–19. issn: 1744-4292. doi: 10.15252/msb.202110490.



## **Appendix B**

### High-Throughput Quantification of Population Dynamics using Luminescence

---

**Authors:** Malte Muetter<sup>a</sup>, Daniel C. Angst<sup>a</sup>, Roland R. Regoes<sup>a</sup>, Sebastian Bonhoeffer<sup>a</sup>

<sup>a</sup>*Institute of Integrative Biology, Department for Environmental System Science, ETH Zurich, 8092 Zurich, Switzerland*

---

*Supplementary Information*

## B1 Mathematical descriptions

**Light-related terminology.** In this manuscript, *total luminosity* ( $L$ ) refers to the total light output produced by  $B$  bacteria of a *bioluminescent* bacterial culture in a well with volume  $V_w$ . During the *luminescence assays*, we capture a fraction  $\kappa$  of the total luminosity ( $\phi B$ ) as light intensity  $I(t) = \kappa \phi B$ . We call the exponential decline rates based on these intensities *luminescence-based rates*,  $\psi_I$ . We use *cell-specific luminosity* ( $\phi$ ) for light output per cell and *volume-specific luminosity* ( $\theta$ ) for light output per unit cell volume. When  $I(t)$  is normalized by the measured optical density, we obtain  $\omega$ , the *OD-normalized light intensity*.  $J(t)$  is the light intensity  $I(t)$  adjusted by the relative change in cell volume  $\frac{v_0}{v(t)}$ .

**Testing for linearity between bacterial density and luminescent light intensity.** To test whether bacterial density and bacterial luminescent light intensity are linearly related, we grew three replicate overnight cultures. To replenish nutrients, we diluted each culture 1:10 in fresh LB medium and incubated for 60 minutes. We subsequently performed a 10-fold dilution series in a 384-well white plate (Greiner, 781073) and immediately measured the light intensity (see Fig. 1 in the main text). Each plate included wells containing only medium to determine a blank (median  $\approx 37.33$  rlu), which we subtracted from all measurements.

We assessed linearity between light intensity ( $I$ ) and bacterial density ( $b$ ) by fitting a linear model without intercept on the original scale,

$$I_i = m \cdot b_i,$$

which corresponds to a log-log regression with intercept:

$$\ln(I_i) = \ln(m) + \ln(b_i).$$

Summing over all  $n$  observations gives

$$n \ln(m) = \sum_{i=1}^n \ln(I_i) - \sum_{i=1}^n \ln(b_i),$$

The optimal conversion factor  $m$  is then

$$m = \frac{\left(\prod_{i=1}^n I_i\right)^{\frac{1}{n}}}{\left(\prod_{i=1}^n b_i\right)^{\frac{1}{n}}},$$

yielding  $m = 0.006 \frac{\text{rlu ml}}{\text{CFU}}$ .

We observed a linear relationship ( $R^2 = 0.987$ ,  $F = 1164.14$ ,  $p < 10^{-14}$ ) between bacterial density and light intensity for intensities above 20 rlu ( $\sim 3 \times 10^2$  CFU/ml). Consequently, we use 20 rlu as the lower detection limit for luminescence. Additionally, we conclude that  $\kappa$  is independent of the bacterial density (no overshadowing effects), within the relevant range of densities. Since the plate reader setup remains constant within an experiment, we assume  $\kappa$  to be constant for following analyses.

**Rate of change of CFU count.** To infer the rate of change of CFU, we assume bacteria spend only a short time in the low-nutrient dilution medium, so replication and death are negligible during that phase.

Most colonies originate from clusters only comprising a single cell, but some from founding clusters of multiple cells. Let  $f(n)$  be the probability that a randomly chosen cluster contains  $n$  bacteria. A cluster of size  $n$  forms a colony with probability

$$1 - (p_E)^n, \quad (\text{B1})$$

where  $p_E$  is the probability that a lineage originating from a single bacterium goes extinct (extinction probability). The mean probability that a plated cluster forms a colony is:

$$\bar{g} = \sum_{n=1}^N f(n) (1 - (p_E)^n). \quad (\text{B2})$$

The mean cluster size is

$$\bar{n} = \sum_{n=1}^N n f(n). \quad (\text{B3})$$

The mean number of colonies emerging per plated bacterium can be approximated by:

$$\eta = \frac{\bar{g}}{\bar{n}}, \quad \eta \in [0, 1]. \quad (\text{B4})$$

The predicted CFU per ml given a bacterial density  $b = \frac{B}{V_w}$ , with  $B$  the number of bacteria per well and  $V_w$  the constant well volume, is:

$$\text{CFU} = \eta \frac{B}{V_w}. \quad (\text{B5})$$

Taking the logarithmic derivative yields:

$$\psi_{\text{CFU}} = \frac{d}{dt} \ln(\text{CFU}) = \frac{d}{dt} \ln(\eta) + \frac{d}{dt} \ln(B). \quad (\text{B6})$$

In practice  $\eta$  is often unknown. We can only estimate  $\psi_B$  from CFU data if we assume that  $\eta$  is constant over time.

$$\psi_{\text{CFU}} = \frac{d}{dt} \ln(B) = \psi_B. \quad (\text{B7})$$

To justify a constant  $\eta$  we must assume that the cluster-size distribution  $f(n)$  and the extinction probability  $p_E$  do not change over time. Both assumptions may fail, for example if cells filament or if the division or death rate change. We discuss the behaviour of  $p_E$  below.

**Rate of change of luminescence.** The observed light intensity  $I$  is a fraction  $\kappa$  of the total luminosity ( $\phi B$ ) of a bioluminescent culture, where  $\phi$  is the cell-specific luminosity (the amount of light emitted by one bacterium). The light intensity can thus be written as:

$$I = \kappa\phi B. \quad (\text{B8})$$

The rate of change of light intensity is therefore:

$$\psi_I = \frac{d}{dt} \ln(I) = \frac{d(\ln(\kappa) + \ln(\phi) + \ln(B))}{dt}. \quad (\text{B9})$$

We assume that  $\kappa$  remains constant over time, as we explained above (“Testing for linearity between bacterial density and luminescent light intensity”). If we assume that the cell-specific luminosity  $\phi$  is also constant,  $\psi_I$  equals the rate of bacterial count change  $\psi_B$ , as Equation B9 simplifies to:

$$\psi_I = \frac{d}{dt} \ln(I) = \frac{d}{dt} \ln(B) = \psi_B. \quad (\text{B10})$$

**Rate of change of volume-corrected luminescence.** Alternatively, we can link the measured light intensity to the number of bacteria using the mean cell-specific volume ( $v$ ) and the volume-specific luminosity ( $\theta$ ):

$$I = \kappa\theta v B. \quad (\text{B11})$$

Defining the volume-corrected luminescence as  $J(t) = I(t)v_0/v(t)$ , we can compute its rate of change as:

$$\psi_J = \frac{d(\ln(I \cdot v_0/v))}{dt} = \frac{d(\ln(\kappa) + \ln(v_0) + \ln(\theta) + \ln(B))}{dt}. \quad (\text{B12})$$

If we assume that the volume-specific luminosity  $\theta$  is constant, this estimate equals the rate of change of the number of living bacteria ( $B$ ):

$$\psi_J = \frac{d}{dt} \ln(I \cdot v_0/v) = \frac{d}{dt} \ln(B) = \psi_B. \quad (\text{B13})$$

**Change of light intensity is closer to the rate of change of total cell-volume than to the rate of change of number of bacteria.** We made two empirical observations under all tested drug conditions:

(i) *For the subset of drugs imaged using microscopy, the mean specific cell volume never significantly decreased between the first and second time point:*

$$\frac{d \ln v}{dt} \geq 0 \quad (\text{B14})$$

The rate of change of total cell volume is given by:

$$\psi_V = \frac{d \ln(vB)}{dt} = \frac{d \ln v}{dt} + \psi_B. \quad (\text{B15})$$

From this relation and observation (i), we directly obtain:

$$\boxed{\psi_V \geq \psi_B} \quad (\text{B16})$$

(ii) *The rate of change of volume-corrected light intensity was never significantly lower than the corresponding rate of change of CFU:*

$$\psi_I = \frac{d \ln J}{dt} \geq \psi_{\text{CFU}} \quad (\text{B17})$$

Since we can express the light intensity as  $I = \kappa\theta v B$ , the volume-corrected luminescence rate becomes:

$$\psi_I = \frac{d}{dt} \ln(\kappa\theta v_0 B) = \psi_B + \frac{d \ln \theta}{dt}. \quad (\text{B18})$$

Observation (ii) thus implies:

$$\psi_B + \frac{d \ln \theta}{dt} \geq \psi_{\text{CFU}} \quad (\text{B19})$$

If we make the assumption that the rate of change of CFU equals that of bacterial count ( $\psi_{\text{CFU}} = \psi_B$ ) we obtain:

$$\frac{d \ln \theta}{dt} \geq 0 \quad (\text{B20})$$

Using the rate of change of light intensity we get:

$$\psi_I = \frac{d \ln(\kappa\theta v B)}{dt} = \psi_V + \frac{d \ln \theta}{dt}. \quad (\text{B21})$$

From this relation and Equation B20, we follow:

$$\boxed{\psi_I \geq \psi_V} \quad (\text{B22})$$

Combining Equation B16 and Equation B22 yields:

$$\psi_I \geq \psi_V \geq \psi_B \quad (\text{B23})$$

allowing us to conclude that, during our experiments, the luminescence-based rate is closer to the rate of change of total cell volume (likely identical to the rate of change of biomass) than to the rate of change of bacterial count.

**Colony formation – birth-death Markov Model.** We use a basic birth-death Markov model, as described by [1], [2], [3], and [4], to model the probability that a single plated bacterium creates a colony.

In this model, as in [1],  $P_0(t)$  describes the probability that the population originating from this single bacterium goes extinct by the time  $t$ :

$$P_0(t) = \frac{\delta}{\lambda} \cdot \frac{E(t) - 1}{E(t) - \frac{\delta}{\lambda}}, \quad (\text{B24})$$

where  $\delta$  is the death rate,  $\lambda$  the division rate, and  $E(t) = e^{(\lambda-\delta)t}$ . For  $t \rightarrow \infty$ ,  $P_0(t)$  converges to the extinction probability  $p_E$  for a lineage originating from a single cell.

$$p_E = \begin{cases} 1, & \text{if } \lambda \leq \delta, \\ \frac{\delta}{\lambda}, & \text{if } \lambda > \delta. \end{cases} \quad (\text{B25})$$

**Colony formation for bacteriostatic and bactericidal drugs.** In the following, we call the death and division rate in the absence of treatment  $\delta_0$  and  $\lambda_0$ , respectively, and the treatment-induced increase in death and reduction in division rate  $\delta_T$  and  $\lambda_T$ , respectively. We then rewrite the net growth rate as:

$$\psi = \lambda_0 - \lambda_T - \delta_0 - \delta_T \quad (\text{B26})$$

Furthermore, we define the combined treatment effect:

$$\tau = \psi_0 - \psi = \delta_T + \lambda_T \quad (\text{B27})$$

We write the probability of colony formation (from a single cell) as:

$$p_E = \begin{cases} 1, & \text{if } \lambda_0 - \lambda_T \leq \delta_0 + \delta_T, \\ \frac{\delta_0 + \delta_T}{\lambda_0 - \lambda_T}, & \text{if } \lambda_0 - \lambda_T > \delta_0 + \delta_T. \end{cases} \quad (\text{B28})$$

We then define the extinction probability for purely bacteriostatic drugs ( $\delta_T = 0$  and  $\lambda_T = \tau$ ) as:

$$p_{E,\text{stat}} = \begin{cases} 1, & \text{if } \lambda_0 - \tau \leq \delta_0, \\ \frac{\delta_0}{\lambda_0 - \tau}, & \text{if } \lambda_0 - \tau > \delta_0. \end{cases} \quad (\text{B29})$$

We define the extinction probability for purely bactericidal drugs ( $\delta_T = \tau$  and  $\lambda_T = 0$ ) as:

$$p_{E,\text{cidal}} = \begin{cases} 1, & \text{if } \lambda_0 \leq \delta_0 + \tau, \\ \frac{\delta_0 + \tau}{\lambda_0}, & \text{if } \lambda_0 > \delta_0 + \tau. \end{cases} \quad (\text{B30})$$

In Fig. B37, we plot the colony formation probability for a single bacterium plated on agar ( $p_C = 1 - p_E$ ) as a function of the treatment effect  $\tau$ , showing purely bacteriostatic (red) and purely bactericidal (blue) drugs.

## B2 Filamentation Model

To model bacterial filamentation we discretize the cell volumes into  $K$  classes indexed by  $i \in \{1, 2, \dots, K\}$ . Each class contains the bacterial density  $b_i(t)$  of cells with volume

$$v_i = i\epsilon, \quad (\text{B31})$$

where  $\epsilon$  is a unit volume increment. We define the following rules for growth, division, and death of cells

- cells in class  $i = 1$  cannot divide
- cells in class  $i = K$  cannot grow
- cells in class  $i = 1, \dots, K-1$  shift from class  $i$  to  $i+1$  at rate  $\gamma$
- cells in class  $i = 2, \dots, K$  divide at rate  $\lambda$ , resulting in a redistribution cells from class  $i$  into smaller classes (e.g. if  $i$  is even, two cells appear in class  $i/2$ ; if  $i$  is odd, one cell each appears in classes  $\frac{i-1}{2}$  and  $\frac{i+1}{2}$ ).
- cells in all classes die at rate  $\delta$ .

We collect the populations into a vector

$$\vec{b}(t) = (b_1(t), b_2(t), \dots, b_K(t))^T,$$

and write the dynamics as

$$\frac{d\vec{b}}{dt} = \lambda \Lambda \vec{b} + \gamma \Gamma \vec{b} - \delta \vec{b}, \quad (\text{B32})$$

where  $\Lambda$  and  $\Gamma$  are transition matrices for division and growth, respectively. An example form for  $\Gamma$  (volume acquisition) is

$$\Gamma = \begin{pmatrix} -1 & 0 & 0 & 0 & \cdots & 0 & 0 \\ 1 & -1 & 0 & 0 & \cdots & 0 & 0 \\ 0 & 1 & -1 & 0 & \cdots & 0 & 0 \\ \vdots & \vdots & \vdots & \vdots & \ddots & \vdots & \vdots \\ 0 & 0 & 0 & 0 & \cdots & 1 & 0 \end{pmatrix},$$

which shifts cells from class  $i$  to  $i + 1$ . An example  $\Lambda$  (division) might be

$$\Lambda = \begin{pmatrix} 0 & 2 & 1 & 0 & \cdots & 0 \\ 0 & -1 & 1 & 0 & \cdots & 0 \\ 0 & 0 & -1 & 1 & \cdots & 0 \\ \vdots & \vdots & \vdots & \vdots & \ddots & \vdots \\ 0 & 0 & 0 & 0 & \cdots & -1 \end{pmatrix}.$$

We assume that the volume of the two new cells after division is identical to the original volume of the parent cell before division:

$$\sum_{i=1}^K i (\Lambda \vec{b})_i = 0. \quad (\text{B33})$$

Furthermore the volume acquisition does not impact the number of cells:

$$\sum_{i=1}^K (\Gamma \vec{b})_i = 0. \quad (\text{B34})$$

**Population-level quantities.** We define the total bacterial density across all volume classes as

$$b(t) = \sum_{i=1}^K b_i(t), \quad (\text{B35})$$

and *total biovolume density*:

$$V(t) = \epsilon \sum_{i=1}^K i b_i(t) = \sum_{i=1}^K v_i b_i(t). \quad (\text{B36})$$

Then the *mean cell volume* is

$$v(t) = \frac{V(t)}{b(t)}. \quad (\text{B37})$$

In the finite model, boundary effects arise because the smallest cells cannot divide and the largest cannot grow. In the continuum limit  $\epsilon \rightarrow 0$ ,  $K \rightarrow \infty$ , these effects vanish and all cells experience uniform rates, so the following equalities hold:

$$\frac{db}{dt} = (\lambda - \delta) b, \quad (\text{B38})$$

$$\frac{dV}{dt} = \epsilon \gamma b - \delta V, \quad (\text{B39})$$

$$\frac{dv}{dt} = \epsilon \gamma - \lambda v. \quad (\text{B40})$$

Setting  $\frac{dv}{dt} = 0$  yields the equilibrium mean volume

$$v_{\text{eq}} = \frac{\epsilon \gamma}{\lambda}. \quad (\text{B41})$$

Integrating Equation B38 gives

$$b(t) = b_0 \exp((\lambda - \delta)t). \quad (\text{B42})$$

Substituting this result into Equation B39 and integrating with the integrating factor  $\exp(\delta t)$  yields the analytic solution for the total biovolume density across all size classes:

$$V(t) = v_{\text{eq}} b(t) + (V_0 - v_{\text{eq}} b_0) \exp(-\delta t). \quad (\text{B43})$$

Finally, writing  $v_0 = V_0/b_0$ , we obtain the analytical solution for the mean cell volume:

$$v(t) = v_{\text{eq}} + (v_0 - v_{\text{eq}}) \exp(-\lambda t). \quad (\text{B44})$$

**Parameter sensitivity.** We evaluated the impact of changes in the division rate,  $\Delta\lambda \in [-1.5, 0.5]$ , and the death rate,  $\delta \in \{0, 2, 4\}$ , on the difference between the luminescence-based rate and the true net growth rate. To this end, we set the treatment-free division rate to  $\lambda_0 = 1.5$ , the treatment-free death rate to  $\delta_0 = 0$ , the biovolume acquisition rate in the presence and absence of treatment to  $\gamma = 150 h^{-1}$ , the size of a volume increment to  $\epsilon = 0.04 \mu m^3$ , and volume-specific luminosity to  $\theta = 0.015$ . We simulated each parameter set for four hours using  $K = 1000$ . Furthermore we added the estimate based on luminescence if the first two hours of data are excluded.

**Volume correction and parameter estimation** To correct the light signal for dynamic changes in biovolume, we combine two sources of information: (i) two morphology snapshots before ( $v_{\text{obs},0}$ ) and after 2 hours of treatment ( $v_{\text{obs},2h}$ ), and (ii) the luminescence time series  $I_{\text{obs}}(t_i)$ .

We first rewrite Equation B44 using the equilibrium-to-initial volume ratio  $\alpha = v_{\text{eq}}/v_0$  as:

$$v(t) = \alpha v_0 + (1 - \alpha) v_0 e^{-\lambda t}. \quad (\text{B45})$$

To avoid fitting  $\alpha$  as a free parameter, we insert  $v_{\text{obs},0}$  and  $v_{\text{obs},2h}$  into Equation B45 to express  $\alpha$  as a function of  $\lambda$ :

$$\alpha(\lambda) = \frac{v_{\text{obs},2h} - v_{\text{obs},0} e^{-2\lambda}}{v_{\text{obs},0}(1 - e^{-2\lambda})}, \quad \alpha > 0. \quad (\text{B46})$$

Assuming constant volume-specific luminosity, we insert this constrained  $\alpha$  into Equation B11 to obtain:

$$I(t) = I_0 e^{(\lambda-\delta)t} \left[ \alpha + (1 - \alpha) e^{-\lambda t} \right], \quad (\text{B47})$$

with scale parameter  $I_0 = \kappa \theta v_{\text{obs},0} b_0 V_w$ .

To estimate the division rate  $\lambda$  and death rate  $\delta$ , we eliminate the nuisance parameter  $I_0$  by defining

$$F_i := e^{(\lambda-\delta)t_i} \left[ \alpha + (1 - \alpha) e^{-\lambda t_i} \right], \quad (\text{B48})$$

so that

$$\ln I(t_i) = \ln I_0 + \ln F_i. \quad (\text{B49})$$

Minimizing the residual sum of squares over  $\ln I_0$  yields the optimal

$$\ln I_0^* = \overline{\ln I_{\text{obs}}} - \overline{\ln F}, \quad (\text{B50})$$

where the overline denotes the sample mean across all  $i$ .

Minimizing the residual  $\ln I(t_i) - \ln I_{\text{obs}}(t_i)$  by substituting (B49) and (B50) yields the final loss function:

$$\mathcal{L}(\lambda, \delta) = \sum_{i=1}^n \left[ \left( \ln F_i - \overline{\ln F} \right) - \left( \ln I_{\text{obs}}(t_i) - \overline{\ln I_{\text{obs}}} \right) \right]^2. \quad (\text{B51})$$

To balance the dataset of observed specific volumes  $v$ , we sample 200 values per replicate and pool them. We then use the same bootstrapped light intensity datasets as in the main method for estimating  $\psi_I$ . For each bootstrap sample, we randomly pair one  $v_{\text{obs},0}$  and one  $v_{\text{obs},2h}$  with one luminescence trajectory and minimize (B51) over the biologically plausible region:

$$0.01 \leq \lambda \leq 1.75, \quad \delta \geq 0.$$

The remaining quantities  $\psi = \lambda - \delta$ ,  $\alpha(\lambda)$ , and  $I_0^*$  are computed algebraically.

### B3 Experiments

**SOS experiment.** We conducted this experiment to test whether activating the SOS response by UV light would increase the specific luminosity and thereby explain the shallower decline of light intensity compared to the decline in CFU counts. This hypothesis rests on the possibility that the phage promoter driving the lux cassette up-regulates when the cell experiences stress.

To test this, we diluted three replicate overnight cultures 1:100 and grew them for approximately 1.5 h to mid-exponential phase. Each of the three exponential-phase cultures was split into two aliquots: one was assigned to UV treatment and placed in the upper half of a white 96-well plate (rows B–D), while the other served as an untreated control in the lower half (rows E–G) (Greiner, 655098).

We started the experiment by measuring luminescence and OD in the plate reader. Then we alternated between exposing the strains for repeated intervals to UV light in a cross-linker (Hoefer, UVC 500 crosslinker, at  $10 \frac{\mu\text{J}}{\text{cm}^2}$ ) in a temperature-regulated environment ( $36.5^\circ\text{C}$ ); followed by luminescence and OD measurements. During UV exposure, we shielded the control samples by covering the lower half of the plate with a metal lid. The durations of UV treatment were 30 s, 1 min, 2 min, 4 min and 8 min.

OD increased in both UV-treated and control cultures; however, UV exposure visibly impaired OD growth compared to the controls (Fig. B21a). We normalized the luminescence signals (Fig. B21b) by dividing through the OD signal, resulting in the OD-normalized light intensity  $\omega$  (Fig. B21c). We observed that the OD-normalized light intensity of UV-treated cultures falls with the duration of

treatment compared to the OD-normalized light intensity of the controls ( $\omega_{UV} - \omega_{ctrl}$ ; see Fig. B21d; t-test,  $p = 3 \cdot 10^{-5}$  for the last timepoint).

Based on these results, we find it unlikely that upregulation of the promoter explains the shallower decline of light intensity compared to that of CFU count. However, we cannot exclude the possibility that this result does not hold if the SOS response is triggered by another mechanism.

**Morphology evaluation.** We analyzed the microscopy images in several steps. First, we manually applied lower and upper thresholds to the red and green channel to enhance the visual contrast (Fig. B22–Fig. B34). Next, we used “Ilastik-1.4.0” to infer the probability that each pixel in the thresholded green channel image belonged to a bacterium. Ilastik employs a neural network trained directly on the microscopy images.

Subsequently, we used a Python script ([5]) to convert these probabilities into markers representing individual bacteria. Misidentified markers were manually excluded, e.g., if they only partially covered a bacterium or covered multiple overlapping bacteria. For each marker, we fitted a spline through its center, providing the spline length  $l_s$ . We then optimized the radius  $r_s$  by maximizing the marker area within a distance  $r_s$  from the spline while minimizing the area within  $r_s$  that did not belong to the marker.

Using these parameters, we calculated for each bacterium the length  $l_b = l_s + 2 \cdot r_s$ , width  $w_b = 2 \cdot r_s$ , and volume  $v = 2 \cdot \pi \cdot r_s^2 \cdot l_s + \frac{4}{3} \cdot \pi \cdot r_s^3$ . To create a volume distribution for each treatment, we resampled the fitted volume estimates from each image (replicate) 200 times with replacement, preserving the original sample size, and aggregated the resulting datasets. Based on these distributions, we determined whether cells were significantly filamented using the significance criterion described in the methods section of the main paper.

**Antimicrobial peptide deactivation experiment.** To assess whether pexiganan-treated bacteria continued to die in a 1:100 diluted PBS environment, we exposed exponential-phase cultures to  $16 \frac{\mu\text{g}}{\text{mL}}$  pexiganan for 1 min. Following this treatment,  $10 \mu\text{L}$  of each culture was diluted in  $990 \mu\text{L}$  of PBS supplemented with 0, 1, 10, or  $100 \text{ mM CaCl}_2$  or  $\text{MgCl}_2$ . Every 45 min, we sampled from each diluted culture and plated  $10 \mu\text{L}$  aliquots using the automated plating method described in the methods section of the main paper.

We observed a substantial effect of both supplements on the measured bacterial density (Fig. B38a, b). Increasing the supplement concentration consistently resulted in higher bacterial densities, indicating that the supplemented ions reduce bacterial killing. Most data points for the unsupplemented medium resulted in empty agar plates. The highest CFU count was observed for strains diluted in  $100 \text{ mM MgCl}_2$  (Table B4).

**Manual pexiganan time-kill curve experiment.** In this setup, we captured four time points within 5 min using CFU plus the pre-treatment bacterial density. The experiment was performed manually using the traditional CFU plating method. Round agar plates (Sarstedt, 82.1473.001) containing 25 mL of agar were used, and 100  $\mu$ L of each dilution was plated. This approach increases sensitivity by using 100  $\mu$ L, rather than 10  $\mu$ L, for plating.

Cultures were treated in a 96-deepwell plate (Greiner, 780285) by adding 100  $\mu$ L of a 10x stock to 900  $\mu$ L of exponential-phase culture. Samples were taken directly from the deepwell plate, and two simultaneous dilution series were prepared in a 96-well plate (Greiner, 655101) at each time point to halt the killing. One dilution series was prepared in pure PBS, and the other in PBS supplemented with 100 mM MgCl<sub>2</sub>.

For this experiment, we plated three dilutions (factors of 100, 1,000, and 10,000) and counted the colonies on all plates. We observed that when PBS without MgCl<sub>2</sub> was used, higher dilution factors led to higher CFU estimates (Fig. B39). This discrepancy diminished over time, in parallel with a weakening of the observed kill rate. In contrast, when the dilution medium was supplemented with MgCl<sub>2</sub>, we did not observe this effect.

**Supernatant experiment.** During the measured pexiganan kill curve described above, we observed a steep decline in CFU counts, followed by a nearly constant plateau. Two non-exclusive explanations may account for this observed decrease in killing: (i) the surviving bacteria are persisters or resistant to the AMP, or (ii) the AMP molecules become deactivated, leaving the supernatant without killing activity.

To investigate the supernatant's remaining bactericidal effects, we conducted a multi-step experiment:

**Step 1: preparation.** Three overnight (O/N) cultures were diluted 1:100 in LB and incubated at 37 °C with shaking for 2 h. From each culture, we took three samples: one to measure the bacterial density before treatment, the second (1 ml) to accumulate pure bacteria for supernatant exposure, and the third 1.35 mL was reserved for supernatant production and measuring the initial kill rate.

**Step 2: purification of bacteria.** To purify bacteria we pelleted the previously collected 1 mL bacterial aliquots at 3000  $\times g$  for 5 min, discarded the supernatant and stored them in the fridge.

**Step 3: initial killing and supernatant production.** To generate the supernatant, each 1.35 mL sample was treated with a 160  $\frac{\mu\text{g}}{\text{mL}}$  pexiganan stock at a 1:10 ratio, yielding a final concentration of 16  $\frac{\mu\text{g}}{\text{mL}}$ . After 5 min, we plated samples for CFU counts and centrifuged the remaining culture at maximum speed for 2 min to remove cellular debris. Plate counts of these treated samples revealed rapid bacterial killing (rate of CFU count change  $\psi_{\text{CFU}} \approx -46$  per hour) (Fig. B40, Table B5). We collected 1 mL of the clarified supernatant for the subsequent exposure experiment.

**Step 4: supernatant killing.** In that final step we dissolved the pelleted bacteria (from step 2) in the

supernatant collected during step 3. After another 5 min incubation, we plated samples (dilutions 1:100, 1:1,000, and 1:10,000) to estimate bacterial density. No significant killing was observed, indicating that the supernatant alone no longer exhibited bactericidal activity—supporting explanation (ii), without rejecting (i).

Our current hypothesis is that AMP molecules bind to the surface of intact bacteria and to newly exposed targets from lysed bacteria, thereby becoming deactivated. Thus, cells that survive the initial kill phase may have an increased chance of continued survival. Possible explanations for why specific bacteria survive this phase include reduced surface area due to clumping or adhesion to well walls, smaller cell size, and other factors that might confer protection, potentially related to the cell cycle.

Table B1 – Drugs used in this study, their MICs, working concentrations, and stock solvents. In the MIC column, we report the highest concentration of the dilution series (numerator) and the maximum inhibiting dilution (denominator). Kanamycin ( $50 \frac{\mu\text{g}}{\text{mL}}$ ) was used as the selection marker for the *lux* operon.

drug	MIC [ $\frac{\mu\text{g}}{\text{mL}}$ ]	cwork [ $\frac{\mu\text{g}}{\text{mL}}$ ]	cwork [MIC]	solvent	supplier
Amoxicillin	$\frac{10}{4} = 2.50$	25	10	DMSO	Sigma, A8523
Ampicillin	$\frac{100}{128} = 0.78$	10, 2	12.8, 2.56	water	Sigma, A9518
Cefepime	$\frac{4}{256} = 0.02$	0.15	9.6	DMSO	ThermoFisher, J66237
Ceftazidime	$\frac{4}{64} = 0.06$	0.62	10	DMSO	Sigma, PHR1847
Cefuroxime	$\frac{4}{2} = 2.00$	16	8	water	Sigma, C4417
Chloramphenicol	$\frac{128}{64} = 2.00$	20	10	DMSO	Sigma, C0378
Ciprofloxacin	$\frac{1}{128} = 0.01$	0.08	10	water	Sigma, 17850
Colistin	$\frac{50}{64} = 0.78$	1.6	2.05	water	Sigma, C4461
Doripenem	$\frac{4}{256} = 0.02$	0.16	10.24	water	VWR, ACRO463870010
Fosfomycin	$\frac{4}{4} = 1.00$	8	8	water	VWR, APOS-BIM0107
Imipenem	$\frac{5}{64} = 0.08$	1	12.8	water	Sigma, PHR1796
Mecilinam	$\frac{10}{128} = 0.08$	0.78	10	DMSO	Sigma, 33447
Meropenem	$\frac{5}{512} = 0.01$	0.1	10.24	water	Sigma, PHR1772
Penicillin	$\frac{500}{32} = 15.62$	100	6.4	water	Roth, HP48.2
Pexiganan	$\frac{64}{32} = 2.00$	8, 16	4, 8	water	Sigma, SML3787
Piperacillin	$\frac{10}{16} = 0.62$	6.25	10	DMSO	Sigma, J66419
Polymyxin B	$\frac{50}{32} = 1.56$	2.5	1.6	water	Roth, 0235.1
Rifampicin	$\frac{40}{16} = 2.50$	25	10	DMSO	Sigma, R3501
Tetracycline	$\frac{10}{32} = 0.31$	3.12	10	DMSO	Sigma, T3383
Trimethoprim	$\frac{10}{128} = 0.08$	0.78	10	DMSO	Sigma, T7883

Table B2 – Point estimates and 95% percentile intervals of  $\psi_{\text{CFU}}$ ,  $\psi_I$ ,  $\psi_I^*$ , and  $\psi_J$  for different treatments.  $\text{Sig}_X$  indicates whether the rate of change of signal  $X \in \{I, I^*, J\}$  differs significantly (\*) from the distribution of  $\psi_{\text{CFU}}$ , or not (n.s.), based on the significance criterion defined in the Methods section. Estimates are based on data from the CFU-luminescence assays (see Methods).

	$\psi_{\text{CFU}} [\frac{1}{\text{h}}]$	$\psi_I [\frac{1}{\text{h}}]$	$\text{sig}_I$	$\psi_I^* [\frac{1}{\text{h}}]$	$\text{sig}_{I^*}$	$\psi_J [\frac{1}{\text{h}}]$	$\text{sig}_J$
<b>ampicillin</b> 10 $\frac{\mu\text{g}}{\text{ml}}$	-3.23 [-4.11, -2.54]	-2.41 [-2.91, -2.11]	*			-2.63 [-3.31, -2.29]	n.s.
<b>ampicillin</b> 2 $\frac{\mu\text{g}}{\text{ml}}$	-0.81 [-1.19, -0.37]	-0.30 [-0.41, -0.22]	*				
<b>amoxicillin</b> 25 $\frac{\mu\text{g}}{\text{ml}}$	-2.15 [-2.42, -1.88]	-2.04 [-2.21, -1.86]	n.s.				
<b>cefepime</b> 0.15 $\frac{\mu\text{g}}{\text{ml}}$	-1.17 [-1.50, -0.85]	-0.47 [-0.74, -0.24]	*	-0.88 [-1.13, -0.65]	*		
<b>ceftazidime</b> 0.62 $\frac{\mu\text{g}}{\text{ml}}$	-0.88 [-1.06, -0.71]	-0.09 [-0.24, 0.04]	*			-0.38 [-0.52, -0.15]	*
<b>cefuroxime</b> 16 $\frac{\mu\text{g}}{\text{ml}}$	-1.59 [-2.41, -0.99]	-1.41 [-1.64, -1.25]	n.s.	-1.62 [-1.92, -1.34]	n.s.		
<b>chloramphenicol</b> 20 $\frac{\mu\text{g}}{\text{ml}}$	0.05 [-0.11, 0.20]	0.04 [-0.03, 0.10]	n.s.				
<b>ciprofloxacin</b> 0.078 $\frac{\mu\text{g}}{\text{ml}}$	-1.96 [-2.29, -1.64]	0.83 [0.44, 1.17]	*			0.48 [0.09, 0.90]	*
<b>colistin</b> 1.6 $\frac{\mu\text{g}}{\text{ml}}$	-1.00 [-1.45, -0.52]	-0.93 [-1.26, -0.66]	n.s.				
<b>doripenem</b> 0.16 $\frac{\mu\text{g}}{\text{ml}}$	-0.54 [-0.83, -0.25]	-0.24 [-0.37, -0.15]	*	-0.37 [-0.53, -0.26]	*		
<b>fosfomycin</b> 8 $\frac{\mu\text{g}}{\text{ml}}$	-1.22 [-1.65, -0.83]	-1.12 [-1.37, -0.93]	n.s.				
<b>imipenem</b> 1 $\frac{\mu\text{g}}{\text{ml}}$	-1.42 [-2.06, -0.72]	0.00 [-0.16, 0.14]	*	-0.32 [-0.45, -0.22]	*		
<b>mecillinam</b> 0.78 $\frac{\mu\text{g}}{\text{ml}}$	-0.32 [-0.57, -0.10]	0.02 [-0.17, 0.17]	*	-0.34 [-0.47, -0.20]	n.s.		
<b>meropenem</b> 0.1 $\frac{\mu\text{g}}{\text{ml}}$	-1.85 [-2.36, -1.32]	-0.16 [-0.47, 0.10]	*			-0.55 [-0.80, -0.21]	*
<b>penicillin</b> 100 $\frac{\mu\text{g}}{\text{ml}}$	-2.17 [-2.78, -1.66]	-2.20 [-2.53, -1.94]	n.s.				
<b>piperacillin</b> 6.25 $\frac{\mu\text{g}}{\text{ml}}$	-0.26 [-0.51, 0.02]	0.09 [-0.01, 0.19]	*				
<b>polymyxinB</b> 2.5 $\frac{\mu\text{g}}{\text{ml}}$	-1.45 [-1.73, -1.22]	-1.41 [-1.87, -1.07]	n.s.				
<b>rifampicin</b> 25 $\frac{\mu\text{g}}{\text{ml}}$	-0.23 [-0.40, 0.04]	-0.15 [-0.23, -0.07]	n.s.				
<b>tetracycline</b> 3.125 $\frac{\mu\text{g}}{\text{ml}}$	-0.06 [-0.12, 0.00]	-0.01 [-0.07, 0.05]	n.s.				
<b>trimethoprim</b> 0.78 $\frac{\mu\text{g}}{\text{ml}}$	-0.61 [-0.76, -0.47]	0.48 [0.38, 0.59]	*			0.34 [0.18, 0.51]	*
<b>pexiganan</b> 8 $\frac{\mu\text{g}}{\text{ml}}$	-44.59 [-66.19, -20.08]	-45.95 [-48.21, -43.34]	n.s.				
<b>pexiganan</b> 16 $\frac{\mu\text{g}}{\text{ml}}$	-61.63 [-93.40, 1.26]	-60.27 [-63.06, -56.42]	n.s.				

Table B3 – Bootstrapped 95% confidence intervals and point estimates for the length, width, and volume of cells after 2 h of treatment, estimated from microscopy images. Significance was assessed by comparing the confidence intervals of cell volumes for each antibiotic treatment to the untreated control (control\_2h), as described in the Methods section of the main paper.

	L_low	L_up	L_mean	W_low	W_up	W_mean	V_low	V_up	V_mean	V_sig
control_2h	2.28	4.92	3.41	0.77	1.4	1.09	2	6.51	3.89	ref.
amoxicillin	2.64	10.77	5.09	0.47	1.37	1.17	1.93	9.67	6.21	n.s.
ampicillin	3.87	27.14	12.36	0.93	1.67	1.27	5.7	30.39	16.67	sig.
ceftazidime	32.05	68.69	54.54	0.67	1.22	0.95	11.52	80.86	40.42	sig.
ciprofloxacin	10.88	36.82	21.77	0.7	1.27	1.03	6.35	45.7	19.55	sig.
colistin	2.19	4.53	3.14	0.6	1.59	1.07	1	8.32	3.71	n.s.
fosfomycin	1.77	5.32	3.18	0.69	1.15	0.93	1.09	4.75	2.65	n.s.
meropenem	3.44	10.61	5.9	1.13	3.71	2.26	5.33	71.01	31.11	sig.
rifampicin	2.41	8.38	4.77	0.59	1.4	0.98	1.15	9.44	4.32	n.s.
tetracycline	2.43	7.7	4.71	0.65	1.71	1.08	1.29	13.4	5.25	n.s.
trimethoprim	4.67	30.74	12.19	0.65	1.29	0.93	2.64	19.79	9.05	sig.

Table B4 – Estimated group means and 95% confidence intervals from an ordinary least squares (OLS) model fitted to log-transformed CFU data, collected from the first sampled time point after diluting pexiganan-treated strains in supplemented PBS. Grouping is based on the supplement ( $\text{CaCl}_2$  or  $\text{MgCl}_2$ ) and concentration (0 mM to 100 mM). Confidence intervals were computed using heteroscedasticity-consistent standard errors (HC3). The compact letter display (cld) indicates groups that are not significantly different by sharing a common letter, based on mutual inclusion of their 95% confidence intervals.

group	mean	ci_lower	ci_upper	cld
$\text{CaCl}_2$ (0 mM)	-0.00	-0.00	0.00	a
$\text{CaCl}_2$ (1 mM)	2.77	-0.56	6.09	b
$\text{CaCl}_2$ (10 mM)	5.06	4.92	5.20	c
$\text{CaCl}_2$ (100 mM)	5.85	5.38	6.31	d
$\text{MgCl}_2$ (0 mM)	-0.00	-0.00	0.00	a
$\text{MgCl}_2$ (1 mM)	2.77	-0.56	6.09	b
$\text{MgCl}_2$ (10 mM)	5.31	5.20	5.42	e
$\text{MgCl}_2$ (100 mM)	6.36	6.27	6.46	f

Table B5 – Comparison of kill rates [ $h^{-1}$ ] between cultures treated with pexiganan ( $16 \frac{\mu\text{g}}{\text{mL}}$ ) for 5 minutes and cultures exposed to the supernatant collected after the kill assay. The two rates differ significantly; the confidence interval of the rate of change of CFU in the supernatant includes zero.

	mean	lower	upper
<b>experiment</b>			
pexiganan	-46.980603	-63.153906	-35.797836
supernatant	1.281551	-2.187859	5.111196

Table B6 – Primer sequences used for  $\lambda$ -red mediated integration of the *luxCDABE* operon into *E. coli*. Lowercase letters indicate homology regions binding to the *lux* operon on the plasmid; uppercase letters indicate chromosomal homology regions at the integration site.

Primer name	Sequence (5' → 3')
forward primer	CGGTACGGCTGACCATCGGCTGCCAGTGC <sup>G</sup> GGAGTTTCGTAcccgtaaggcagcggta
reverse primer	AGTCAGCGATATCCATTTCGCGAATCCGGAGTGTAAAGAAtaggtctagggcggcggaa

Fig. B1 – Light intensity scales linearly with bacterial density. Serial tenfold dilutions of bacterial cultures were prepared in a 384-well white microplate, and luminescence was measured immediately. Linear regression of the luminescence signal against bacterial density (CFU) yielded a conversion factor of  $m_{\text{fit}} = 0.006 \text{ rlu} \cdot \text{ml} \cdot \text{CFU}^{-1}$ . The high correlation ( $R^2 = 0.987$  in log-log space) confirms a linear relationship between luminescence and bacterial density.

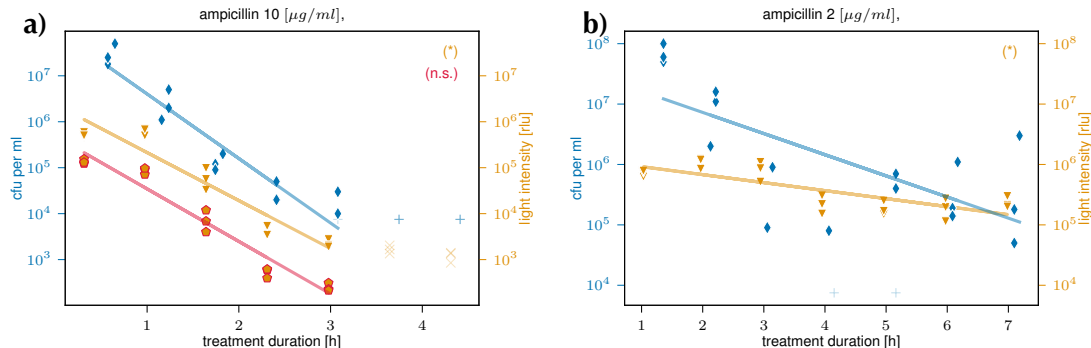
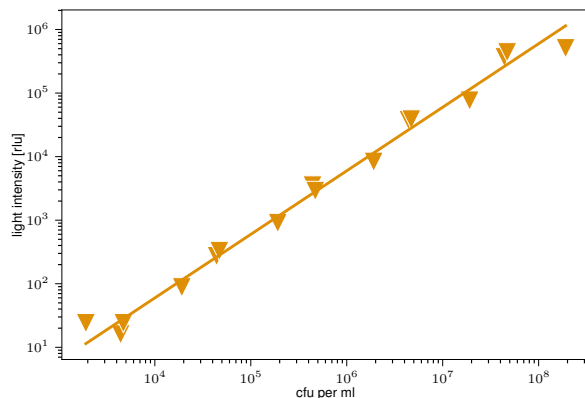
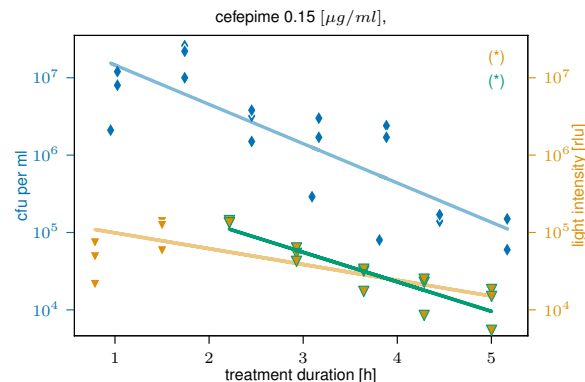


Fig. B2 – Ampicillin. The CFU signal is shown as blue diamonds and the light intensity as orange triangles for data points above their respective detection limits ( $10^4 \text{ CFU/mL}$  for CFU and  $20 \text{ rlu}$  for luminescence). Lines represent log-linear fits to the corresponding signals. The morphology-corrected luminescence signal is shown as orange pentagons with red frames, and the corresponding rate fit indicated by a red line. ‘+’ indicates data points below detection limit or otherwise excluded (for CFU, symbolically plotted at  $10^4 \text{ CFU/mL}$  to visualize missing data), and if a signal ends early (due to dropping below its detection limit), the corresponding data point of the other signal was cut to the same endpoint for a consistent comparison. These excluded data points are marked as ‘X’.

Fig. B3 – Cefepime. The CFU signal is shown as blue diamonds and the light intensity as orange triangles for data points above their respective detection limits ( $10^4 \text{ CFU/mL}$  for CFU and  $20 \text{ rlu}$  for luminescence). Lines represent log-linear fits to the corresponding signals. Green-framed data points and corresponding green fit lines indicate analyses excluding early data points until the first peak.



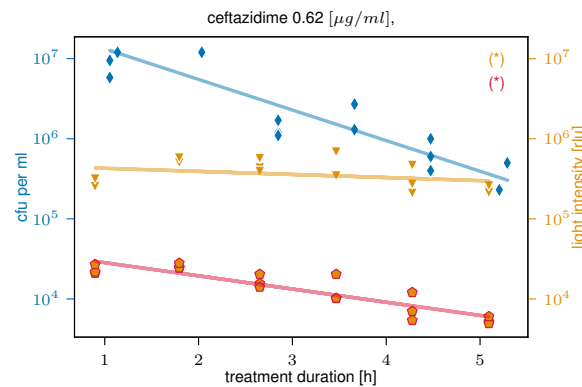


Fig. B4 – Ceftazidime. The CFU signal is shown as blue diamonds and the light intensity as orange triangles for data points above their respective detection limits ( $10^4$  CFU/mL for CFU and 20 rlu for luminescence). Lines represent log-linear fits to the corresponding signals. The morphology-corrected luminescence signal is shown as orange pentagons with red frames, and the corresponding rate fit indicated by a red line.

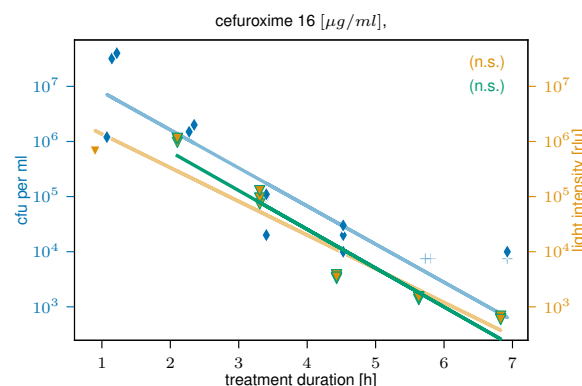


Fig. B5 – Cefuroxime. The CFU signal is shown as blue diamonds and the light intensity as orange triangles for data points above their respective detection limits ( $10^4$  CFU/mL for CFU and 20 rlu for luminescence). Lines represent log-linear fits to the corresponding signals. ‘+’ indicates data points below detection limit or otherwise excluded (for CFU, symbolically plotted at  $10^4$  CFU/mL to visualize missing data).

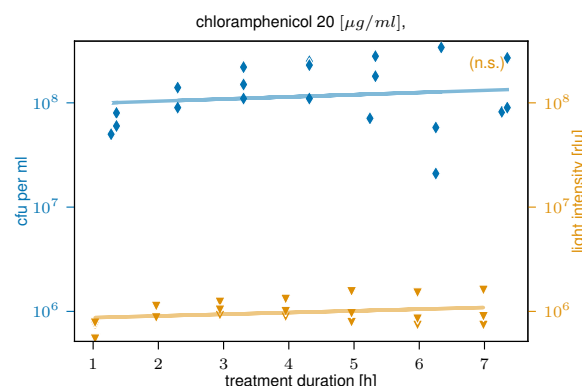


Fig. B6 – Chloramphenicol. The CFU signal is shown as blue diamonds and the light intensity as orange triangles for data points above their respective detection limits ( $10^4$  CFU/mL for CFU and 20 rlu for luminescence). Lines represent log-linear fits to the corresponding signals.

Fig. B7 – Ciprofloxacin. The CFU signal is shown as blue diamonds and the light intensity as orange triangles for data points above their respective detection limits ( $10^4$  CFU/mL for CFU and 20 rlu for luminescence). Lines represent log-linear fits to the corresponding signals. The morphology-corrected luminescence signal is shown as orange pentagons with red frames, and the corresponding rate fit indicated by a red line.

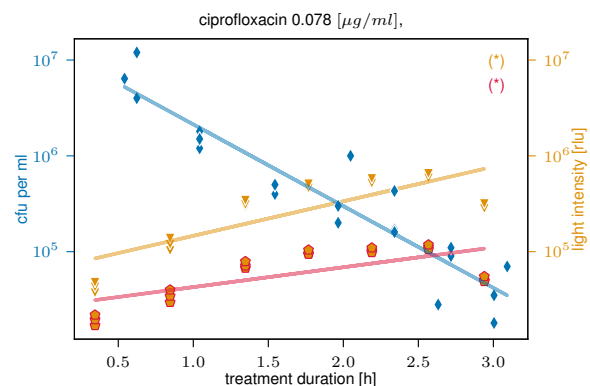


Fig. B8 – Colistin. The CFU signal is shown as blue diamonds and the light intensity as orange triangles for data points above their respective detection limits ( $10^4$  CFU/mL for CFU and 20 rlu for luminescence). Lines represent log-linear fits to the corresponding signals. '+' indicates data points below detection limit or otherwise excluded (for CFU, symbolically plotted at  $10^4$  CFU/mL to visualize missing data)

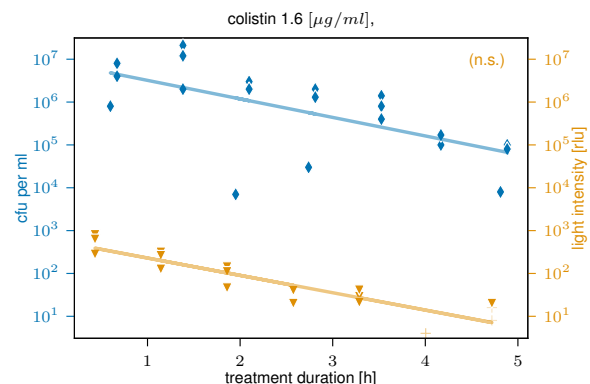
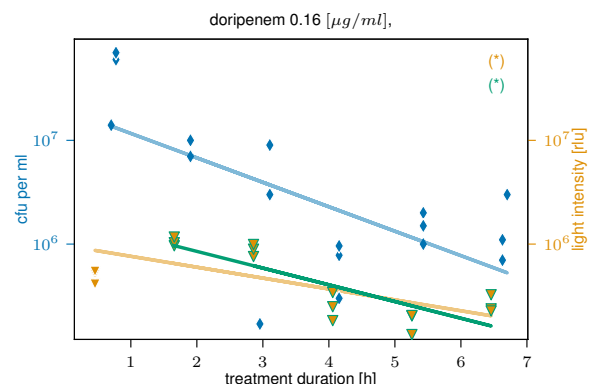


Fig. B9 – Doripenem. The CFU signal is shown as blue diamonds and the light intensity as orange triangles for data points above their respective detection limits ( $10^4$  CFU/mL for CFU and 20 rlu for luminescence). Lines represent log-linear fits to the corresponding signals. Green-framed data points and corresponding green fit lines indicate analyses excluding early data points until the first peak.



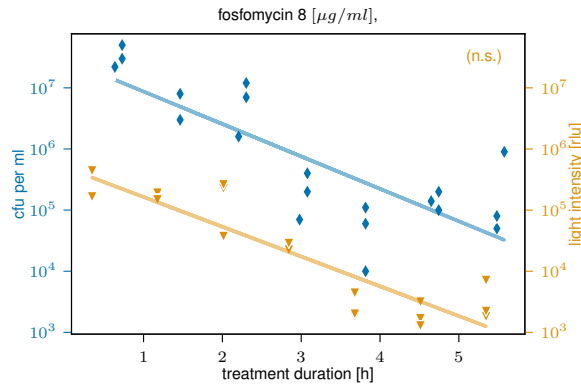


Fig. B10 – Fosfomycin. The CFU signal is shown as blue diamonds and the light intensity as orange triangles for data points above their respective detection limits ( $10^4$  CFU/mL for CFU and 20 rlu for luminescence). Lines represent log-linear fits to the corresponding signals.

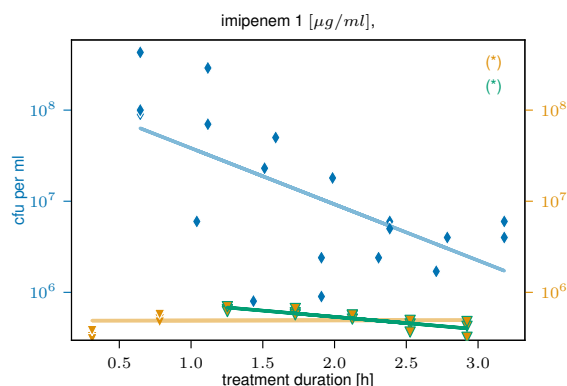


Fig. B11 – Imipenem. The CFU signal is shown as blue diamonds and the light intensity as orange triangles for data points above their respective detection limits ( $10^4$  CFU/mL for CFU and 20 rlu for luminescence). Lines represent log-linear fits to the corresponding signals. ‘+’ indicates data points below detection limit or otherwise excluded (for CFU, symbolically plotted at  $10^4$  CFU/mL to visualize missing data).

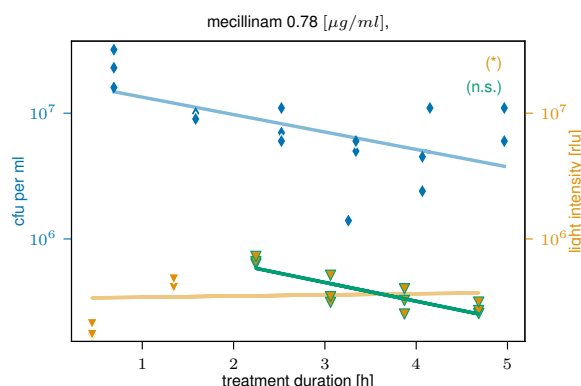


Fig. B12 – Mecillinam. The CFU signal is shown as blue diamonds and the light intensity as orange triangles for data points above their respective detection limits ( $10^4$  CFU/mL for CFU and 20 rlu for luminescence). Lines represent log-linear fits to the corresponding signals.

Fig. B13 – Meropenem. The CFU signal is shown as blue diamonds and the light intensity as orange triangles for data points above their respective detection limits ( $10^4$  CFU/mL for CFU and 20 rlu for luminescence). Lines represent log-linear fits to the corresponding signals. The morphology-corrected luminescence signal is shown as orange pentagons with red frames, and the corresponding rate fit indicated by a red line. ‘+’ indicates data points below detection limit or otherwise excluded (for CFU, symbolically plotted at  $10^4$  CFU/mL to visualize missing data).

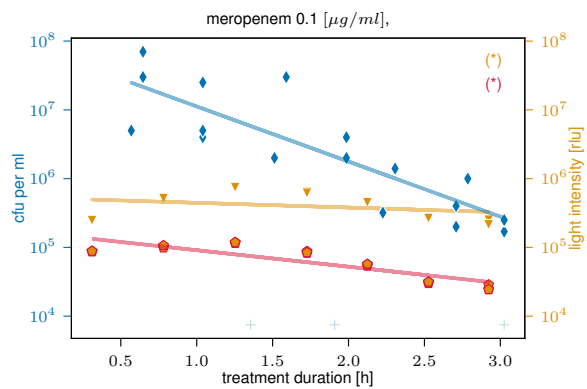


Fig. B14 – Penicillin. The CFU signal is shown as blue diamonds and the light intensity as orange triangles for data points above their respective detection limits ( $10^4$  CFU/mL for CFU and 20 rlu for luminescence). Lines represent log-linear fits to the corresponding signals. ‘+’ indicates data points below detection limit or otherwise excluded (for CFU, symbolically plotted at  $10^4$  CFU/mL to visualize missing data), and If a signal ends early (due to dropping below its detection limit), the corresponding data point of the other signal was cut to the same endpoint for a consistent comparison. These excluded data points are marked as ‘X’.

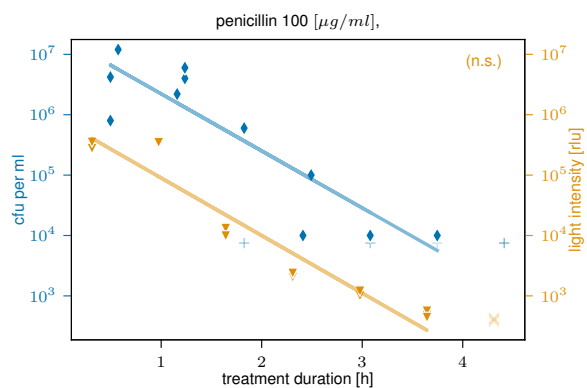
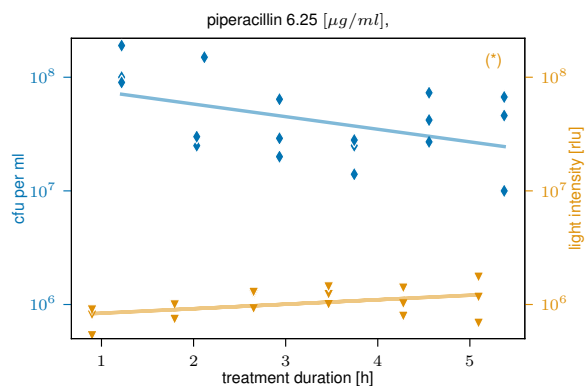


Fig. B15 – Piperacillin. The CFU signal is shown as blue diamonds and the light intensity as orange triangles for data points above their respective detection limits ( $10^4$  CFU/mL for CFU and 20 rlu for luminescence). Lines represent log-linear fits to the corresponding signals.



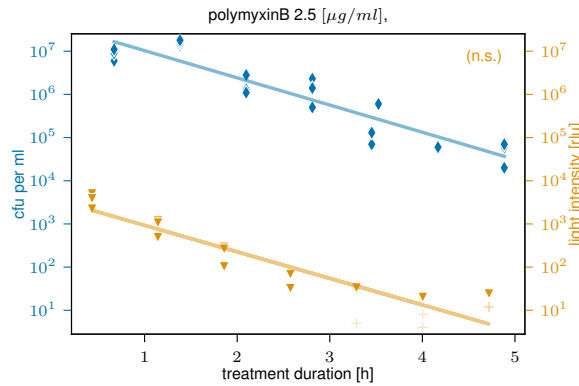


Fig. B16 – Polymyxin B. The CFU signal is shown as blue diamonds and the light intensity as orange triangles for data points above their respective detection limits ( $10^4$  CFU/mL for CFU and 20 rlu for luminescence). Lines represent log-linear fits to the corresponding signals. ‘+’ indicates data points below detection limit or otherwise excluded (for CFU, symbolically plotted at  $10^4$  CFU/mL to visualize missing data).

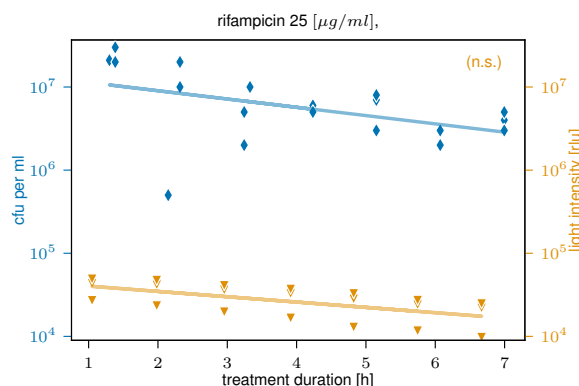


Fig. B17 – Rifampicin (25  $\mu$ g/mL). The CFU signal is shown as blue diamonds and the light intensity as orange triangles for data points above their respective detection limits ( $10^4$  CFU/mL for CFU and 20 rlu for luminescence). Lines represent log-linear fits to the corresponding signals.

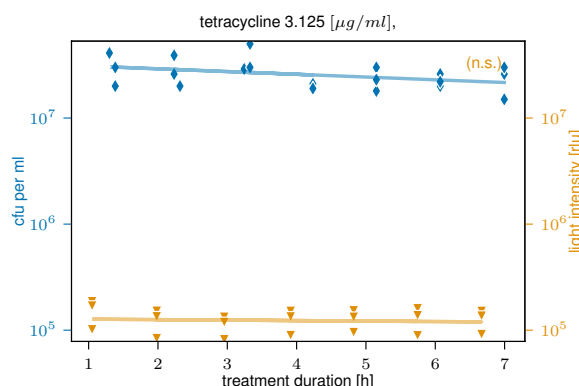


Fig. B18 – Tetracycline. The CFU signal is shown as blue diamonds and the light intensity as orange triangles for data points above their respective detection limits ( $10^4$  CFU/mL for CFU and 20 rlu for luminescence). Lines represent log-linear fits to the corresponding signals.

Fig. B19 – Trimethoprim. The CFU signal is shown as blue diamonds and the light intensity as orange triangles for data points above their respective detection limits ( $10^4$  CFU/mL for CFU and 20 rlu for luminescence). Lines represent log-linear fits to the corresponding signals. The morphology-corrected luminescence signal is shown as orange pentagons with red frames, and the corresponding rate fit indicated by a red line.

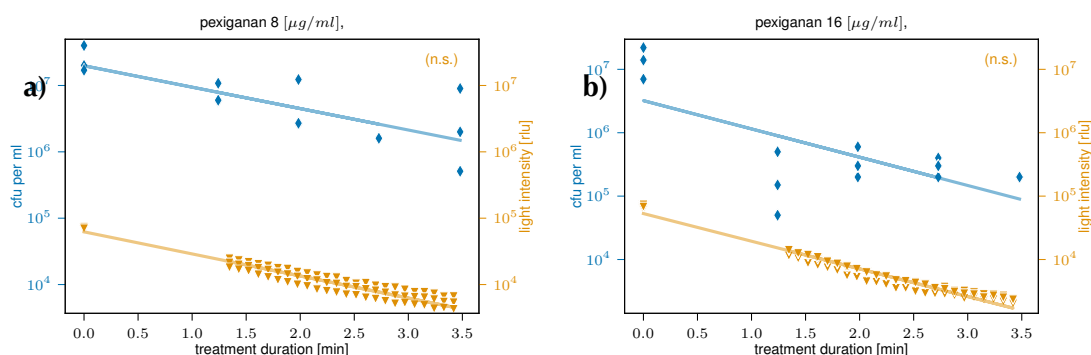
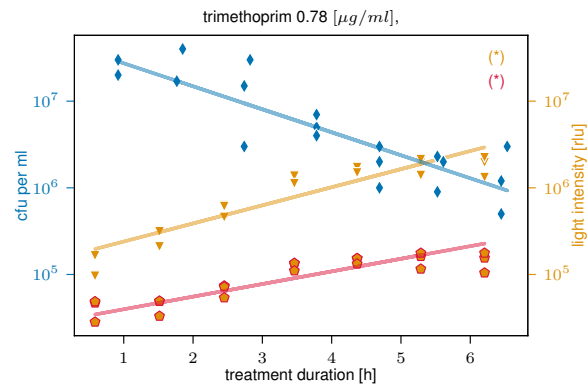


Fig. B20 – Comparison of the CFU and luminescence signals from the pexiganan kill curve experiment using the liquid handling platform. The first data points at  $t_0$  represent the pretreatment CFU and light intensity values.

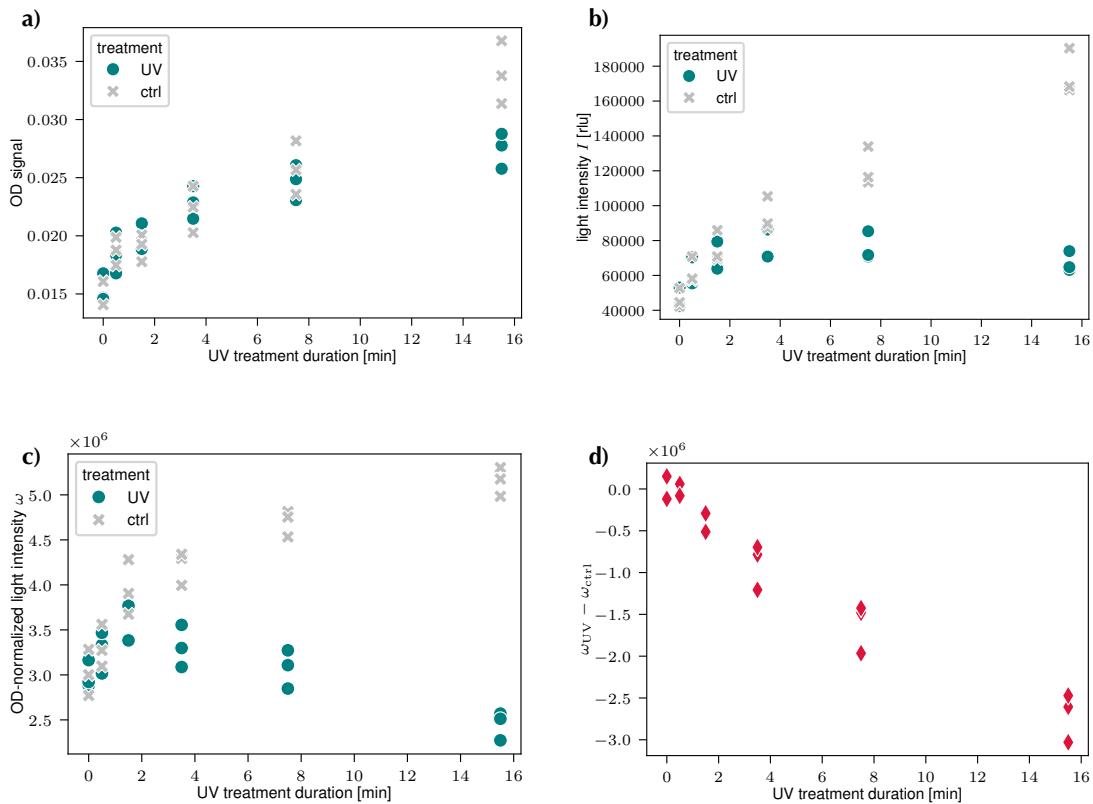


Fig. B21 – Panel plot showing the effects of UV treatment on bacterial density (approximated by OD) and light intensity ( $I$ ) over time by comparing treated (UV) and untreated (ctrl) cultures. (a) Optical density (OD), (b) light intensity, (c) OD-specific light intensity  $\omega = I(t)/OD(t)$ , and (d) the difference in OD-specific light intensity between UV-treated and control.

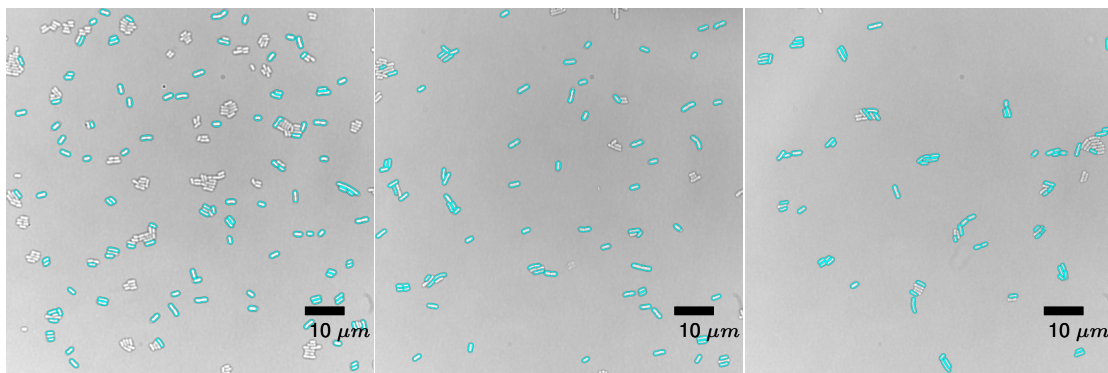


Fig. B22 – Microscopy images of control (before treatment) samples. Each image represents a different replicate. We plotted the green channel of the recorded images in greyscale. The red channel, capturing propidium iodide activity, is overlaid in red. Bacterial shapes detected by the algorithm are outlined in cyan.

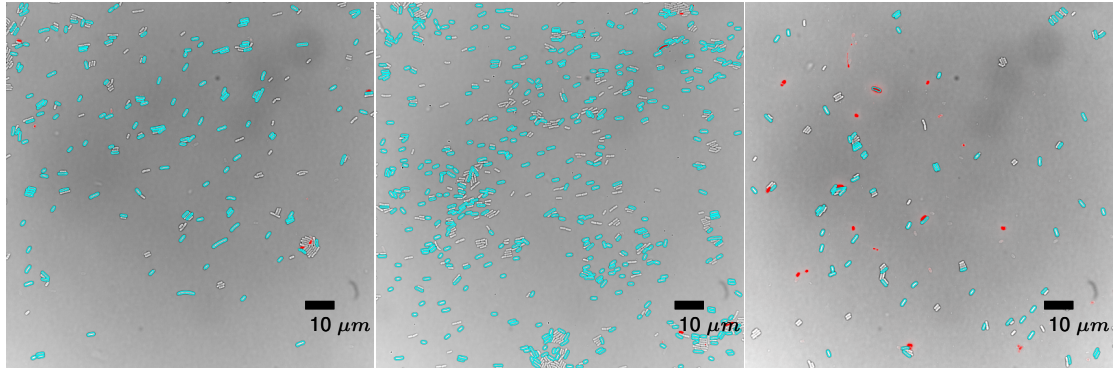


Fig. B23 – Microscopy images of control (after 2 hours) samples. Each image represents a different replicate. We plotted the green channel of the recorded images in greyscale. The red channel, capturing propidium iodide activity, is overlaid in red. Bacterial shapes detected by the algorithm are outlined in cyan.

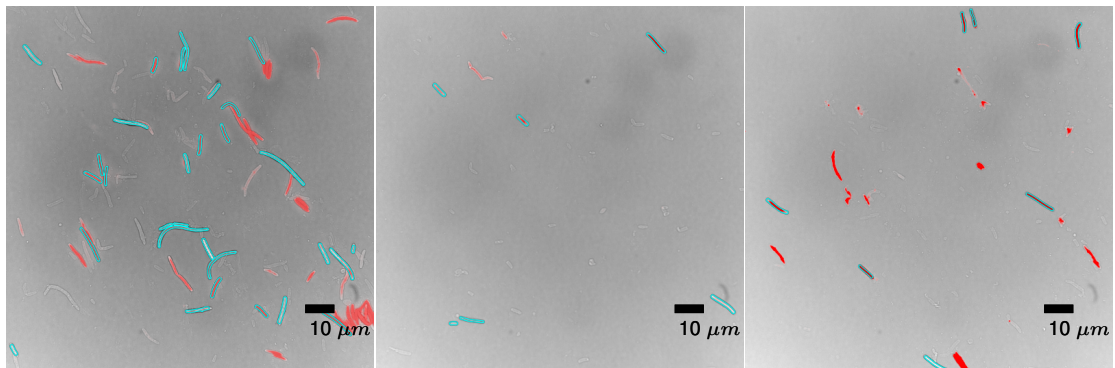


Fig. B24 – Microscopy images of cells treated with ampicillin. Each image represents a different replicate. We plotted the green channel of the recorded images in greyscale. The red channel, capturing propidium iodide activity, is overlaid in red. Bacterial shapes detected by the algorithm are outlined in cyan.

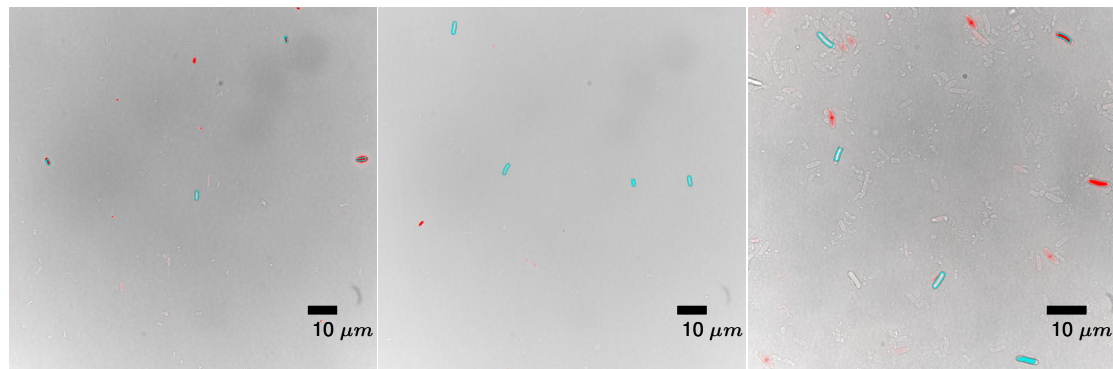


Fig. B25 – Microscopy images of cells treated with amoxicillin. Each image represents a different replicate. We plotted the green channel of the recorded images in greyscale. The red channel, capturing propidium iodide activity, is overlaid in red. Bacterial shapes detected by the algorithm are outlined in cyan.

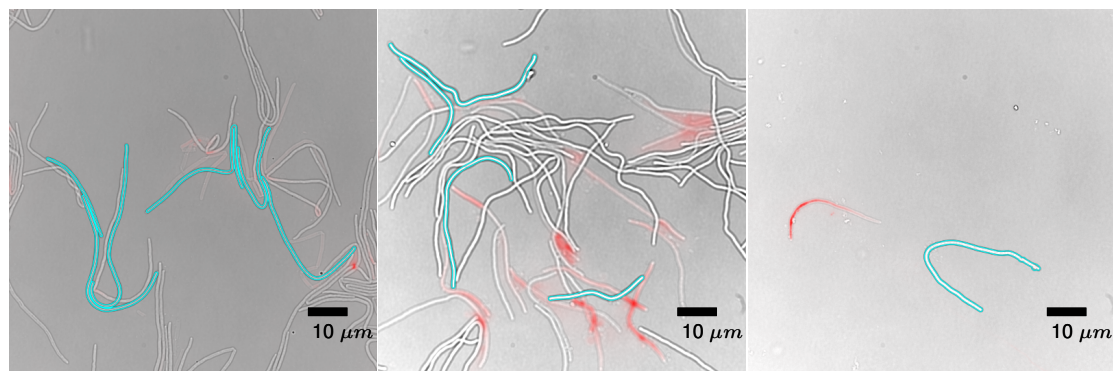


Fig. B26 – Microscopy images of cells treated with ceftazidime. Each image represents a different replicate. We plotted the green channel of the recorded images in greyscale. The red channel, capturing propidium iodide activity, is overlaid in red. Bacterial shapes detected by the algorithm are outlined in cyan.

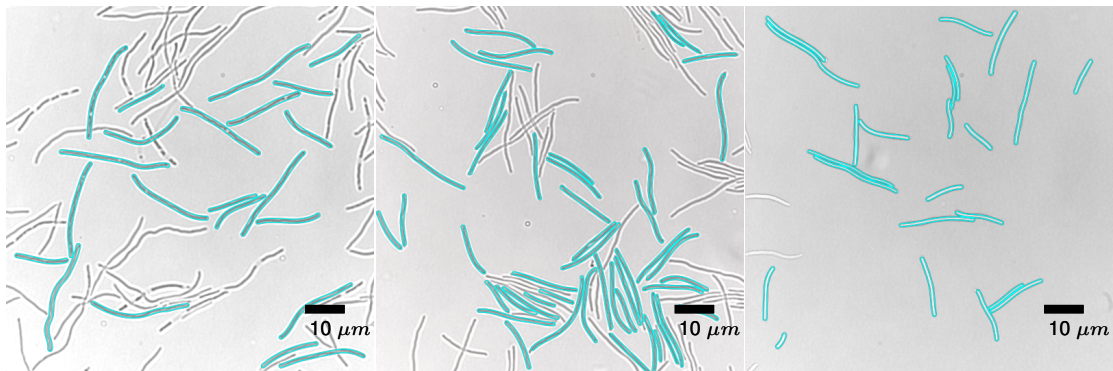


Fig. B27 – Microscopy images of cells treated with ciprofloxacin. Each image represents a different replicate. The white gaps can indicate the start of cell division (cells are not fixed). We plotted the green channel of the recorded images in greyscale. The red channel, capturing propidium iodide activity, is overlaid in red. Bacterial shapes detected by the algorithm are outlined in cyan.

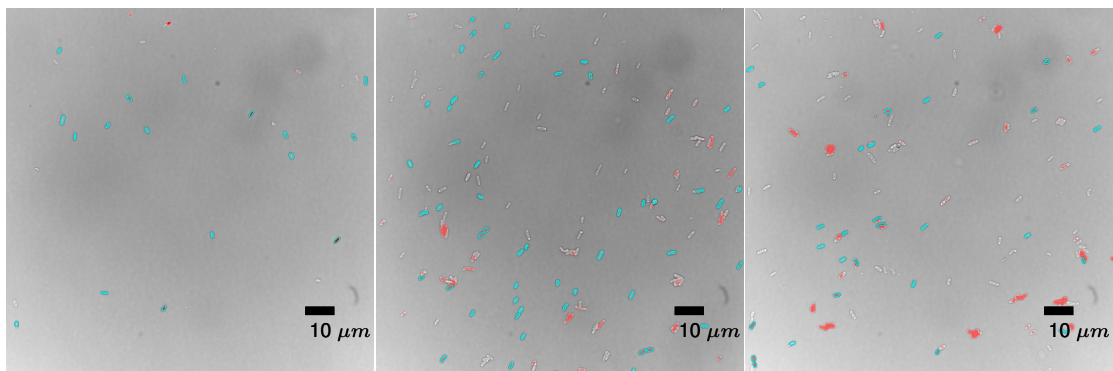


Fig. B28 – Microscopy images of cells treated with colistin. Each image represents a different replicate. We plotted the green channel of the recorded images in greyscale. The red channel, capturing propidium iodide activity, is overlaid in red. Bacterial shapes detected by the algorithm are outlined in cyan.

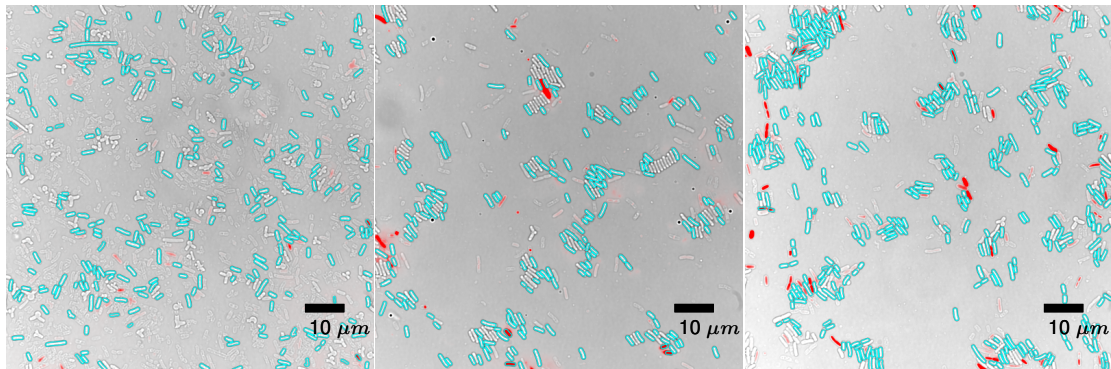


Fig. B29 – Microscopy images of cells treated with fosfomycin. Each image represents a different replicate. We plotted the green channel of the recorded images in greyscale. The red channel, capturing propidium iodide activity, is overlaid in red. Bacterial shapes detected by the algorithm are outlined in cyan.

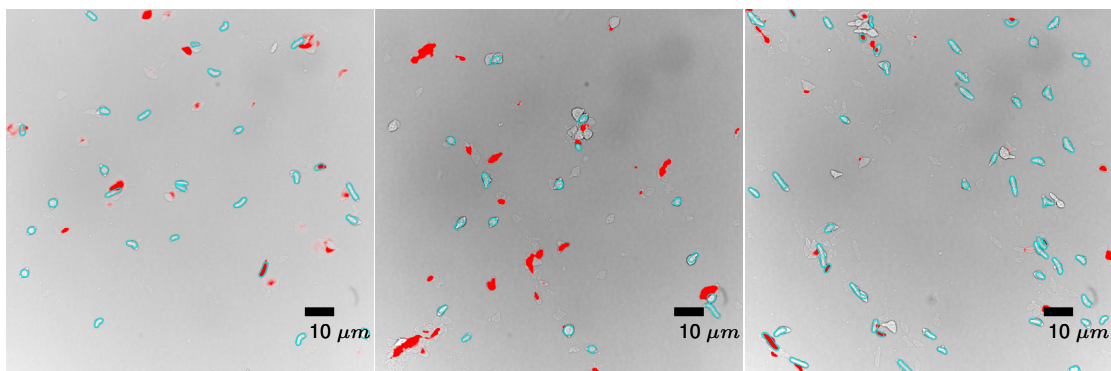


Fig. B30 – Microscopy images of cells treated with meropenem. Each image represents a different replicate. We plotted the green channel of the recorded images in greyscale. The red channel, capturing propidium iodide activity, is overlaid in red. Bacterial shapes detected by the algorithm are outlined in cyan.

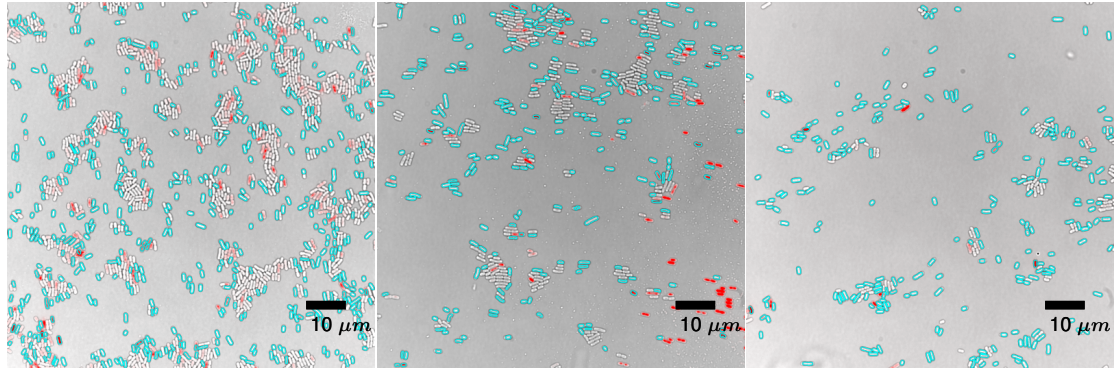


Fig. B31 – Microscopy images of cells treated with pexiganan. Each image represents a different replicate. We plotted the green channel of the recorded images in greyscale. The red channel, capturing propidium iodide activity, is overlaid in red. Bacterial shapes detected by the algorithm are outlined in cyan.

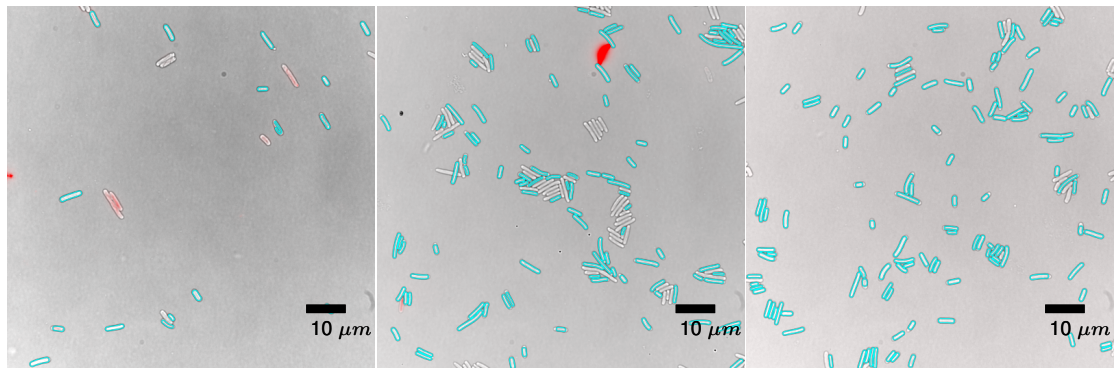


Fig. B32 – Microscopy images of cells treated with rifampicin. Each image represents a different replicate. We plotted the green channel of the recorded images in greyscale. The red channel, capturing propidium iodide activity, is overlaid in red. Bacterial shapes detected by the algorithm are outlined in cyan.

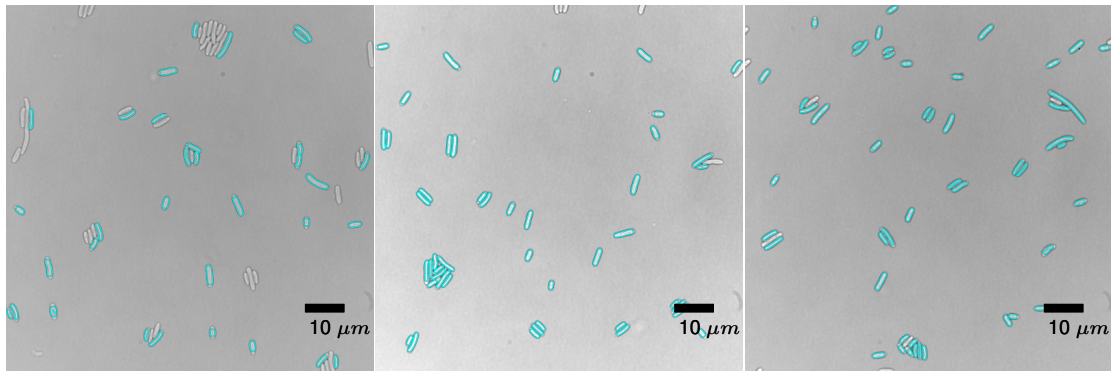


Fig. B33 – Microscopy images of cells treated with tetracycline. Each image represents a different replicate. We plotted the green channel of the recorded images in greyscale. The red channel, capturing propidium iodide activity, is overlaid in red. Bacterial shapes detected by the algorithm are outlined in cyan.

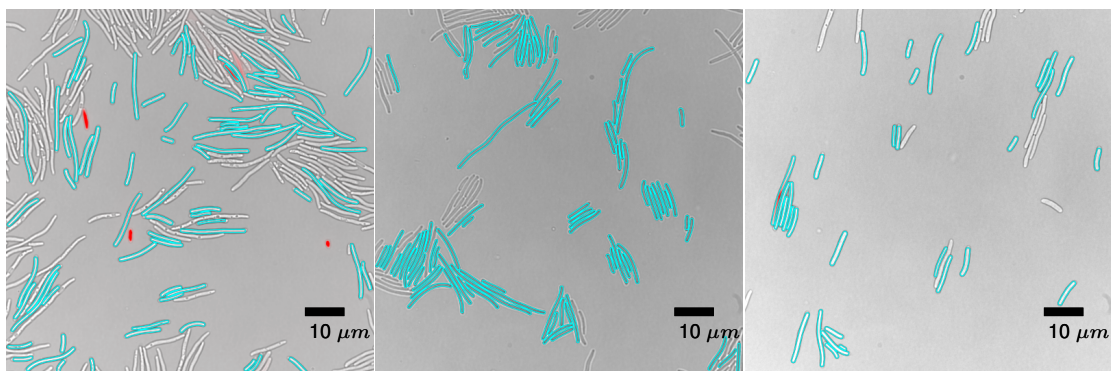


Fig. B34 – Microscopy images of cells treated with trimethoprim. Each image represents a different replicate. We plotted the green channel of the recorded images in greyscale. The red channel, capturing propidium iodide activity, is overlaid in red. Bacterial shapes detected by the algorithm are outlined in cyan.

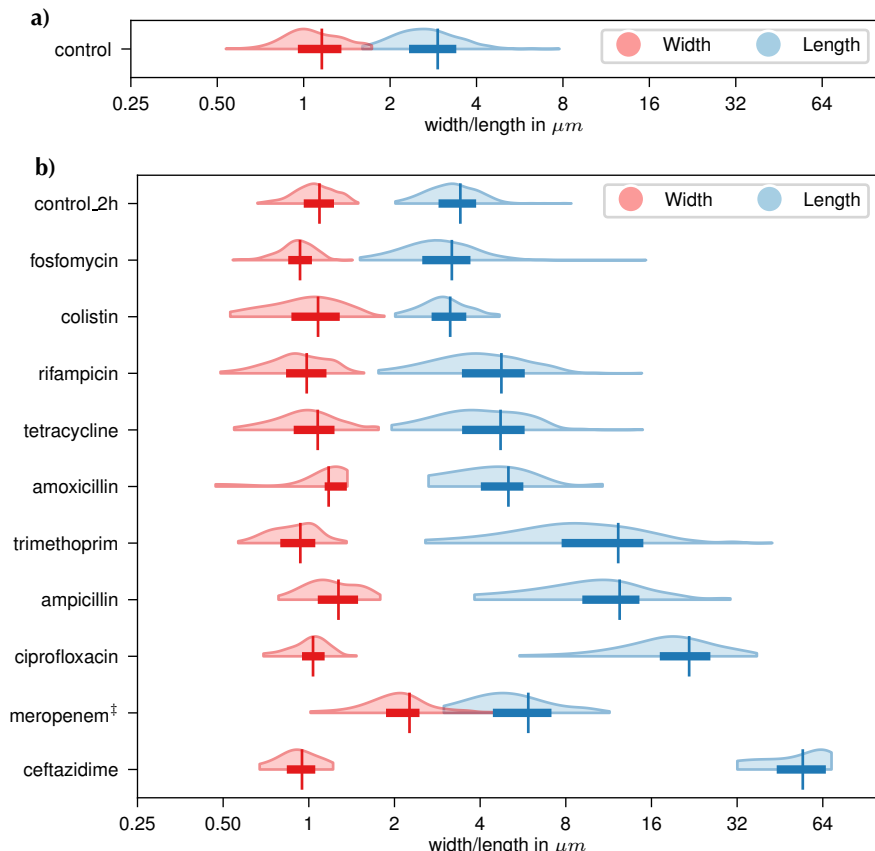


Fig. B35 – Pooled density distributions (95% prediction intervals) of cell widths (red) and lengths (blue), obtained from microscopy images (a) before and (b) after 2 h of antibiotic treatment. Boxes indicate the interquartile range (Q1–Q3), and the mean is marked by (|). <sup>‡</sup> Poor fit quality for meropenem-treated cells, which adopt a lemon-like shape (Fig. B30), due to our algorithm assuming cylindrical geometry.

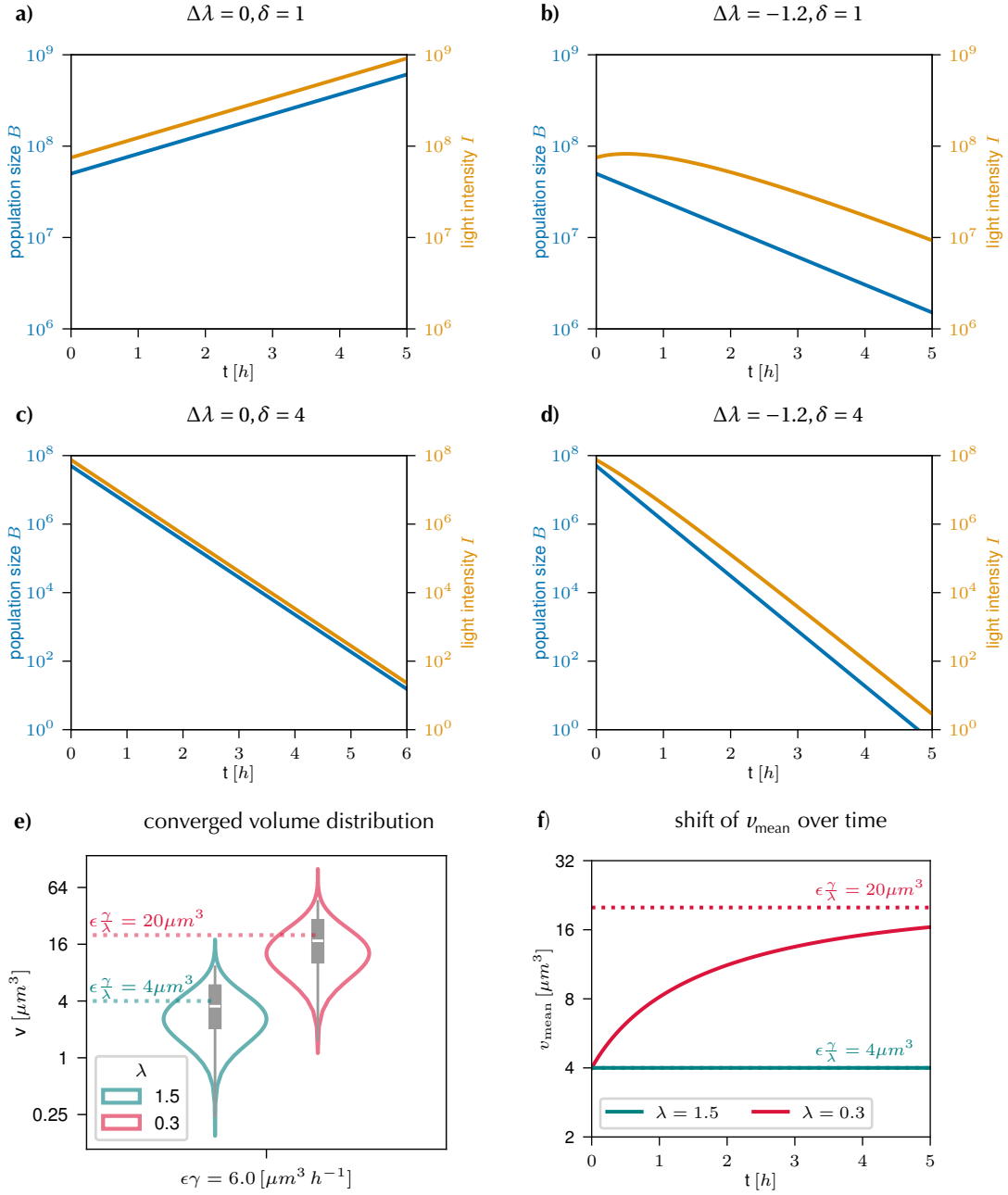


Fig. B36 – Illustrative simulations using the filamentation model relating (a–d) bacterial population size (blue) and light intensity (orange) under different combinations of treatment-induced changes in division rate ( $\Delta\lambda$ ) and death rate ( $\delta$ ). Panel (e) shows the distributions of converged cell volumes for  $\lambda = 0.3$  and  $\lambda = 1.5$ . Panel (f) shows the shift of mean cell volumes over time for  $\Delta\lambda = -1.2$  and  $\Delta\lambda = 0$ . For all simulations, we used  $\lambda_0 = 1.5$ ,  $\gamma = 150$ ,  $\phi = 0.015$ , and  $\epsilon = 0.04$ . As shown in panel (b), treatment-induced filamentation can lead to a temporary discrepancy between luminescence- and CFU-based rates.

Fig. B37 – Example of the probability of colony formation  $p_C = 1 - p_E$  (see Appendix B1) for a single plated bacterium. Blue shows  $p_C$  for a purely bactericidal drug ( $\lambda_T = 0$ ) and red for a purely bacteriostatic drug ( $\delta_T = 0$ ), plotted over the treatment effect  $\tau = \delta_T + \lambda_T$ . In this illustrative example we use  $\lambda_0 = 1.35 h^{-1}$  and  $\delta_0 = 0.1 h^{-1}$ .

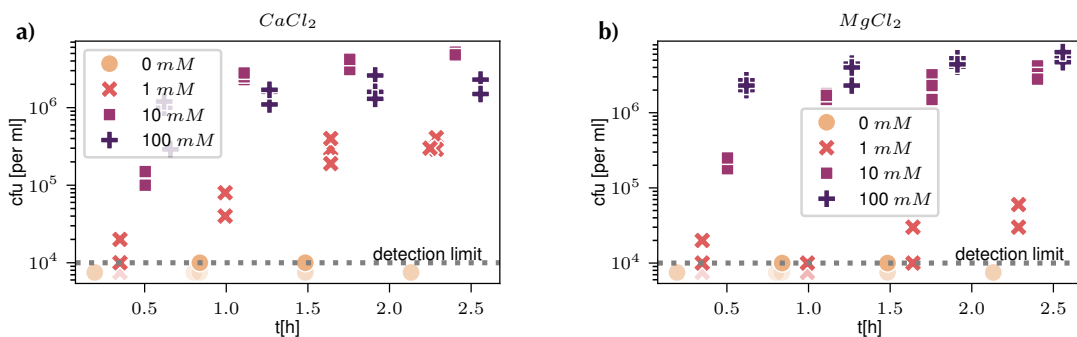
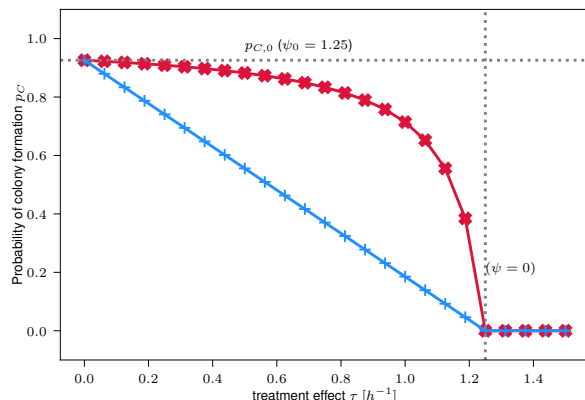


Fig. B38 – CFU measured over time in supplemented dilution media. Bacterial cultures treated for 1 min with 16  $\mu\text{g}/\text{ml}$  pexiganan were diluted (1:100) in PBS supplemented with varying concentrations of (a)  $\text{CaCl}_2$  and (b)  $\text{MgCl}_2$ . Diluted samples were repeatedly plated over time to test whether supplementation prevents further bacterial killing.

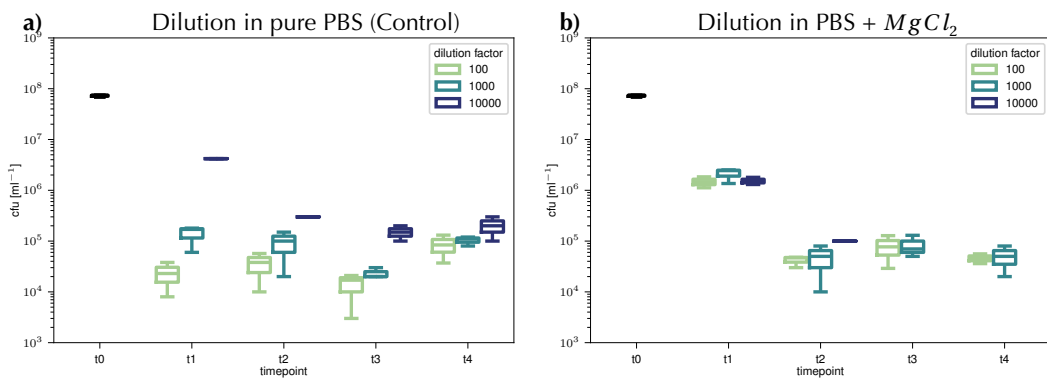


Fig. B39 – CFU time-kill curves for pexiganan, performed manually, comparing dilution in (a) unsupplemented PBS and (b) PBS supplemented with 100 mM  $\text{MgCl}_2$ . Timepoints correspond to:  $t_0 \approx 0\text{s}$ ,  $t_1 \approx 20\text{s}$ ,  $t_2 \approx 2\text{min}$ ,  $t_3 \approx 3\text{min}20\text{s}$ , and  $t_4 \approx 5\text{min}$ . The black boxplot ( $t_0$ ) indicates the pre-treatment bacterial density.

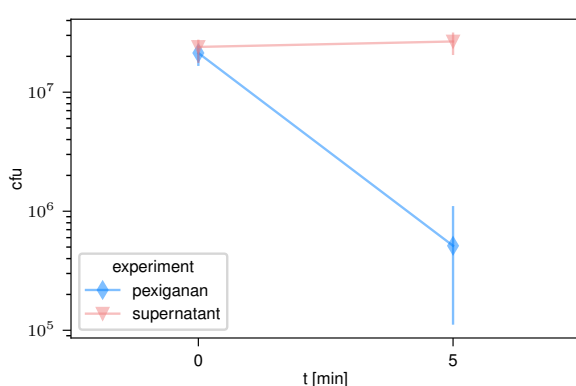


Fig. B40 – Experiment AMP kill curve vs supernatant kill curve. Here we show the original AMP-Killcurve in blue and the change of CFU over time in the supernatant. The error bars show the min/max interval of the three replicates. Table B5 lists the confidence interval and mean for the bootstrapped rates. According to the significance criterion (defined in methods) these two rates are significantly different. The confidence interval of the rate of change of CFU in the supernatant includes zero.

## Bibliography

- [1] J. Coates et al. "Antibiotic-induced population fluctuations and stochastic clearance of bacteria". In: *eLife* 7 (2018), pp. 1–26. issn: 2050084X. doi: [10.7554/eLife.32976](https://doi.org/10.7554/eLife.32976).
- [2] A. S. Novozhilov, G. P. Karev, and E. V. Koonin. "Biological applications of the theory of birth-and-death processes". In: *Brief Bioinform.* 7.1 (2006), pp. 70–85. issn: 14675463. doi: [10.1093/bib/bbk006](https://doi.org/10.1093/bib/bbk006).
- [3] D. G. Kendall. "On the Generalized "Birth-and-Death" Process". In: *Ann. Math. Stat.* 19.1 (1948), pp. 1–15. issn: 0003-4851. doi: [10.1214/aoms/1177730285](https://doi.org/10.1214/aoms/1177730285).
- [4] W. Feller. "Die Grundlagen der Volterrascchen Theorie des Kampfes ums Dasein in wahrscheinlichkeitstheoretischer Behandlung". In: *Acta Biotheor.* 5.1 (1939), pp. 11–40. issn: 15728358. doi: [10.1007/BF01602932](https://doi.org/10.1007/BF01602932).
- [5] M. Muetter. *Software Repo for the Luminescence Paper*. Apr. 2025. doi: [10.5281/zenodo.15261184](https://doi.org/10.5281/zenodo.15261184). url: <https://doi.org/10.5281/zenodo.15261184>.

## Appendix C

### Antimicrobial Combination Effects at Sub-inhibitory Doses do not Reliably Predict Effects at Inhibitory Concentrations

---

**Authors:** Malte Muetter<sup>a</sup>, Daniel C. Angst<sup>a</sup>, Roland R. Regoes<sup>a</sup>, Sebastian Bonhoeffer<sup>a</sup>

<sup>a</sup>*Institute of Integrative Biology, Department for Environmental System Science, ETH Zurich, 8092 Zurich, Switzerland*

---

*Supplementary Information*

### C1 Time weighted net growth rates

We define  $\psi$  as the linearly time weighted average of the temporal net growth rate  $\hat{\psi}$ :

$$\psi = \int_0^T \hat{\psi}(t) w(t) dt = \frac{2}{T^2} \int_0^T (T-u) \hat{\psi}(u) du, \text{ with } w(t) = \frac{2}{T^2} (T-t) \quad (\text{C1})$$

where the kernel  $w(t)$  decreases linearly from  $T$  to 0 and is normalised such  $\int_0^T w(t) dt = 1$ . To derive  $\psi$  from the luminescence trajectories  $I(t) = I_0 e^{\int_0^t \hat{\psi}(u) du}$ , we first normalise

$$y(t) = \frac{I(t)}{I(0)}. \quad (\text{C2})$$

We then define the log-normalised trajectory

$$Y(t) = \ln y(t) = \ln I(t) - \ln I(0) = \int_0^t \hat{\psi}(u) du, \quad (\text{C3})$$

and integrate  $Y(t)$  over time, by applying Fubini's theorem:

$$\int_0^T Y(t) dt = \int_0^T \left( \int_0^t \hat{\psi}(u) du \right) dt = \int_0^T (T-u) \hat{\psi}(u) du, \quad (\text{C4})$$

so that

$$\psi = \frac{2}{T^2} \int_0^T Y(t) dt. \quad (\text{C5})$$

We define the treatment effect as the time-weighted difference between the temporal net growth rates. This corresponds to the scaled area between two curves (control and treatment):

$$\int_0^T (Y_{\text{ctrl}}(t) - Y_{\text{treat}}(t)) dt = \int_0^T (T-t) (\hat{\psi}_{\text{ctrl}}(t) - \hat{\psi}_{\text{treat}}(t)) dt, \quad (\text{C6})$$

and is identical to the difference of the time-weighted net growth rates:

$$\tau = \psi_{\text{ctrl}} - \psi_{\text{treat}} = \frac{2}{T^2} \int_0^T (Y_{\text{ctrl}}(t) - Y_{\text{treat}}(t)) dt. \quad (\text{C7})$$

#### Intuition for $\psi$ and $\tau$ .

*Non-monophasic case.* If rates vary over time,  $\tau$  represents a time-weighted average of instantaneous rate differences,

$$\tau = 2/T^2 \int_0^T (T-t) (\hat{\psi}_{\text{ctrl}}(t) - \hat{\psi}_{\text{treat}}(t)) dt,$$

where the weighting factor  $(T-t)$  decreases linearly from  $T$  to 0. Early rate differences thus contribute more strongly than later ones. This weighting is desirable because an early population reduction affects the population for longer than a delayed effect, even if both trajectories reach the same endpoint.

*Constant-rate case.* If the temporal net growth rate is constant  $\hat{\psi}(t) = \hat{\psi}$ , Equation C5, the time weighted net growth rate, simplifies to:  $\psi = \hat{\psi}$ .

## C2 Quantifying Light Noise

We quantified stray light by using a calibration plate in which six source wells (E5, E12, E20, L5, L12, L20) contained 50  $\mu\text{L}$  of luminescent overnight culture. All other wells were empty. A single luminescence read of all wells yielded raw intensities  $\hat{I}$ . We calculated the ratio of raw light intensities  $\hat{I}_e/\hat{I}_l$  between empty wells  $e$  and the nearest luminescent culture well  $l$  as a function of the distance between their midpoints  $d_{el}$  (with diagonal neighbours at a distance  $\sqrt{2}$ ). For each discrete distance  $d_{el}$ , we summarised ratios by their median to obtain a kernel  $r(d)$  (Fig. C11). We estimate the light contribution from well  $l$  into well  $e$  as  $\hat{I}_{el} = r(d_{el}) \hat{I}_l$ . For each experimental plate and time point, we corrected each well by subtracting received light noise,

$$I_e = \hat{I}_e - \sum_l r(d_{el}) \hat{I}_l, \quad (\text{C8})$$

where the sum is restricted to wells within  $d \leq 3$ .

## C3 Drug conditions and response functions

**Single-drug pharmacodynamic curves.** For each drug  $i$  we describe the relationship between concentration  $c$  and net growth rate by the fitted pharmacodynamic curve

$$f_i(c) = \psi_0 - \frac{(\psi_0 - \psi_{\min,i})(c/z_{\text{MIC},i})^{\kappa_i}}{(c/z_{\text{MIC},i})^{\kappa_i} - (\psi_{\min,i}/\psi_0)}, \quad [0, \infty) \rightarrow [\psi_{\min,i}, \psi_0]. \quad (\text{C9})$$

**Closed-form inversion.** Using Equation C9, the inverse  $f_i^{-1}$  can be written in closed form as

$$f_i^{-1}(\psi) = z_{\text{MIC},i} \left( \frac{(\psi_0 - \psi) \psi_{\min,i} / \psi_0}{(\psi_0 - \psi) - (\psi_0 - \psi_{\min,i})} \right)^{1/\kappa_i}, \quad \psi \in [\psi_{\min,i}, \psi_0]. \quad (\text{C10})$$

**Cartesian conditions.** A *condition* is defined by a set of drug concentrations  $\{c_i\}$ , with drug  $i \in \{\text{AMO, CHL, COL, PEN, POL, TET}\}$ . The control condition corresponds to  $\{c_i = 0 \forall i\}$  and is denoted by  $\emptyset$ .

Throughout this work, quantities ( $X$ ) characterising a treatment condition are written as functions of the underlying condition  $X(\{c_i\})$ . For brevity, we write  $X(c_A)$  when only one drug is present,  $X(c_A, c_B)$  when two drugs are present, and  $X(\emptyset)$  if no drug is present (control).

**Polar pharmacodynamic curves.** For two-drug combinations, conditions are parameterized in polar coordinates  $(z, \phi)$ , and the corresponding effective growth rate is written as

$$g(z, \phi) = \psi_0 - \frac{(\psi_0 - \psi_{\min}(\phi))(z/z_{\text{MIC}}(\phi))^{\kappa(\phi)}}{(z/z_{\text{MIC}}(\phi))^{\kappa(\phi)} - \psi_{\min}(\phi)/\psi_0}. \quad (\text{C11})$$

#### C4 Bliss independence

Bliss independence is defined by assuming that the probabilities of a cell being killed by drugs  $A$  and  $B$  within a fixed observation window are statistically independent [1]. Under this assumption,

$$p_{AB}^{\text{Bliss}} = p_A + p_B - p_A p_B, \quad (\text{C12})$$

where  $p_A$  and  $p_B$  denote the single-drug kill probabilities within  $T$ .

**Time-varying hazards.** Let  $\hat{\tau}_i(t) \geq 0$  denote a time-dependent kill hazard under treatment  $i$ . The survival fraction at time  $T$  is  $S_i(T) = \exp(-\int_0^T \hat{\tau}_i(u) du)$ . Bliss independence implies multiplicative survival  $S_{AB}(T) = S_A(T) S_B(T)$ , hence additive cumulative hazards:

$$\int_0^T \hat{\tau}_{AB}^{\text{Bliss}}(u) du = \int_0^T \hat{\tau}_A(u) du + \int_0^T \hat{\tau}_B(u) du. \quad (\text{C13})$$

To connect this survival formulation to the growth-based log-trajectories, we interpret the instantaneous treatment effect as the reduction in temporal net growth relative to the untreated control, i.e.  $\hat{\tau}_i(t) = \hat{\psi}_{\text{ctrl}}(t) - \hat{\psi}_i(t)$ . Substituting  $Y_i(t) = \int_0^t \hat{\psi}_i(u) du$  (Equation C3), it follows that:

$$Y_i(t) = Y_{\text{ctrl}}(t) - \int_0^t \hat{\tau}_i(u) du.$$

Using additive cumulative hazards under Bliss then yields

$$Y_{AB}^{\text{Bliss}}(t) = Y_A(t) + Y_B(t) - Y_{\text{ctrl}}(t). \quad (\text{C14})$$

Integrating Equation C14 over time yields the Bliss prediction for the effective treatment effect:

$$\tau^{\text{Bliss}}(c_A, c_B) = \tau(c_A) + \tau(c_B). \quad (\text{C15})$$

**Bliss-based interaction score  $\mu$ .** Based on the Bliss expectation for a combination at concentrations  $(c_A, c_B)$ , we define the interaction score as the normalised divergence from the expectation:

$$\mu(c_A, c_B) = \frac{\tau(c_A) + \tau(c_B) - \tau(c_A, c_B)}{\text{median}(\tau(c_A)) + \text{median}(\tau(c_B))}. \quad (\text{C16})$$

To avoid division by zero, normalisation is performed using the medians of the monotherapy effects. The score is only evaluated for conditions  $(c_A, c_B)$  classified as eligible, defined as those where the combined effect  $\tau(c_A, c_B)$  and at least one of the single-drug effects,  $\tau(c_A)$  or  $\tau(c_B)$ , are significant.

**Interpreting the bliss interaction score  $\mu$ .**

Positive values of  $\mu$  indicate synergy ( $\tau(c_A, c_B) > \tau(c_A) + \tau(c_B)$ ), negative values indicate antagonism, and  $\mu = 0$  corresponds to independence.

## C5 Loewe additivity

Loewe additivity is a form of dose additivity, formalising self-additivity, i.e. that a drug combined with itself should behave like a higher dose of the same drug [2]. This concept is independent of the particular choice of effect measure, provided the effect can be represented on a shared, monotone dose-response scale. In our case, this effect scale is the effective net growth rate  $\psi$  (see Equation C5).

For a combination with the observed effect  $\psi(c_A, c_B)$ , Loewe additivity requires that the fractions of the equivalent single-drug concentrations sum to one,

$$\frac{c_A}{f_A^{-1}(\psi(c_A, c_B))} + \frac{c_B}{f_B^{-1}(\psi(c_A, c_B))} = 1, \quad (\text{C17})$$

where  $f_A$  and  $f_B$  are the pharmacodynamic curves mapping concentrations to  $\psi$ , and  $f_A^{-1}$  and  $f_B^{-1}$  map an effect level  $\psi$  to the corresponding equivalent single-drug concentration. For the well-based interaction analysis, we use the fitted pharmacodynamic curve (Equation C9) as the pharmacodynamic function  $f_i$ , whereas for the surface-based analysis, we infer  $f_i$  from the single-drug edge profiles of the checkerboard surface splines. The Loewe prediction  $\psi_{\text{Loewe}}(c_A, c_B)$  is obtained by numerically solving Equation 4.2 for  $\psi$ .

**Loewe interaction score ( $\nu$ ).** We quantify deviations from Loewe additivity using:

$$\nu(c_A, c_B) = \frac{c_A}{f_A^{-1}(\psi(c_A, c_B))} + \frac{c_B}{f_B^{-1}(\psi(c_A, c_B))} - 1. \quad (\text{C18})$$

Because  $f_A^{-1}$  and  $f_B^{-1}$  are only defined on  $\text{Im}(f_A) = [\psi_{\min,A}, \psi_0]$  and  $\text{Im}(f_B) = [\psi_{\min,B}, \psi_0]$ ,  $\nu$  is only defined if

$$\psi(c_A, c_B) \in \text{Im}(f_A) \cap \text{Im}(f_B) = [\max(\psi_{\min,A}, \psi_{\min,B}), \psi_0]. \quad (\text{C19})$$

The score is only evaluated for conditions  $(c_A, c_B)$  classified as eligible, defined as those where the combined effect  $\tau(c_A, c_B)$  and at least one of the single-drug effects,  $\tau(c_A)$  or  $\tau(c_B)$ , are significant.

### Interpreting the Loewe interaction score $\nu$ .

By construction  $\nu = 0$  corresponds to Loewe additivity,  $\nu < 0$  indicates synergy, and  $\nu > 0$  indicates antagonism.

Because Loewe additivity requires equivalent single-drug concentrations for both drugs at the observed effect level,  $\nu$  can only be evaluated when  $\psi(c_A, c_B)$  lies in the overlap of the two single-drug effect ranges, i.e.  $\psi \geq \max(\psi_{\min,A}, \psi_{\min,B})$ .

## C6 Peptide–antibiotic interaction model

We consider two drugs,  $A$  and  $B$ , acting on a population with a size trajectory  $x(t)$ . Drug  $A$  represents a peptide-like effect that causes an instantaneous multiplicative reduction in population size by a factor  $\alpha \in (0, 1]$ , whereas drug  $B$  represents a conventional antibiotic that changes the subsequent net growth rate but does not cause an initial drop. We assume that the combination of two drugs induces a sharp drop by the factor  $\alpha$  followed by net growth, determined by drug  $B$ :

$$\begin{aligned}x_{\text{ctrl}}(t) &= x_0 \exp(\hat{\psi}_{\text{ctrl}} t), \\x_B(t) &= x_0 \exp(\hat{\psi}_B t), \\x_A(t) &= \alpha x_{\text{ctrl}}(t), \\x_{AB}(t) &= \alpha x_B(t),\end{aligned}$$

and:

$$\begin{aligned}Y_{\text{ctrl}}(t) &= \ln x_0 + \hat{\psi}_{\text{ctrl}} t, \\Y_B(t) &= \ln x_0 + \hat{\psi}_B t, \\Y_A(t) &= Y_{\text{ctrl}}(t) + \ln \alpha, \\Y_{AB}(t) &= Y_B(t) + \ln \alpha.\end{aligned}$$

Using the definition of effective-rate  $\tau_i = \frac{2}{T^2} \int_0^T (Y_i(t) - Y_{\text{ctrl}}(t)) dt$ , we obtain the following.

$$\tau_A = \frac{2}{T^2} \int_0^T (-\ln \alpha) dt, \quad \tau_B = \frac{2}{T^2} \int_0^T (\hat{\psi}_{\text{ctrl}} - \hat{\psi}_B) t dt,$$

and

$$\tau_{AB} = \frac{2}{T^2} \int_0^T ((\hat{\psi}_{\text{ctrl}} - \hat{\psi}_B) t - \ln \alpha) dt. \quad (\text{C20})$$

Separating the two terms in Equation C20 yields

$$\tau_{AB} = \tau_A + \tau_B, \quad (\text{C21})$$

which matches the Bliss expectation for the combined treatment effect.

## C7 Condition-wise interaction inference on the checkerboard

Each condition  $\{c_i\}$  is realised by a pool of biological replicate wells  $\mathcal{W}(c_A, c_B)$ , from which effective growth rates are inferred, as described above. Treatment effects are estimated by bootstrap resampling from the pools of replicate wells. We draw  $B = 200$  pairs consisting of one control well and one condition well, sampled with replacement from  $\mathcal{W}(\emptyset)$  and  $\mathcal{W}(c_A, c_B)$ , respectively. For each draw  $b$ , the treatment effect is defined as

$$\tau_b(c_A, c_B) = \psi_b(\emptyset) - \psi_b(c_A, c_B),$$

yielding a bootstrap distribution of treatment effects.

For combination conditions, the corresponding single-drug growth rates  $\psi_b(c_A, 0)$  and  $\psi_b(0, c_B)$  are sampled simultaneously and included in each bootstrap draw, as they are required for interaction analysis.

**Regime-wise aggregation across checkerboard conditions.** To summarise interactions for a given drug pair within a regime (sub-inhibitory or inhibitory), we combine the condition-wise bootstrap interaction estimates from all eligible checkerboard cells. For each regime, we sampled 200 eligible conditions with replacement, using sampling probabilities proportional to

$$w(\phi) = \sin(2\phi). \quad (\text{C22})$$

This excludes single-drug checkerboard edges and gives the highest weight to near-equal mixing. For every sampled condition, we draw one interaction score from its condition-wise bootstrap distribution. Repeating this procedure yields an aggregated distribution, from which we report the median and central 95% interval for the regime-level interaction estimate.

## C8 Continuous interaction surfaces and geometric exploration

**Density-based restriction of the surface domain.** For some drugs, the empirical data density decreases at high concentrations as trajectories drop below the detection limit and are excluded. We therefore restrict the checkerboard to the high-density subdomain. For each drug pair, we compute, for every grid cell  $(i, j)$ , the valid fraction  $f(i, j) = n_{\text{valid}}(i, j)/4$  (with  $n_{\text{valid}}$  counting non-NaN values of  $\psi$ ). We then fit a monotone-decreasing helper surface  $f_{\text{dens}}(i, j)$  by alternating one-dimensional isotonic regression sweeps (`sklearn.isotonic.IsotonicRegression`) along both index axes, followed by bivariate spline interpolation on the  $(i, j)$  grid (`scipy.interpolate.RectBivariateSpline`). Cells with  $f_{\text{dens}}(i, j) < f_{\text{min}}$  are excluded, and all subsequent bootstrap resampling and surface-spline fitting are performed only on the remaining cells.

**Bootstrap datasets and coordinate transform.** For each pair of drugs  $(A, B)$  we first collect all wells belonging to that pair together with their estimated effective net growth rates  $\psi$ . Each well is indexed by a normalised concentration pair  $(z_A, z_B)$ . To stabilise interpolation near zero, we transform the axes to  $Z_A = \log_2(z_A + 1)$  and  $Z_B = \log_2(z_B + 1)$ . For each bootstrap draw  $b$  we generate a resampled surface dataset by sampling, with replacement, one well for every occupied grid point, and retaining its triplet  $(Z_A, Z_B, \psi)$ .

**Monotone surface construction.** For each bootstrap dataset we enforce a monotone-decreasing  $\psi$ -surface by alternating one-dimensional isotonic regressions along rows and columns. This is important to ensure that the backtransformation  $z_\phi(\psi)$  is unique. Specifically, for each column and then for each row we apply an isotonic regression with a nonincreasing constraint using `sklearn.isotonic.IsotonicRegression` [3]. On each monotone grid we fit a bivariate spline  $s_{AB}^{(b)}(Z_A, Z_B)$  using `scipy.interpolate.RectBivariateSpline` with a linear basis functions in both directions. For each drug combination we calculate a consensus surface  $\psi^{\text{cons}}$  based on the median of the single splines.

## C9 Single-drug inoculum effect analysis

During data analysis, we noted that inocula varied more than expected, which we traced to variability induced by the pintool. Across all wells, the pre-treatment luminescence mean was ( $\langle I_0 \rangle = 4.61 \times 10^4$  RLU) and the standard deviation was ( $\sigma(I_0) = 6.89 \times 10^4$  RLU), between experiments ( $\sigma_{\text{between}} = 4.33 \times 10^4$  RLU) and within experiments ( $\sigma_{\text{within}} = 5.47 \times 10^4$  RLU). To investigate whether the observed net growth rates  $\psi$  systematically depended on inoculum size, we used the pre-treatment luminescence signal ( $I_0$ ) as a proxy for initial cell density.

For all single-drug conditions, we fitted an ordinary least-squares regression of  $\psi$  on  $I_0$  to obtain a concentration-specific slope  $\beta_{\text{inoculum}}(c_i)$  together with a confidence interval, the value  $p$  and the determination coefficient  $R^2$ . These slopes and their uncertainty summaries were visualised

as concentration–slope profiles with 95% intervals in Fig. C12. Across AMO, CHL, PEN, and TET, the estimated slopes were negligible across concentrations, whereas COL and POL showed the strongest dependence on  $I_0$  at intermediate concentrations (around 1  $\frac{\mu\text{g}}{\text{mL}}$ ).

To assess whether inoculum size varies systematically along the one-dimensional concentration index, we pooled all single-drug wells and mapped each well to its concentration index. We then performed a permutation test by permuting the light intensity across the concentration indices to obtain a null distribution. We found no evidence for a systematic trend of inoculum size with index in our data ( $p = 0.092$ ), suggesting that inoculum variation contributes noise but does not introduce a strong directional bias along the concentration series. Consistent with this, the inoculum effect primarily adds scatter at intermediate concentrations of COL and POL, contributing to the increased spread in the corresponding single-drug PD curves.

APPENDIX C. ANTIMICROBIAL COMBINATION EFFECTS AT SUB-INHIBITORY DOSES DO NOT RELIABLY PREDICT EFFECTS AT INHIBITORY CONCENTRATIONS

---

Table C1 – Fitted single-drug pharmacodynamic (PD) curve parameters for Equation C9. For each antibiotic, we report the point estimates of  $\psi_0$ ,  $\psi_{\min}$ ,  $\kappa$ , and  $z_{\text{MIC}}$ , together with the corresponding lower (L) and upper (U) uncertainty bounds (95% intervals).

drug	$\psi_0$	$\psi_0^{\text{L}}$	$\psi_0^{\text{U}}$	$\psi_{\min}$	$\psi_{\min}^{\text{L}}$	$\psi_{\min}^{\text{U}}$	$\kappa$	$\kappa^{\text{L}}$	$\kappa^{\text{U}}$	$z_{\text{MIC}}$	$z_{\text{MIC}}^{\text{L}}$	$z_{\text{MIC}}^{\text{U}}$
POL	1.70	1.47	1.94	-4.43	-5.37	-3.48	1.48	1.01	1.95	0.51	0.42	0.59
TET	1.77	1.75	1.79	-0.24	-0.28	-0.20	1.15	1.07	1.22	15.15	13.80	16.49
AMO	1.73	1.70	1.77	-3.93	-4.02	-3.84	1.69	1.60	1.77	8.42	8.18	8.66
COL	1.78	1.60	1.96	-6.08	-6.97	-5.18	1.48	1.18	1.78	0.58	0.52	0.65
CHL	1.78	1.75	1.81	-0.93	-1.02	-0.84	0.96	0.88	1.04	54.11	50.45	57.77
PEN	1.78	1.73	1.83	-4.54	-4.84	-4.24	1.07	0.99	1.16	153.86	146.77	160.94

Table C2 – Interaction types (N: no-interaction, S: synergistic, A: antagonistic) for each drug combination based on Loewe additivity ( $\mu$ ) and Bliss independence ( $\nu$ ), evaluated separately for sub-inhibitory and inhibitory concentration regimes based on bootstrap confidence intervals.

drug A	drug B	Bliss score $\mu$		Loewe score $\nu$	
		sub-inhibitory	inhibitory	sub-inhibitory	inhibitory
AMO	CHL	N	A	A	N
AMO	COL	N	A	A	A
AMO	PEN	S	A	N	N
AMO	POL	A	A	A	A
AMO	TET	A	A	A	N
CHL	COL	N	S	N	S
CHL	PEN	N	A	A	N
CHL	POL	S	S	S	S
CHL	TET	N	A	S	S
COL	PEN	A	A	A	A
COL	POL	N	N	A	N
COL	TET	N	S	A	S
PEN	POL	N	N	A	N
PEN	TET	N	A	A	N
POL	TET	N	S	A	S

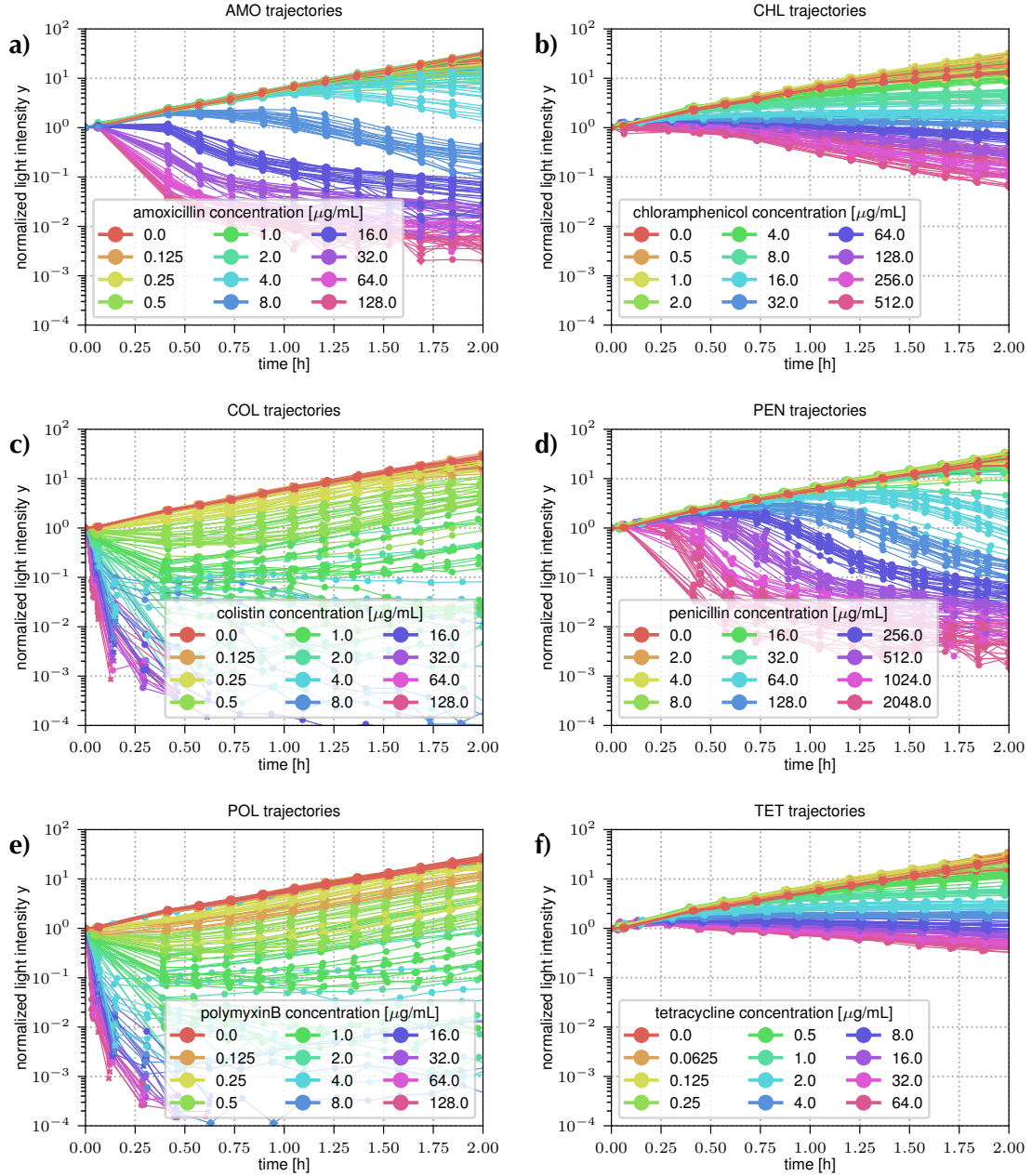


Fig. C1 – Normalised luminescence trajectories  $y = \frac{I}{I(0)}$  for single-drug treatments. Panels (a–f) show trajectories across 12 single-drug concentrations for amoxicillin (AMO), chloramphenicol (CHL), colistin (COL), penicillin (PEN), polymyxin B (POL), and tetracycline (TET), respectively. For each concentration, we show 20 replicate curves obtained from five independent combination experiments (per drug) with four biological replicates each. For trajectories that fall temporarily (less than 20% of datapoints) below the detection limit, we substituted the respective timepoints with the detection limit (diamonds). The last regular datapoint of an invalid trajectory (more than 20% below the detection limit) is indicated with an “x”, and all other datapoints are shown as circles.

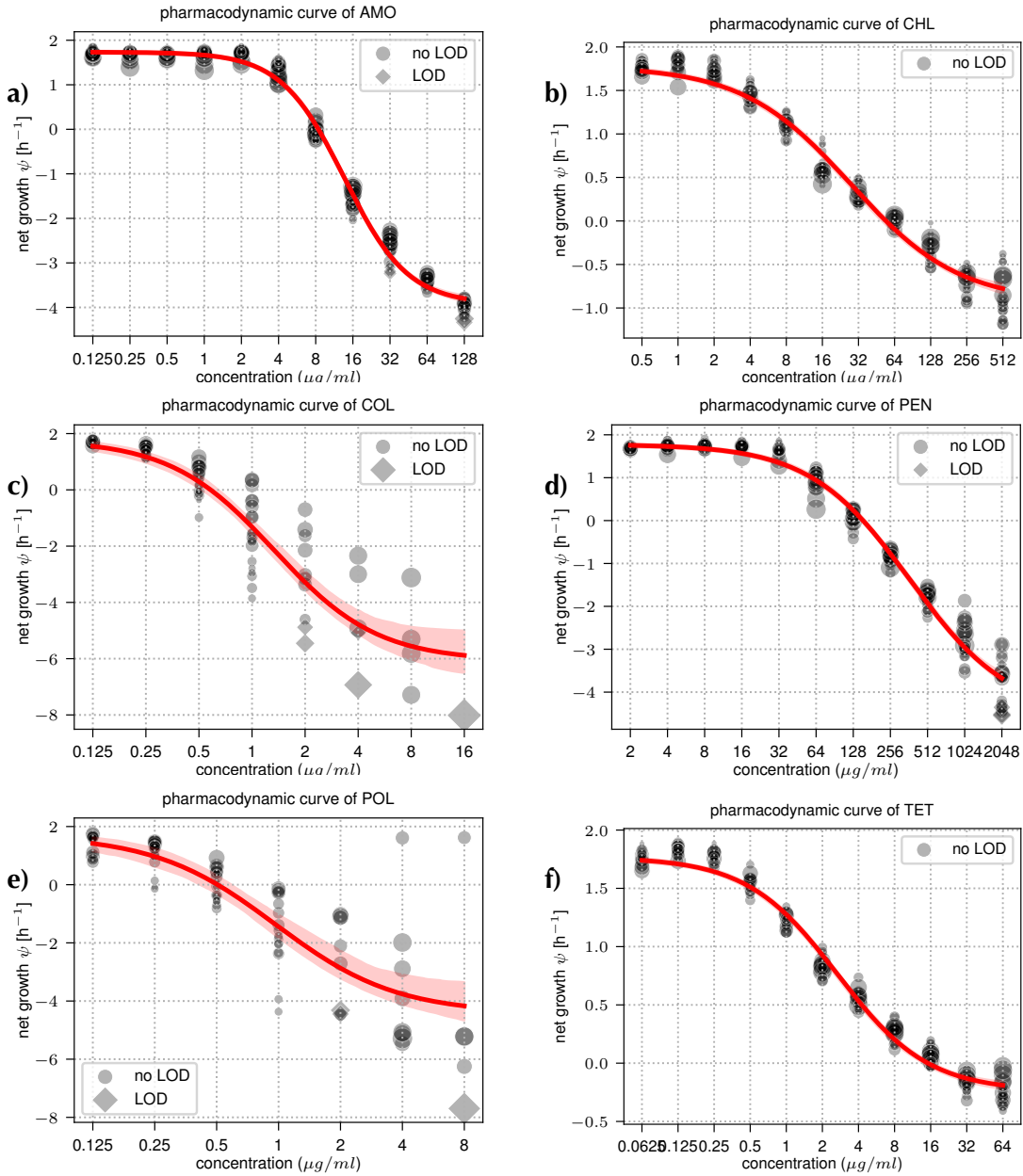


Fig. C2 – Panels (a–f) show the single-drug pharmacodynamic curves corresponding to the time-course data for amoxicillin (AMO), chloramphenicol (CHL), colistin (COL), penicillin (PEN), polymyxin B (POL), and tetracycline (TET), respectively. For each concentration, we aggregate time-weighted net growth rate estimates from 20 replicates obtained from five independent combination experiments (per drug) with four biological replicates each. We included only “valid” estimates, defined as trajectories with less than 20% of timepoints below the LoD. Valid estimates containing LoD-censored timepoints are shown as diamonds, and estimates without LoD-censored timepoints are shown as circles. Marker size is scaled with  $\log_{10}$  of the inoculum  $I(0)$ . Curve parameters are fitted per drug using nonlinear least squares, and the shown confidence band is obtained from the parameter covariance matrix.

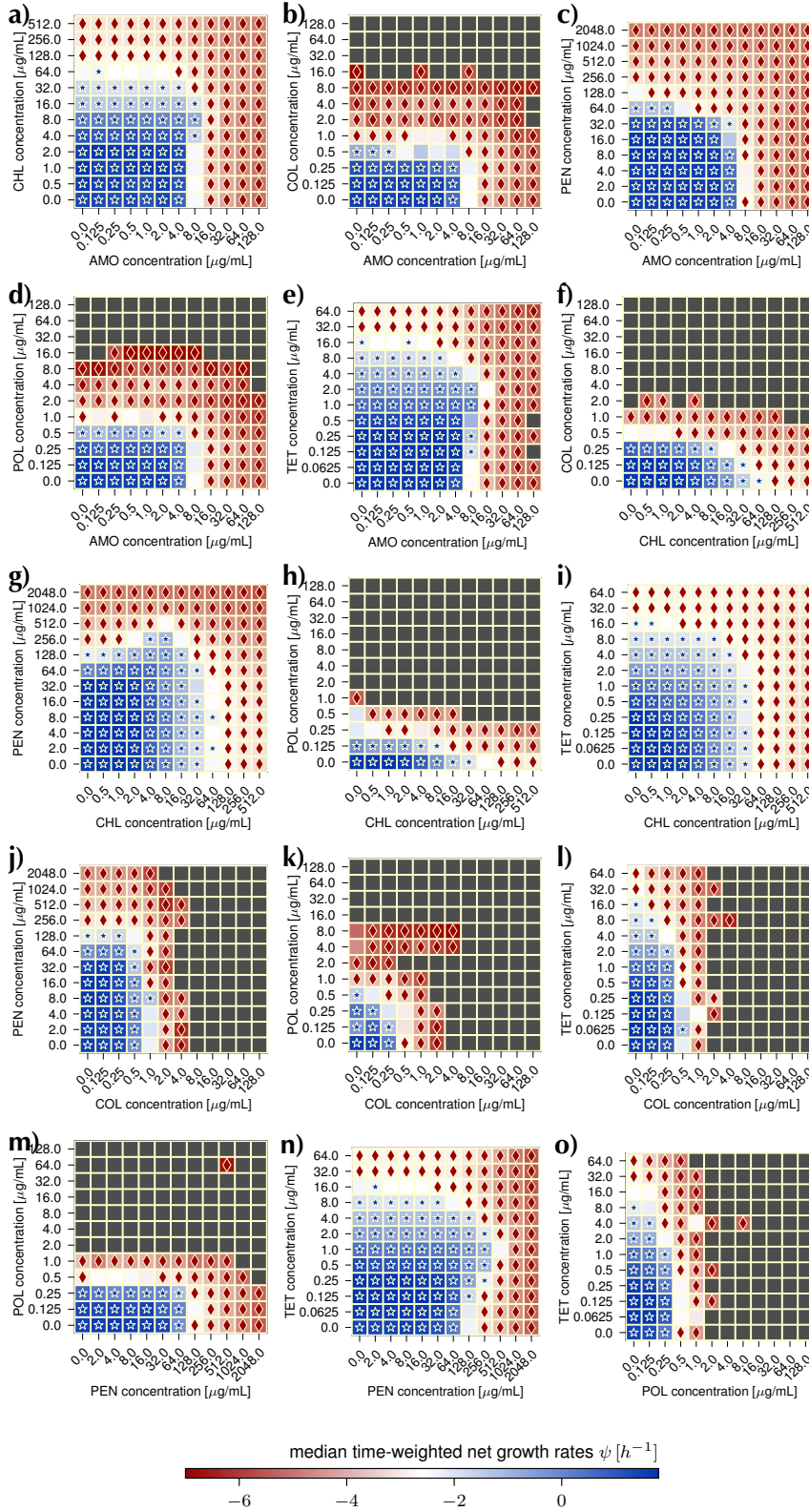
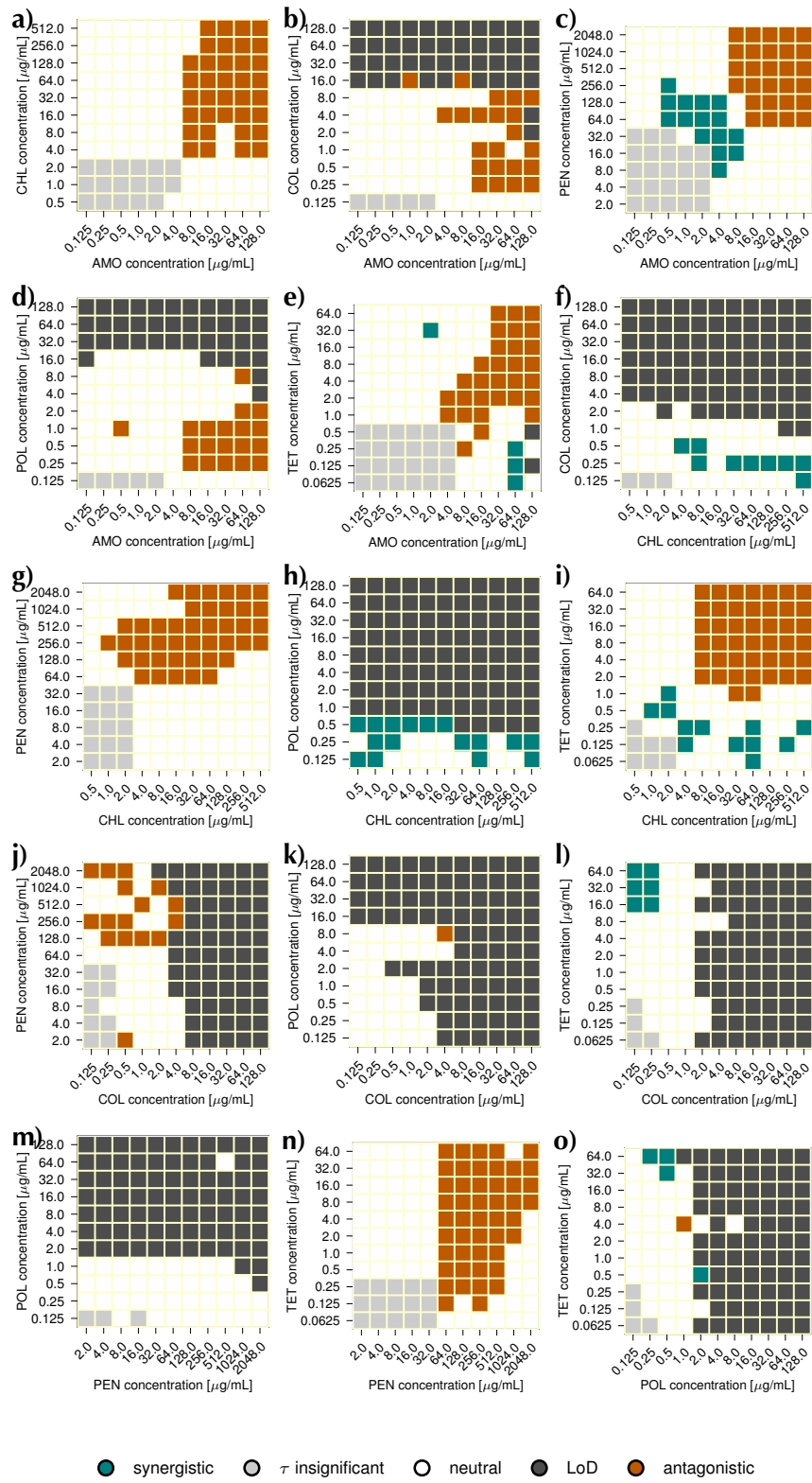


Fig. C3 – Median time-weighted net growth rate  $\psi$  across all drug combinations measured in checkerboard assays. Each panel corresponds to one drug pair, and each cell represents a condition  $(c_A, c_B)$ . Colors indicate the median estimate of  $\psi$  across bootstrap resamples. Stars denote significantly positive growth, diamonds significantly negative growth (see Methods).

Fig. C4 – Bliss interaction classification based on the distribution of Bliss interaction scores  $\mu$ . For each concentration pair, treatment effects were resampled to obtain a distribution of the Bliss interaction index  $\mu$ . Cells are colored according to statistical significance: teal indicates synergistic interactions (95% confidence interval entirely below zero), orange indicates antagonistic interactions (95% confidence interval entirely above zero), and white indicates no significant deviation from additivity. We overlaid cells where all estimates were “invalid” due to LoD in dark grey, and cells that are not eligible (because either the combined treatment effect or both single-drug treatment effects are not significant) in light grey (see Methods, Data preprocessing).



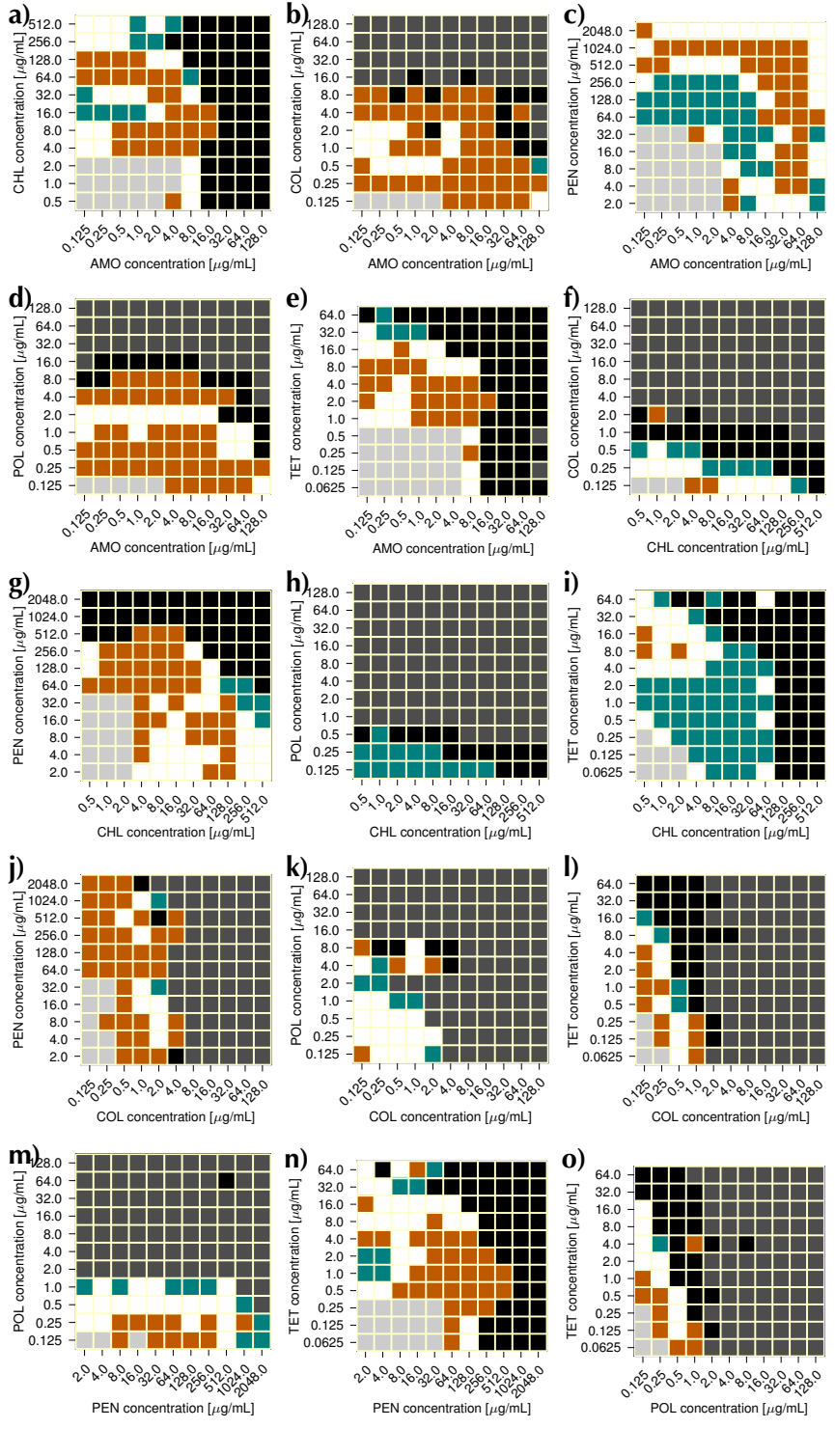


Fig. C5 – Loewe interaction classification based on the distribution of Loewe interaction scores  $v$ . Teal indicates significant synergy (95% confidence interval entirely below 0), orange indicates significant antagonism (95% confidence interval entirely above 0), and white indicates that the confidence interval contains 0. We overlaid cells where all estimates were “invalid” due to LoD in dark grey, and cells that are not eligible (because either the combined treatment effect; or both single-drug treatment effects are not significant) in light grey. Black cells indicate that Loewe additivity is undefined because the combined time-weighted net growth is smaller than at least one of the single-drug minimal net growth rates (see Methods, Data preprocessing).

● synergistic   ●  $\tau$  insignificant   ○ neutral   ● LoD   ● antagonistic   ●  $v$  undefined

APPENDIX C. ANTIMICROBIAL COMBINATION EFFECTS AT SUB-INHIBITORY DOSES DO NOT RELIABLY PREDICT EFFECTS AT INHIBITORY CONCENTRATIONS

a)

a)

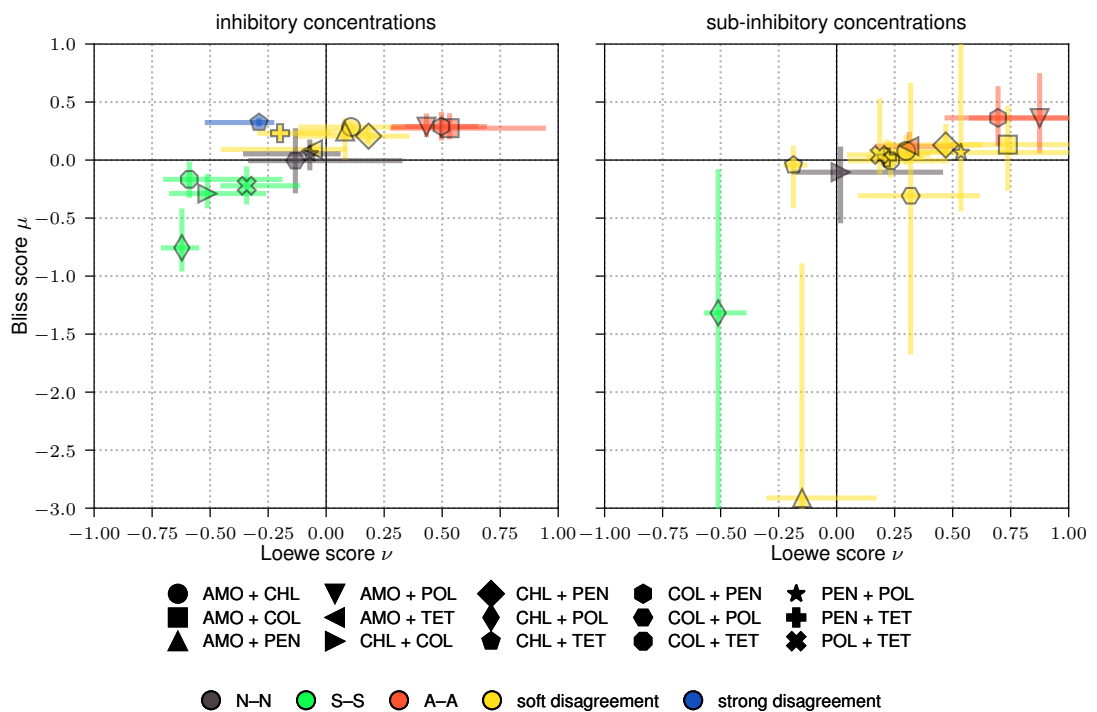


Fig. C6 – Comparison of Loewe and Bliss interaction scores in two growth regimes. (a) Inhibitory (super-MIC) concentrations. (b) Sub-inhibitory (sub-MIC) concentrations. Each point represents a drug combination with error bars indicating bootstrap confidence intervals. Colors encode agreement or disagreement between Loewe and Bliss classifications.

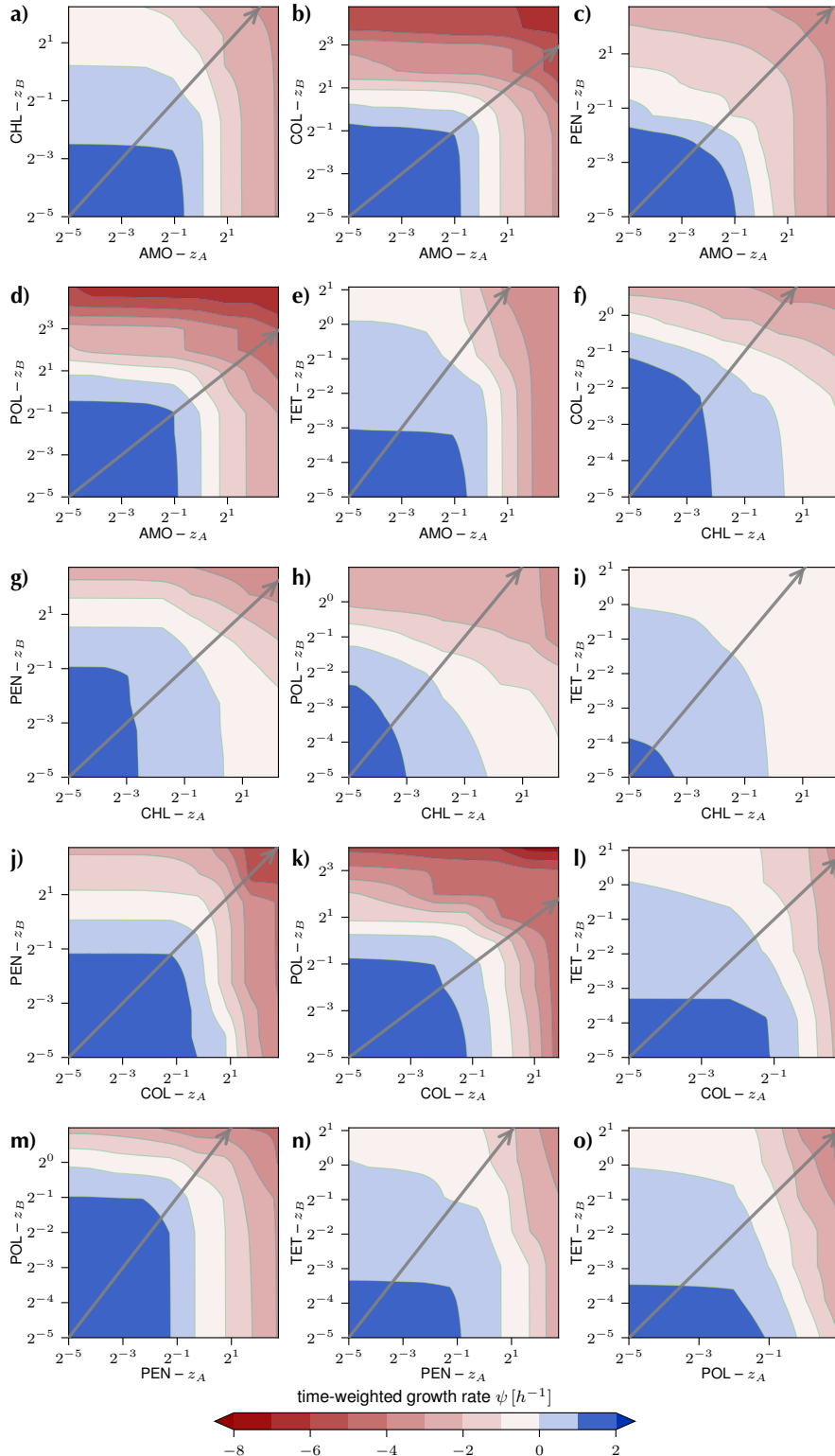
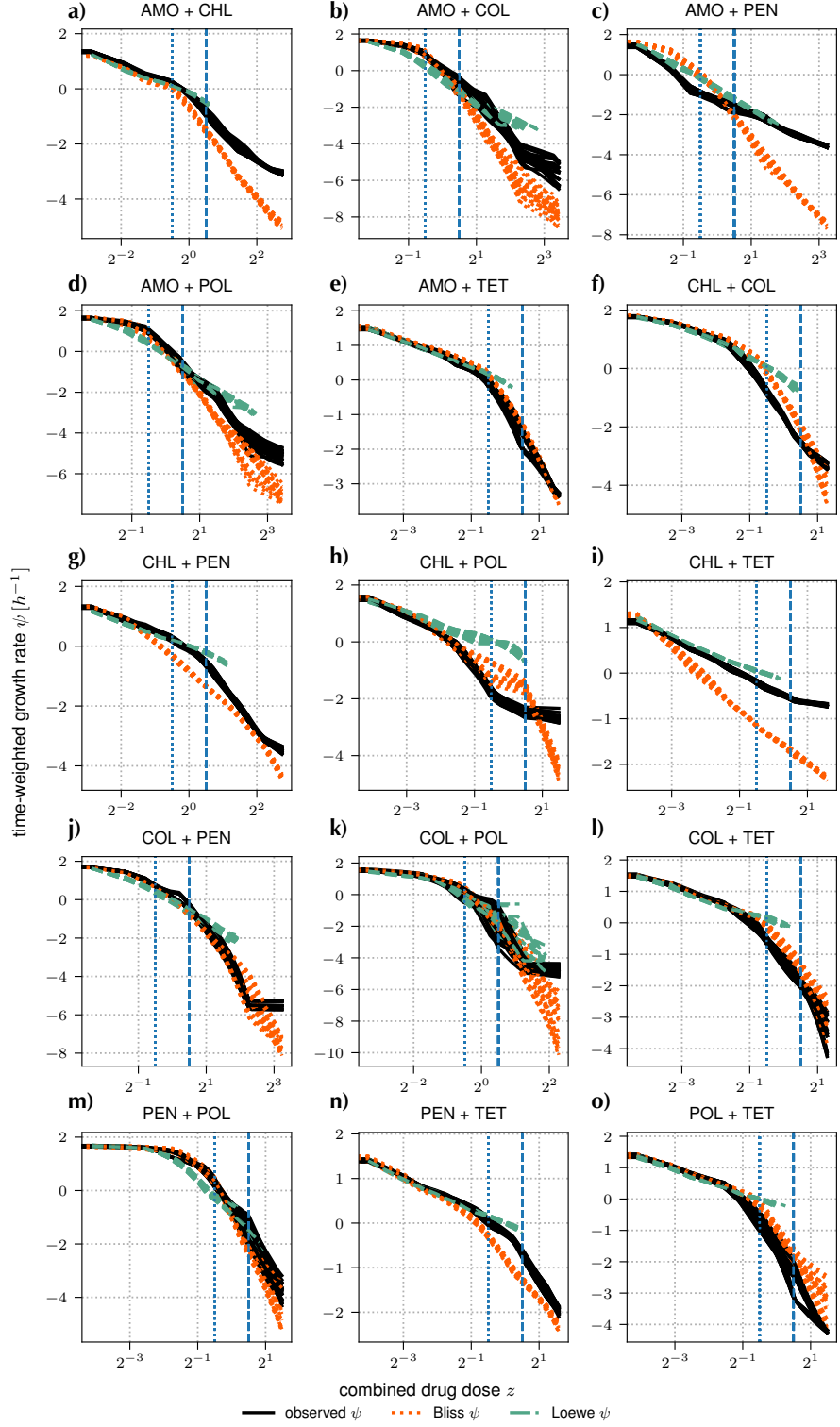


Fig. C7 – Time-weighted net growth rate surfaces for all drug combinations. Each panel shows the topography of the median spline, estimated from the empirical time-weighted net growth rate estimates on the concentration grid. Colors indicate the magnitude of  $\psi$ , with negative values (reds) corresponding to net killing and positive values (blues) to net growth.

Fig. C8 – Polar pharmacodynamic curves for all drug combinations. For each drug pair, we show one-dimensional cuts through the  $\psi$ -surface splines at  $\phi = 45^\circ$  (equal mixing in units of zMIC), plotting  $\psi$  as a function of the combined dose  $z$ . The blue dotted line marks  $z = 1/\sqrt{2}$ , corresponding to both single-drug doses being at  $0.5\text{zMIC}$ , and the blue dashed line marks  $z = \sqrt{2}$ , corresponding to both single-drug concentrations being at  $1\text{zMIC}$ . Black, solid curves show the median surface-derived  $\psi$ , with corresponding Bliss (orange, dotted) and Loewe (teal, dashed-dotted) predictions evaluated along the same path ( $z, \phi$ ). Synergy/Antagonism corresponds to the reference model prediction of  $\psi$  being above/below the observed isobole (black).



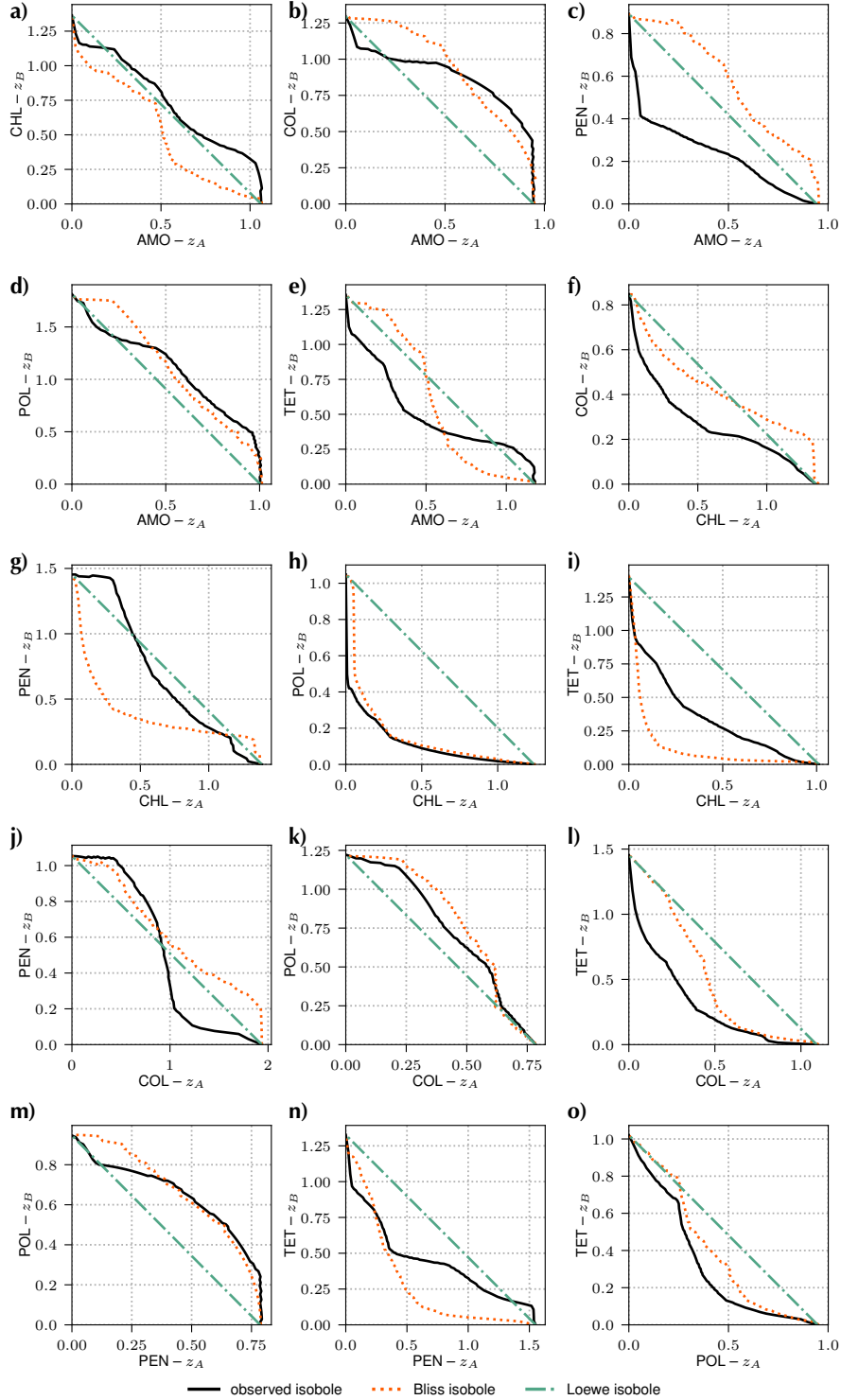
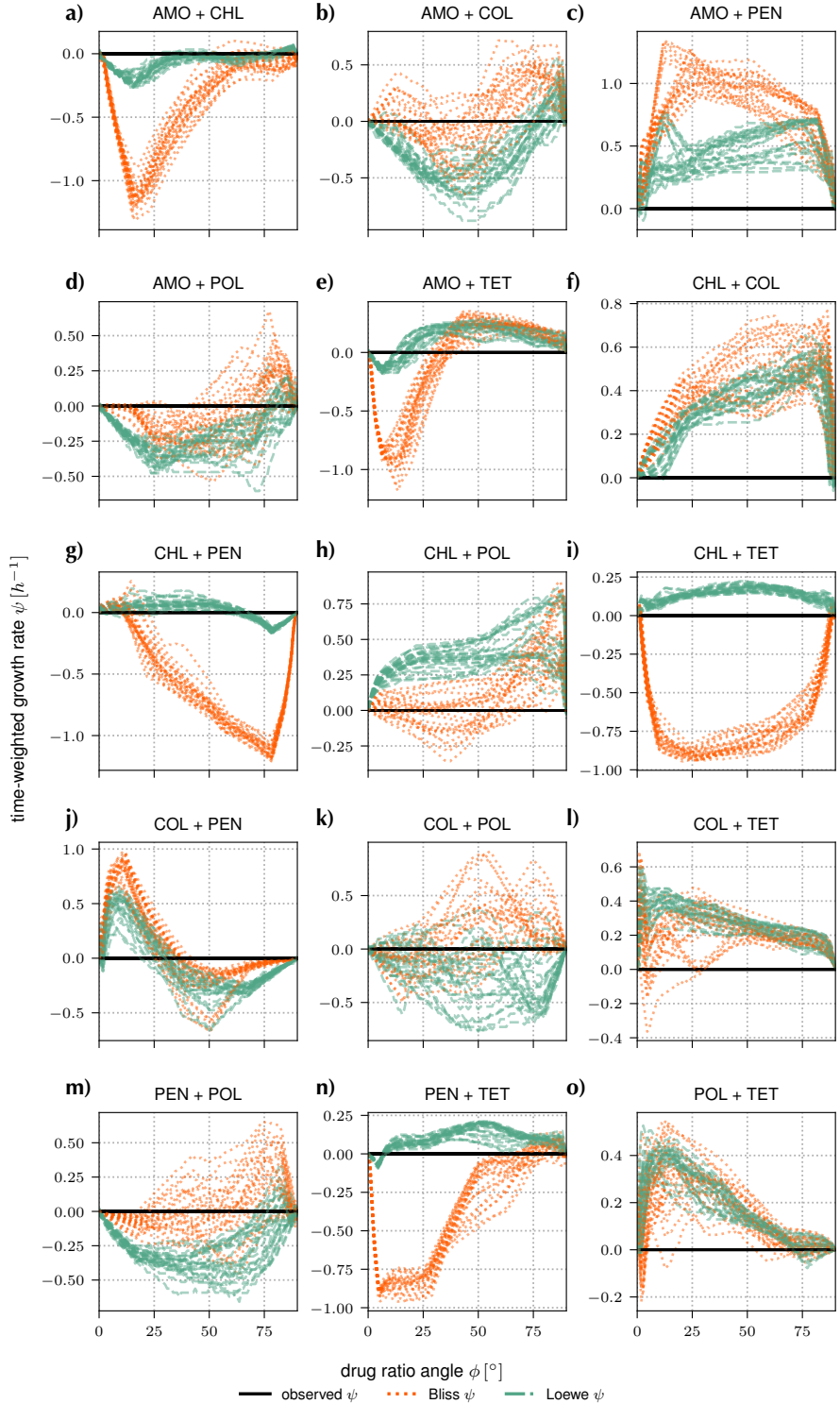


Fig. C9 – Panels a–o show isoboles of the time-weighted net growth rate at  $\psi = 0 \text{ h}^{-1}$  (black solid line) on the median response surfaces for all combinations. In addition, we plot the Loewe-based isobole (teal, dash-dotted), based on equivalent single-drug concentrations, and the Bliss-based isobole (orange, dotted), based on single-drug treatment effects. A curve lying left/below a reference model indicates synergy (less drug is needed to achieve the same effect), whereas a curve lying right/above indicates antagonism (more drug is needed to achieve the same effect).

Fig. C10 – Angular interaction profiles for all drug combinations. For each drug pair, we extract isoboles (paths of constant  $\psi = 0 h^{-1}$ ) from the  $\psi$ -surface splines. Along the path  $(z, \phi)_i$ , we evaluate Bliss- (orange, dotted) and Loewe- (teal, dash-dotted) based predictions for  $\psi$  and plot them as a function of the mixing angle  $\phi$ . Synergy/Antagonism corresponds to the reference model prediction of  $\psi$  being above/below the observed isobole (black).



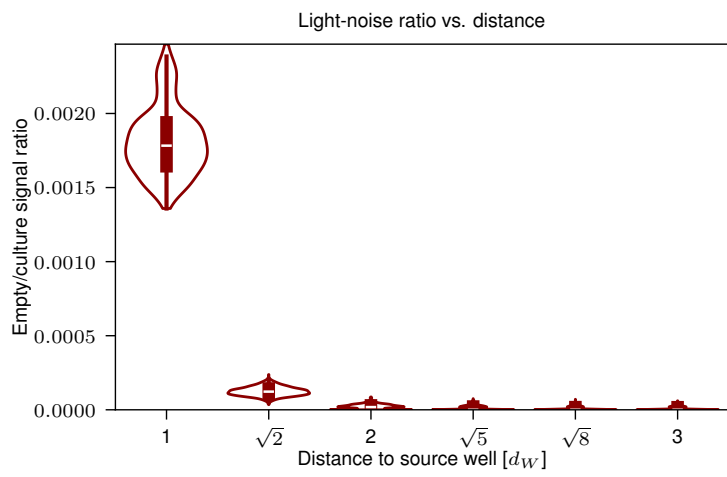


Fig. C11 – Stray light distribution, showing the fraction of light intensity emitted by a bioluminescent culture in a source well that arrives in neighbouring wells, as a function of the center-to-center distance to the source well in well lengths  $d_W$ . Here  $d_W = 1$  corresponds to the direct horizontal or vertical neighbour, and  $d_W = \sqrt{2}$  to a direct diagonal neighbour.

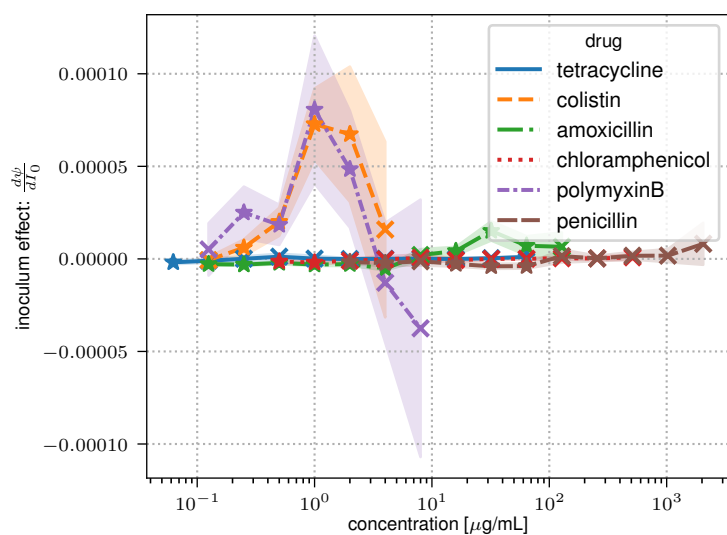


Fig. C12 – Slope of the inoculum effect ( $d\psi/dI_0$ ) as a function of drug concentration. For each drug and concentration, slopes ( $d\psi/dI_0$ ) are obtained by regressing the observed net growth rates across inocula, with uncertainty estimated from the regression standard error. Crosses denote concentrations with non-significant inoculum effects, whereas stars indicate statistically significant effects.

## Bibliography

- [1] .C. I. BLISS. "THE TOXICITY OF POISONS APPLIED JOINTLY1". In: *Annals of Applied Biology* 26.3 (1939), pp. 585–615. doi: 10.1111/j.1744-7348.1939.tb06990.x.
- [2] .S. Loewe and H. Muischnek. "Über Kombinationswirkungen". In: *Archiv für Experimentelle Pathologie und Pharmakologie* 114.5-6 (1926), pp. 313–326. doi: 10.1007/BF01952257.
- [3] .F. Pedregosa et al. "Scikit-learn: Machine Learning in Python". In: *J. Mach. Learn. Res.* 12 (Jan. 2011), pp. 2825–2830. issn: 15324435. doi: 10.48550/arXiv.1201.0490. arXiv: 1201.0490. url: <https://arxiv.org/pdf/1201.0490.pdf>.